

PL- ~~Capt O. RICE~~
~~T. D. A. 7264~~
NATIONAL AERONAUTICS AND SPACE ADMINISTRATION

Technical Memorandum 33-355

*Proceedings
of the
2nd Aerospace Mechanisms Symposium*

*Held at the University of Santa Clara
Santa Clara, California
May 4-5, 1967*

*Edited by
George G. Herzl*

**JET PROPULSION LABORATORY
CALIFORNIA INSTITUTE OF TECHNOLOGY
PASADENA, CALIFORNIA**

August 15, 1967



NATIONAL AERONAUTICS AND SPACE ADMINISTRATION

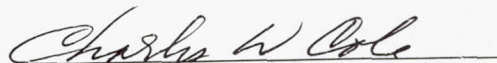
Technical Memorandum 33-355

*Proceedings
of the
2nd Aerospace Mechanisms Symposium*

*Held at the University of Santa Clara
Santa Clara, California
May 4-5, 1967*

*Edited by
George G. Herzl*

Approved by:



Charles W. Cole, Manager
Engineering Mechanics Division

**JET PROPULSION LABORATORY
CALIFORNIA INSTITUTE OF TECHNOLOGY
PASADENA, CALIFORNIA**

August 15, 1967

TECHNICAL MEMORANDUM 33-355

Copyright © 1967
Jet Propulsion Laboratory
California Institute of Technology

Prepared Under Contract No. NAS 7-100
National Aeronautics & Space Administration

Preface

The 2nd Aerospace Mechanisms Symposium, held at the University of Santa Clara on May 4-5, 1967, was sponsored by the University of Santa Clara, the Jet Propulsion Laboratory, and Lockheed Missiles and Space Company. The Symposium brought together approximately 200 representatives of more than 50 organizations concerned with mechanisms for use in space.

The organizing committee included Richard K. Pefley and Stein Weissenberger, University of Santa Clara; Alfred L. Rinaldo and George G. Herzl, Lockheed Missiles and Space Company; William J. Schimandle and Peter T. Lyman, Jet Propulsion Laboratory; and James L. Adams, Stanford University. This committee also served as the review board for papers submitted for the Symposium.

Management representatives of the sponsoring organizations, who gave active support and encouragement, were the Very Reverend Patrick Donohoe and Robert Parden, of the University of Santa Clara; William H. Pickering and Charles Cole, of the Jet Propulsion Laboratory; and Jack Nash, Wayland Griffith, Potter Kerfoot, and Roy Niewald of Lockheed.

Others who assisted in preparing for the Symposium included Eugene Fisher of the University of Santa Clara, who handled many of the details of the meeting, and Mrs. Mary Fran Buehler, Jet Propulsion Laboratory, who edited the papers presented.

The meeting was divided into four sessions, with the following chairmen:

May 4, Morning Session	Robert F. Steidel, University of California at Berkeley
May 4, Afternoon Session	Ralph Hallet, NASA Ames Research Center
May 5, Morning Session	Wallace C. Buzzard, Wright-Patterson Air Force Base
May 5, Afternoon Session	John B. Wilhelm, Martin Marietta Corporation

A feature of the Symposium was a panel discussion "Friction, Lubrication, and Bearings in Space." Members of the panel were Donald H. Buckley, NASA Lewis Research Center; Francis J. Clauss, Lockheed Missiles and Space Company; and Joseph Frisch, University of California at Berkeley. The moderator was W. J. Schimandle, Jet Propulsion Laboratory. In order to encourage uninhibited discussion, the panel session was not recorded. The introductory remarks of the three panel members may be found on pages 111 to 130 of these *Proceedings*.

George G. Herzl
Symposium Chairman

Organizations Represented at the 2nd Aerospace Mechanisms Symposium

Abrams Instrument Corporation	NASA Ames Research Center
Aerojet-General Corporation	NASA Langley Research Center
Applied Technology, Inc.	NASA Lewis Research Center
Ball Brothers Research Corporation	Northrop Corporation
Bellcomm, Inc.	Ohio State University
The Bendix Corporation	Perkin-Elmer Corporation
The Boeing Company	Philco-Ford Corporation
Dalmo Victor Company	Purdue University
DeHavilland Aircraft of Canada, Ltd.	Quantic Industries, Inc.
Douglas Aircraft Company	Radio Corporation of America, Astro-Electronics Division
Eastman Kodak Company	Ryan Aeronautical Company
Edgerton, Germeshausen & Grier, Inc.	Santa Barbara Research Center
Fairchild Hiller Corporation	Sperry Rand Corporation
General Electric Company	Stanford Linear Accelerator Center
General Motors Corporation Defense Research Laboratories	Stanford University
General Precision Link Group, Ordnance Division	Sylvania Electric Products, Inc.
Grumman Aircraft Engineering Corporation	TRW Systems Group
Hexcel Products Inc.	United States Air Force
Hughes Aircraft Company	United States Naval Postgraduate School
International Business Machines Corporation	United Technology Center
Jet Propulsion Laboratory	University of California, Berkeley
Jewett Company	University of California, Davis
Johns Hopkins University	University of Santa Clara
Lockheed Missiles and Space Company	Varian Associates
Martin Marietta Corporation	Vitro Laboratories
Microseal Corporation	Wright-Patterson Air Force Base

Contents

Space Molecular Sink Simulator Facility , by J. B. Stephens	1
Latch Diaphragm Release Mechanism , by G. Gibbons, A. Ventura, and A. Kaehler	9
A Stepper Motor for the Surveyor Spacecraft , by Frank A. Glassow	15
The Design of Mechanical Linkwork for Aerospace , by Bernard Roth	25
Lunar Orbiter Photo-subsystem Mechanisms , by George Bradley	33
Yo-Yo Despin Mechanisms , by Kenneth S. Bush	41
Deployable Solar Array , by T. Berry	51
Surveyor Television Mechanisms , by J. B. Gudikunst	59
Lunar Module Alightment System , by Richard A. Hilderman, William H. Mueller, and Morton Mantus	67
Mechanical Design of Scanning Instruments , by G. A. Bunson	77
Collet Release Mechanism , by Daniel O. Ramos	85
The Surveyor Thermal Switch , by T. E. Deal	93
The Integrated Rocket Spin-Up Launch Mechanism , by John Hillan	101
The Behavior of Lubrication System Components in a Vacuum Environment , by Donald H. Buckley	111
Lubrication As Part of Total Design , by Francis J. Clauss	121
Surface Interaction Between Aluminum Single Crystals at 10^{-10} Torr , by Joseph Frisch	125
Double-Acting, Rotary-Solenoid-Actuated Shutter , by Allen G. Ford	131
The BI-STEM—A New Technique in Unfurlable Structures , by J. D. MacNaughton, H. N. Weyman, and E. Groskopf	139
Despinning the ATS Satellite , by J. P. Dallas	147
Weld-Alloy , by John C. McDonald and J. C. Olsen	155
New Closed Tubular Extendible Boom , by Bruce B. Rennie	163
Self-Destruct Charge Ordnance Component of the Agena D Vehicle Self-Destruct System , by Allan Howard Smith	171
List of Attendees	179

Opening Remarks

George G. Herzl
Lockheed Missiles and Space Company

In the name of the Symposium's organizing committee, I wish to welcome you to the 2nd Aerospace Mechanisms Symposium. This Symposium is sponsored by the University of Santa Clara, the Jet Propulsion Laboratory of the California Institute of Technology, and Lockheed Missiles and Space Company. We are pleased to have attendees from many parts of the United States and from abroad, representing government agencies, universities, and industrial organizations.

Types of mechanisms and mechanical components are changing very rapidly to satisfy the ever-increasing requirements for aerospace performance. The size, the number of components, and the cost of mechanisms are constantly increasing—thus creating a severe demand for greater reliability in mechanisms. At the same time, the task of the mechanisms designer is becoming increasingly difficult, since fuller utilization of mechanisms in the space environment requires knowledge and ingenuity beyond that required in conventional mechanisms design.

The accumulation of necessary empirical or research data is often limited by our lack of knowledge about the behavior of mechanisms in the space environment, or by our lack of available time. The economic factor involved in designing mechanisms under increasing competition is also of growing importance. Since a sizable portion of the entire United States space effort is devoted to the design and fabrication of aerospace mechanisms, it is of the utmost importance to collect and disseminate all available and up-to-date information about mechanisms. To this end, we are sponsoring this Symposium to provide a common platform for discussing problems encountered in mechanisms for many aerospace applications. We hope to achieve a great deal of cross-pollination of ideas among the various projects and among the participants of the Symposium. Mechanisms are the very backbone of modern spacecraft, and there is every indication that future spacecraft will contain even more sophisticated mechanisms.

In organizing this Symposium, we were encouraged by the favorable comments about the First Aerospace Mechanisms Symposium, held in 1966. This year, we have extended the program to include a panel discussion on bearings and lubrication in space, with a question-and-answer period. We have also allotted more time for discussion after each paper and have added informal gathering sessions at the end of each day.

We received many fine papers for this Symposium, and I wish to thank the authors for their efforts. We had more good papers, however, than the available time would permit. Therefore, we selected for presentation those papers that are of widest possible interest on various types of aerospace mechanisms and those that convey the most generally applicable experience. We urged each author to discuss the blind alleys, and especially the failures, he encountered in the course of his work. He learned his lesson from them, and we want to learn ours. If this Symposium achieves nothing else but the prevention of one failure—in flight or in development—it will have performed a valuable service to the overall United States space effort.

Space Molecular Sink Simulator Facility*

J. B. Stephens
Jet Propulsion Laboratory
Pasadena, California

The results of research, design, and development efforts for a space molecular sink simulation facility now under construction are summarized. The chamber wall shrouds capture 99.97% of most of the gases that emanate from a test item. Cryogenic quartz crystal microbalances will be used to measure the molecular fluxes from the test item, and a mass spectrometer will be used to identify them.

I. Introduction

This paper summarizes the description and uses of a space molecular sink simulator facility (10-ft MOLSINK) currently being completed at JPL.¹ (An 18-in. pilot model has been in operation for about 1½ years.) The immediate objective of the MOLSINK project is to provide a prototype vacuum chamber in which surface-effect phenomena related to spacecraft technology can be studied.

*This paper presents the results of one phase of research carried out at the Jet Propulsion Laboratory, California Institute of Technology, under Contract No. NAS 7-100, sponsored by the National Aeronautics and Space Administration.

¹A detailed description and analysis of the MOLSINK facility will be presented in *Space Molecular Sink Simulator Facility*, Technical Report 32-1110, Jet Propulsion Laboratory, Pasadena, Calif., to be published.

As a by-product of developing the facility, refining the operating techniques, and calibrating the instrumentation, actual spacecraft components and materials can be experimented with and tested in the 10-ft MOLSINK chamber. Cold-welding of mechanisms, degradation of thermal control coatings, contamination of optical elements, interaction of ion-engine and chemical rocket exhausts with spacecraft surfaces, and viability of microorganisms in the space environment are examples of interest to spacecraft designers. These require a highly permissive environment, such as that produced by the MOLSINK, for acceptable experimental investigation. In addition, investigators in the basic research field of gas-surface interactions have expressed interest, and some experiments involving low-energy neutral molecular flux impinging on chemically active cryogenic surfaces are planned.

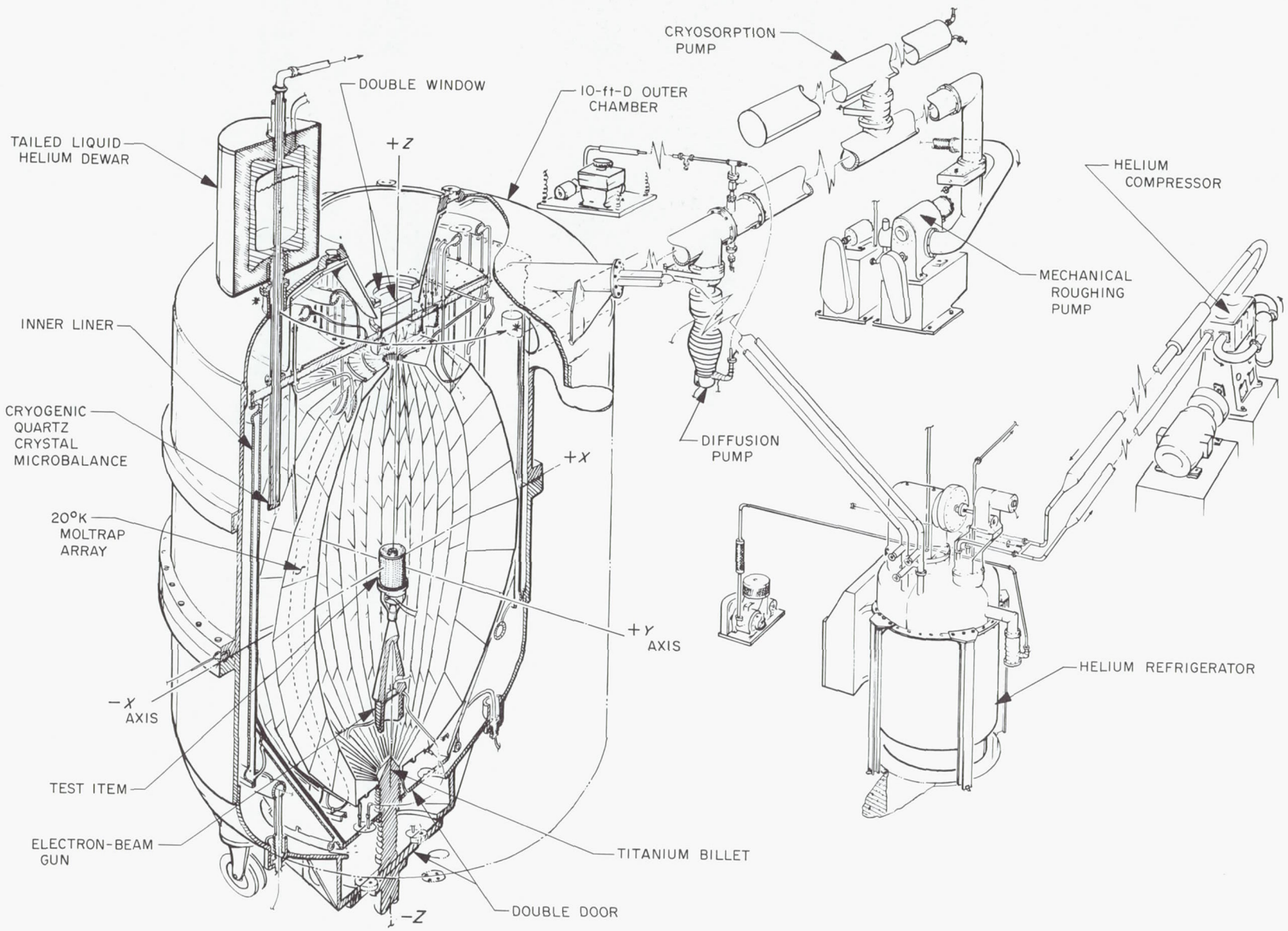


Fig. 1. Schematic drawing of the MOLSINK facility

II. MOLSINK Operation

A MOLSINK chamber differs from other extreme-high-vacuum chambers in that its walls pump, or capture, virtually all the gas molecules that impinge upon them. The overall facility is schematically presented in Fig. 1. The outer carbon steel pressure vessel is sealed with O-rings and is rough-pumped with a combination of a mechanical pump and a large sorption pump. It is sustained in the high-vacuum range with an oil diffusion pump. The stainless steel vacuum-tight inner liner is cooled with liquid nitrogen and is rough-pumped through the inner door, which is closed during sustained operation. Figures 2 and 3 show the chamber being reassembled after decontamination by glass bead blasting. The molecular trap is shown in its shipping frame in Figs. 4 and 5. This aluminum sheet-metal wedge-fin array will be cooled to 20°K by a 1000-w helium refrigerator and

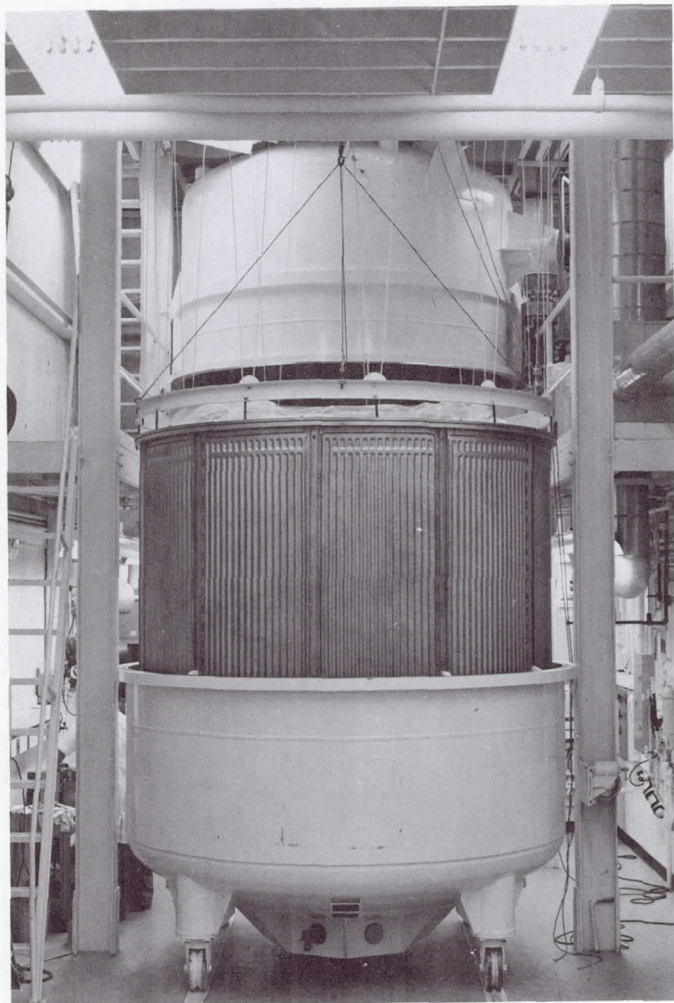


Fig. 2. Assembly of inner liner of MOLSINK facility

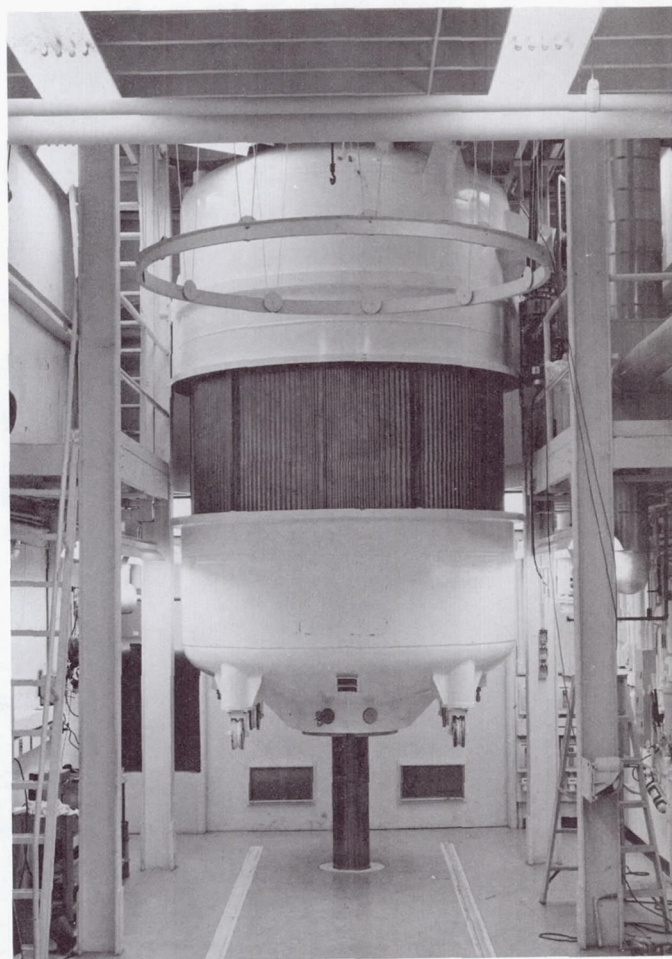


Fig. 3. Assembly of lower half of MOLSINK chamber, with hydraulic ram

will allow only a few in 10,000 O₂, N₂, Ar, CO, and CO₂ molecules to return in the direction of the test item.

This molecular trap array is also expected to be a very efficient chemisorption pump, in that it will be continuously coated on its inner surface with titanium produced by the electron beam sublimator inside the cone shown in Fig. 6. Calculations indicate that hydrogen will be chemisorption-pumped at 7×10^6 liters/sec and that other cryopumped gases will probably be chemically fixed on the surface, thus preventing their evaporation during warmup.

III. Theoretical Analysis

A theoretical analysis shows the radial-fin and wedge-fin arrays to reflected molecular flux distributions as

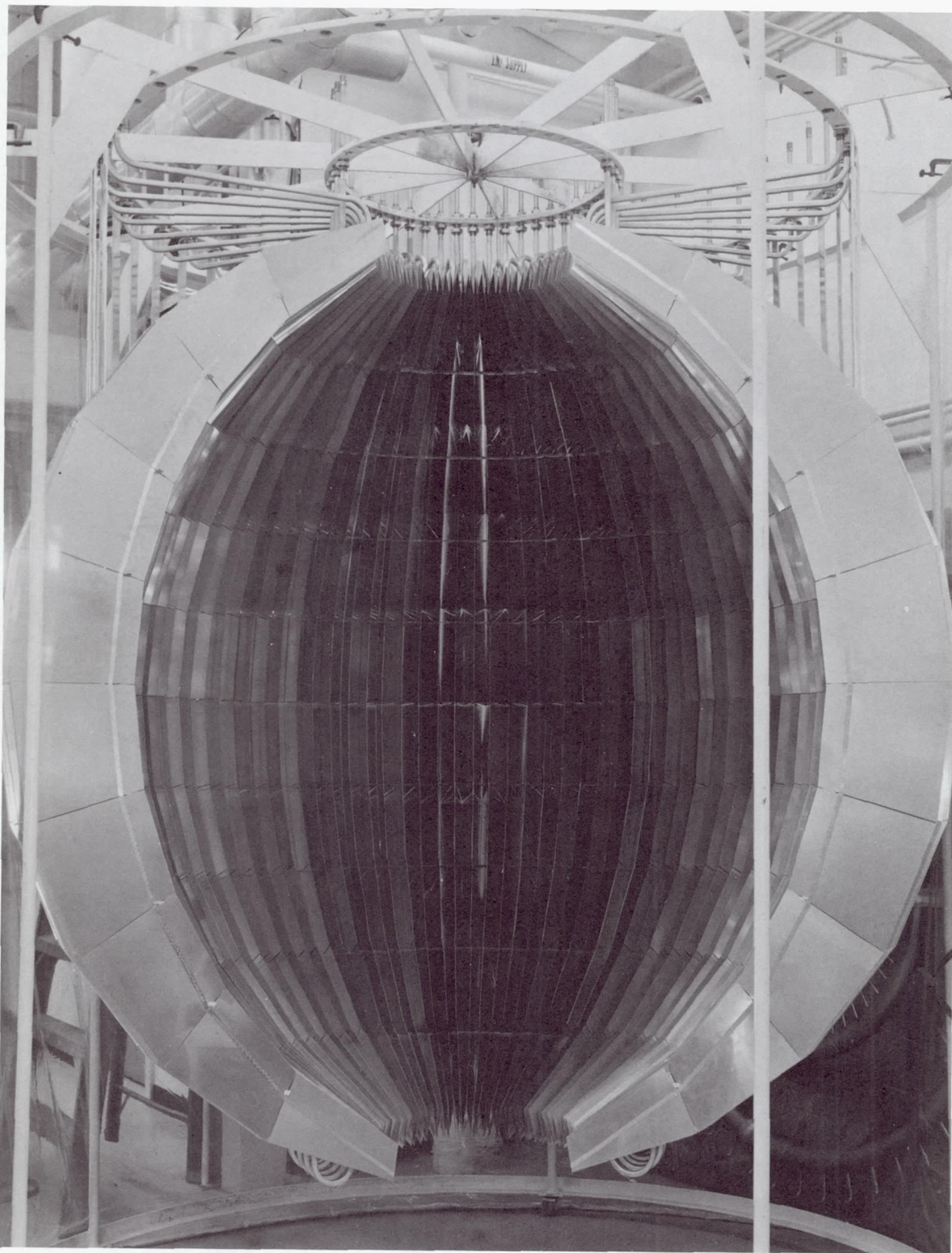


Fig. 4. One half of the molecular trap, in shipping frame

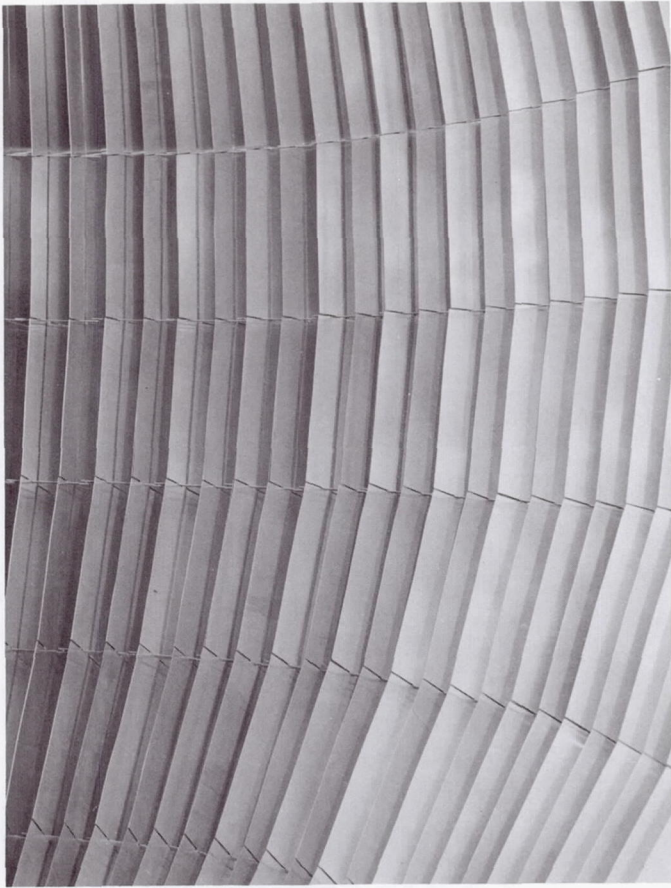


Fig. 5. Closeup of the molecular trap

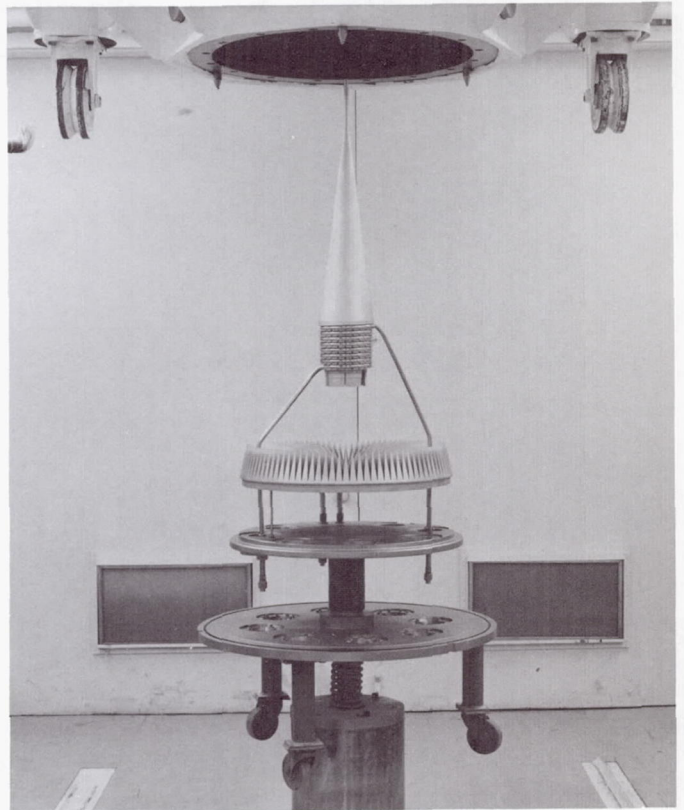


Fig. 6. Partly assembled double door with electron-beam gun cone in place

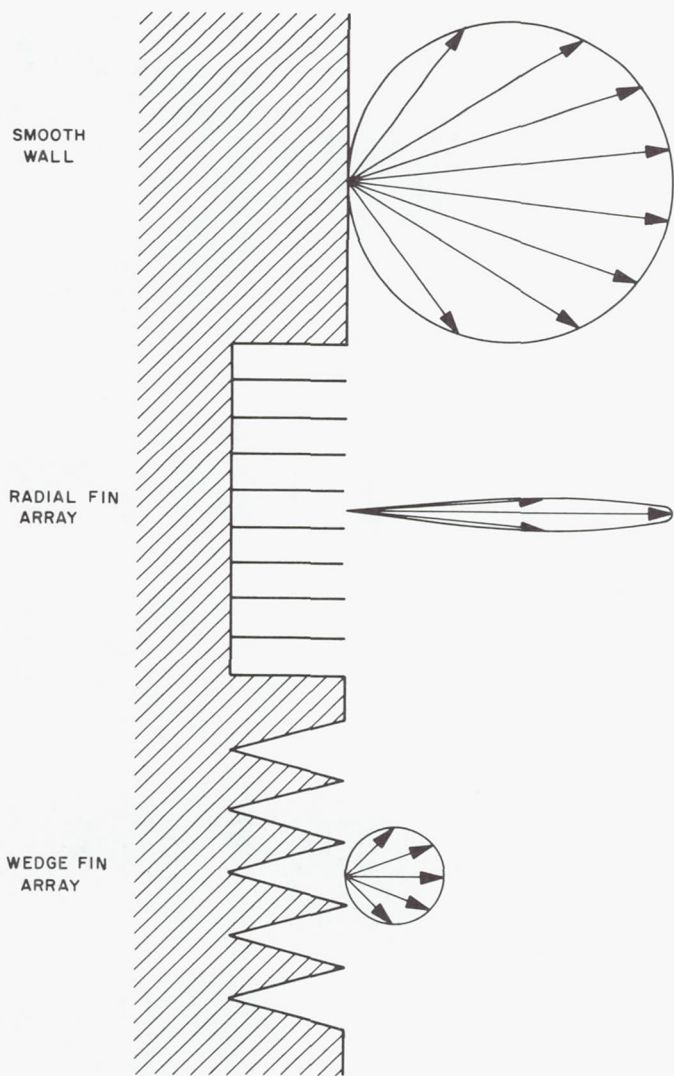


Fig. 7. Reflected molecular flux distributions of radial-fin and wedge-fin arrays, compared with that of a flat surface

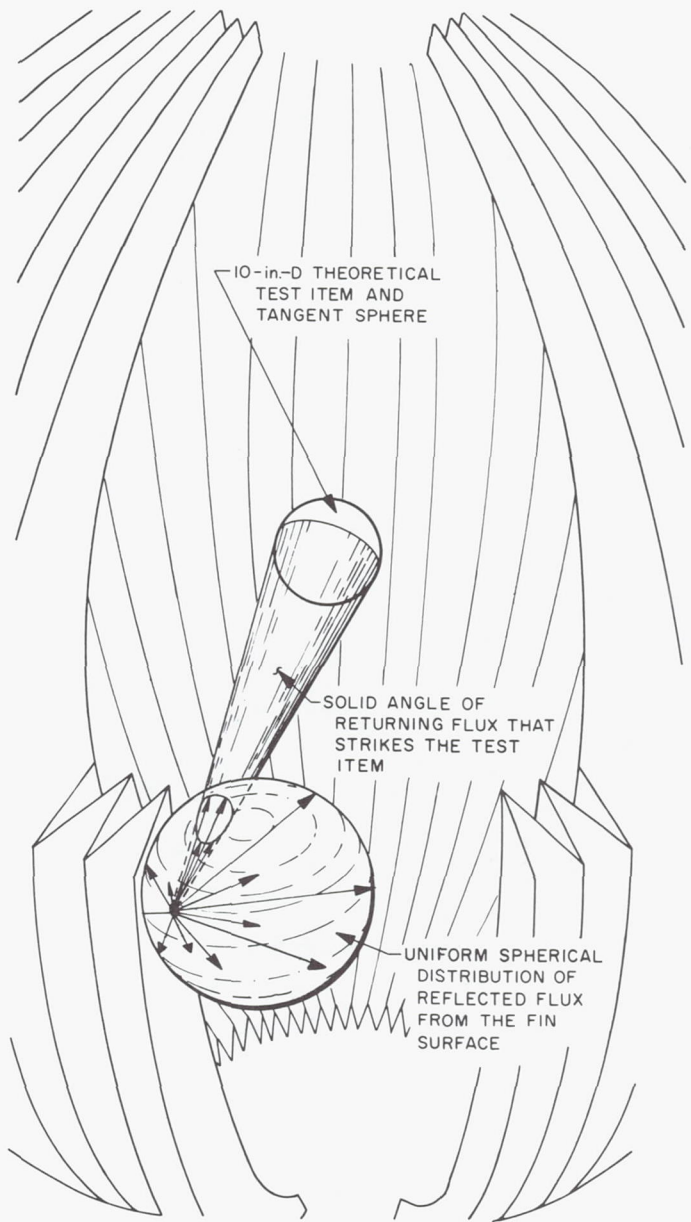


Fig. 8. The relation of Knudsen's cosine distribution to the actual molecular trap array surfaces

shown in Fig. 7, in comparison with that of a flat surface. Figure 8 relates Knudsen's law to the molecular trap configuration where all wall surfaces exposed to the test item are canted as much as possible relative to the test item. This law states that the number of molecules emerging from a surface in a certain direction is proportional to the cosine of the angle made by that direction and the normal to the local surface. As can be seen in Fig. 8, most of the rebounding molecules restrike the adjacent fin surface, where an even larger fraction are captured due to their initial accommodation at the first encounter.

IV. Instrumentation

Temperature and pressure instrumentation of the chamber will include conventional thermocouples, gas bulb thermometers, quartz crystal thermometers, thermocouple gages, and high- and low-pressure ionization gages.

The results of most surface-effect experiments and tests would be of little analytical value without instrumentation to determine the quantity and direction of the

various molecular fluxes impinging on and emanating from the test item or experiment. Also of interest is the time rate of change of the mass of gases interchanging with surfaces at various temperatures and chemical compositions. Two instruments are currently being considered to provide this information: the cryogenic quartz crystal microbalance and a cryogenic mass spectrometer. Both of these instruments are planned to be mounted on the tail of the liquid-helium Dewar shown in Fig. 1 and will operate at 3°K. The cryogenic quartz crystal microbalance, which was developed in the research and development program for this facility and has been widely used in the pilot model, has demonstrated a sensitivity

of 1/100 of one monolayer. The mass spectrometer design is not fully underway, but its operation at 3°K with a cold space charge ionizer and a combination mass and ion detector should provide adequate sensitivity.

V. Conclusions

Because of the space limitations of this paper, no attempt has been made to cover this subject completely. Rather, it is hoped that an introduction to this new kind of facility will stimulate consideration of experimental explorations which heretofore have not been possible.

Latch Diaphragm Release Mechanism

G. Gibbons, A. Ventura, and A. Kaehler
Lockheed Missiles and Space Company
Sunnyvale, California

The design and development of a mechanism for the separation of payloads in space are described. Development test failures of the diaphragm and associated structures, and other development problems, are also discussed. The diaphragm release mechanism was qualified by (1) flight confidence tests demonstrating clean separation with no indication of release abnormalities, and (2) flight tests that proved the reliability of the integrated structure and the release mechanism. These tests satisfied the critical requirements for trajectory accuracy and release time.

I. Introduction

The purpose of this study was to design a structural attachment to release and separate a payload from a rocket in flight. The attachment was required to be light-weight and inexpensive, to fit within the structural constraints and restrictions of the envelope, and to release quickly and cleanly.

The design constraints established for the latch diaphragm separation device precluded the use of auxiliary timed electrical signals, batteries, or a pyrotechnic assembly. Moreover, because separation joints involving hooks or balls require a preload larger than the moment introduced by side loads, it was desirable to design a joint that did not require a preload.

The specific design goals for the separation device were as follows:

- (1) High reliability.
- (2) The ability to produce a clean separation without fragmentation.
- (3) The ability to withstand temperatures of 250° F.
- (4) An indefinite shelf life.
- (5) Minimum weight.
- (6) Minimum equipment requirement for installation and checkout.

II. Design Selection

During conceptual design studies, a method of payload separation in conjunction with a rocket motor was required. The decision was made to utilize the payload-ejection rocket motor thrust and nozzle-plug system for initiation of separation. After several preliminary layouts, a collapsible-type mechanical-release diaphragm was selected for development testing.

During this testing, three preliminary configurations of the latch diaphragm were evaluated (Fig. 1), and Configuration B was selected (Fig. 2). This testing consisted of impacting an aluminum cylinder on the latch diaphragm and measuring the deflection. The cylinder was accelerated to the required velocity of 100 ft/sec with the HY-GE Shock Simulator.

The selected configuration consists of a structural connection and separation component that is basically composed of a flat plate with slots running into a circular

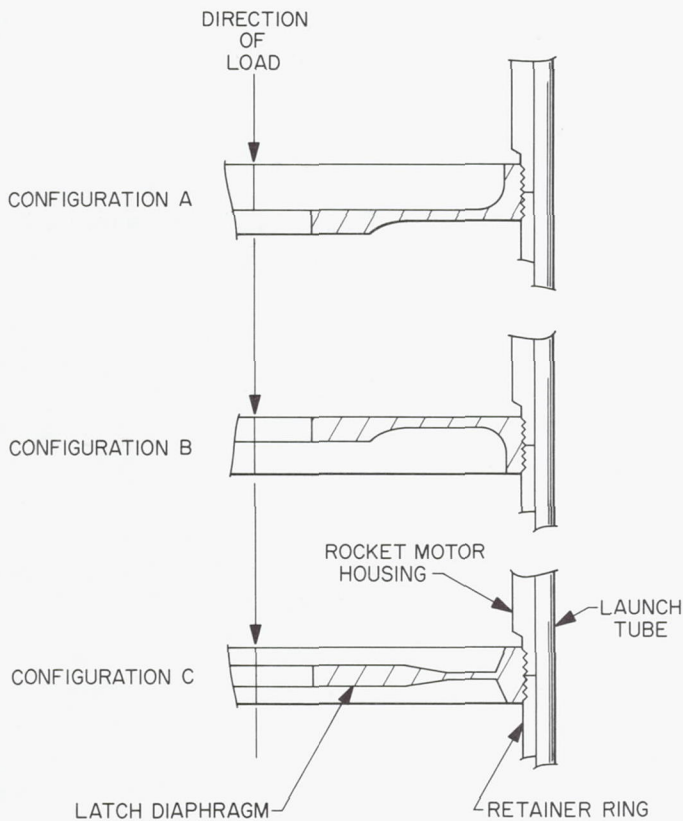


Fig. 1. Latch diaphragm configurations. Each configuration was tested with two variations each, created by varying the number of peripheral segments



Fig. 2. Selected diaphragm Configuration B. Shown after the testing described in Sec. II

hub, producing rectangular peripheral segments (legs) on which externally threaded flanges are provided. These flanges are used to structurally attach the rocket motor housing to the retainer ring at the separation interface (Figs. 1 and 2).

III. Operation of Diaphragm at Release

Release is based upon the fact that the diaphragm deforms uniformly around its periphery, thus releasing the rocket motor housing completely at the threaded interface (Fig. 3) when subjected to the following force factors:

- (1) Rocket motor nozzle-plug impact.
- (2) Exhaust gas dynamic pressure.
- (3) Rocket motor thrust-tension load.
- (4) Torque preload of the threaded joint.
- (5) Exhaust temperature effects.

The rocket motor nozzle-plug impact and the exhaust gas dynamics are the two major forces effecting release. The energy available to release the payload or collapse the diaphragm is approximated by assuming that the impact load is applied symmetrically and that half the

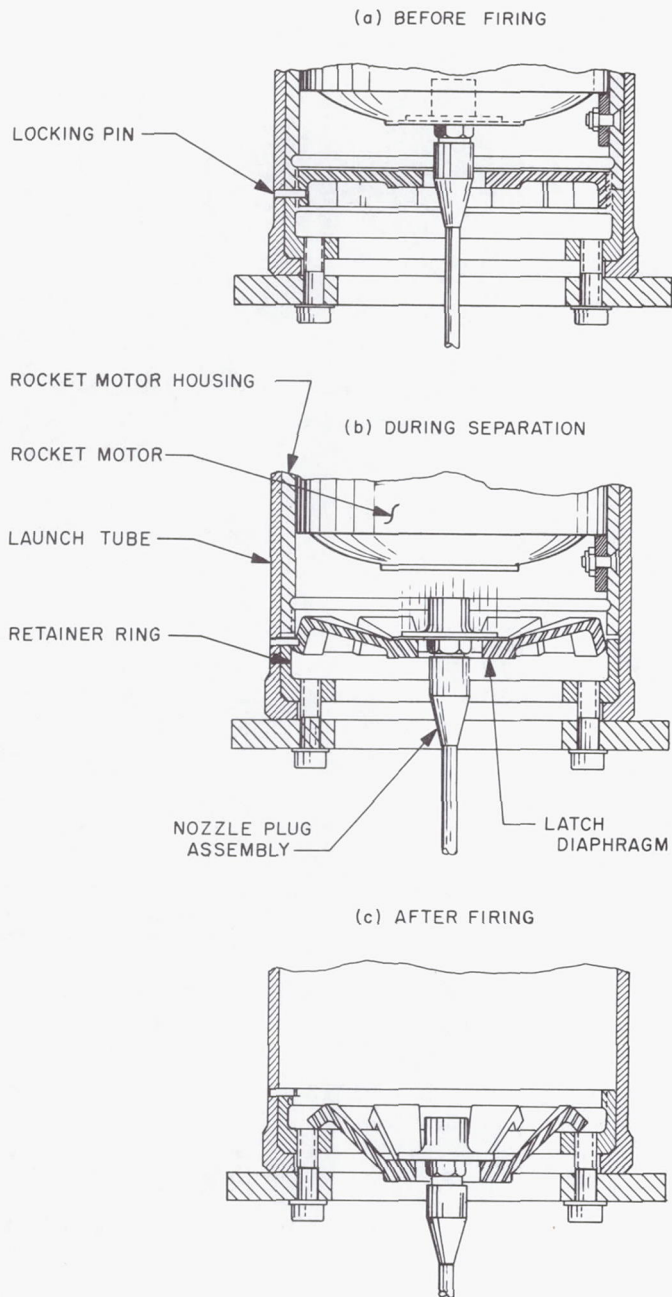


Fig. 3. Separation sequence

energy is transferred from the nozzle-plug system to the diaphragm. The energy equation then is

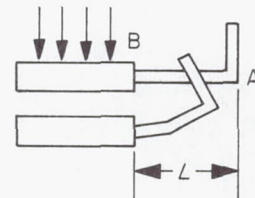
$$PY = \frac{W}{4g} (v_1^2 - v_0^2)$$

where P is the total impact load, Y is the deflection of the hub, W is the weight of the plug, and v is the impact velocity.

The spring constant of the mechanism is

$$K = \frac{Y}{P} \quad \text{and} \quad PY = \frac{Y^2}{K}$$

The latch diaphragm segments (legs) connecting the threaded flanges to the central circular hub are rectangular in section, as shown below:



The segments may be assumed fixed at the flange end A, and free but guided at the inner hub B, where the load is applied. Under these conditions the deflection at point B is

$$Y = \frac{P_s L^3}{12EI}$$

or the spring constant per segment becomes

$$K_s = \frac{Y}{P} = \frac{L^3}{12EI}$$

where Y is the deflection, K_s is the spring constant, and P_s is the pressure per segment (E is the modulus of elasticity; I is the modulus of inertia).

IV. Dynamic Analysis of Diaphragm

Rocket motor chamber pressure at the time of nozzle-plug blowout is approximately 300 psi.

Gas dynamic forces, acting on the nozzle plug after blowout, are added to determine the total velocity of the nozzle plug, which is approximately 100 ft/sec. The nozzle-plug characteristics are as follows:

- (1) Weight, 0.2 lb.
- (2) Outer diameter, 1.2 in.
- (3) Velocity at impact, 100 ft/sec (approximately).

The dynamic response analysis shows that the tension load on the separation joint, which is attributed to rocket motor thrust and pressure buildup, is approximately

350 lb. Approximately 0.25-in. deflection at the center of the diaphragm is indicated, producing 0.09-in. movement at the threaded flanges. This is ample for the occurrence of separation.

V. Testing Procedures

Testing included subsystem tests and flight confidence tests.

A. Subsystem Tests

Subsystem tests confirmed preliminary design concepts and functional adequacy of the diaphragm configuration. Package release (first motion) occurred in 7.5 and 7.7 msec after fire signal to the rocket motor. The first visual sign of ignition (smoke) occurred in 5.1 msec; thus, the time required to build up rocket motor pressure and shear out the nozzle plug is 5.1 msec. By subtracting 5.1 msec from 7.7 msec, a rough estimate is established for the time required for release of the package (2.6 msec). This would indicate that the latch diaphragm is released immediately upon impact by the rocket motor nozzle plug. Visual examination of the specimens indicated that there was no damage to the threads on the rocket motor housing or retainer ring (Fig. 4). However, all the peripheral segments (legs) (Fig. 5) were melted off the circular hub

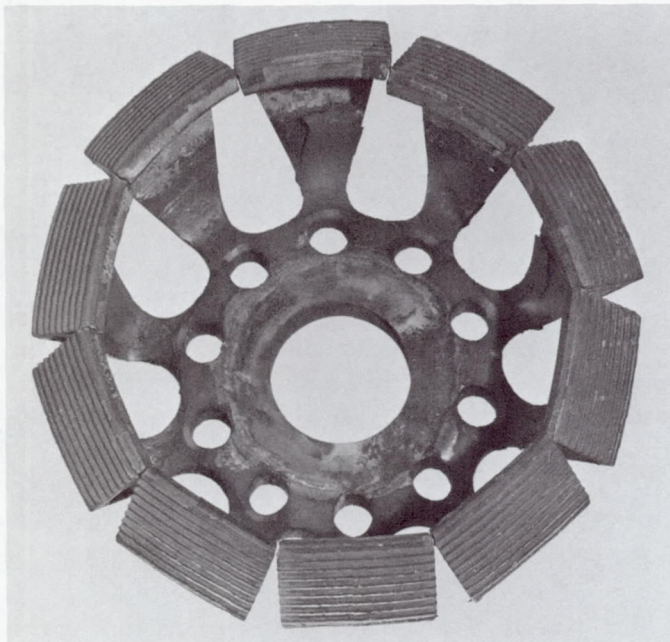


Fig. 4. Latch diaphragm, after firing

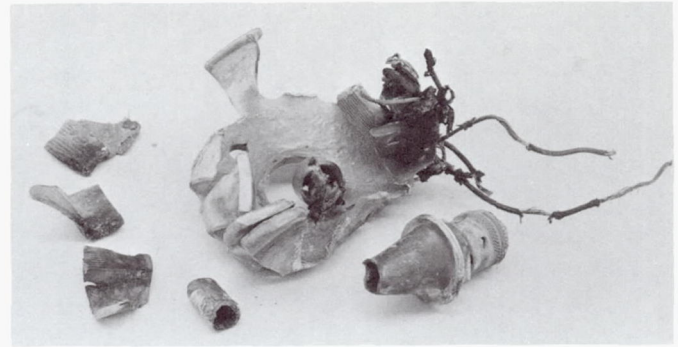


Fig. 5. Latch diaphragm and nozzle plug fragments after functional test

by the temperature and pressure created by the rocket motor exhaust gases. Since this fragmentation was not considered satisfactory for this mission, a material substitution was made from aluminum to steel. Also, at this time, the diaphragm was installed with the threaded flanges up instead of down, thus allowing the diaphragm to collapse and fall back instead of bending. A comparison is offered in Fig. 1 between Configurations A and B.

B. Flight Confidence Tests

Environmental and functional events performed on the retaining structure and release diaphragm proved satisfactory with two exceptions, described below.

During random vibration, the diaphragm became unthreaded and released the payload. A dowel pin was pressed into the launcher housing to prevent diaphragm unthreading (Fig. 3a). A 200-psi buildup occurred in the launch tube at about 15 msec after fire signal, which coincides with the maximum pressure peak of the rocket motor. It was determined that the steel diaphragm was blocking the gas flow, and additional venting was added to the launch tube (Fig. 6).

During two simulation tests, the trajectory accuracy was 1.3 and 0.9 deg, respectively, from a straight line, as determined on a 30-ft-long vertical range.

VI. Conclusion

A critical need is expressed in certain programs for a separation device that is highly reliable, inexpensive, and light in weight. Flight tests show that the latch diaphragm release mechanism, described in this paper, meets these requirements.

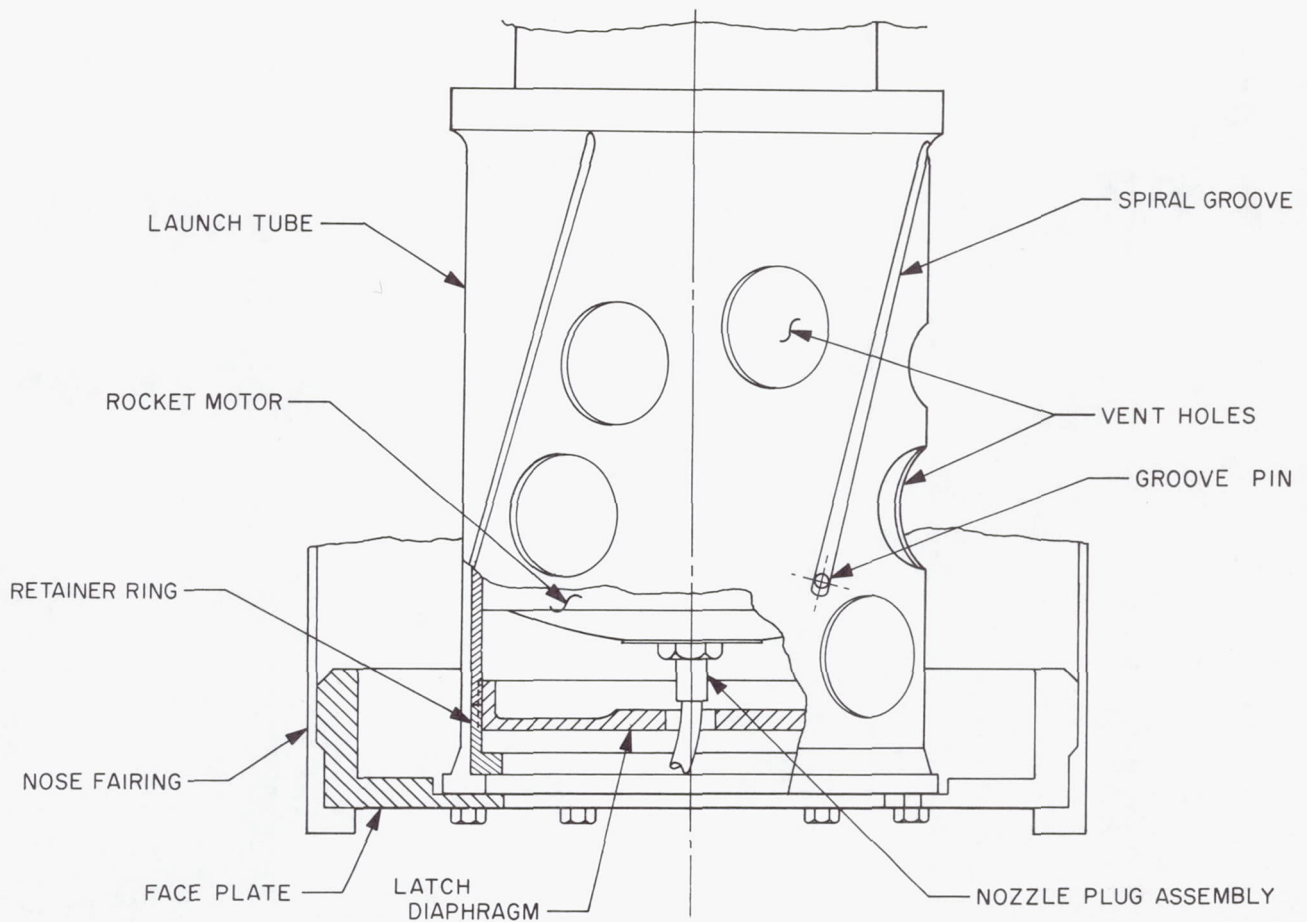


Fig. 6. Steel latch diaphragm shown inverted in payload launcher assembly

Current designs for the future use of the latch diaphragm in missile programs indicate that the diaphragm

material should be aluminum with a rubber thermal covering, to provide the best weight and function trade-off.

A Stepper Motor for the Surveyor Spacecraft

Frank A. Glassow
Hughes Aircraft Company
Los Angeles, California

The high-gain TV transmitting antenna and the solar panel on Surveyor are pointed at the earth and sun respectively by means of a four-axis positioning mechanism. Each axis of the positioner is rotated with a solenoid stepper motor and appropriate reduction gearing for producing adequate torque and step size. The stepper motor employs a unique camming arrangement for converting the linear motion of the solenoid to shaft rotation. Optimization of the magnetic structure and coil characteristics has resulted in a high torque-to-weight ratio as a basic feature of the design.

Analysis and intensive development testing resulted in the capability to exceed required performance levels by a 2-to-1 margin. Conclusions indicate that the stepper motor provides extremely desirable characteristics for space mechanisms.

I. Introduction

The success of the *Surveyor* spacecraft depends heavily on its ability to position a high-gain TV transmitting antenna normal to the earth line and a solar panel normal to the sun line. High-quality 600-line TV pictures are obtained with relatively low power as a result of the directional properties of the planar array antenna, and battery power is replenished by means of the solar panel

at all times the sun is in view. A four-axis positioning mechanism is used on *Surveyor* to accomplish these functions. It is the central mast of the spacecraft and contains the necessary bearings, drives, position indicators, locking devices, and supporting structure for all positioning requirements. Figure 1 illustrates the spacecraft with the antenna and solar panel positioner mounted near the center of the space frame.

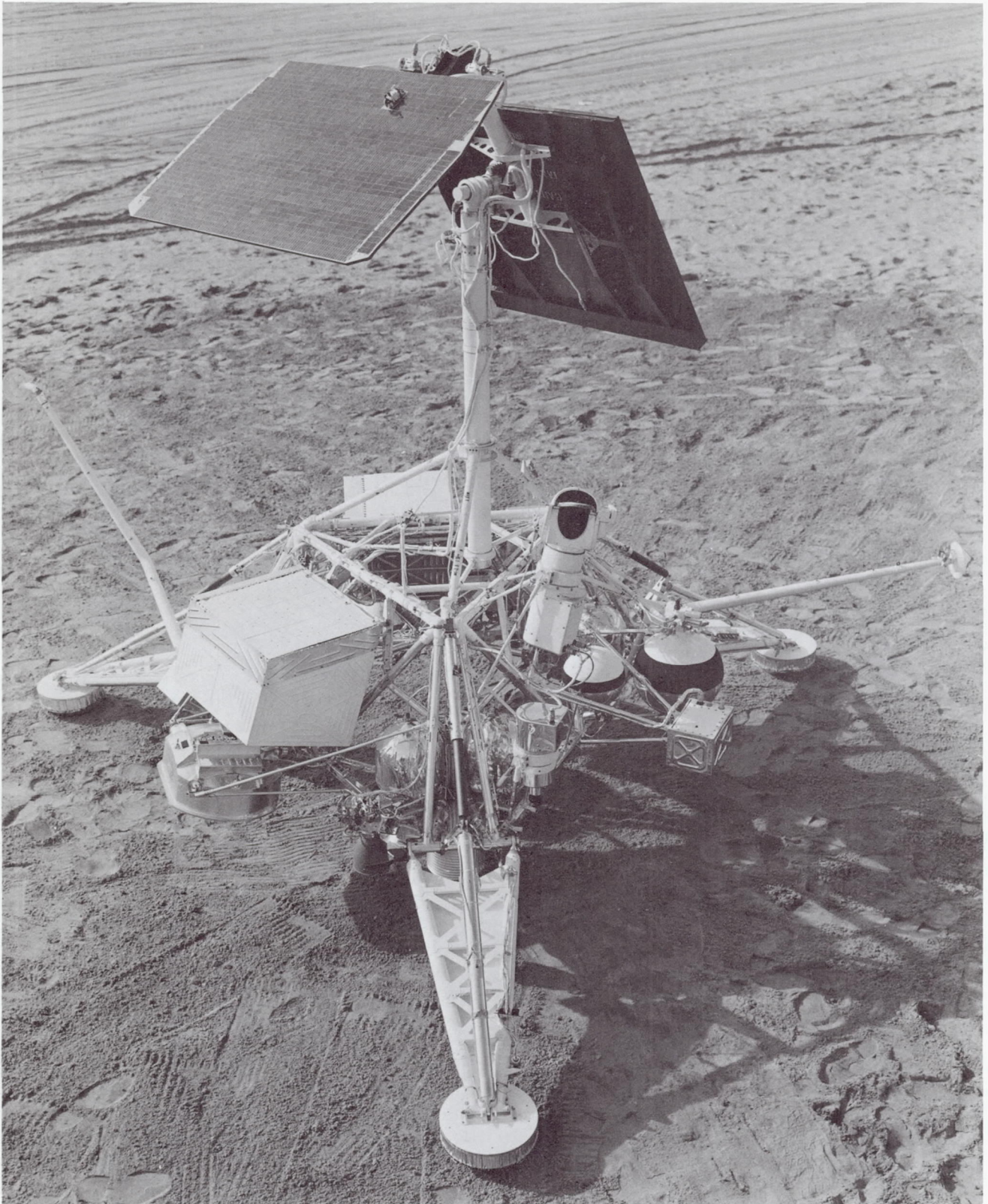


Fig. 1. The Surveyor spacecraft

II. The Antenna/Solar Panel Positioner

Figure 2 illustrates the positioning mechanism in semi-schematic form with angular travel of roll, elevation, polar, and solar axes indicated. During launch and landing all axes are locked either by pyrotechnically actuated lock pins or irreversible gears so that excessive loads are not reflected into the drive transmissions. In flight the roll and solar axes are unlocked, permitting solar energy to be collected for battery charging. These axes are re-locked with spring-actuated lock pins shortly before landing.

ing so that landing shocks will not damage the drives. After landing, squibs are fired to unlock all axes, thereby permitting complete articulation of the mechanism.

III. The Drive Assemblies

Each of the four drives in the positioner employs an identical stepper motor that will rotate in 40-deg increments in either direction, depending on which coil receives direct current pulses. For the roll, elevation, and

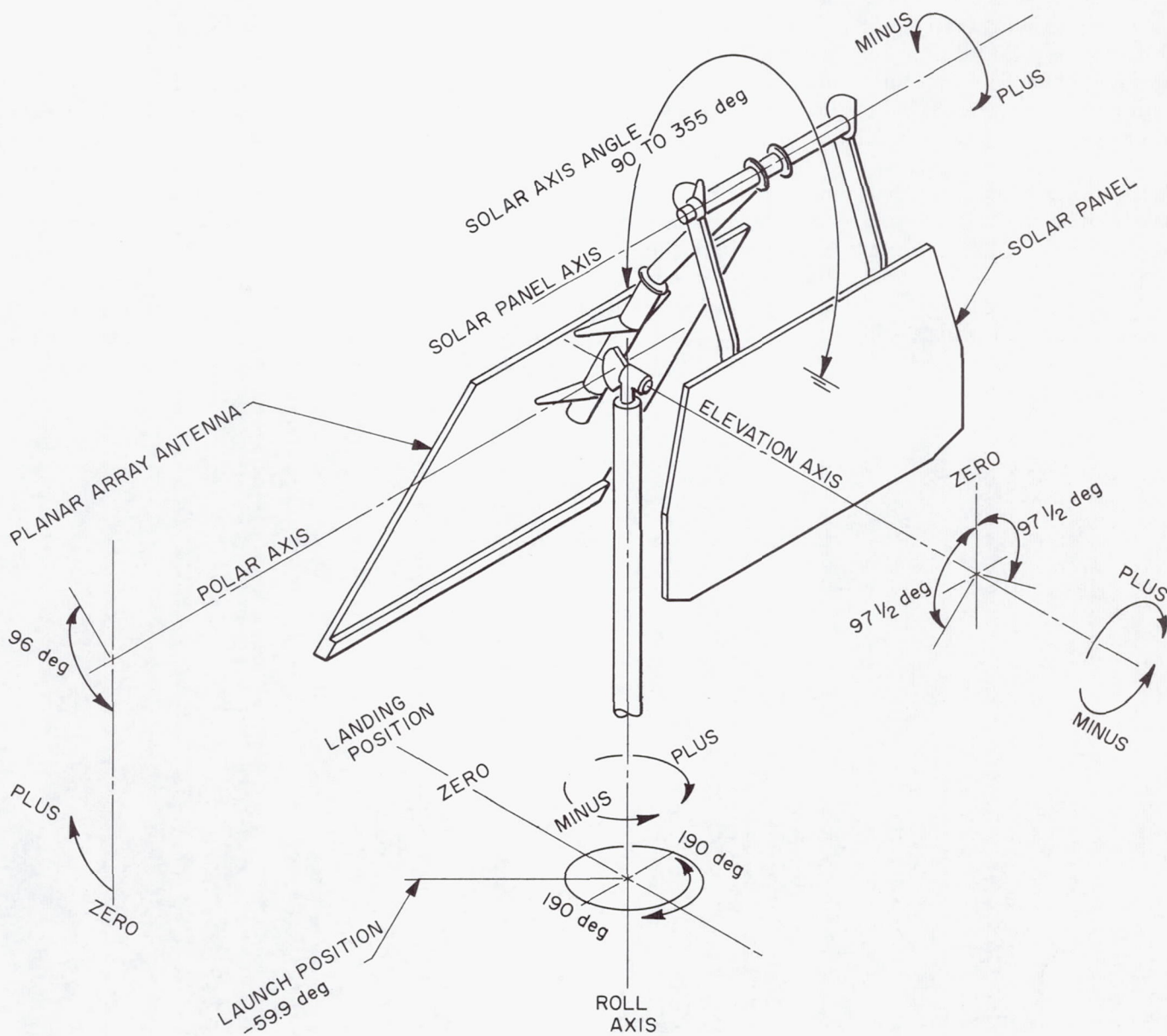


Fig. 2. The Surveyor antenna/solar panel positioning mechanism

solar axes, the motor drives into a three-stage planetary transmission having a ratio of 289 to 1. The polar axis drive employs a two-stage planetary gear train of 14.6-to-1 ratio, but it drives a cone worm gear in a worm-sector gear combination that provides additional reduction and irreversibility. A typical drive assembly appears in Fig. 3. The drive transmission, motor, and position-indicating potentiometer are contained within a thin-walled cylindrical housing that is closed at the rear with a soldered cover plate. The only other opening to the housing is at the output shaft, where a spring-loaded Teflon seal is employed. The weight and complexity of a hermetic seal at the output shaft were avoided in favor of design features that permit operation in the vacuum of space. The shaft seal is provided with the intent of maintaining a pressure within the drive mechanism somewhat higher than that encountered in outer space after gas flow out of the housing changes from laminar to molecular.

The gear train employs aluminum spur gears mounted on aluminum pins. Hard-anodize finish is used in combination with dry film lubrication, resulting in life far exceeding requirements. Three planet gears are used in each stage, except the output stage of the longer gear trains, where five planets are required to transmit the output torque of up to 500 in.-lb.

A position-indicating potentiometer of the conventional wire-wound type is contained within each drive except the polar drive, where it is externally mounted on the positioning mechanism. The potentiometers are driven with anti-backlash gears and provide telemetry signals of axis position. The resistance elements of the potentiometers have been treated with niobium diselenide, a conductive dry lubricant, to enhance life in vacuum. This is largely a precautionary measure, since life requirements are not severe.

IV. The Stepper Motor

The stepper motor is the primary subject of this paper since it is believed to be a unique design, and a number of challenging problems were solved in the course of its development. It may be noted that during the course of the *Surveyor* program several attempts were made to purchase a stepper motor from an established vendor for this space application. Either vendors were not interested in the subject because of low quantities and severe requirements, or their products were inadequate for the job. Consequently, the design described herein was conceived and developed as an in-house effort.

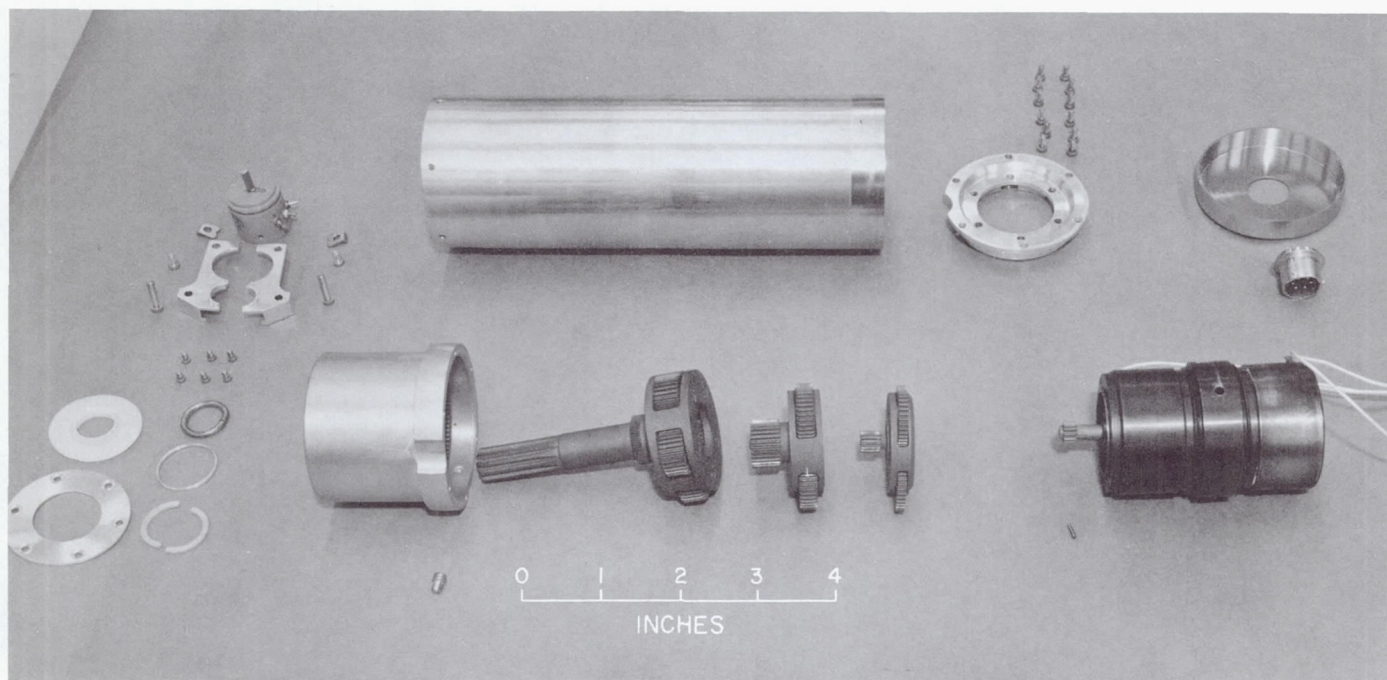


Fig. 3. Typical stepper motor drive assembly

A solenoid stepper motor was chosen for this application over a permanent magnet or variable-reluctance type for the following reasons:

- (1) High torque-to-weight ratio.
- (2) Comparatively simple electromagnetics.
- (3) A relatively long step per pulse, which simplified driving electronics and output gearing.
- (4) Inherent positive mechanical detent with high-torque holding capacity.

The stepper motor itself is ideally suited for the positioner since a precise angular motion occurs for each 45-msec pulse applied to the motor. It is also a brushless direct current device requiring no quiescent power or inversion circuitry.

The operation of the stepper motor may be understood by referring to Fig. 4, a cross-sectional view of the motor. Energizing either of the coils with a direct current pulse

produces electromagnetic force that causes the appropriate armature to move in an axial direction. The magnetic flux path for solenoid action passes through a fixed core at one end of the coil, through the motor housing surrounding the coil, and across each of two fixed air gaps into the armature and finally through the armature and the working air gap inside the coil. Axial motion of the armature during the power stroke is opposed by a helical spring nested inside the armature and bearing on an internal shoulder. The spring reacts against the inner race of a shaft bearing, and, therefore, rotates with the motor shaft as does the armature. The latter occurs because of a three-lobed sprocket which couples the armature to the shaft, still permitting axial armature motion since the sprocket lobes slide in slots on the back side of the armature.

Rotary motion is imparted to the armature during both its power stroke and return stroke. This is accomplished with three ball bearing cam followers, equally spaced at the periphery of the armature, and is best understood by referring to Fig. 5. As the armature moves into the coil,

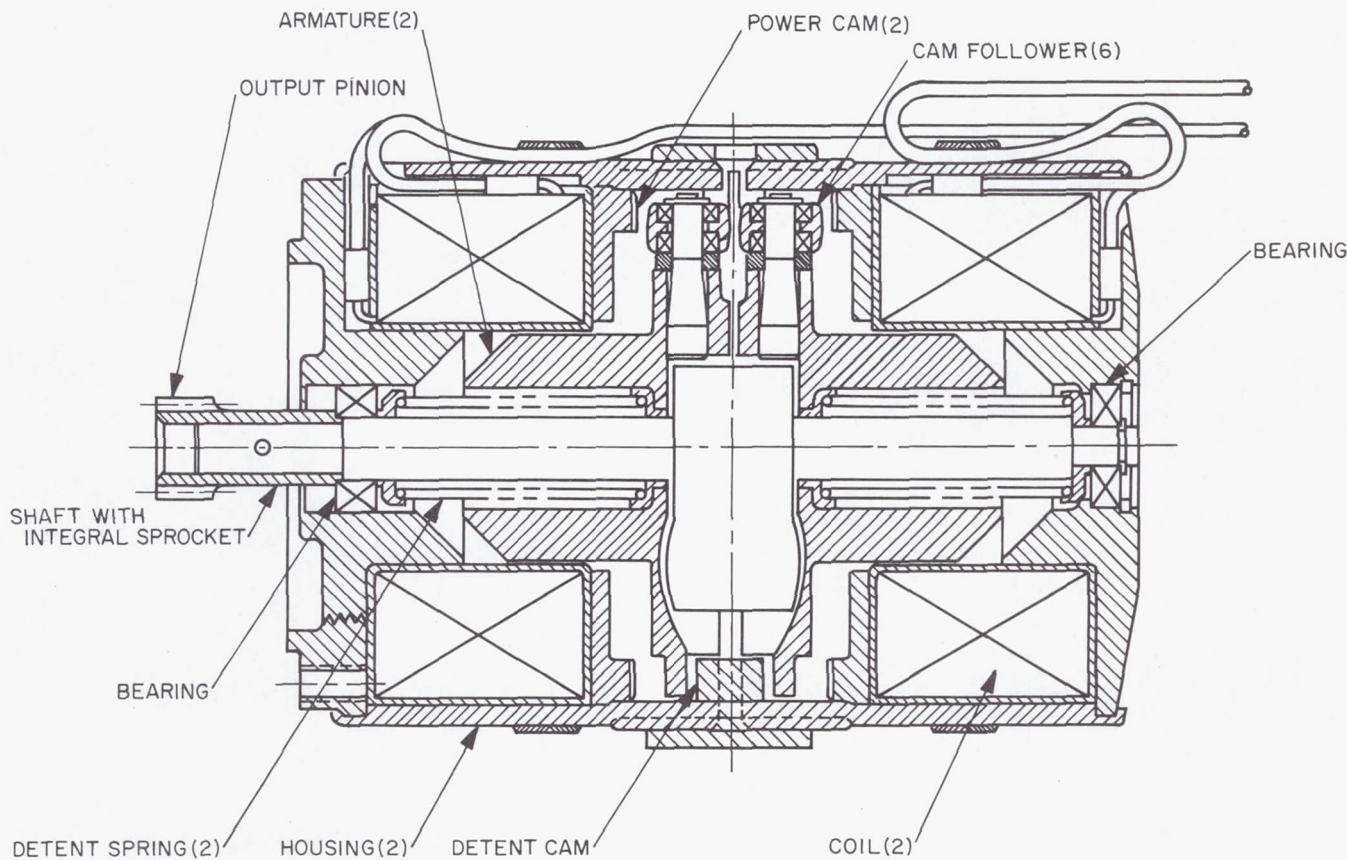


Fig. 4. Cross section of stepper motor

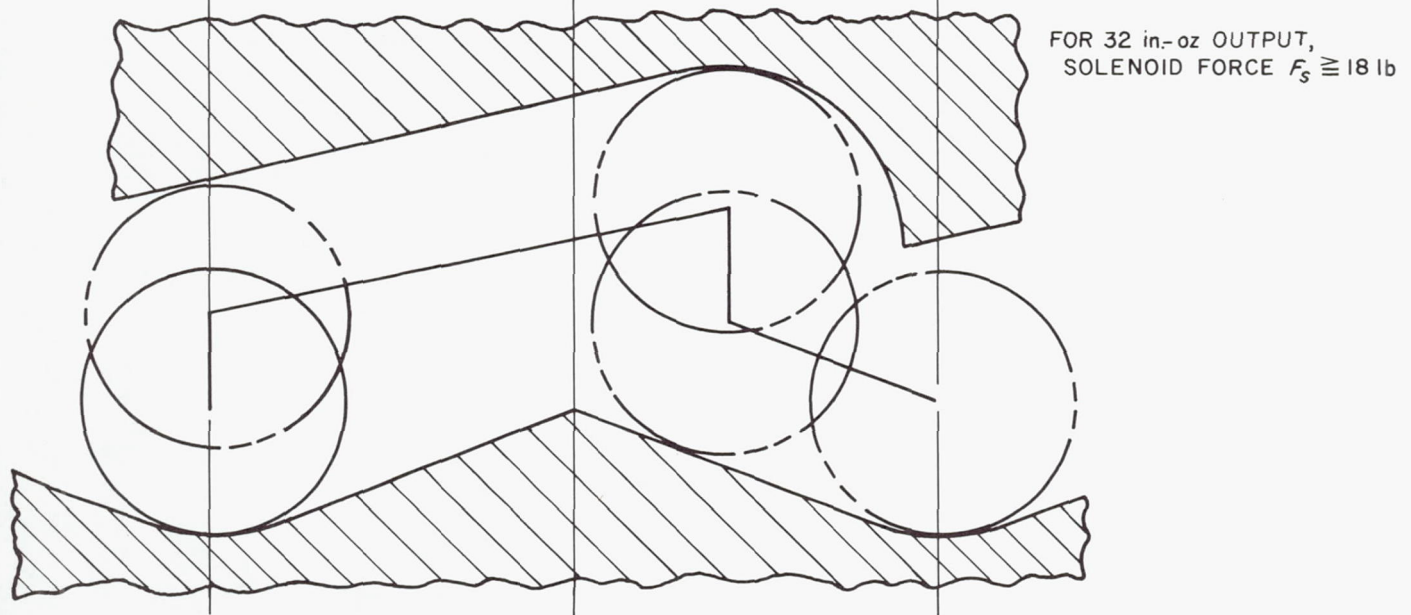
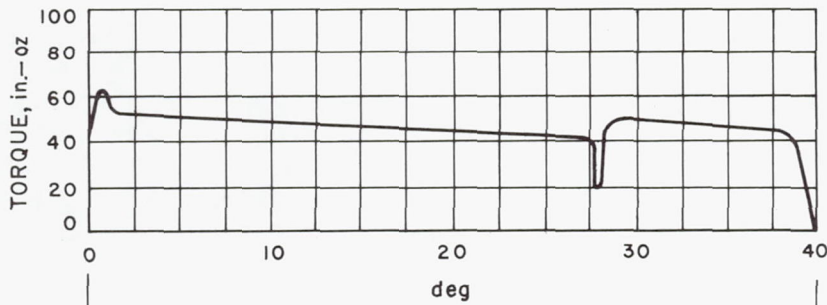


Fig. 5. Cam follower sequence in stepper motor

the cam followers encounter the rises of three of nine equal profiles on the power stroke cam. The armature must rotate about 28 deg to allow the followers to reach the low points of the cam surfaces. Upon de-energization of the coil, the helical spring pushes the armature axially a small distance until the cam followers encounter three equally spaced cam slopes on the detent cam. The armature rotates about 12 deg further until the cam followers come to rest at a low point between adjacent rises. Thus the shaft has been rotated 40 deg or one-ninth of a revolution.

During the powered portion of a step, the armature in the unused section of the motor presents a load to the motor since its cam followers must be rolled up the inclines of the detent cam in opposition to the spring force. This stored energy assists the detent portion of the step during which both armatures are acting identically. Analysis of internal loading of the motor leads to the generation of a nonlinear profile on the power cam in

order to provide a nearly constant net output torque throughout the step. The following expression describes the power stroke torque:

$$T = R_m \left[(F_e - F_{ps} - F_f) \tan \theta_p - (F_{ds}) \tan \theta_d \right]_{0 \text{ deg}}^{28 \text{ deg}}$$

where

- T = output torque, power stroke
- R_m = radius of cam follower contact
- F_e = electromagnetic force
- F_{ps} = spring force, powered side
- F_f = frictional forces
- θ_p = power cam angle
- F_{ds} = spring force, de-energized side
- θ_d = detent cam angle

Table 1. Physical parameters

Parameter	Value
Weight, lb	1.2
Length, in.	2.53
Diameter, in.	1.81
Step length, deg	40
Temperature range, °F	-225 to +260
Life, steps	120,000
Pressure, torr	<10 ⁻⁶

Parameters and features applicable to the stepper motor appear in Tables 1 and 2.

Detailed parts of the stepper motor are shown in Fig. 6.

V. Problems and Solutions

In the course of developing the stepper motor, an early problem was encountered with obtaining sufficient durability of the cam followers. Impact loading as a result of

Table 2. Operational parameters

Parameter	Value
Torque, in.-oz	
Rated	27
Maximum	35
Pulse length, msec	45
Coil resistance, Ω	0.66
Duty cycle at 2 pulses/sec	15 min on/15 min off
Maximum pulse rate, pulses/sec	11
Current, amp	
Nominal	10.5
Maximum	17.8

solenoid action caused failure of the cam follower bearings. The solution evolved into a two-fold approach. Load was distributed between two ball bearings in each follower, with outer races contained within a steel tire, as one measure. In addition, compliance was added to the cam follower shaft to absorb impact. The shaft is cantilevered from its welded joint to the armature and is tapered to the extremity where the cam follower bearings are mounted.

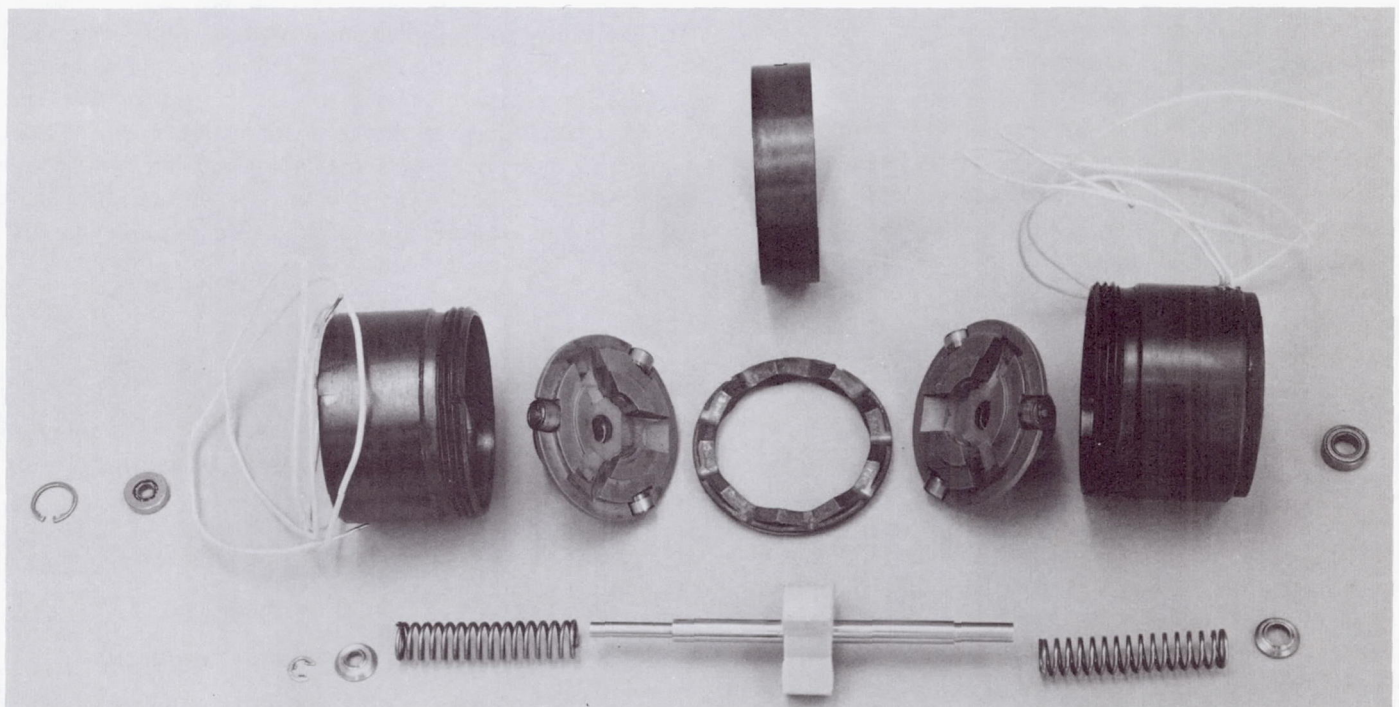


Fig. 6. The disassembled stepper motor

Initially the sprocket that couples the armatures to the output shaft was made of a self-lubricating plastic material called polycarbonate. This feature worked well at ambient and low temperatures but failed quickly at high temperatures, where the material weakened and disintegrated under impact loads. The released design contains a sprocket made of A-286 hardened steel with an impact-absorbing feature. It is lubricated with a dry film lubricant where it contacts the armatures.

The coil was never a problem in this stepper motor but had been in previous stepper motors used in the program. To preclude problems, the coil was wound on a bobbin machined from high-temperature plastic, using copper magnet wire with a polyimide insulation. The coil is potted in place with a heat-conducting potting material, thus ensuring good heat conduction into the motor housing. Early tests of complete drive assemblies in thermal vacuum conditions revealed that the coil adjacent to the gear box reached maximum temperatures of 350°F while the outboard coil temperature rose to over 500°F under similar operating conditions. This condition was equalized and limited to 350°F peak temperature by providing a copper heat-conducting path between the outboard end of the motor and the aluminum drive assembly housing.

The stepper motor is required to deliver rated output over a wide range of temperature and battery charge conditions, the most difficult being high temperature (260°F) and low battery (10.5-amp pulse). An analysis of wire sizes for the existing coil geometry in the range of number 14 gage to number 25 gage revealed that maximum ampere-turns under worst-case conditions were obtained with a coil wound with number 20 gage wire. Consequently, the motor has been optimized to provide its specified output at worst conditions in the *Surveyor* mission profile. At all other conditions, the output far exceeds requirements.

VI. Test Program

A design verification test program or development test period occurred, with five motors being used. All of the problems discussed above and a few others of less significance were uncovered and solved during this test period. So successful was the preliminary test program that two stepper motors contained in drive assemblies met all formal qualification requirements in a 22-day

period. The qualification program included the following tests:

- (1) Electrical characteristics.
- (2) Functional performance.
- (3) Vibration.
- (4) Shock.
- (5) Interim performance.
- (6) Thermal vacuum.
- (7) Interim performance.
- (8) Ultimate life (thermal vacuum).
- (9) Interim performance.

As a rule, the *Surveyor* stepper motors lead a much more hectic life on earth than they will ever encounter on the moon. Once lunar landing has occurred and initial positioning has been accomplished, only small angular travel is required on any axis each 24-hour period during lunar day. On the earth, a number of functional performance tests are run as soon as the motor is assembled. Additional loading tests occur following completion of the drive assembly. Once the drive assemblies are incorporated into the antenna/solar panel positioning mechanism, life begins in earnest with a series of unit tests involving vibration, thermal vacuum, and loading. After the mechanism is installed on a *Surveyor* spacecraft, at least one more vibration test is performed, and as many as three mission sequences occur, involving solar thermal vacuum conditions. Additional loading tests occur at the launching site prior to encapsulation and launch. All of this testing consumes from 20 to 80% of the rated life of the motor, making the ultimate life requirement an extremely important factor.

VII. The Stepper Motor in Space

There are many advantages in using stepper motors for positioning applications in aerospace mechanisms. These are briefly reviewed below:

- (1) The motor operates on short dc pulses; therefore,
 - (a) There is low power consumption.
 - (b) There is no quiescent power requirement.
 - (c) Pulse counting determines position accurately.
 - (d) Power inversion circuitry is not required.

- (2) The motor is basically a simple dc machine with no brushes or make-and-break electrical contacts.
- (3) A solenoid stepper motor produces a relatively high output torque with a minimum of moving parts or complexity.
- (4) A high holding torque is provided when the motor is at rest.

The stepper motor has proved to be a very useful and reliable tool on the *Surveyor* spacecraft. Its many desirable features and proven performance should make it very attractive for additional positioning applications in the exploration of space, the moon, and the planets. It is particularly well adapted to the positioning of directional antennas, solar panels, and optical devices, as well as various sensors and manipulators. It should be possible to increase its life and reliability greatly, making it even more attractive for space mechanisms.

The Design of Mechanical Linkwork for Aerospace

Bernard Roth
Stanford University
Stanford, California

The design of mechanical linkwork has in recent years been the subject of an ever-increasing number of theoretical investigations. Thanks to the ubiquity of the digital computer, many of these theoretical investigations can be readily applied to assist the mechanical designer. The primary purpose of this paper is to give the flavor of these new developments and indicate some potential applications.

I. Introduction

The basic idea behind much of the theory of kinematic synthesis is to mechanize motion requirements by utilizing the minimum number of moving parts and the simplest joints. (Such requirements are, of course, consistent with the basic tenets of simplicity and reliability inherent in space technology.) In order to accomplish a synthesis, one does not seek an "exact" solution, but attempts instead to find an approximation that will perform the desired task within a specific tolerance. The usual approach is to specify a set of positions at which there is to be no error (the so-called precision positions) and attempt to minimize the error elsewhere. If the error requirements are stringent, or if several precision posi-

tions are required, simple cut-and-try techniques will generally not succeed, and we must resort to more rational procedures.

In addition to well-known planar mechanisms, there exist spherical and spatial mechanisms. Spatial mechanisms offer the greatest variety of possible motions and may accomplish the same function as a more complicated planar mechanism. In the past it has been very difficult — if not impossible — to design spatial linkages, and hence they were rarely used. However, analytical computer-oriented techniques have now made it possible to apply systematic methods to the design of this vast class of potentially useful linkages.

In what follows, examples are given to illustrate some of the most common types of synthesis problems. In solving the six examples presented, either of two methods was used:

- (1) The geometrical constraint method. This relied on determining those special points or lines in a moving body which have several positions on a specified locus, such as a circle, sphere, cylinder, hyperboloid, etc.
- (2) The direct method. This relied on determining a set of equations relating the unknown linkage dimensions to the specified linkage motion requirements.

Both of these methods generally require the solution of a nonlinear set of algebraic equations. With the aid of a modern computer, such problems are easy to solve. Since the equations are nonlinear, there are generally several solutions. Obviously, this is a desirable characteristic. (The mechanism designer rarely shares the mathematicians' passion for unique solutions.) In reading the next section, it should be kept in mind that the examples are intended merely to illustrate typical problems, and

that there are many possible variations to both the problem statements and the proposed solutions.

II. Sample Problems

A. Relative Motion of Two Bodies

The most basic type of problem is to determine the dimensions of a linkage that guides one member relative to a nonadjacent member. This problem usually occurs in one of two forms:

- (1) Guiding a floating link (a so-called coupler) relative to a fixed member.
- (2) Coordinating the motion of two cranks (the so-called function generation problem).

An example of (1) is shown in Fig. 1. It has been previously suggested that a similar spatial four-bar linkage be used to guide a solar panel (the coupler) relative to the spacecraft (the fixed link). In this arrangement, one of the cranks has a turning and a turn-slide joint along skew axes, while the other crank has one turning and one spherical joint. Most methods of synthesizing such a

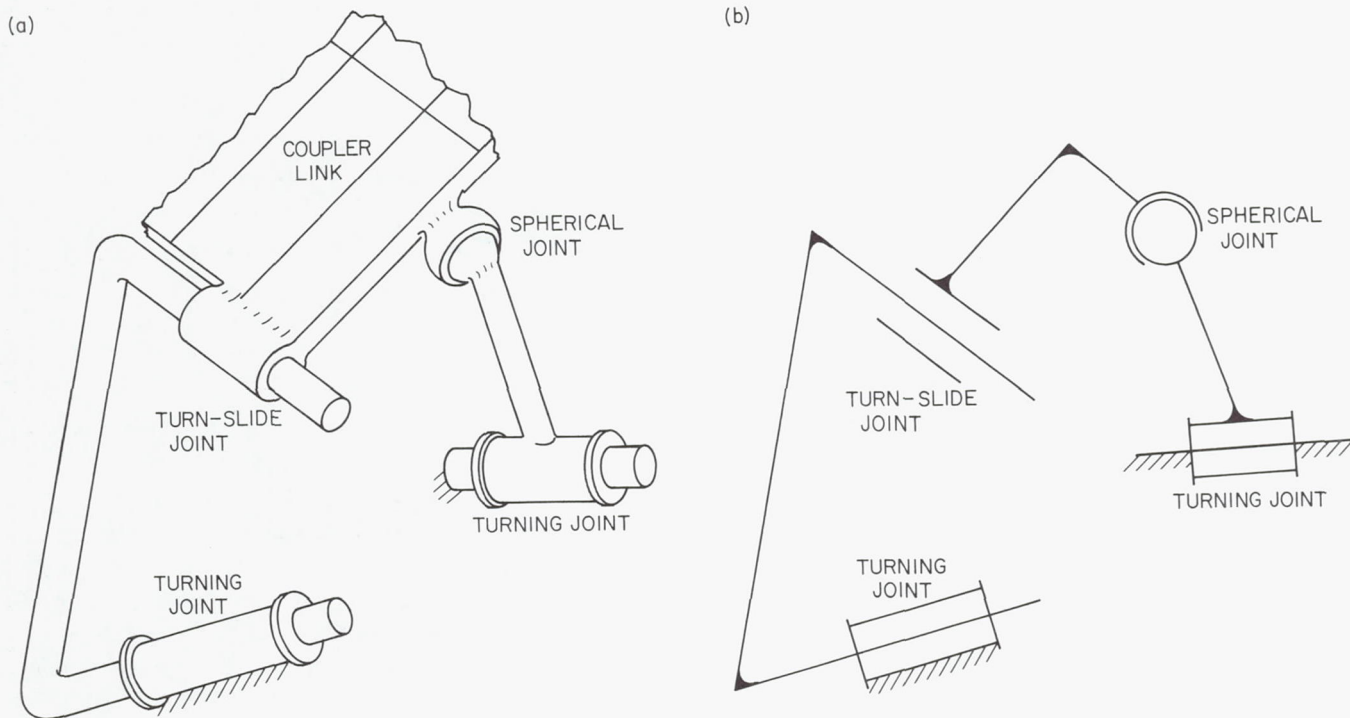


Fig. 1. A spatial four-bar linkage with a defined coupler motion. Fig. 1b is a skeleton drawing of the linkage shown in Fig. 1a

spatial four-bar linkage require the designer to specify the closed and open positions and several intermediate positions of the panel. The problem is solved by determining which lines and/or points in the moving and fixed bodies may be used as centers for the joints (Refs. 12, 13, 14).¹ In this problem, up to three precision positions may be specified.

An illustration of (2) is given in Fig. 2. Here the problem is to design a spatial four-bar linkage that acts as a nonlinear connection between two skew shafts. The most direct method of determining the linkage dimensions is to use equations relating the input and output rotation to the linkage parameters. This has been done most elegantly by Levitskii and Shakvazian (Ref. 11). In one of their examples, they obtain a linkage that approximates $y = \log x$ in the interval $x = 1$ to $x = 10$ to within a maximum error of 0.008% of the total range of y . These results attest to the high accuracy obtainable by such approximations. The authors specified eight precision positions in this particular design.

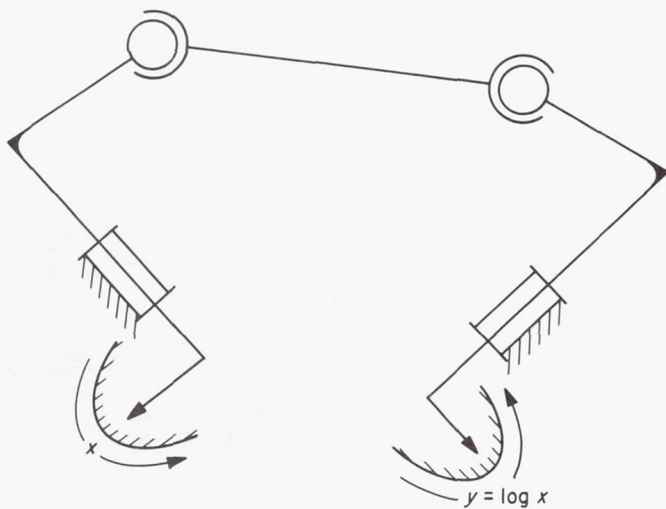


Fig. 2. A spatial four-bar linkage with rotating cranks that move according to a specified functional relationship

B. Points Moving on Specified Point-Paths

Conceptually, an entirely different set of problems involves the path of one point attached to a body in planar motion, or the path of a point or a line attached to a body in spatial motion. Often, such problems do not require a unique set of positions of any one body and

¹Reference numbers designate items in the bibliography.

hence it may be possible to choose part of the linkage (or even the entire linkage) arbitrarily. We divide such problems into three classes:

- (1) Find a point or line (attached to a known linkage) that approximates a specified path or ruling.
- (2) Determine a linkage such that one of its coupler-points approximates a specified path.
- (3) Determine a linkage such that one of its coupler-points approximates a specified path according to a given timing cycle. For planar four-bar linkages, this problem is the same as problems (A-1) and (A-2) (Refs. 4, 5).

As an example of (1), consider the five-bar "dwell" linkage shown in Fig. 3. This linkage was designed so that its turn-slide output crank would undergo an approximate dwell. Here the three-bar loop and the output axis are completely arbitrary. The design is effected by determining a line l_1 in the coupler of the three-bar; during part of the motion, l_1 remains (approximately) at a fixed distance and angle from some other line L (Ref. 14).

Another example of (1) is shown in Fig. 4. Here we have started with an arbitrary planar four-bar linkage and were required to find a point P in the coupler plane which approximates a portion of a parabolic arc (Refs. 6, 8). We can, in fact, determine points in any coupler which approximate any curve whatsoever (Ref. 6).

An example of (2) is Fig. 5, which illustrates a geared five-bar linkage whose dimensions have been determined so that the hinge point P approximates a specified path (Ref. 7). This synthesis was accomplished by writing equations in which the link lengths were the unknowns and nine of the precision positions of P were specified.

Finally, Fig. 6 is an example of type (3). Here it is required that point P take up certain positions P_i while the crank (with the two turning pairs) moves through specified angles ψ_i . If we select the input crank arbitrarily, this synthesis may be accomplished by finding a point S in the coupler which, in the several specified positions, lies on a sphere relative to the fixed link. We are generally at liberty to specify seven sets of precision values for ψ_i and P_i (Ref. 12).

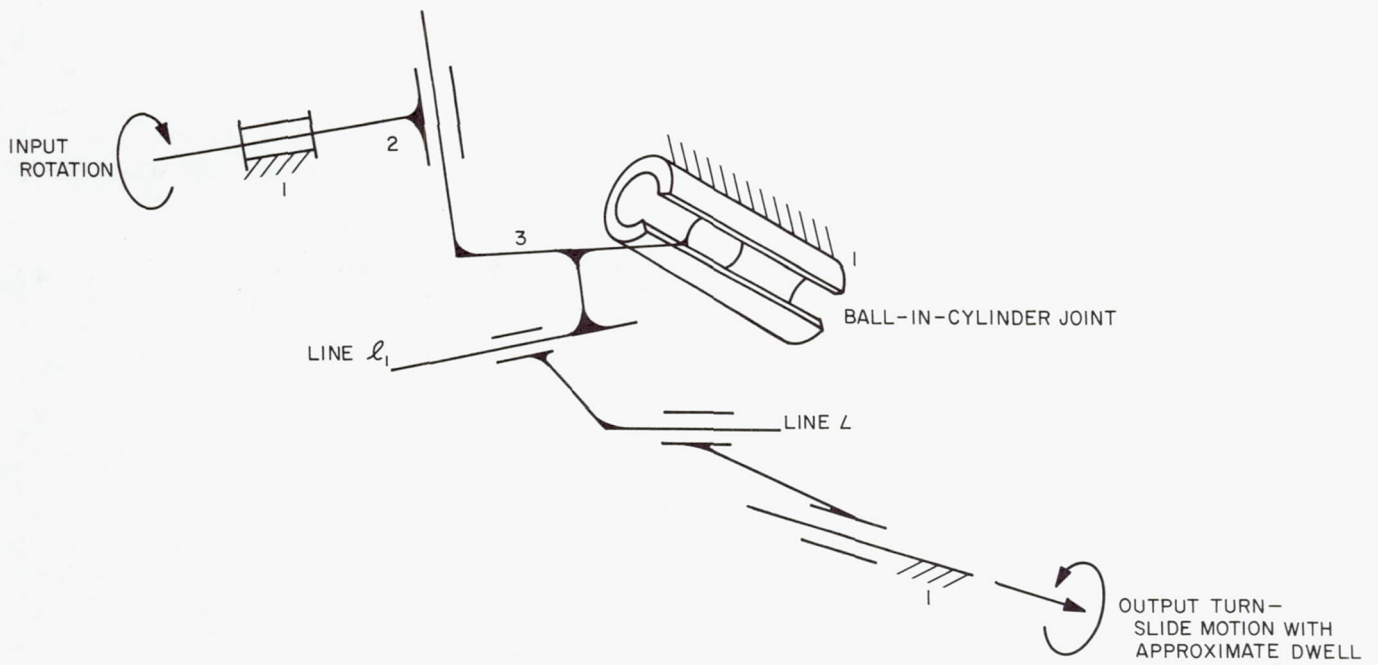


Fig. 3. A spatial five-bar linkage. In this application, links 1, 2, and 3 are chosen arbitrarily, while lines l_1 and L are determined analytically

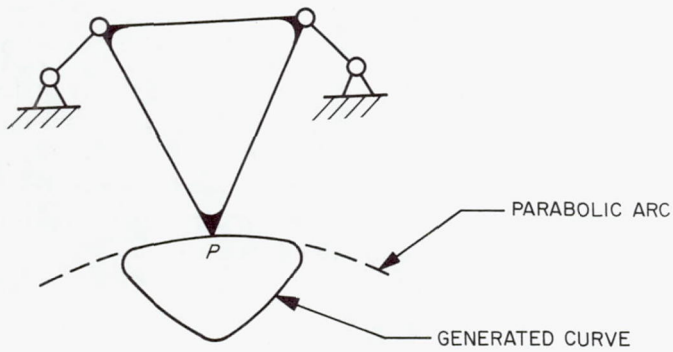


Fig. 4. Planar four-bar linkage

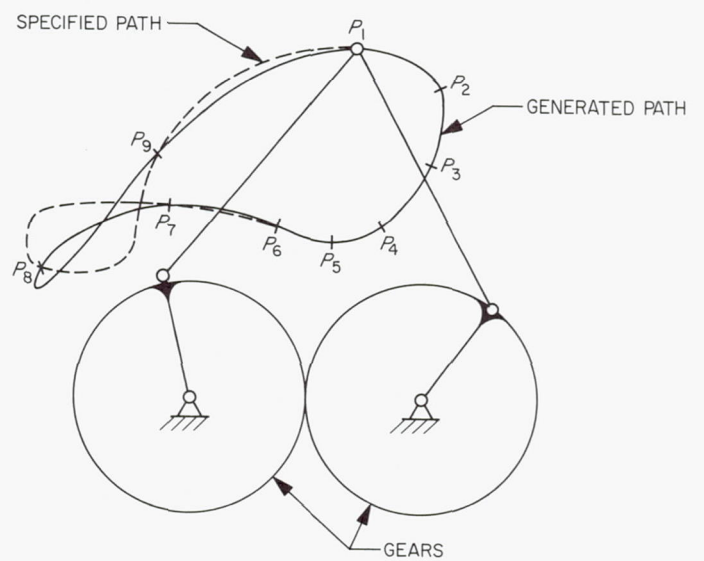


Fig. 5. Planar geared five-bar linkage. The points P_1, P_2, \dots, P_9 represent the points where the specified and generated paths coincide

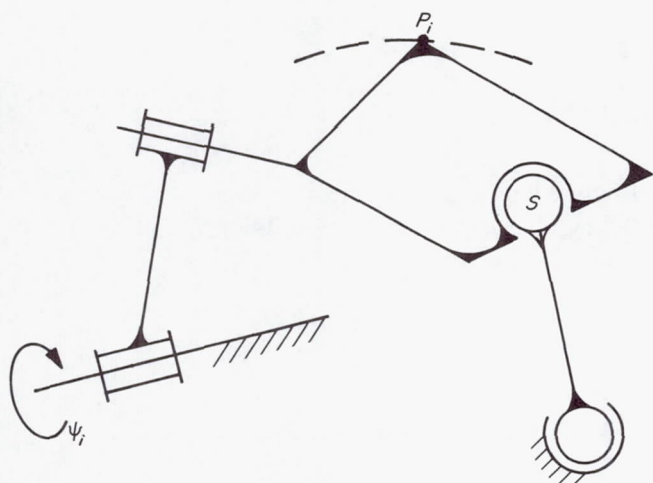


Fig. 6. A spatial four-bar linkage used to generate a curve in space according to a specified timing cycle. Note that this linkage is an inversion of the one shown in Fig. 2

III. Discussion and Conclusions

The solution of most of the foregoing examples requires fairly extensive computations, which, considering the iterative nature of the design process, will usually have to be repeated several times in any one design situation. Hence, it is fairly obvious that the use of a digital computer is indicated. Most researchers have, in fact, developed computer programs in order to illustrate and check the theory. These programs are generally available to designers. (For specific details, refer to the papers listed in the bibliography.)

The examples in this paper have concentrated on spatial linkages since it is felt that they offer some advantages over planar ones. This is especially true in the aerospace industry, where the possibility of obtaining complex motions with fewer parts is especially attractive and where dynamic effects and inertia balancing are usually not important. In fact, in some space applications an "input" crank never goes through a full cycle, and the entire design may be based on requirements for only a small range of the motion.

The possibilities are vast, both as to the type of linkages and type of problems. Hence, no attempt has been made to be exhaustive. The several examples presented herein are intended to act as a catalyst, stimulating the designer to view his own linkage problems in a new context and encouraging him to make use of the new computer-oriented design techniques.

The near future will see many more developments in the theory of kinematic synthesis. Not only will more complex problems be considered, but questions such as force transmission (Ref. 10) and optimization (Ref. 9) will also be treated as part of the motion synthesis problem. The study of spatial mechanisms, which has long been neglected, will now become one of the areas of greatest activity.

Those designers who are willing to undergo the painful process of "reading the literature" will find their efforts well rewarded. It is toward this end that a selected bibliography is included in this paper.

Selected Bibliography

The following bibliography lists primary English language references in each area. Some of these are difficult to read, but they all contain their own bibliographies, and the interested reader can use these to advantage.

I. General Background

1. Hartenberg, R. S., and Denavit, J., *Kinematic Synthesis of Linkages*. McGraw-Hill Book Co., Inc., New York, 1964.
2. Hall, A. S., *Kinematics and Linkage Design*. Balt Publishers, West Lafayette, Ind., 1966.
3. Rothbart, H. A., *Mechanical Design and Systems Handbook* (see Kinematics section). McGraw-Hill Book Co., Inc., New York, 1964.

II. Synthesis of Planar Linkages

A. Relative Motion of Two Planes

4. Freudenstein, F., and Sandor, G. N., "Synthesis of Path-Generating Mechanisms by Means of a Programmed Digital Computer," *Trans. ASME, Ser. B: J. Eng. Ind.*, Vol. 81, pp. 159-167, 1959.
5. Primrose, E. J. F., Freudenstein, F., and Sandor, G. N., "Finite Burmester Theory in Plane Kinematics," *Trans. ASME, Ser. E: J. Appl. Mech.*, Vol. 86, pp. 683-693, 1964.

B. Motion of Points in the Coupler Plane

6. Freudenstein, F., "Higher Path-Curvature Analysis in Plane Kinematics," *Trans. ASME, Ser. B: J. Eng. Ind.*, Vol. 87, pp. 184-190, 1965.
7. Roth, B., and Freudenstein, F., "Synthesis of Path-Generating Mechanisms by Numerical Methods," *Trans. ASME, Ser. B: J. Eng. Ind.*, Vol. 85, pp. 298-306, 1963.
8. Sandor, G. N., and Freudenstein, F., "Higher-Order Plane Motion Theories in Kinematic Synthesis," ASME Paper No. 66-Mech-25, 1966.

C. Optimization of Solutions

9. Fox, R. L., and Willmert, K. D., "Optimum Design of Curve-Generating Linkages with Inequality Constraints," ASME Paper No. 66-Mech-20, 1966.
10. Roth, B., Freudenstein, F., and Sandor, G. N., "Synthesis of Four-Link-Path-Generating Mechanisms With Optimum Transmission Characteristics," *Transactions of 7th Conference on Mechanisms*, pp. 44-48, October 1962.

III. Synthesis of Spatial Linkages

A. Function Generation

11. Levitskii, N. I., and Shakvazian, K. K., "Synthesis of Four-Element Spatial Mechanisms With Lower Pairs," *International Journal of Mechanical Sciences*, Vol. 2, pp. 76-92, 1960.

B. Motion of Points and Lines

12. Roth, B., "The Kinematics of Motion Through Finitely Separated Positions," ASME Paper No. 67-APM-2.
13. Roth, B., "Finite Position Theory Applied to Mechanism Synthesis," ASME Paper No. 67-APM-39.
14. Roth, B., "On the Screw Axes and Other Special Lines Associated With Spatial Displacements of a Rigid Body," ASME Paper No. 66-Mech-7.

Lunar Orbiter Photo-subsystem Mechanisms*

George Bradley
The Boeing Company
Seattle, Washington

The design and development of the photo-subsystem that was successfully operated on the Lunar Orbiter spacecraft are described. The various components of the photo-subsystem, such as the film transport, vacuum and mechanical clamps, 24-in. focal-plane shutter, processor-dryer, and optical mechanical scan system, are described in detail.

I. Introduction

The *Lunar Orbiter I* mission in August 1966 reported a wealth of detailed information about the moon's surface that had been previously unavailable to mankind. Although the moon is our closest neighbor, its surface characteristics had previously been defined only at a relatively gross level by astronomical study over the past several centuries and at a localized level by the *Ranger* and *Surveyor* spacecraft.

To provide the reliability necessary for the *Lunar Orbiter* mission, a photo-subsystem was designed that used, where possible, flight-proven concepts and components to provide a versatile, lightweight, high-performance photo-acquisition system.

*All work described in this paper was accomplished under NASA Contract NAS 1-3800.

In this system, a strip of film is driven past the camera, clamped in place, and exposed by action of the shutter. The exposed film is then processed and dried, and the resulting photograph is read out by an optical mechanical scanner.

II. Photo-subsystem Mechanisms

The photo-subsystem is composed of the following:

- (1) The film transport system, which comprises rollers for film tracking and a vacuum and mechanical clamp for holding the film firmly on the platen during picture-taking.
- (2) A 24-in. focal-plane shutter.
- (3) A processor-dryer for on-the-spot developing of film.

- (4) An optical mechanical scan system for converting photography to video intelligence.
- (5) Various other assemblies appropriate to the various modes of operation.

A. The Film Transport System

Figure 1 shows the film path through the photo-subsystem, as well as the handling mechanisms that store

and supply film on demand to film-user portions of the subsystem. The supply and take-up spools have a capacity of 260 ft. The supply looper stores 2.0 in. of film and acts as a buffer between supply and camera drives.

The film advance drive is powered by a 28-v dc reversible motor with a gear system and a metering-roller mechanism. The control signal sets the motor for forward operation and turns the motor on. This same signal also

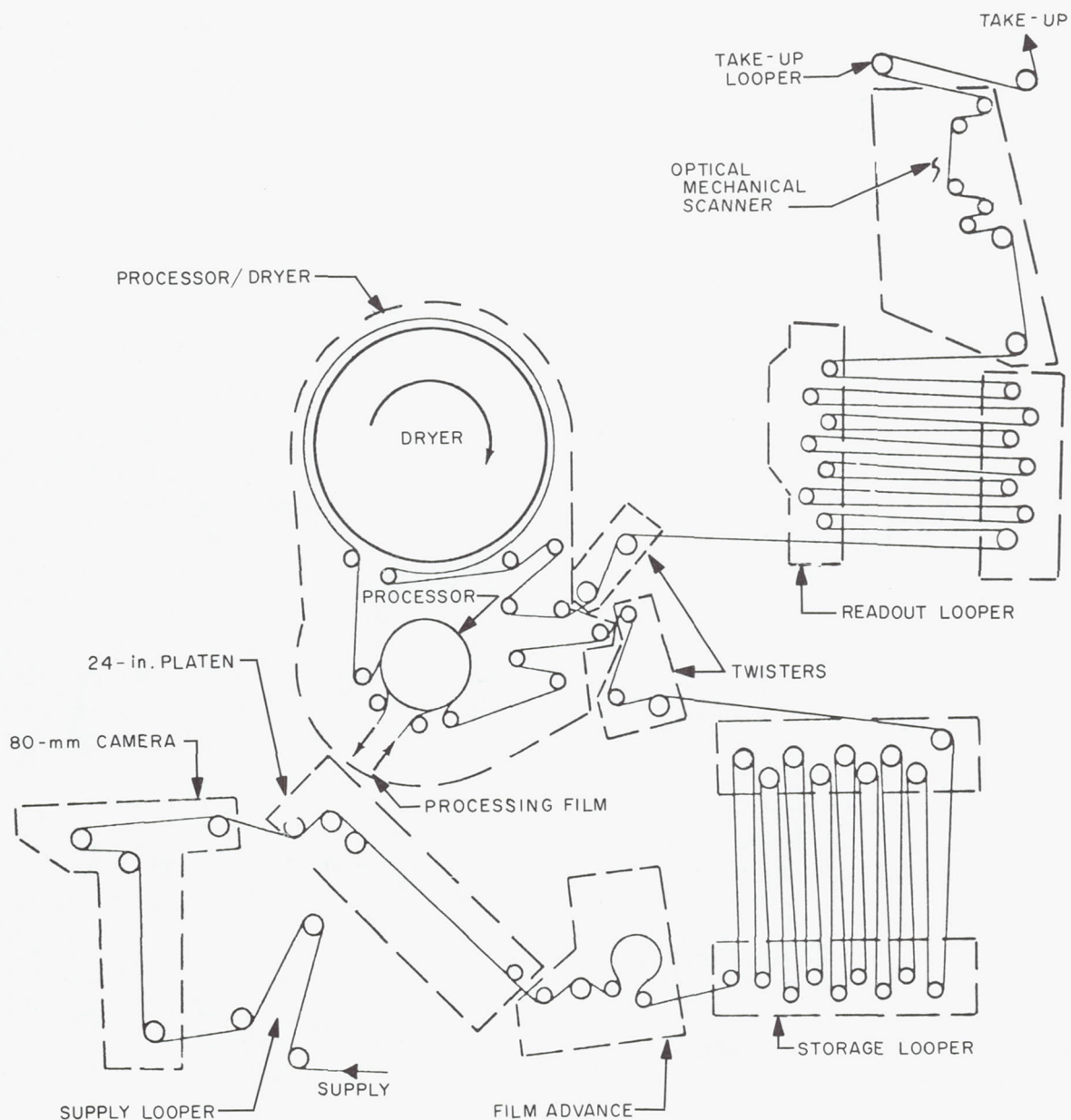


Fig. 1. The film transport system

releases the drive brake; the drive then advances film through the camera. The rate of advance is 11.7 in./sec (or one frame per second). A metering roller accurately measures the quantity of film being pulled through the camera by the drive. When one frame of film has passed the metering roller, an encoder coupled to the roller sends a signal to the command control system, which switches the motor off.

B. The Platen

The high-resolution system photographs the lunar surface in discrete frames and, for a framing camera of this type, the platen must perform two functions:

- (1) The film must be held tightly against the flat platen to coincide with the flat image plane produced by the lens.
- (2) The platen must move the film at the correct velocity to coincide with the image motion, providing image motion compensation (IMC) to reduce image smear to an acceptable level.

After unexposed film has been advanced across the platen, the platen clamps the edges of the film mechanically. When mechanical clamping has been completed, a bellows draws a partial vacuum through small holes and channels in the platen surface. The partial vacuum holds the film tightly against the platen, producing a flat film plane. The mechanical clamp/vacuum draw sequence is started by a control pulse either from the velocity to height (V/H) sensor or from a 0.4-cps generator, if the V/H sensor is off. The mechanical clamp/vacuum draw sequence continues for a total of from 0.44 to 2.79 sec, depending on the V/H rate if the V/H sensor is on, or for 0.625 sec if the V/H sensor is off. During this time, exposure of the film takes place. When the mechanical clamp/vacuum draw sequence is complete, the platen releases the film, and the film-advance motor removes the exposed film from the platen by drawing 11.7 in. of film through the camera.

During the exposure, the platen moves the clamped film at the correct velocity to minimize image smear. The platen is driven by the V/H sensor output cam for a total of approximately 0.3 in. The V/H linkage is such that the platen cycles continuously at the correct velocity whenever the V/H sensor is turned on. Film clamping and vacuum draw are then programmed at the correct time within the platen cycle.

C. The Focal-Plane Shutter

The shutter assembly, which includes a 24-in., constant-velocity, variable-slit, focal-plane shutter, is attached to the camera structure in front of the 24-in. platen (Fig. 2).

The shutter consists of two curtains, each stretched between two rollers. Exposure takes place when the edge of the first curtain moves across the width of the film, with the edge of the second curtain following the first at a precise distance. Because the curtain velocity is constant, varying the distance between the two curtains produces a change in the exposure time. For this shutter, slit widths (or curtain separations) of 2, 1, and 1/2 in. can be selected by command. These slit widths result in exposure times of 1/25, 1/50, and 1/100 sec, respectively.

The shutter curtain-to-film spacing is 0.500 in., producing a minimum shutter efficiency of 84%, based on a 24-in., $f/5.6$ lens. The shutter is capable of completing each cycle (forward motion and return) in 0.100 sec and cycles at a maximum rate of one operation per 1.6 sec.

Operation of the shutter is started by a solenoid releasing the screen rollers; the rollers then rotate at a precise velocity produced by springs within the roller spindles. At the same time, a kicker spring assembly accelerates the shutter-return motor shaft, bringing the motor shaft to the correct velocity. When the exposure has been completed, the motor returns the screens, torquing the spindle springs and resetting the kicker assembly for the next actuation. During the shutter-return portion of the cycle, the screens overlap, preventing a second exposure of the film. Between cycles, the shutter is closed and light-tight.

D. The Storage Looper

The camera storage looper is a storage buffer between the film-advance drive and the processor-dryer. The looper has nine rollers on a fixed carriage and nine corresponding rollers on a movable carriage. The two roller carriages are mechanically connected by carriage guide shafts. Film is looped back and forth around corresponding roller pairs in the two carriages. A negator spring exerts a constant tension, tending to pull the two roller carriages apart. When film is supplied to the looper, the spring tension pulls the roller groups apart, drawing film into the looper.

The total mechanical film capacity of the looper is approximately 258 in. or 22 frames. The looper contents,

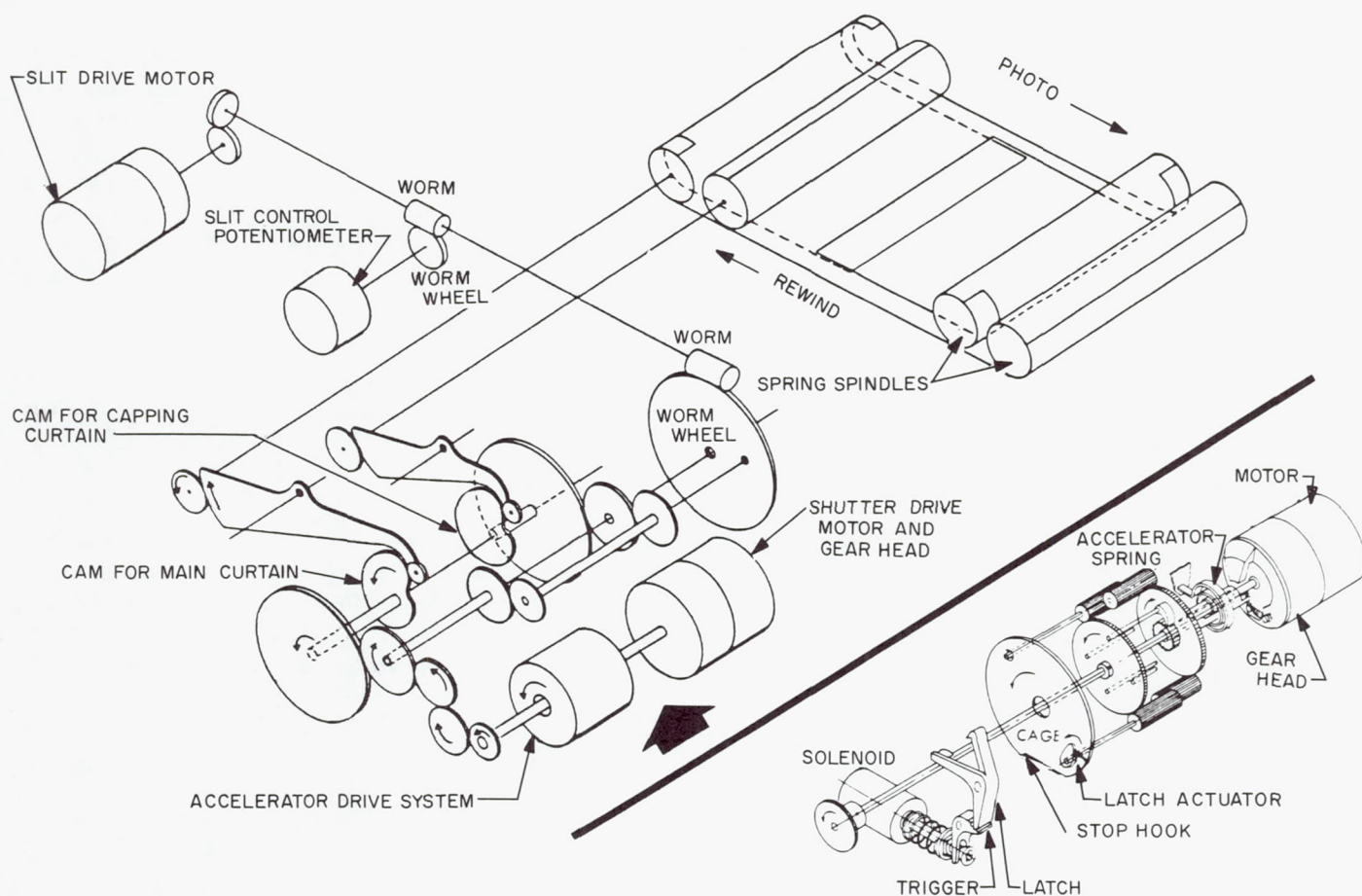


Fig. 2. Mechanical schematic drawing of the focal-plane shutter

in a range of 0 to 21.5 ft, are monitored by a gear-driven potentiometer and converted to a 0- to 5-v dc analog signal. The negator spring in this looper exerts a constant film tension of 1.75 lb, regardless of the quantity of film in the looper. The looper accepts film from the camera drive at a rate of 11.7 in./sec and delivers film to the processor-dryer at a rate of 0 to 75 in./min.

E. The Processor-Dryer

The processor laminates the Type SO-243 film with the processing film, holding the two together for the required length of time and separating them when processing is complete. Film is advanced through the processor by frictional contact between the film and the processing film (which is, in turn, driven by the drive motor). The processor consists of: (a) a cylindrical 3-in.-diameter processing drum, (b) an internal drum resistance heater with sliding electrical contacts, (c) temperature control electronics, and (d) a temperature-monitoring telemetry

point. These are housed in a cylindrical compartment. The drum rotates freely and contains the heater. The temperature control and monitoring electronics are in the electronics assembly outside the film enclosure.

The processing time is 3.4 min, and the processor temperature is maintained at $85 \pm 2.5^\circ\text{F}$ during processing. The drum temperature, in a range of 40 to 100°F , is converted to a 0- to 5-v dc analog signal.

The dryer provides the necessary time and temperature to dry the processed film. This component consists of: (a) a drying drum (over which the film is passed), (b) an internal drum resistance heater, with sliding electrical contacts, (c) temperature control and monitoring electronics (located in the electronics assembly outside the film enclosure), and (d) humidity pads. The 9-in.-diameter drum is not driven but rotates freely as the processed film passes through the system. The humidity pads are located on the inside wall of the dryer compartment.

The photographic film is wrapped approximately 310 deg around the dryer drum, with a drying time of approximately 11.4 min. A temperature of $95 \pm 5^\circ\text{F}$ is maintained by a thermistor-controlled heater; some heat is supplied by the processing film drive motor. The humidity pads absorb most of the moisture evaporated from the film.

F. The Readout Looper

The readout looper (Fig. 1) follows the processor-dryer, and stores 48.0 in. (four exposures) of film for limited amounts of readout. The processed film is fed from the readout looper into the optical mechanical scanner (OMS).

G. The Optical Mechanical Scanner

The optical mechanical scanner (Fig. 3) is used to read out the processed film by imaging a moving spot of light across the film in front of a photomultiplier tube. The lens scanning system minifies the scan line 22.5 times and focuses it on the film. The line is moved laterally across the film by drawing the lens carriage parallel to the film plane with a 80-v (peak to peak), 2-phase, 400-cycle, synchronous motor with a gear clutch-cam mechanism.

During both quick-look and final readout modes, the processed film is moved continuously at a measured rate in the reverse direction by means of a geared metering roller as shown in Fig. 4. Three cam-driven operations take place:

- (1) A high-precision cylindrical cam moves a scanning lens across the film.
- (2) A simple cam operates the film clamp so that focus is obtained (with respect to the OMS lens).
- (3) A simple cam step advances film in the readout gate at the end of each scan.

The motor is turned on when motor signals are supplied from the command control programmer to the power-switch circuitry for the readout control electronics. During a scan of a framelet, the metering roller slowly draws film out of a loop on the readout looper side of the readout gate and continuously feeds the readout looper (Fig. 4). The roller in this looper is connected by a lever to a similar roller and loop on the take-up side of the readout gate. As film is drawn out of the output loop, the lever transmits the force, and the input loop is enlarged and draws film at the same steady rate out of the film take-up assembly. Between these loops, the film

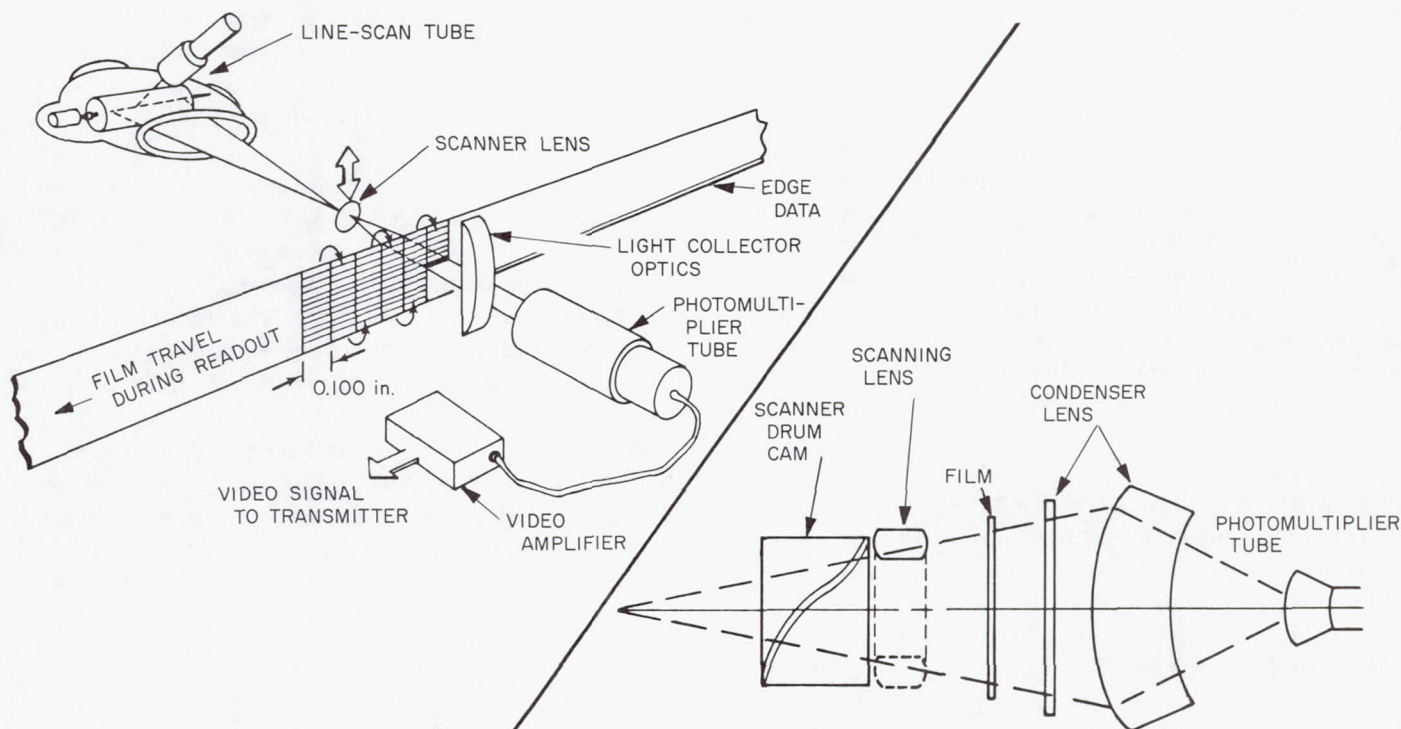


Fig. 3. The optical mechanical scanner

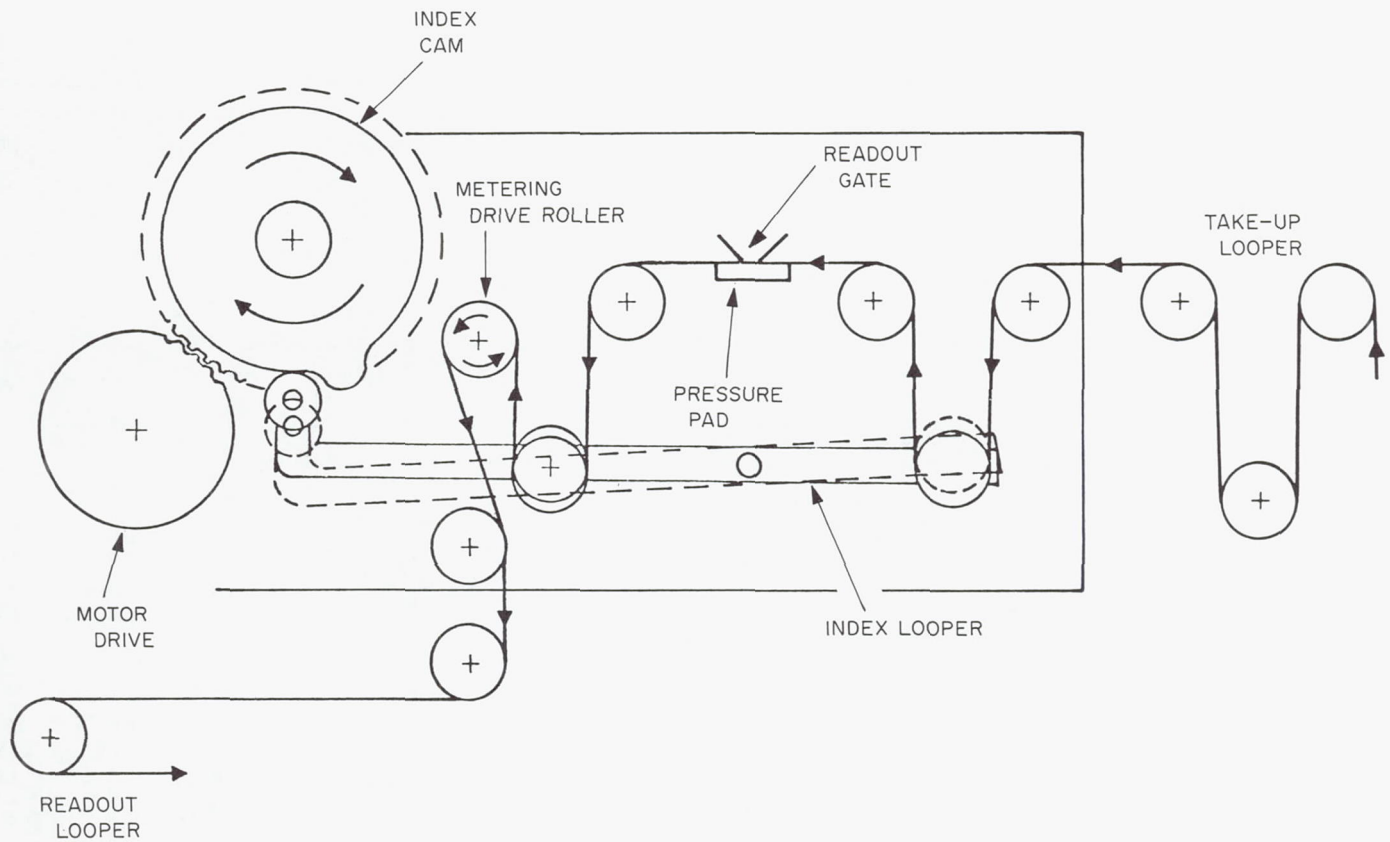


Fig. 4. The film-advance mechanism for the optical mechanical scanner

clamp holds the film section being scanned stationary in the readout gate.

When the end of the scan (or scanning lens turn-around) is reached, the cam-operated gate opens, and the lever between the loops is cam-driven to move film in step fashion through the gate. The film clamp recloses, and scan resumes back across the film. The cams are all 2-cycle, to accomplish back-and-forth scan operation. The metering roller supplies an accurate 0.100 in. of film in each framelet. The sequence continues moving the scanning lens back and forth across the film and advancing the film through the readout system until an inhibit command is received.

Attached to the cam is a 2-segment encoder switch whose logic indicates two positions of the optical mechanical scanner. The spot-stop condition indicates that the OMS is positioned at its farthest excursion on the pre-exposed, calibration side of the film where the film clamp is released. When the readout is commanded OFF, the drive mechanism continues until it arrives at the spot-stop position. This turns the drive motor off. During modes where film travels in the forward direction through

the readout gate, the readout drive-motor clutch is disengaged by a signal from the command control programmer and, with the clutch disengaged and the clamp released, film free-wheels through the OMS.

The other encoder segment generates a focus-stop signal (FSS). This signal indicates that the OMS is positioned over the pre-exposed portion of the film clamped in the readout gate. When the readout drive is commanded ON the first time, the OMS will leave the spot-stop position and move the short distance to the focus-stop position, where the FSS will turn the drive off. This allows the scan line to be focused and the photovideo gain to be adjusted on pre-exposed lines in the film by real-time commands. After the readout drive has been turned on a second time by a ground command, readout scanning is continuous, and focus spot-stop will not turn the optical mechanical scanner off during subsequent passes over the focus-stop position.

H. Other Assemblies

The take-up looper stores 2 in. of film and acts as a buffer between the take-up drive and other system drives.

Twisters reorient the film path to allow most efficient use of available space in the photo-subsystem. The twister design is simply a series of rollers, oriented around a helix mount, which converts a horizontal film plane to another plane 90 deg opposed to that plane. Film tensions in the supply looper and the storage looper aid film advance from the supply spool and the camera. High film tension is required at the take-up looper to make it the dominant looper for controlling take-up operation.

All of the loopers have a common basic design to achieve lightweight construction, i.e., column-supported

end frames and simply supported roller shafts. Negator springs are used as a simple method of achieving constant tension over the looper carriage ranges.

III. Conclusion

The *Lunar Orbiter* photo-subsystem has demonstrated that a series of simple mechanisms, each of them amenable to simple analysis, can result in a very reliable complex system, and that precise metering and flawless timing of switching functions between component mechanisms are a major factor in a successful mission.

Yo-Yo Despin Mechanisms

Kenneth S. Bush
NASA Langley Research Center
Langley Station, Hampton, Virginia

This paper describes the analytical background and practical design considerations of the three principal types of yo-yo despin mechanisms: (1) single-stage (rigid), (2) two-stage, and (3) stretch yo-yo. The principal advantages and disadvantages of each method are enumerated and explained. The results of the calculations and of the actual flight tests for each type of yo-yo despin mechanism are also presented.

I. Introduction

Spin stabilization has proved very reliable in maintaining angular orientation of the last stages of vehicles used for injection of spacecraft into orbit or for maintaining acceptable payload trim angles of ballistic probes. Mission or experimental criteria, however, often require a reduction in the initial spin rate to a value lower than that required for stabilization.

Spin reduction has been accomplished by such devices as "retro" jets utilizing an active sensing system, fixed-impulse despin motors, or a yo-yo despin system. The yo-yo despin system, first proposed by the Jet Propulsion Laboratory (Ref. 1), consists of two pieces of cables with weight on the ends. The release of the weights and cables from the spinning spacecraft discards sufficient momen-

tum to reduce the spin to the desired value. This so-called conventional yo-yo despin system has been utilized in many space applications.

Modified versions of the simple yo-yo, such as a two-stage despin system, provide advantages such as increased accuracy over the single-stage system, but not without added complexity. The latest version utilized at the Langley Research Center (LRC) is a "stretch" yo-yo, which employs tension springs, cables, and weights to partially compensate for errors in initial spin rate and physical constants existing at the time of initiation of the despin system. The stretch yo-yo system was conceived by Henry J. Cornille of Goddard Space Flight Center (Ref. 2), with analytical theory reported by Dr. Joseph V. Fedor (Ref. 3).

II. Fundamental Principle of Yo-Yo Despin

The principle of yo-yo despin is illustrated in Fig. 1, which shows the various phases of operation. Phase I takes place while the weight and cable are tangent to the cylindrical drum. In general, it is during this phase that the major portion of energy is transferred. Phase II takes place while the weight and cable rotate on an arc about the point of attachment. Weight release is usually at a point approximating a position radially in line with an

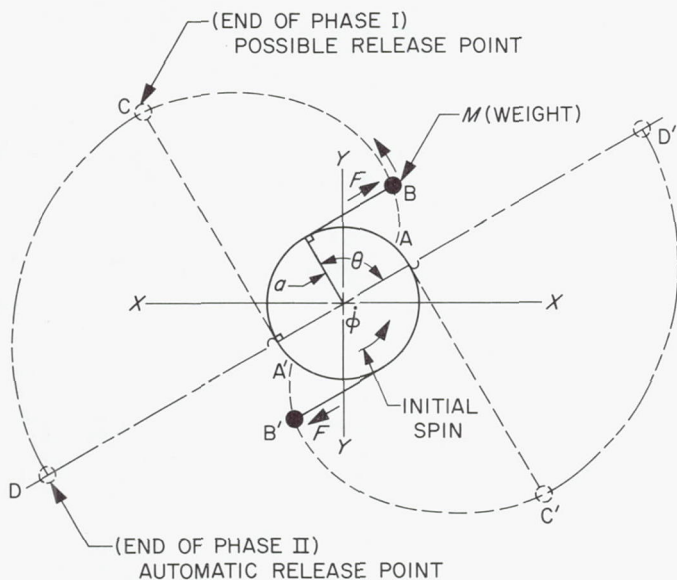


Fig. 1. Yo-yo operation

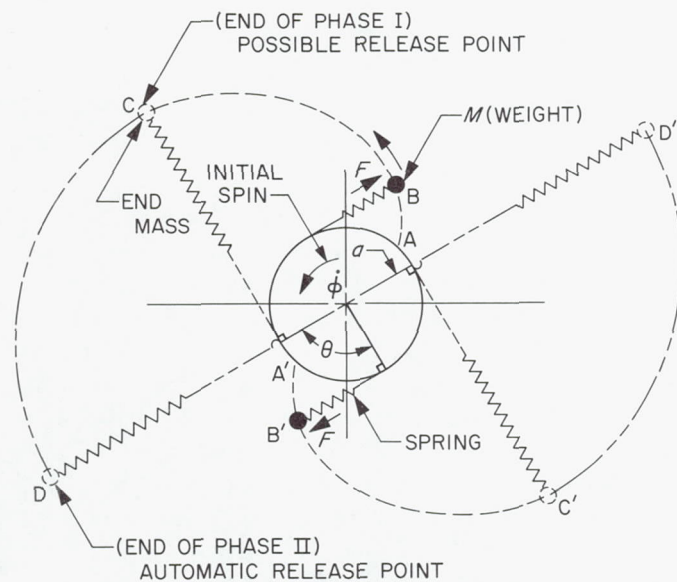


Fig. 2. Stretch yo-yo operation

element of radius. Figure 2 shows a stretch yo-yo with the same basic features as the conventional system, except that a spring is used as a portion of the cable.

The kinetic energy of the rotating body is transferred to the weight and cable during transition of the weight from its initial position to the release point of the cable from the body. At the time of release the required amount of momentum has been transferred to the yo weight and cable, which are discarded at time of release. From the start of the first event (yo-weight movement) the operation is self-sustaining and progresses until the despin operation is completed.

The yo-yo system is a very simple means of accomplishing spacecraft despin, is mechanically simple, and uses only basic scientific principles in its operation.

The basic theory of the yo-yo system is that of the conservation of energy and momentum and is illustrated by the following equation:

$$T = \frac{1}{2} I \dot{\phi}^2 + \frac{1}{2} M (\dot{x}^2 + \dot{y}^2)$$

where

T = total kinetic energy

$\dot{\phi}$ = spin rate

I = moment of inertia of spinning body about the spin axis

M = total mass of both weights

\dot{x} = velocity of yo weight in x direction

\dot{y} = velocity of yo weight in y direction

III. System Selection

The selection of the type of despin system must be considered with regard to the specific requirements of each application. The three systems discussed in this paper are listed below with salient characteristics indicated.

A. Single-Stage (Rigid) Yo-Yo System

The simplicity of the single-stage system and associated reliability dictates use when the spacecraft final spin rate is to be zero and accurate prediction of moment of inertia about the spin axis is possible. If despin

requirements are not exacting, this system should also be considered for despin to intermediate spin rates.

B. Two-Stage Yo-Yo Despin System

The two-stage system has application in meeting more exacting final despin rates. The despin may be zero or an intermediate rate. Reduction in spin rate per stage results in a large decrease in percentage of error in the final spin rate.

C. Stretch Yo-Yo Despin System

The stretch yo-yo is an adaptive system that partially compensates for errors in both initial spin and moment of inertia. This system is capable of yielding the most precise despun conditions; however, design complexity and system calibration dictate close examination of the capabilities of the other despin systems.

IV. Typical Despin Systems

A. Single-Stage Yo-Yo Despin System

A system representative of a single-stage yo-yo despin was designed, qualified, and flight-tested on a sounding-rocket program.

1. Design criteria. The system was required to reduce the spin rate of the payload/expended solid rocket motor combination from approximately 270 to 0 ± 6 rpm. The angular deceleration was to be minimized.

2. System description. The single-stage yo-yo shown in Fig. 3 was incorporated in the adapter section between the payload and the last stage of the rocket vehicle. The experiment requirement for low angular deceleration was achieved by the use of three complete wraps of the yo-yo cables. (The time of despin can be related directly to initial spin rate and cable length. That is, the longer the cable, the greater the despin time for a given initial spin rate.) The system as initially designed used separate pyrotechnic release mechanisms to free the yo weights.

During the first spacecraft mission, one yo weight failed to release and prevented proper functioning of the system. The system was modified to incorporate a cable to connect the two yo weights. The connecting cable passed through a tubular guide and passed over the anvils of two pyrotechnic cable cutters. The yo weights were retained against hollow conical seats and had provisions for preloading the connecting cable. Pre-

load was applied to the connecting cable by jack screws bearing against swage fittings which were applied after passing the connecting cable through the weights. The functioning of either cutter severed the cable and provided simultaneous freeing of the weights. The cable, weight, and one half of the cut cable are shown in Fig. 4.

3. Design parameters. Parameters are as follows:

- (1) Roll inertia = 3.83 slug ft².
- (2) Yo weight (each) = 84 g (including cable fittings).
- (3) Drum radius = 10 in.
- (4) Cable length = 15.71 ft.

4. Results. Development tests were conducted at the Langley Research Center in the 60-ft-diameter vacuum sphere at reduced pressure to negate aerodynamic effects. The results of five tests are given in Table 1.

Table 1. Results of five development tests

Parameter	Value for indicated test				
	1	2	3	4	5
Initial spin rate, rpm	287.0	265	250	277.8	271.2
Final spin rate, rpm	0.09	0.20	2.61	1.14	0.84
Time to despin (to second cable release), sec	0.733	0.789	0.750	0.742	0.771
Time between release of cables, sec	—	+0.0009	-0.0096	-0.005	+0.028

Flight tests were conducted utilizing the despin system above on a *Shotput* sounding rocket and a *Scout* vehicle—*San Marco* payload. The *Shotput* final despin rate was 0.1 rpm, and the *Scout* payload was despun to within the design criteria of ± 6 rpm.

5. Summary. The adequacy of the single-stage yo-yo system for the application cited can be attributed to two major factors:

- (1) The system is insensitive to initial spin rate if the final despin rate is zero. Systems designed for final spin rates other than zero would reflect a percentage of error in the final spin equal to the percentage of error in the initial spin.

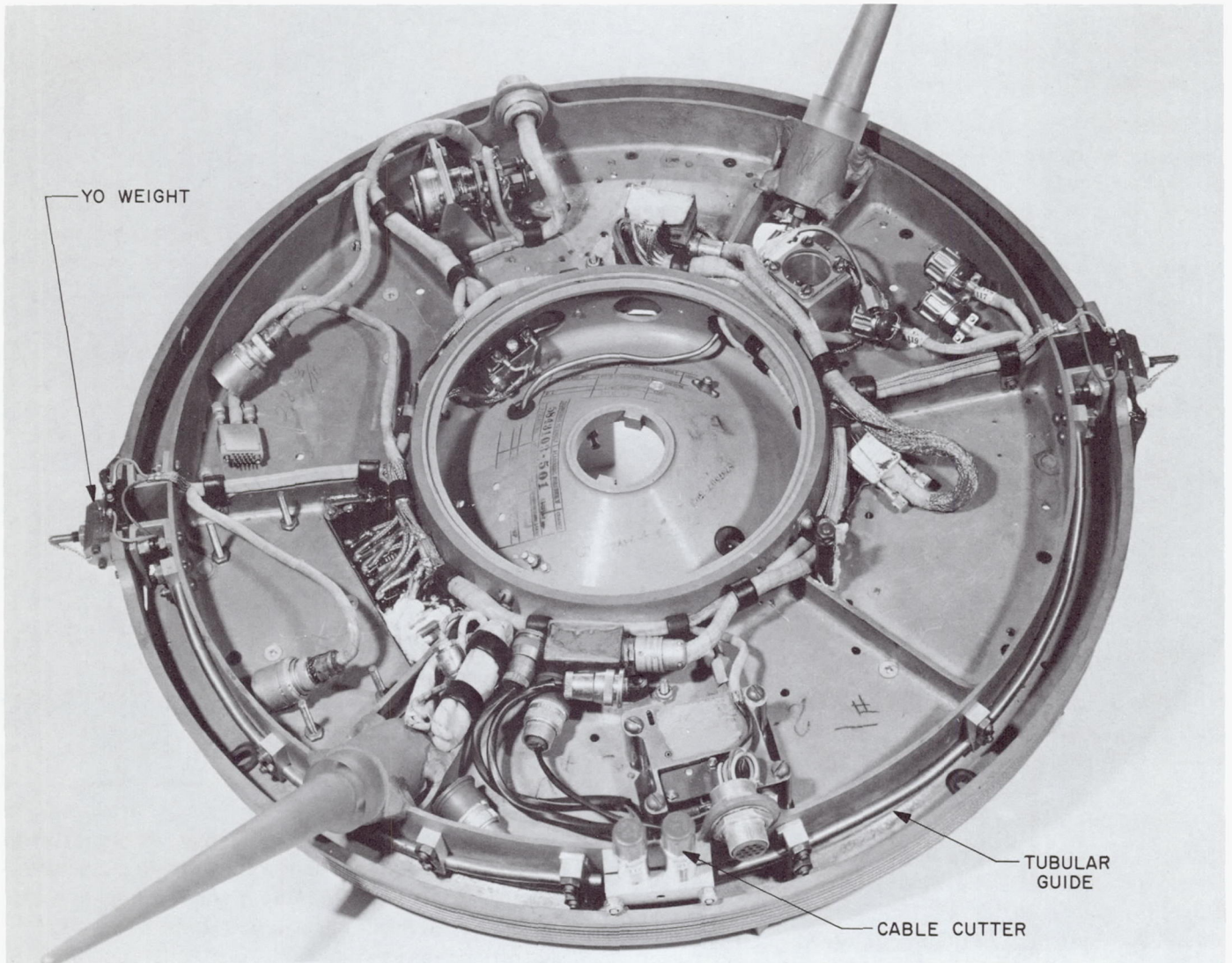


Fig. 3. Single-stage yo-yo despin

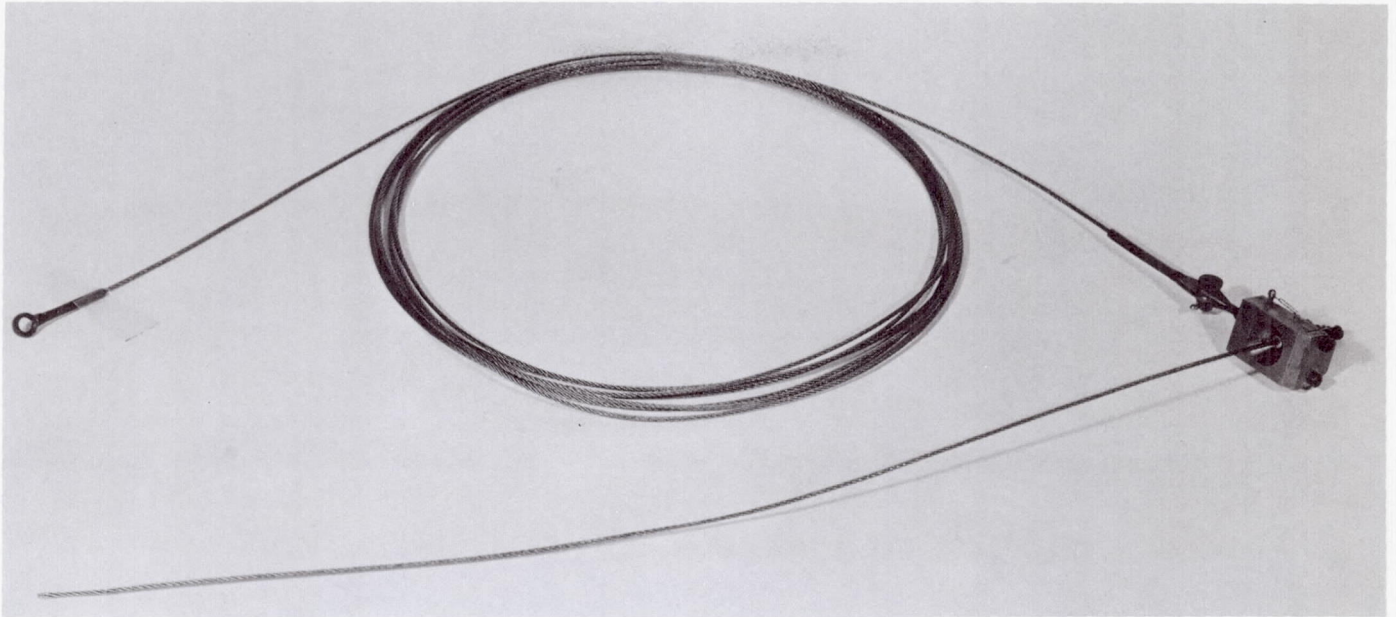


Fig. 4. Single-stage weight and cables

(2) The predicted moment of inertia of the burned-out rocket motor and payload combination was determined by experimental measurement utilizing a rocket motor available from a ground firing test. The close simulation of the moment of inertia with the expended flight rocket motors was extremely fortuitous.

B. Two-Stage Yo-Yo Despin System

A system representative of this type of despin was designed for a NASA Langley Research Center flight project by the Fairchild Stratos Corporation.

1. Design criteria. The system was required to despin the payload, the expended last rocket stage, and the vehicle shroud combination from an initial spin of 600 rpm to effectively zero rpm.

2. System description. The two-stage despin system, shown in Fig. 5, was designed to despin the spacecraft from 600 to 60 rpm during the functioning of the first set of yo-yo weights. The second yo-yo system reduced the spin rate from 60 to effectively zero rpm. Accurate prediction of the roll inertia of the spinning bodies was not possible, because of mass uncertainties in the burned-out rocket motor. The staging of despin permits closer control of the final spin rate. The percent error in the moment of inertia is reflected as a percent error in the spin

rate after each yo-yo stage functions. By using the two-stage system, the error in final spin rate can be greatly reduced.

The system as shown is recessed into the shroud with the heat shield not shown. The yo weights of each system are retained in position by means of a circumferential cable passing through redundant cable cutters diametrically opposite one another. A fitting to permit preloading is part of each restraining cable assembly. The first-stage yo-yo is sequenced through an on-board programmer. The cable cutters are fired, thereby cutting the restraining cable and releasing the first-stage weights. The yo-yo cable attach fittings incorporate a boss that actuates a microswitch at the time of cable release. This switch closure fires a second set of cable cutters, thus releasing the weights of the yo-yo second stage to complete the despin sequence. The release of energy stored in the preloaded restraining cables assures freedom from fouling and provides simultaneous release of the yo weights.

3. Design parameters. Parameters are as follows:

- (1) Roll inertia (first-stage despin) = 7.17 slug ft².
- (2) Roll inertia (second-stage despin) = 7.01 slug ft².
- (3) Yo weight (each) (first stage) = 2.15 lb.
- (4) Yo weight (each) (second stage) = 2.91 lb.
- (5) Drum radius = 0.937 ft.

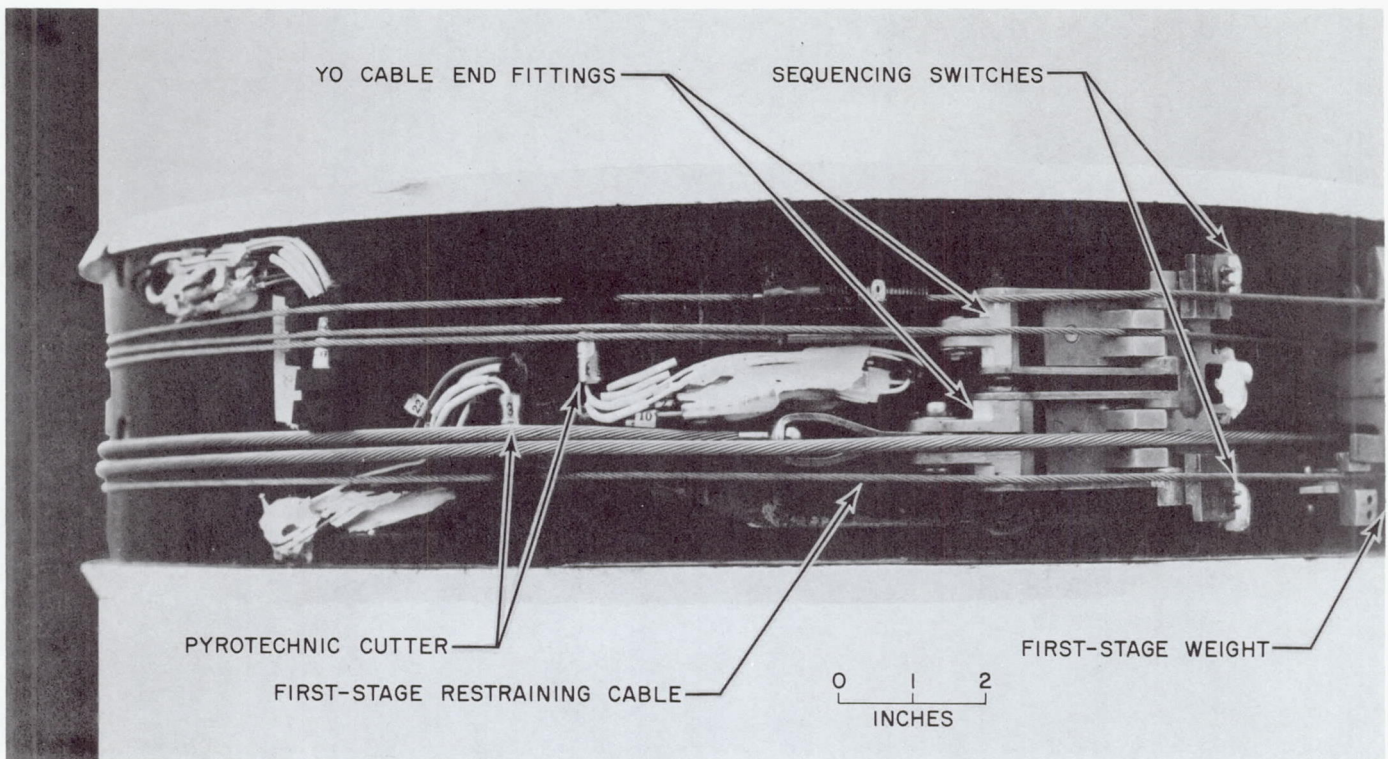


Fig. 5. Two-stage yo-yo despin system

4. Results. The first-stage despin was tested at Fairchild Stratos on a spin table giving a reduction from 597 to 60.26 rpm. The second-stage despin was tested in the LRC 60-ft vacuum sphere at a simulated altitude of 150,000 ft. This test was performed in free fall, reducing the spin from 70 to 1.4 rpm.

A subsequent rocket launch was conducted using this yo-yo despin system, resulting in a residual spin rate of approximately 1/6 rpm.

5. Summary. The adequacy of the two-stage yo-yo despin system was verified for the application cited. Sufficient insensitivity to errors in predicted initial spin rate and moment of inertia was demonstrated in meeting the required final spin rate.

C. Stretch Yo-Yo Despin System

A system representative of this type of despin was designed for a flight program for the NASA Langley Research Center by Honeywell, Incorporated.

1. Design criteria. The system was required to despin the payload and the expended last-stage rocket motor

from an initial spin rate of 312 ± 66 rpm to a final spin rate of 45 ± 6 rpm. The system was to accommodate $\pm 5\%$ variation in roll inertia and $\pm 21\%$ variation in initial spin rate.

2. Systems description. The stretch despin system is shown in Fig. 6. One yo weight, spring, cable, and end fitting are shown in Fig. 7. The selection of the stretch despin concept was dictated by the requirement that the system produce the desired final spin rate with significant variations in initial spin rate ($\pm 15\%$) and in roll inertia ($\pm 5\%$). During normal operation, the spring is expected to stretch a predicted amount. If the initial spin rate is greater or less than nominal, the spring will elongate more or less than normal during yo-yo operation and produce a final spin rate near the design value.

The stretch yo-yo system is also relatively insensitive to departure from the predicted or design moment of inertia. The weight retention and release system utilized dual cable-cutters to sever a cable to free both weights simultaneously. As shown in Fig. 7, the weight has a retaining lip about which the weight rotates on release. The release system consists of an interconnecting cable with attached levers at both ends. Applying tension in

the connecting cable rotates the levers against release pins that retain the weight in position. The release pins are spring-loaded and, upon severing the connecting cable, the pins are withdrawn from the weights. The

yo-yo system is then free to function. Release of the yo-yo weights, springs, and cables from the despun spacecraft occurs when the cable is radially in line with an element of radius.

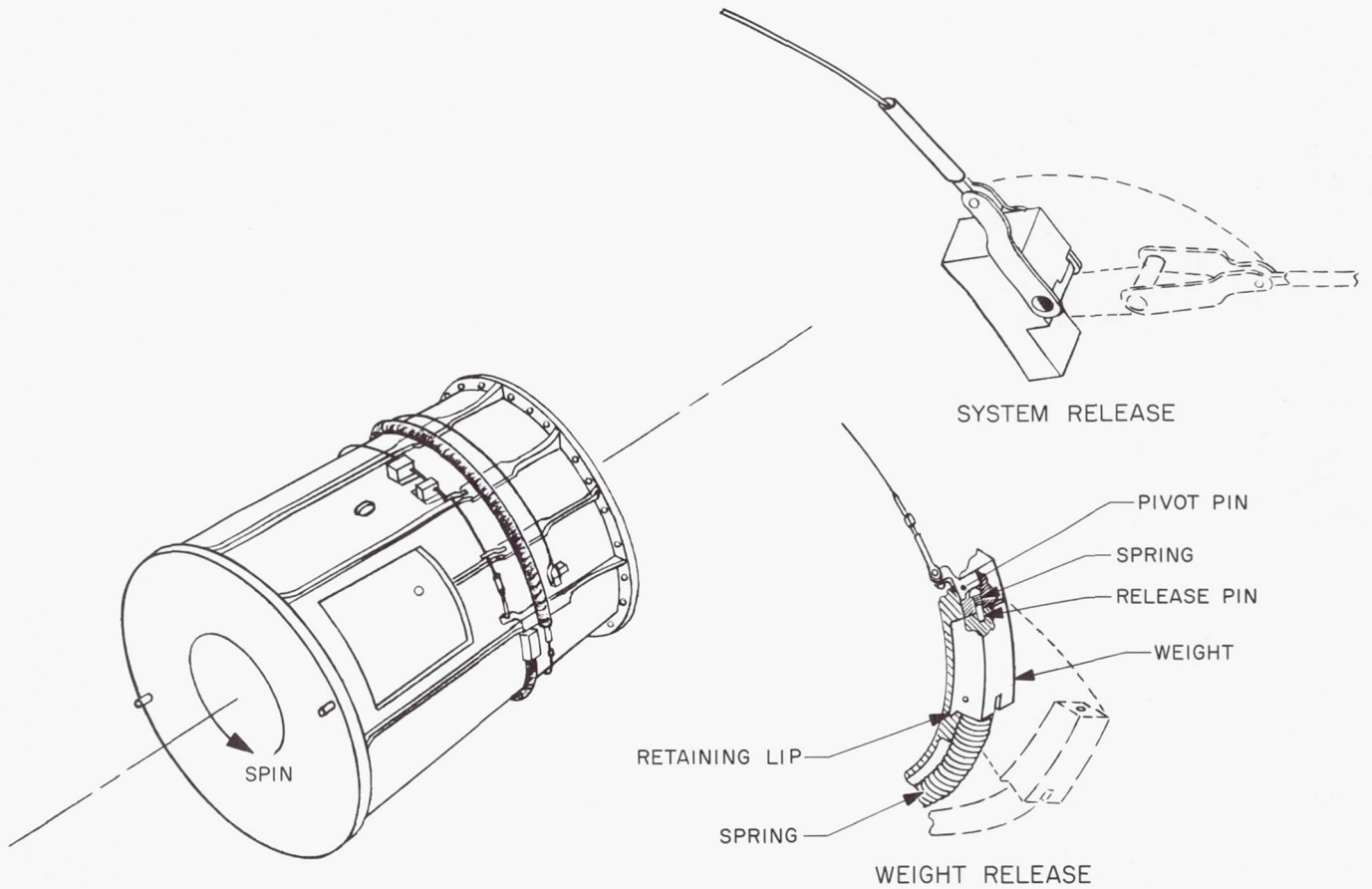


Fig. 6. Stretch yo-yo despin system

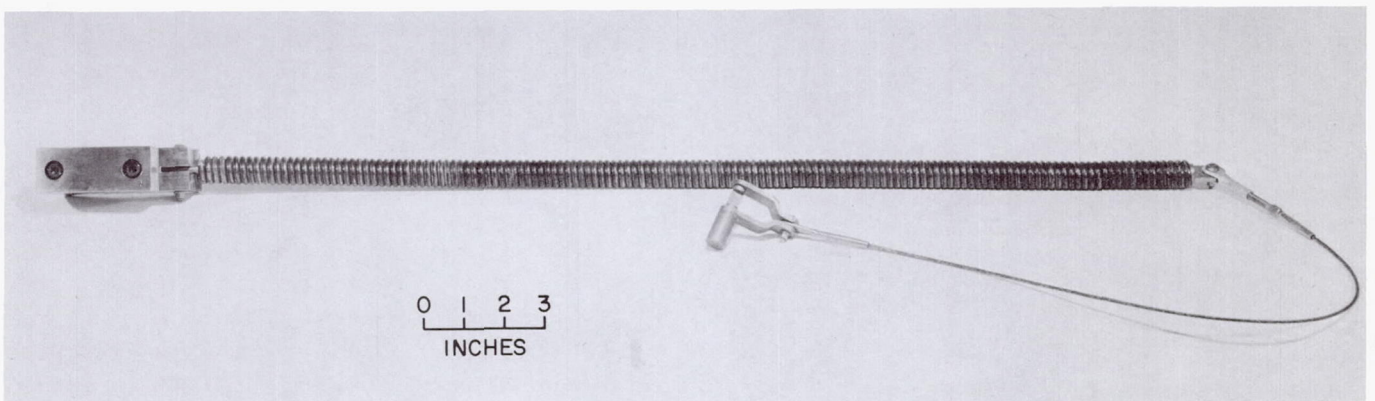


Fig. 7. Stretch yo-yo

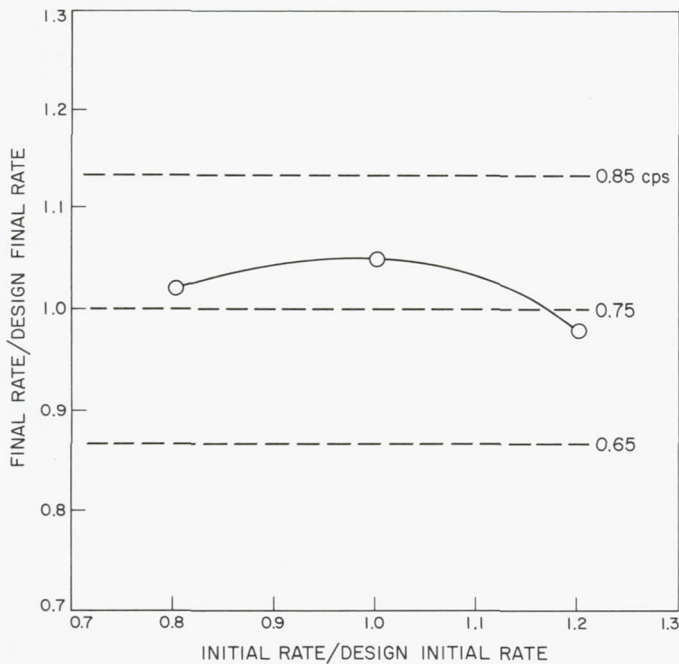


Fig. 8. Stretch yo-yo despin test results

3. Design parameters. Parameters are as follows:

- (1) Roll inertia = 8.12 slug ft².
- (2) Total yo weight = 7.95 lb (including 60% of spring weight).
- (3) Spring constant = 522 lb/ft.
- (4) Spring stretch = 0.5 ft.
- (5) Spring preload = 15 lb.

4. Results. Development tests of the stretch yo-yo system were conducted at Honeywell, Incorporated. Three

tests were conducted to establish the adaptiveness of the stretch yo-yo to variations in initial spin. Figure 8 shows the results of these tests, which verified the performance of the system within the design criteria.

Two flight missions of the *Scanner* spacecraft were flown, and in both cases the despin system operated within the design tolerances.

5. Summary. It has been demonstrated that a stretch yo-yo despin system is adaptive to spacecraft despin applications that require a system to be self-corrective in providing a low percentage error in the final despin rate with a high percentage error in the initial spin rate. The system's low-error final spin rate is not affected drastically by in-flight variations in the predicted spacecraft roll moment of inertia.

V. Conclusions

This paper has presented some of the fundamental principles and performances of three yo-yo-type despin systems. Flight tests of each type have demonstrated that the equations set forth in the reference documents are sound and will permit design of a simple mechanism for despinning rotating bodies in a space environment. These systems can be constructed of basic materials and fabricated by state-of-the-art techniques. The designer is afforded great latitude in the selection of the type of despin system and flexibility in the detailed design of the system and components. Straightforward engineering computations complemented by good design practices should provide a successful despin system.

References

1. Eide, D. G., and Vaughan, C. A., *Equations of Motion and Design Criteria for the Despin of a Vehicle by the Radial Release of Weights and Cables of Finite Mass*, Technical Note D-1012. National Aeronautics and Space Administration, Jan. 1962.
2. Cornille, H. J., Jr., *A Method of Accurately Reducing the Spin Rate of Rotating Spacecraft*, Technical Note D-1420. National Aeronautics and Space Administration, Oct. 1962.
3. Fedor, J. V., *Analytical Theory of the Stretch Yo-Yo for Despin of Satellites*, Technical Note D-1676. National Aeronautics and Space Administration, Apr. 1963.
4. Fedor, J. V., *Theory and Design Curves for a Yo-Yo Despin Mechanism for Satellites*, Technical Note D-708. National Aeronautics and Space Administration, Aug. 1961.

Deployable Solar Array*

T. Berry
Fairchild Hiller Corporation
Germantown, Maryland

Currently flown photovoltaic space power systems rely on either vehicle-body-mounted, fixed-paddle, or rigid-erectable solar arrays. A more recent concept is the deployable solar array, which presents distinct advantages over these systems in higher power-to-weight capability and more advantageous package volume and growth potential.

A description is given of the development, fabrication, and testing of a deployable solar array for a spin-oriented spacecraft application. The design employs a flexible, roller-mounted substrate which is erected by a linkage extension system. The total array area is 35.5 ft². It will fit within a 1.3-ft³ package, weighs 29 lb, and can be deployed vertically under 1-g conditions.

I. Introduction

The high reliability of solar cells, combined with their capacity to furnish power for a considerable time, has led to their use for approximately 95% of current space flights. It is expected that for the foreseeable future they will also provide the bulk of the space power for missions of any extended duration. To date the development of moderate to large solar arrays has focused on the use of fixed, rigid panels and rigid-erectable panels for

mounting these cells. A recurring problem with these methods is packaging for flight loads and making the design compatible with the ever-diminishing volumes allotted within the payload fairings. Optimization of rigid solar panels is now approaching a state of diminishing returns as relates to packaging efficiency and power-to-weight ratio; therefore, new concepts are needed. This paper presents the result of one of the initial efforts in this direction.

Specifically, this paper describes the development, fabrication, and testing of a deployable solar array for a spin-oriented spacecraft application. This approach employs a flexible substrate erected by a linkage extension

*The work reported in this paper was accomplished at the Space and Electronics Systems Division of Fairchild Hiller under Contract NAS 5-9658 with the Goddard Space Flight Center.

system. The motive power for deployment is provided by potential mechanical energy stored in springs. Significant requirements for the design were: (1) a 2π steradian field of view, (2) deployment at spin rates up to 160 rpm, (3) horizontal self-support under 1-g conditions, (4) capability of withstanding the shock, vibration, and acceleration of launch, and (5) the use of nonmagnetic, state-of-the-art, space-qualified materials.

During this program, a 2.16-ft-wide by 8.20-ft-long flexible array system was developed and tested. Back-to-back substrates using silicon solar cells were used to provide the necessary view angle. The arrays are deployed from a pair of synchronized rollers using spring energy and are supported in the deployed configuration by a mechanical linkage. The total area of both arrays is 35.5 ft². The packaged array will fit within a 1.3-ft³ package and weighs 29 lb. This is 1.23 ft²/lb for a deployed array and 0.0318 ft³/ft² for a packaged configuration. The weight of the assembly was slightly more than that anticipated, but is due in part to a decision to deploy it vertically under 1 g. The added weight was approximately 3.2 lb, of which 2.1 lb are springs. Actual flight weight could be reduced to 25.8 lb, increasing the area/weight ratio to 1.37 ft²/lb. The array minus mechanism was fabricated for 2.25 ft²/lb, using 6-mil covers on nominal 13-mil cells. The deployed array is shown in Fig. 1.

Testing included vibration, humidity, and spin deployment of the complete system, and humidity, vibration, tension-fatigue, and thermal cycling of a sample array. During testing no malfunction or serious damage occurred to any of the components or to the mechanism itself.

II. Array

The material chosen for the array substrate is a 3-mil Kapton film. It exhibits very high radiation resistance and has a zero strength temperature of 800°C. Other properties making this material attractive for substrate use is a tensile strength of 20,000 psi, a low moisture uptake, good chemical resistance, and a high dielectric strength. The weight of the 3-mil film is 0.0226 lb/ft².

The solar cells applied to the substrate were 13-mil, 1- × 2-cm silicon. They were mechanically functional but no attempt was made to obtain high electrical efficiency. Six-mil microscope slide stock, trimmed to fit the cells, was used for simulated filters.

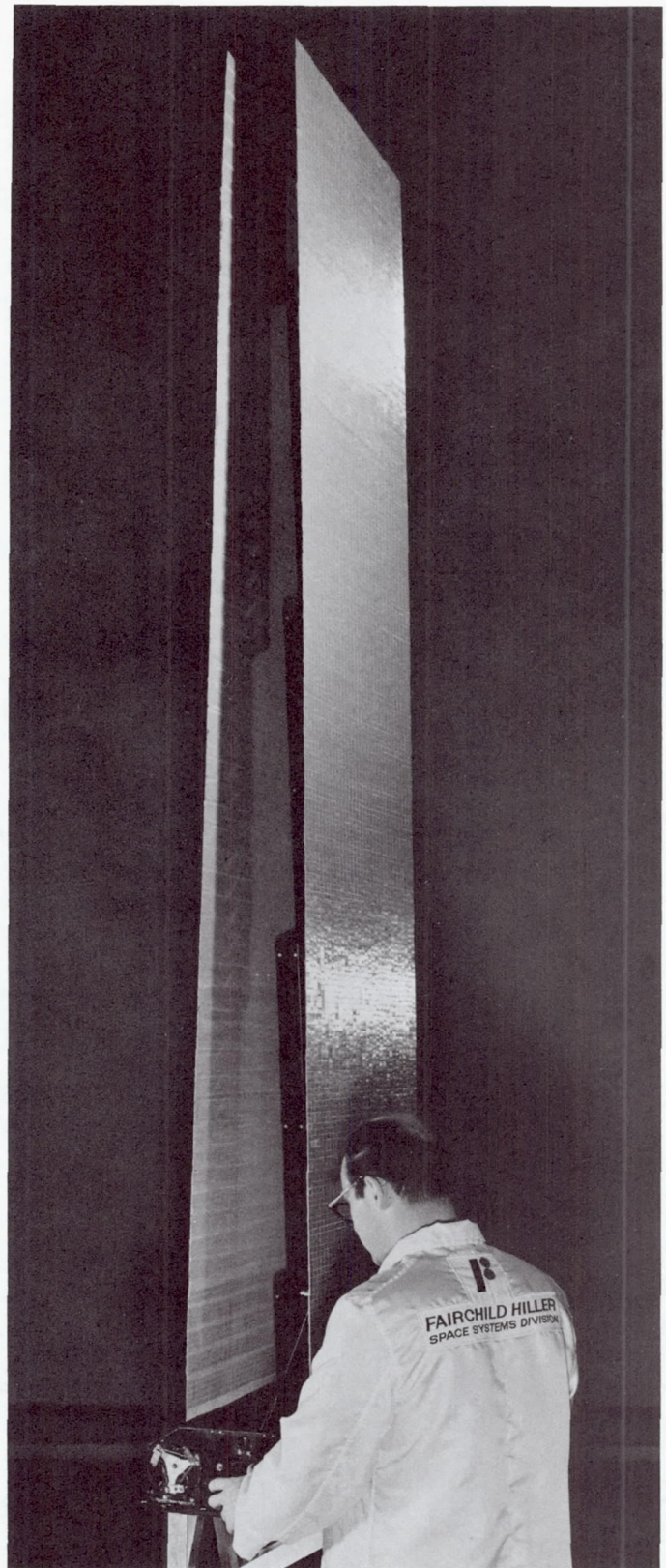


Fig. 1. Deployable solar array

The cell interconnect was expanded silver arranged in a generalized series-parallel circuit with the slots in the material running perpendicular to the flexing axis. A total of 3 ft² of cells was applied to the arrays: 2 ft² at the tip and 1 ft² at the root. These locations were chosen since they represent the most probable areas of cell damage. The remainder of the area is covered by 0.025-in. × 2-cm × 1-cm anodized aluminum chips used for weight and volume simulation.

The cells, both live and simulated, are bonded to the substrate, using RTV 102 and RTV 108 silicon rubber adhesive. These were a compromise between adequate bond strength and adhesion low enough to make replacing damaged or broken cells practical. Cover glass was attached to the front of the live cells, using RTV 602.

Additional stiffness was added to the substrate by magnesium strips bonded to the aft face of the substrate. These help considerably during handling and fabrication.

To prevent scuffing of the cells and breaking of the cover glass, a backing of 0.032-in. polyethylene foam was applied to the aft surface of the array.

The weight of the array, excluding any mechanism, is 0.45 lb/ft² and is distributed as shown in Table 1. These are actual weights based on 425 cells/ft². The weight can be reduced to 0.355 lb/ft² using 8-mil cells.

Table 1. Substrate weight summary

Component	Weight, lb/ft ²
Cover glass	.074
Bond	.022
Cells (13-mil)	.209
Connection	.019
Bond	.061
Substrate	.023
Stiffeners	.018
Bond	.019
Foam	.004
Total	.449

III. Drive and Extension Mechanism Design

The extension mechanism is primarily to deploy the array and support it during and after erection in space.

Secondary requirements involving handling and test have considerably increased the structural requirements, however, and the linkage as presently designed will support itself horizontally, and deploy vertically upwards, under 1-g conditions. The links are rectangular aluminum tubes that are 103.0 in. long when fully extended. Lightning holes have been included to reduce weight and improve accessibility, and an anodic coating was applied for surface protection. Plastic bushings are used throughout to reduce friction. The screwjack is made of titanium for its weight and nonmagnetic properties. The torsion springs in the links are 0.125 square music wire. The design is shown in Fig. 2.

IV. Release Mechanism Design

The release mechanism will support the extension mechanism during vibration, shock, thrust, and spin loading and will prevent inadvertent deployments. The design is shown in Fig. 3. The release sequence is initiated when current is applied to the solenoid. The solenoid is operated only long enough to pull the sliding cam upward to a point where both cam and solenoid armature can be captured by the cam latch. Pulling the cam frees the array gear train, allowing the arrays to start deployment, and displaces the push rod to start release of the linkage. The push rod has locking blocks on each end, which provide a positive interference lock for the restraint levers mounted on the side plates. The levers, when freed, allow the clamping arms to release the front plate, thereby permitting the linkage to deploy.

V. Brake System Design

A damper is required to reduce the radial deployment rate of the arrays and extension mechanism to eliminate excessive side loads due to Coriolis and deceleration forces. The system used is a centrifugal brake driven by the array rollers. Significant components of the device are shown in Fig. 4.

Torque imparted to the rollers by the substrate is transferred to the flyweights through a 21.46-to-1 planetary gear train. The flyweights, under influence of this rotation and the rotation of the spacecraft about its spin axis, cause the friction pads to contact the brake drum, thus restraining deployment.

The gears used in the system are aluminum and are bearing-mounted where necessary to eliminate frictional

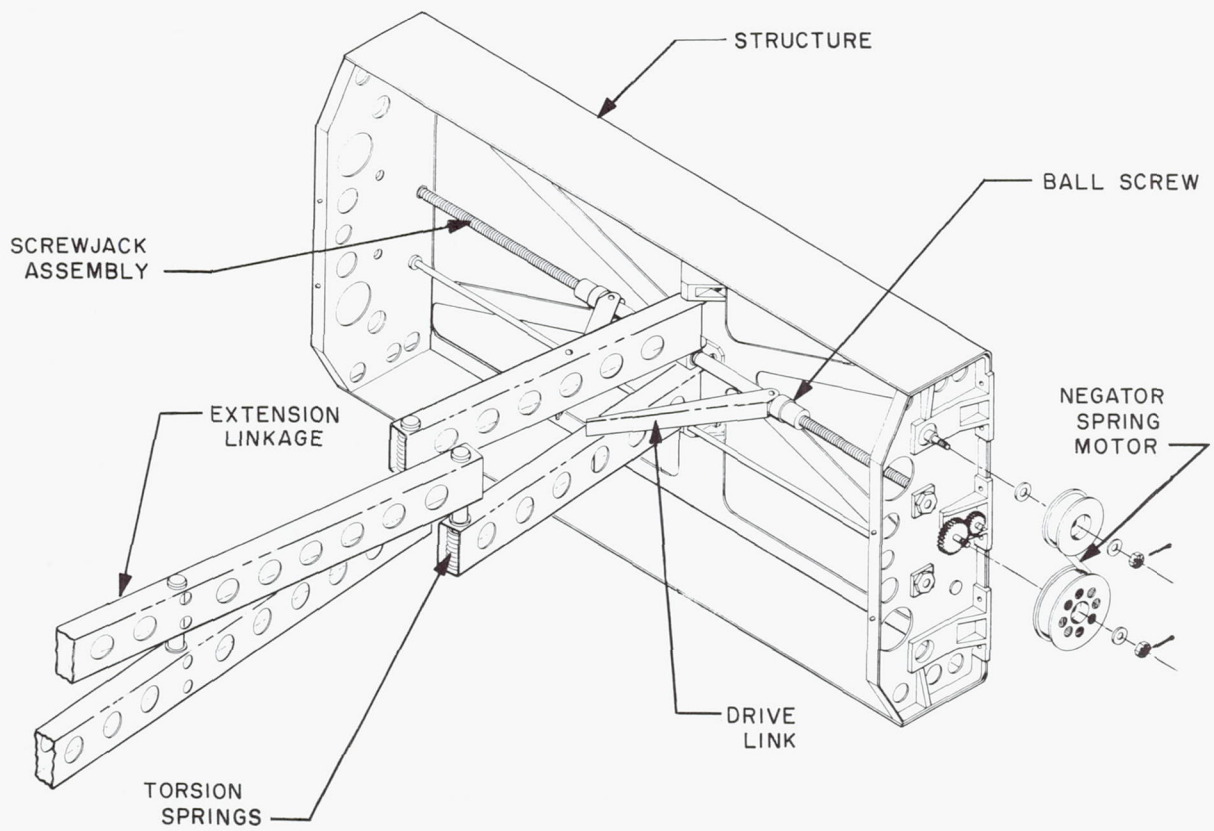


Fig. 2. Drive and extension system

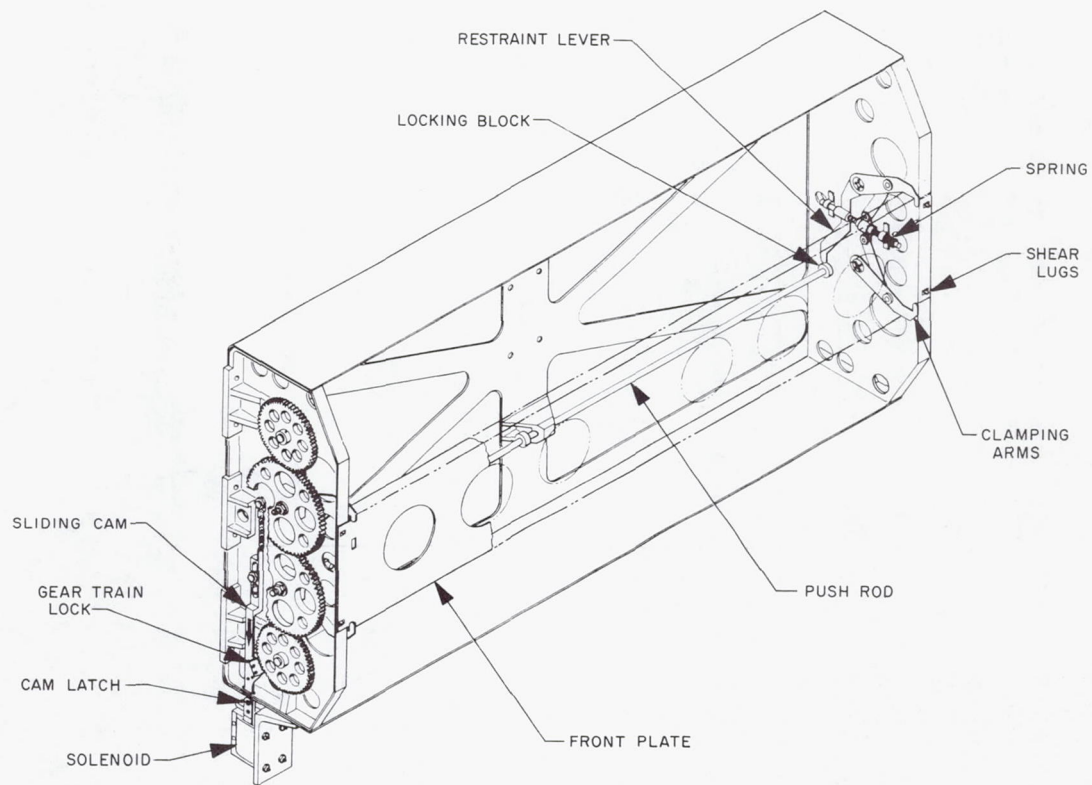


Fig. 3. Release system

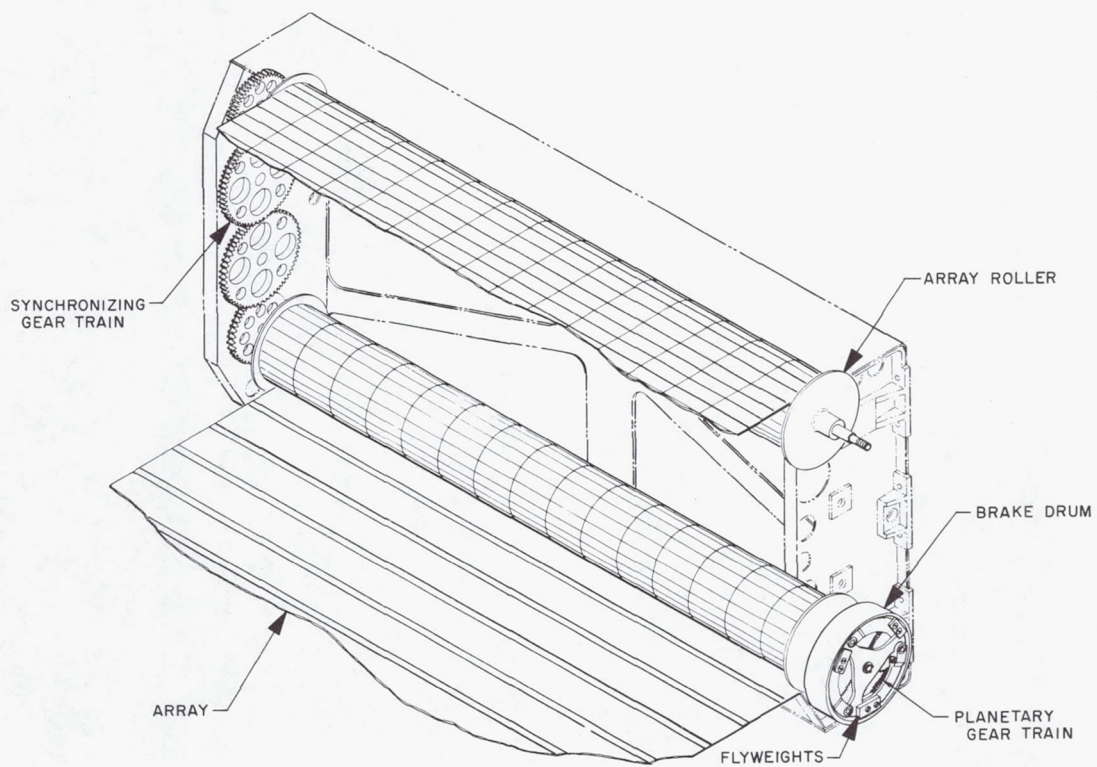


Fig. 4. Brake system

forces for low load applications. The flyweights are made from sintered tungsten. Three weights are employed to provide smoother operation. Teflon brake pads are mounted within the flyweight arms and are a trade-off between very-low-speed deployments where little damping is needed and deployment at high rates where force on the arms compensates for the low frictional characteristics.

VI. Structure Design

The structure design for the deployable solar array was intended to provide a sound base from which to mount the linkage, array, and release mechanism. In addition, the structure also supplies handling and shipping protection and, to some extent, protection against dirt and humidity.

Weight was an important aspect of the design and much effort was made to minimize this through careful selection of materials and processes. The principal load-carrying members are the machined magnesium side plates. They support the array rollers, the front, top, and bottom plates, and the release mechanism. The side plates are intended to be bolted directly to the primary structure of the spacecraft. Material for the balance of the structure is magnesium or aluminum sheet. Protective coatings for the parts are Dow 9 and black anodize, respectively.

VII. Testing

The system testing consisted of spin deployments at various rates, three-axis vibration, and humidity testing to determine storage capabilities. Environmental tests were also performed on the substrate, including thermal cycling, humidity, tension-fatigue, and vibration tests.

A. System Testing

The humidity test was performed in an undeployed configuration. A small amount of oxidation and galvanic corrosion was found. The vibration test produced no failure. Figure 5 is the mechanism response for an input parallel to the roller axis. Accelerometer 3 was mounted on the front plate, and 4 on the end plate. Considerable damping was evident. The spin deployment test setup is shown in Fig. 6. Tests of 40, 60, 80, and 100 rpm were run, and the results are in Fig. 7.

B. Substrate Test

The humidity test indicated no mechanical or electrical performance degradation. Thermal cycling tests

between temperatures of -120 and $+180^{\circ}\text{F}$ were continuously monitored during the 27 cycles and indicated no failures. The results of the vibration test given in

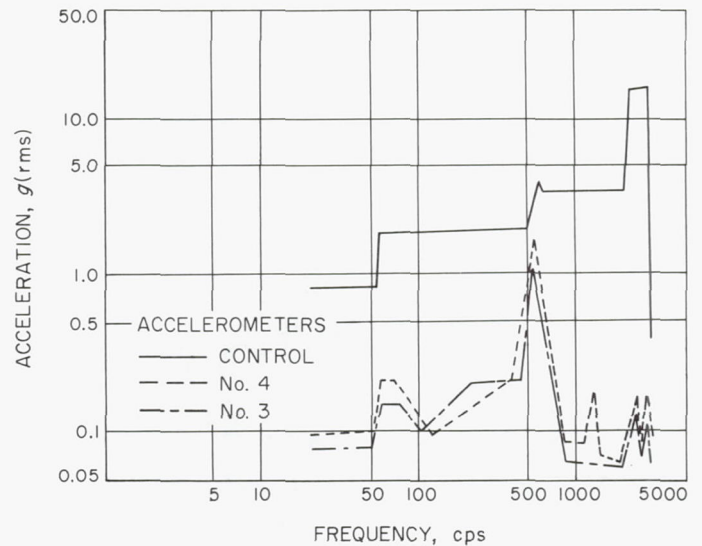


Fig. 5. Vibration test lateral axis (sine)

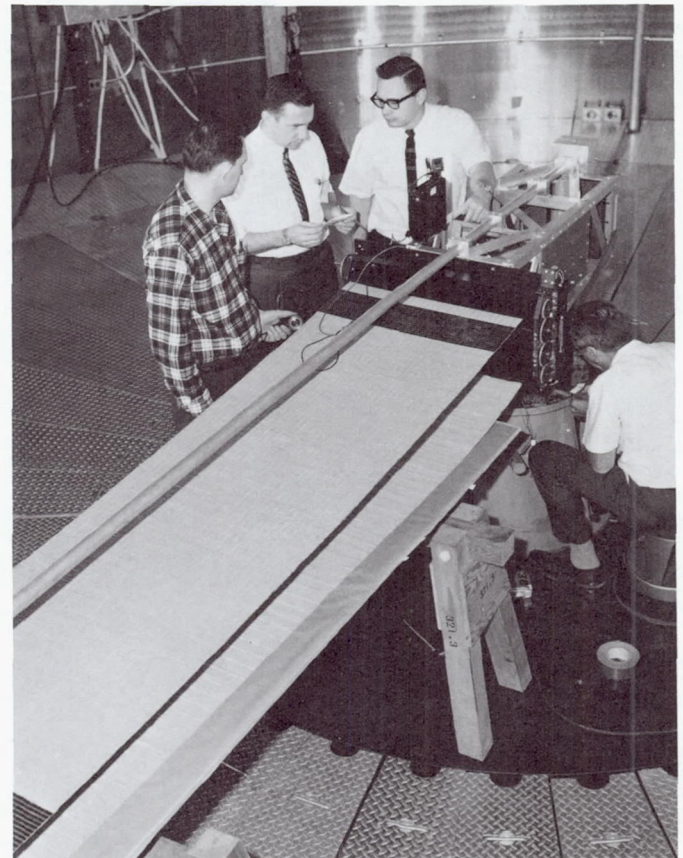


Fig. 6. Spin deployment test set-up

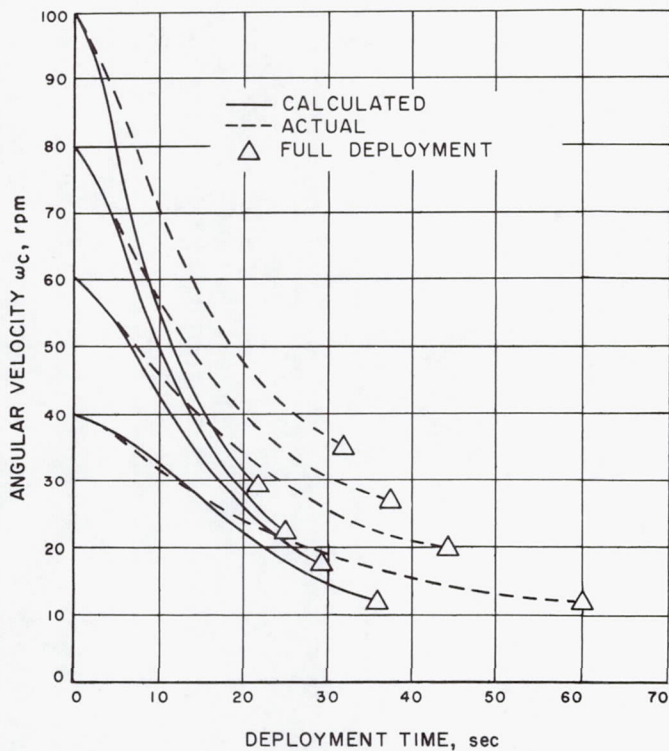


Fig. 7. Calculated and actual deployment times

Fig. 5 indicate that considerable damping is obtained through the foam layers. Visual and electrical checkouts after test indicated no mechanical or electrical degradation. Electrical continuity was maintained throughout the tension-fatigue test, and the output voltage remained constant throughout the 500 cycles.

VIII. Conclusions and Recommendations

The experience gained during development of the deployable solar array has indicated that the concept is

feasible and represents an improvement in weight and packaged volume over existing photovoltaic systems. Specifically, the concept of a flexible substrate for single crystal silicon solar cells has proved workable. The mechanical system used for deployment, although not overly sophisticated, has functioned well under the testing as described. The method of attaching the cells to the substrate, the interconnection for the cells, the methods of handling, and the necessary data on roll diameter and roll buildup have also been established.

Additional items to be considered for future work are radiation testing, more extensive thermal shock testing, and microscopic and metallographic inspection. Thermal testing in a vacuum chamber under simulated flight conditions should also be instituted to support the thermal analysis, and structural natural frequencies of the deployed array are needed for use in despun operational modes.

Investigation to modify the present array into a semi-universal solar power system is recommended. This would include extension mechanism redesign so that links can easily be added or deleted to change the total length. Along with this change is the consideration of making the substrate in modules such that they can also be deleted or added. A secondary advantage of this would be easier fabrication, handling, and inspection.

If the array is to be attached to a vehicle having more than one solar panel, it is advisable to look at various means of simultaneously deploying several solar arrays. A more pressing item than any of the foregoing, however, is to obtain a flight for an experimental array. The need is to gain additional information under actual flight conditions and to demonstrate proven flight capability.

Surveyor Television Mechanisms

J. B. Gudikunst
Hughes Aircraft Company
Culver City, California

This paper describes the mirror assembly, the variable-focal-length lens assembly, the filter wheel assembly, and the focal-plane shutter assembly of the Surveyor spacecraft camera. Detailed design specifications for each component are presented, with particular emphasis on operating conditions in the lunar environment.

I. Introduction

The *Surveyor I* spacecraft (Fig. 1) that Hughes Aircraft Company built under contract to the Jet Propulsion Laboratory (JPL) carried several subsystems containing intricate mechanisms. This spacecraft was successfully soft-landed on the lunar surface at 23:17 (PDT) on June 1, 1966. The television subsystem successfully took 10,338 individual photoframes of the lunar surface; Fig. 2 shows one of the initial photos. This paper briefly describes the major mechanisms of this subsystem: the mirror assembly, the variable-focal-length lens assembly, the filter wheel assembly, and the focal-plane shutter assembly. The overall system has been adequately discussed by Montgomery and Wolf.¹ Figures 3 and 4 show the complete television camera.

¹D. R. Montgomery and F. J. Wolf, "The *Surveyor* Lunar Landing TV System," *IEEE Spectrum*, August 1966.

II. Television Camera

The television camera consists of a vidicon tube, an electronic assembly, an outer housing, and the four mechanisms listed above. The camera must:

- (1) Provide optical images of the lunar surface over 360 deg in azimuth and cover about 40 deg above and 60 deg below the horizontal. The images are to be in a series of discrete azimuth or elevation steps. Each nominal optical and mechanical step in azimuth is to be 3 deg. Each nominal mechanical step in elevation is to be 2.5 deg, which results in an optical step of 5.0 deg.
- (2) Provide both a 600- and a 200-TV-line raster scan mode of operation. The 600-line scan mode furnishes better pictures but requires greater signal bandwidth. The camera employs the 200-line scan

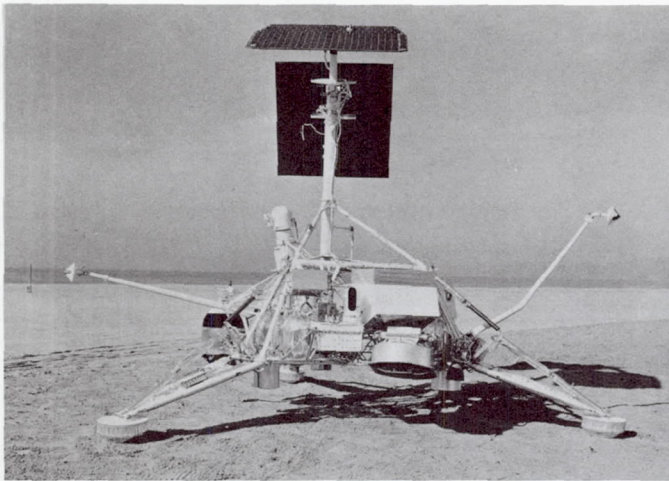


Fig. 1. Surveyor spacecraft

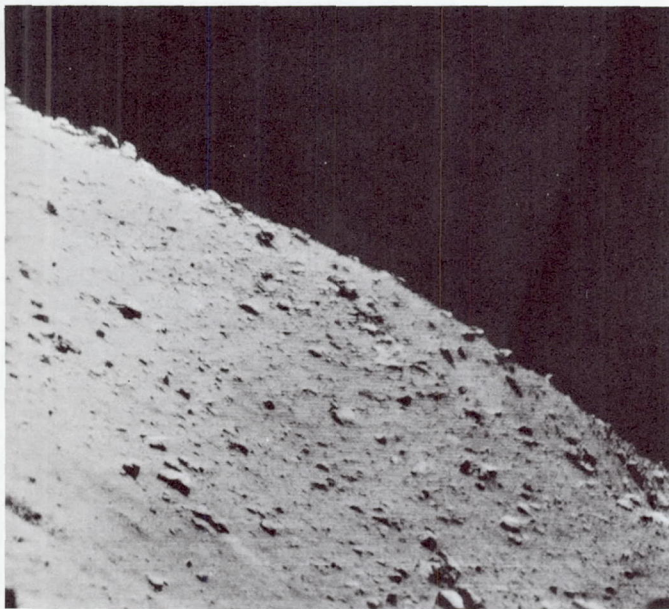


Fig. 2. An early lunar photo sent back by Surveyor I

mode of operation when either the high-power transmitter or the high-gain antenna on the spacecraft fails, and as a consequence the bandwidth is constrained. A 600-TV-line scene is transferred every 3.6 sec, one of 200 TV lines every 60.8 sec.

- (3) Withstand operating temperatures of -25 to 180°F and nonoperating temperatures of -300 to 250°F .
- (4) Operate reliably in the vacuum environment of the surface of the moon, which has been estimated as 1×10^{-13} torr. Basic tests at Hughes Aircraft Company were conducted in a vacuum of about

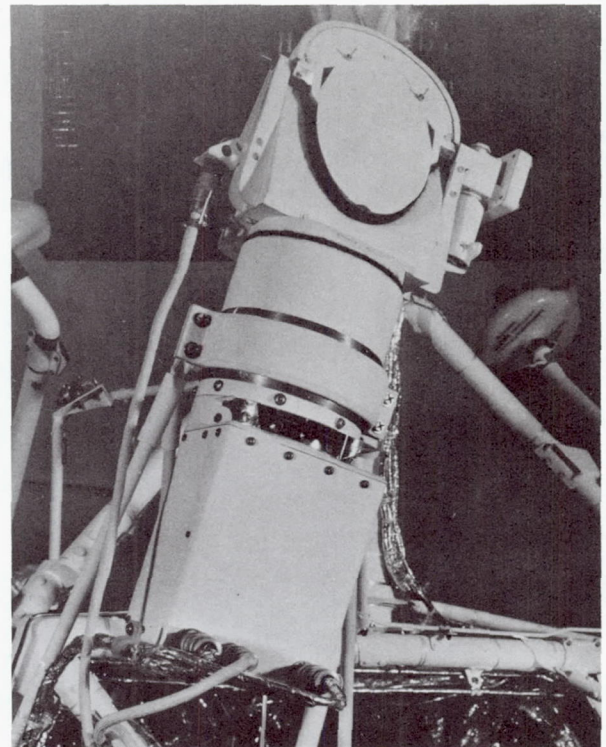


Fig. 3. Complete television camera on Surveyor

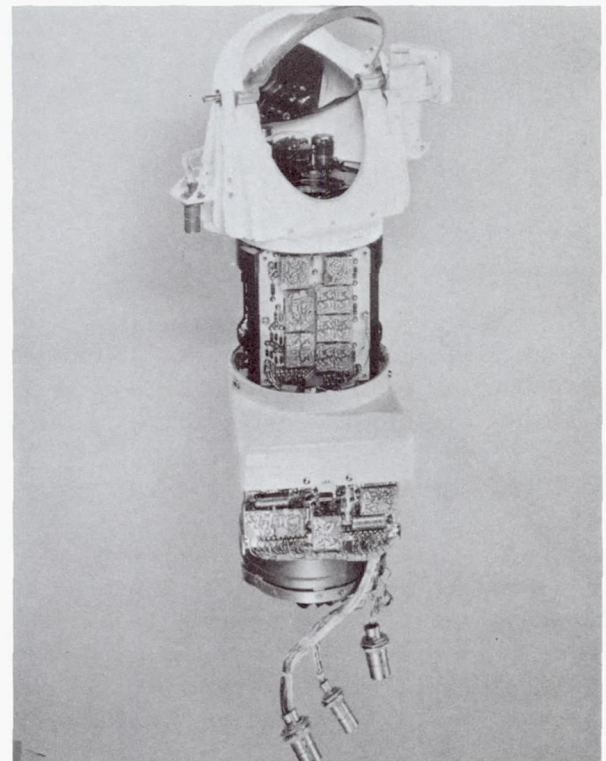


Fig. 4. Surveyor television camera showing mirror and lens assembly

1×10^{-7} torr. Several special verification tests of mechanisms were made at 1×10^{-11} torr to satisfy some who contended that "mechanisms may work at 10^{-7} torr but not at 10^{-11} torr."

- (5) Be no larger than 8 in. in diameter and 24 in. long.
- (6) Weigh no more than 16.1 lb.
- (7) Withstand a vibration of 9 g.

III. Mirror Assembly

Parameters for the mirror assembly are summarized in Table 1.

Three mirror assemblies have been built, Models A (Figs. 3 and 4), B, and C (Figs. 5 and 6). (The *Surveyor* camera and its components are shown in Fig. 7.)

Table 1. Mirror assembly parameters

Parameter	Value
Operating temperature, °F	-50 to 180
Nonoperating temperature, °F	-300 to 250
Weight, lb	4.70
Input power to rotary solenoid	
Voltage, v dc pulsed	12.0 to 27
Pulse duration, msec	100 to 150
Pulse rate, pulses/sec (pps)	4
Azimuth	
Travel	360 deg in 118 steps; each step is 3 deg \pm 3.00 min
Mechanical repeatability of each step	\pm 3.0 min (2 sigma)
Usable life	102,000 scan steps
Gear ratio	12:1
Elevation	
Travel	40 deg up from horizontal (line of sight) 65 deg up from horizontal (mechanical) 60 deg down from horizontal (line of sight) 15 deg down from horizontal (mechanical) 65 deg down (door-closed position)
Mechanical repeatability of each step	\pm 3.0 min (2 sigma)
Usable life	50,000 scan steps
Gear ratio	14:1
Flatness of mirror	0.25 wavelength over entire surface
Vibration	Be able to withstand 12 g

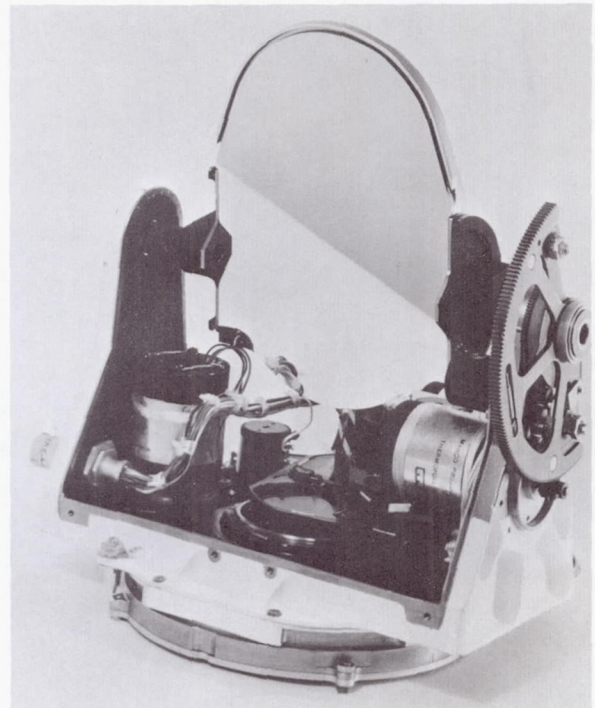


Fig. 5. Model C mirror assembly

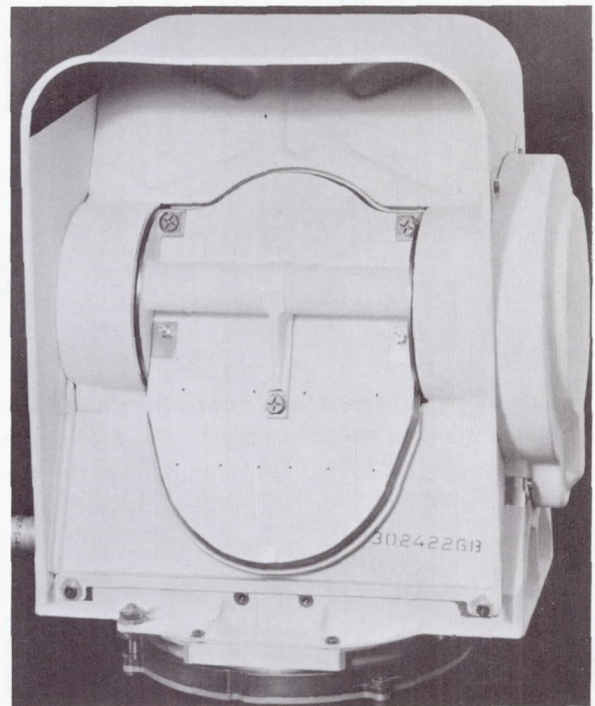


Fig. 6. Model C mirror assembly, closed

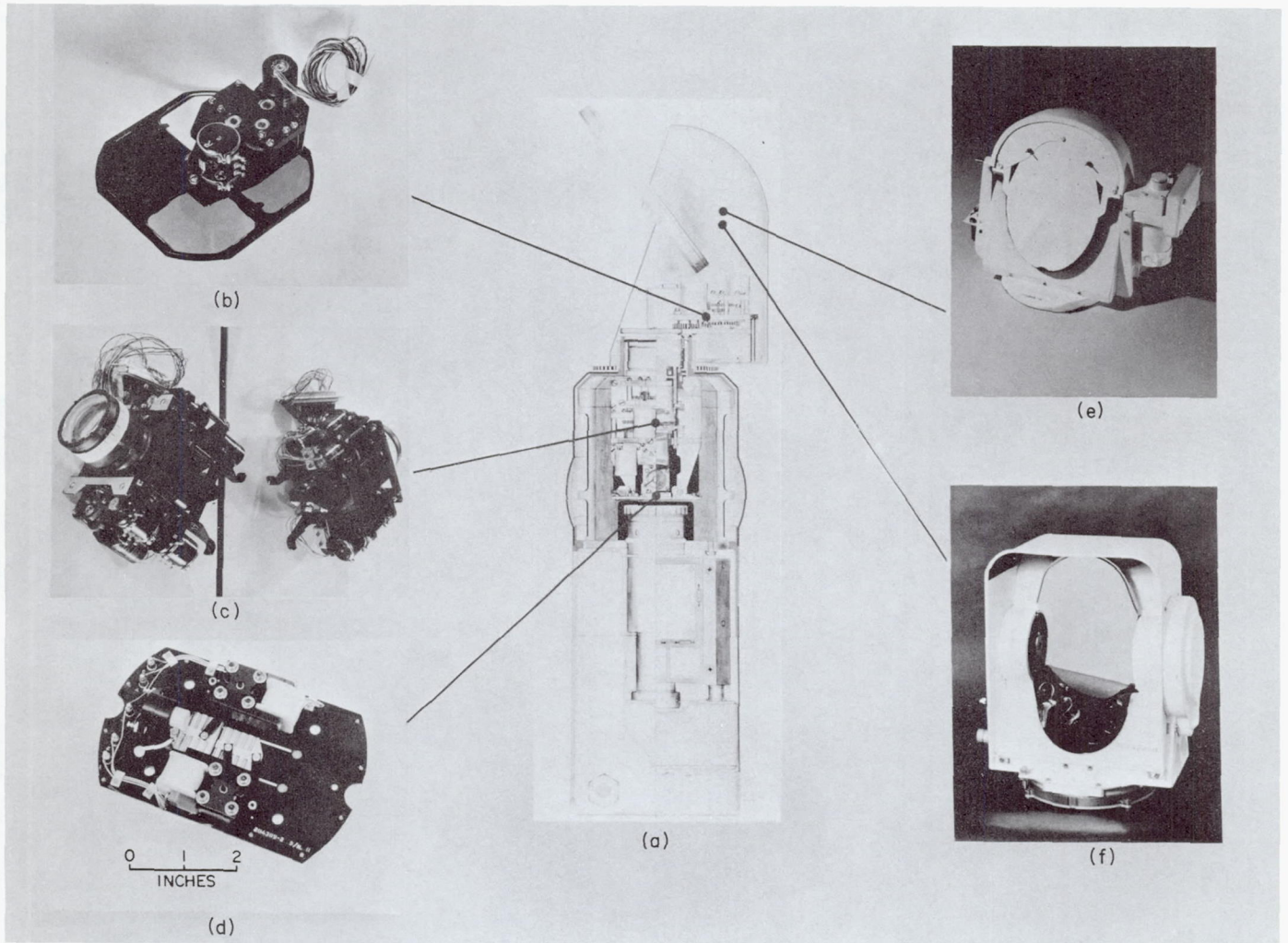


Fig. 7. Surveyor camera and components: (a) the complete camera; (b) the filter wheel assembly; (c) the variable-focal-length lens assembly; (d) the focal-plane shutter assembly; (e) the Model A mirror assembly; and (f) the Model C mirror assembly

Surveyor I was launched with the Model A mirror assembly shown in Figs. 3, 4, and 7e. *Surveyor* spacecraft Nos. 2 through 4 will utilize longer overhead shields (on the Model B assembly) to reduce the amount of stray light entering the camera. Most of the structural elements of the Model A and B mirror assemblies were made of aluminum.

The following problems were encountered in the initial design:

- (1) Components (motors and potentiometers, etc.) were difficult to replace.
- (2) A journal bearing was utilized in azimuth movement. The bearing had excessively high friction torque in various vacuum and thermal environments, and, worse yet, this torque was never consistent. Several hundred tests were run with different lubricants, radial tolerances, vacuum levels, thermal limits, camera angles, azimuth angles, etc., and with one-sixth earth weight to simulate lunar gravity.

Spacecraft No. 5 and up will use the Model C mirror assembly shown in Figs. 5, 6, and 7f. Structural parts of the assembly are machined from solid beryllium for optimum strength-to-weight ratio. The large aluminum static spur gear (on the mirror assembly, the motor and motor pinion walk around a static azimuth gear) was replaced by one made of steel. The entire outer light-shield housing can be easily removed in order that the components and other key mechanisms may be easy to assemble and replace.

Although space was very limited, the journal bearing was replaced with a large preloaded bearing set. Teflon impregnated with MoS₂ is the lubricant for this bearing and is supplied by the duroid slugs that are used as ball separators. The friction torque of this bearing was not only about 2.5 times less, but the torque values were also consistent.

The movable flat mirror is a 10.5- by 15-cm elliptical mirror supported at its axis by a trunnion shaft. The mirror surface is made of Kanogen-coated beryllium upon which aluminum is vacuum-deposited. A silicon monoxide overcoat protects the aluminized surface. The average specular reflectivity is greater than 86%.

Stepper motors are used to obtain the discrete optical look positions in azimuth and elevation. The potentiom-

eter outputs are digitalized and transmitted to earth to enable the operator to know the exact position of the camera.

The light-shield hood of the Model C mirror assembly is also larger than that used with Models A and B.

IV. Variable-Focal-Length Lens Assembly

Parameters for the variable-focal-length lens assembly are summarized in Table 2.

Table 2. Lens assembly parameters

Parameter	Value
Operating temperature, °F	-25 to 165
Nonoperating temperature, °F	-300 to 250
Weight, oz	36
Input power, v dc pulsed	16 to 26
Motors	Size 8 stepper motor
Potentiometers	3-turn, size 11, 5K
Focal length, mm	25 to 100
Field of view, deg	25.3 to 6.43
Life (minimum), cycles	1000
Pulse rate, pps	100
Gear ratio	180:1
Focus	4 ft to infinity
Life (minimum), cycles	10,000
Pulse rate, pps	16
Gear ratio	90:1
Iris	f/4 to f/22
Life (minimum), cycles	15,000
Pulse rate, pps	62.5
Gear ratio	90:1
Resolution, lines/mm	88
Beam splitter	Required for automatic servo control of iris; also acts as fail-safe device to protect vidicon from excessive solar energy
Vibration	Be able to withstand 9 g

This lens assembly (Fig. 7c) meets the key optomechanical requirements for focal length, focus, iris, and stringent optical quality. The Bell and Howell Company made this assembly under subcontract to the Hughes Aircraft Company. In the many developmental tests of various mechanical shapes and types of lubricants that were conducted, Hughes furnished Bell and Howell with the motors and potentiometers.

V. Filter Wheel Assembly

Parameters for the filter wheel assembly are summarized in Table 3.

Table 3. Filter wheel assembly parameters

Parameter	Value
Operating temperature, °F	-25 to 165
Nonoperating temperature, °F	-300 to 250
Weight, oz	11.0
Input power, v dc pulsed	15 to 26.3
Pulse rate, pps	100 ± 5
Gear ratio	100:1
Potentiometer	3-turn, size 11, 5K
Life, cycles	20,000
Vibration	Be able to withstand 36 g

The choose-a-color filter wheel assembly is located inside the mirror assembly (see Fig. 7b). It consists of a stepper motor, a size 11 potentiometer, a 100:1 gear train, and a four-color wheel of red, green, blue, and clear for non-monochromatic observation. The Jet Propulsion Laboratory supplied the filter elements. JPL had used a computer program in matching the spectral response of each vidicon tube with its filters. (If a vidicon is replaced in a camera assembly, the filters are also replaced.) The structure and gears of the filter wheel are made of aluminum.

VI. Focal-Plane Shutter

Parameters for the focal-plane shutter are summarized in Table 4.

The focal-plane shutter (Fig. 7d) that is located between the lens assembly and the vidicon was developed by JPL, was later designed for production, and was produced by the Hughes Aircraft Company.

It operates in either of two modes. In the first, the shutter blades are sequentially driven by a rotary solenoid via a parallel bar linkage across the aperture in the base plate of the shutter in order to allow light to reach the face of the vidicon tube. The time between the start of motion of each blade determines the exposure interval, which is nominally 150 msec; a 20-msec shutter is also available.

Table 4. Focal-plane shutter parameters

Parameter	Value
Operating temperature, °F	-65 to 165
Nonoperating temperature, °F	-300 to 250
Weight (including that of photodiode assembly), oz	6.1
Life	60,000 cycles at a rate of one exposure every 3.6 sec. (A cycle is defined as an opening and closing of the shutter, with the blade returning to its original position.)
Input power, v dc pulsed	15.0 to 26.3
Shutter timing	Capable of providing exposures of 20 and 150 msec
Vibration	Be able to withstand 54 g

In the second mode, the blades can be so positioned that the aperture remains open. This mode is desirable in imaging scenes having very low light levels, such as stars.

The most difficult items in the shutter to design and produce are solenoids, shutters, and blades. Extreme care must be exercised in the choice of materials and in the processing. The drive arms are made of 3003-H14 aluminum sheet 0.010 in. thick and the blades of 2024-T3 aluminum sheet 0.003 in. thick. The blades were carefully liquid-honed and anodized on one side only in order that they might meet the wear life requirements and might present a light-absorbent surface to the vidicon and a heat-reflective surface to the optical aperture.

Since they were adjacent to the vidicon faceplate, the initial shutter assemblies caused undesirable magnetic fields that disturbed the operation of the vidicon. This problem was solved by using a shield consisting of alternate layers of 0.003-in.-thick aluminum and 0.004-in.-thick Conetic AA material.

VII. Lubricant Considerations

A. General

Years of laboratory testing and evaluation in actual space vehicles have convinced most designers that only under special circumstances can oils and greases be used

as lubricants. Three characteristics of these conventional materials make them undesirable for use in outer space.

- (1) Their viscosity varies greatly with temperature.
- (2) They are sensitive to minute quantities of dirt or other abrasives.
- (3) They are volatile.

Sometimes the use of labyrinth seals or reservoirs of semiporous materials can control the escape of volatiles. Contamination due to migration of the base oil has been partially solved by applying barrier coatings. However, volatiles from this source still condense on nearby or remote surfaces and become contaminants. If they condense on lenses or mirrors in television mechanisms, the mission can be jeopardized.

For these reasons, Hughes Aircraft Company expended considerable effort and money to develop and evaluate bonded solid lubricants.

B. Sliding Surfaces

One of the most critical mechanisms in the television camera, in relation to wear life and low friction requirements, is the variable-focal-length lens assembly. Trade-off studies were conducted with respect to both design and lubrication. In the original design of the focus cell, a four-start, standard screw thread was used. In tests, this thread was compared with acme threads of both four-start and one-start design. Four different lubricants

were tested both at the laboratory bench and in actual hardware in an ultra-high vacuum. Table 5 indicates that only the high-pigment, inorganic-bonded coating (D) and the sodium-silicate-base coating (C) could be used for *Surveyor*. Primarily because of its low friction, this high-pigment coating proved to be very effective, particularly on single-start acme threads. Figures 8 through 10 show the threads before and after 20,000 cycles of operation.

C. Gears

A very thin film of this same type of lubricant was applied to the gear teeth in the filter wheel assembly. Considerable torque resistance developed because the solids in the lubricant built up at the roots of the teeth. To solve this problem, better techniques for burnishing the lubricated gears before assembly were developed. The final thickness of the bonded solid lubricant was less than 0.0002 in.

D. Bearings

The selection of bearings was a relatively simple matter since none of those used in the television camera are heavily loaded. As previously mentioned, a MoS₂- and Teflon-lubricated bearing replaced the journal bearing on the mirror assembly azimuth axis. Smaller bearings, utilizing duroid as a cage material, were used throughout the mechanisms. Although the rated load for such bearings is only 10% of that for a similar bearing using a pressed steel retainer, the loads in this application were so light that no problem occurred.

Table 5. Comparison of friction-reducing coatings

Lubricant	Method of application	Coefficient of friction	Remarks	Trade name
Proprietary	Impingement	0.20-0.35	Permitted metallic contact. Very low load-carrying ability.	A
Rhenium and silver	Simultaneous plating	0.18-0.25	Metal transfer caused galling after approximately 4000 cycles.	B
MoS ₂ and graphite; sodium silicate binder	Spray on and bake	Approximately 0.1	Good wear life (20,000 cycles or more) but had higher friction than high-pigment material.	C
MoS ₂ , graphite, and certain proprietary lubricants. High pigment concentration (over 80 percent)	Spray on and bake	0.06-0.08	Good wear life (20,000 cycles or more); soft and easy to burnish in. (Formation of debris minimized by burnishing and vacuum removal of resulting particles before gears were assembled.)	D

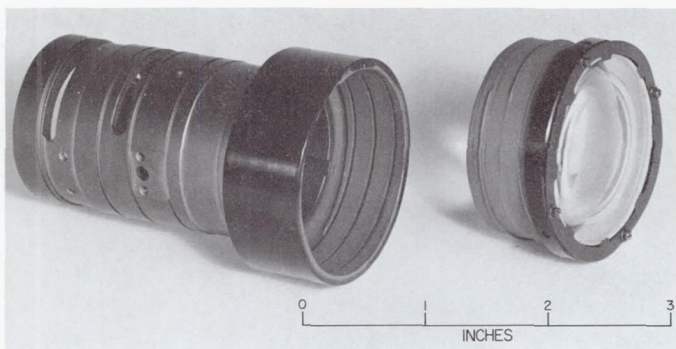


Fig. 8. Lens sleeve lubricated with Lubeco 905 before burnishing (R103290)

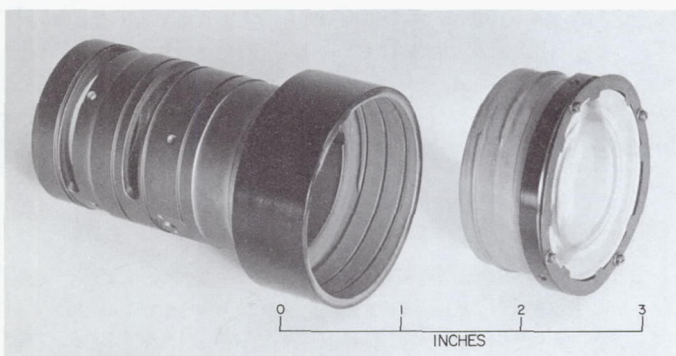


Fig. 9. Lens sleeve lubricated with Lubeco 905 after burnishing (R103292)

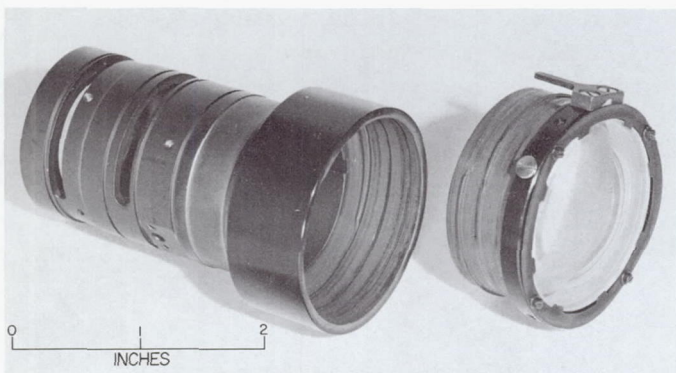


Fig. 10. Lens sleeve lubricated with Lubeco, burnished, and operated for 20,000 cycles (R103367)

E. Potentiometers

Early in 1965, the *Surveyor* television camera was tested in a thermal vacuum. The wire-wound potentiometers had previously been cleaned of all lubricants in order to prevent contamination of adjacent lens surfaces; afterward, some of these potentiometers failed to operate with the power available. Subsequent ultra-high-vacuum tests at Hughes Aircraft Company indicated that metallic seizure was taking place between the unlubricated wire windings and the Paliney No. 7 contact. Hughes Aircraft Company initiated parallel programs to evaluate materials that could be used as lubricants to prevent this seizure. This intensive effort produced two satisfactory solutions.

- (1) The electrically conductive solid lubricant, niobium diselenide, was very effective in preventing seizure in the potentiometers.
- (2) Several new electrically conductive lubricative compacts were found to be potential substitutes for Paliney No. 7.

Niobium diselenide powder on the contact surfaces was selected for *Surveyor* because of time schedules and because it is easy to apply during manufacture.

VIII. Conclusions

Conclusions are as follows:

- (1) Sliding and rotating mechanisms can be made to operate successfully on the lunar surface for up to one-half million cycles, using proper designs and lubricants.
- (2) The greatest problem of the mechanisms on *Surveyor* TV involved acquiring adequate cycles of operation on motors and potentiometers.
- (3) A lubricant comprising molybdenum disulphide, graphite, and certain other proprietary lubricants in a sprayed-on and baked coating worked quite well on the *Surveyor* TV mechanisms.
- (4) Ball bearings under condition of reasonable loads and speeds operate well in the lunar environment.

Lunar Module Alightment System*

Richard A. Hilderman, William H. Mueller, and Morton Mantus
Grumman Aircraft Engineering Corporation
Bethpage, N. Y.

The lunar module (LM) landing phase is one of the most critical phases of the entire Apollo mission. Landing impact is of critical concern because at no other time during the LM mission is there less opportunity for vehicle control. To assure a successful landing, the alightment system must not only provide required shock attenuation for protection of crew and structure, but must also assure stability against overturning after touchdown. The paper discusses important design features of the alightment system, such as geometric arrangement, energy absorber characteristics, and deployment mechanisms. Performance characteristics of the vehicle at touchdown, as found analytically, are presented. Model and full-size testing of the landing system is briefly discussed.

I. Introduction

The aim of Project *Apollo* is manned lunar exploration and subsequent safe return of the astronauts to the earth. The spacecraft consists of the lunar module, the command module, and the service module. Descent to and ascent from the surface of the moon is accomplished by the LM.

The lunar landing phase represents one of the crucial tasks of the overall mission. This phase is usually thought

of as starting at the time of injection from lunar orbit into a trajectory toward the lunar surface. Descent maneuvers end with touchdown on the surface. Thereafter, the alightment system must function to bring the vehicle to rest, guarding against toppling caused by impact forces, as well as to provide shock attenuation for the protection of crew and structure.

It is the purpose of this paper to discuss the more important design features of the landing system and some of the tests conducted to ensure that a reliable mechanism has been designed. A brief discussion of the LM landing performance characteristics is also given.

*This work was performed as part of Contract NAS 9-1100 for NASA.

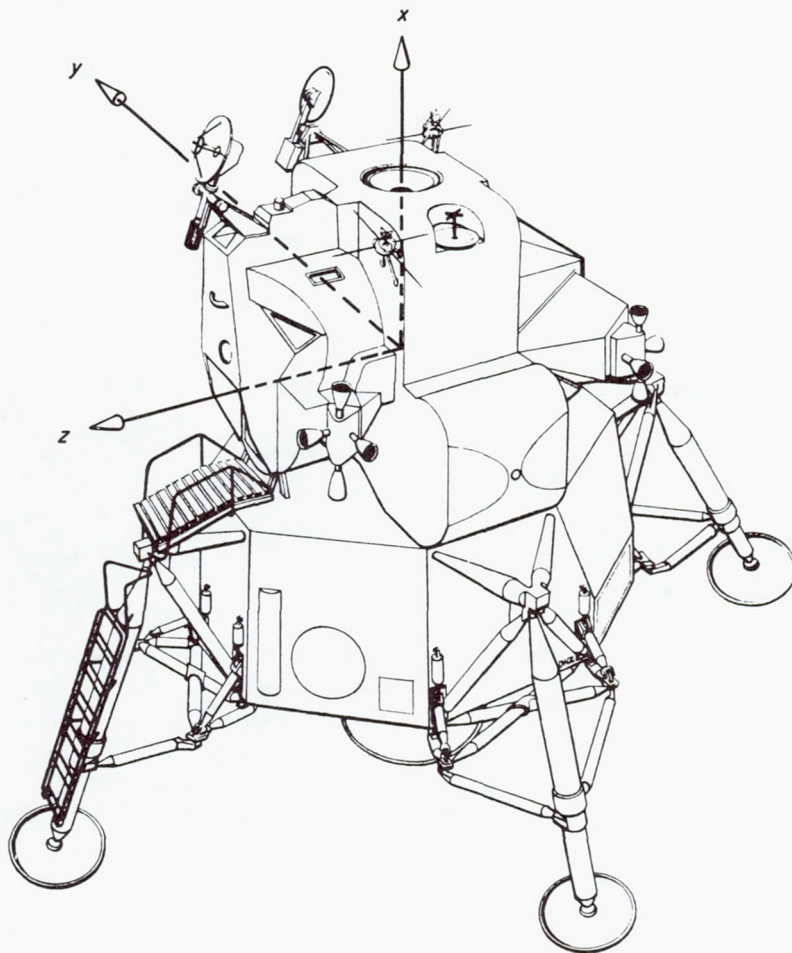


Fig. 1. LM general arrangement

II. General Description of the Lunar Module

The LM consists of a descent stage and ascent stage that are separable at lunar launch or when aborting a mission. The ascent stage houses the crew in a pressurized compartment and contains various LM systems such as the ascent propulsion system, various flight controls, and communication systems. The descent stage contains the descent propulsion system and items of scientific equipment. A pair of box beams arranged in cruciform constitutes the primary load-carrying structure of the descent stage. At the ends of these box beams are four-bar outrigger trusses that serve the dual role of (1) supporting the LM in the spacecraft-LM adapter (SLA) for earth launch and (2) supporting the upper end of the landing gear primary struts. The general arrangement is shown in Fig. 1.

III. General Design Requirements for the Landing Gear

There are certain obvious constraints on the landing gear design. The gear must be compatible with the structural arrangement of the descent stage. It must fit inside the SLA (Fig. 2) and allow for clearance when the LM is withdrawn from the SLA. This maneuver is accomplished after the command module-LM docking that joins the spacecraft components for translunar flight. The gear must clear the dome of the upper stage of the launch vehicle while in the retracted position and should have a simple and positive up-lock arrangement and deployment mechanism. The gear on the +Z axis must provide for a ladder to allow astronaut access to the lunar surface.

During lunar landing, the LM must avoid toppling instability, and energy-absorption requirements must be satisfied without introducing high loads associated with bottoming of a gear. The "at rest" position on the lunar surface must be such that lunar launch is not compromised. It is also desirable that the landing be accomplished with gear loads as small as possible to avoid high shock loads on equipment and structure. Maximum touchdown velocities for design evolved from extensive analytic studies and manned simulation. The maximum values were a vertical speed of 10 fps with no lateral velocity, and a lateral velocity of 4 fps to be combined with vertical velocities to 7 fps.

At ground contact, the spacecraft's X or longitudinal axis may be inclined 6 deg from the local gravity vector,

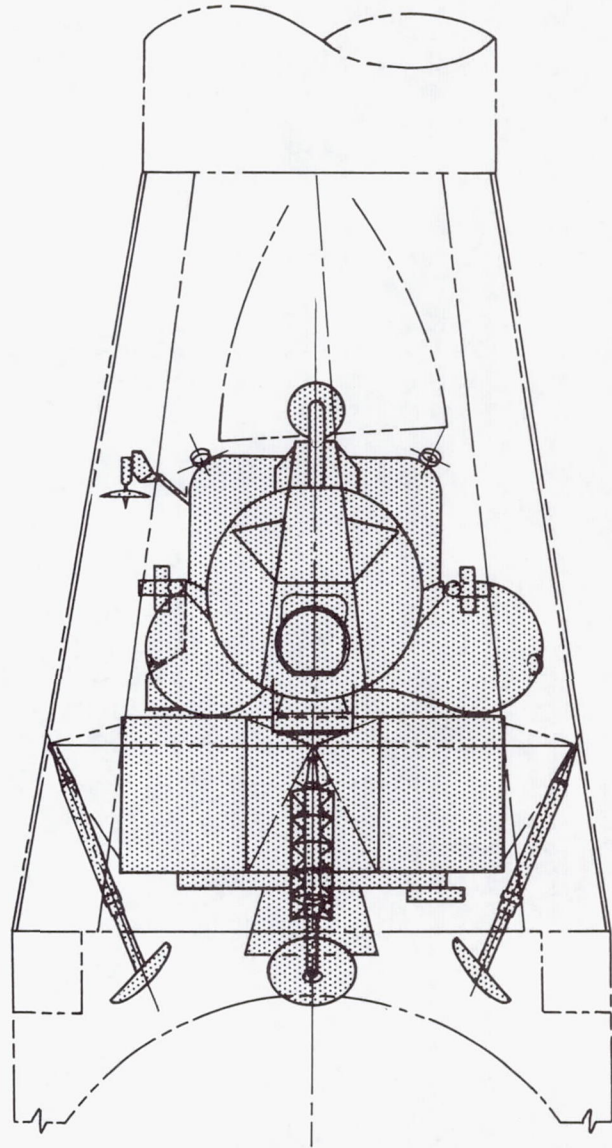


Fig. 2. LM supported in spacecraft LM adapter

and the yaw attitude may be from 0 to 360 deg (since the flight path can be in any direction). Pitch, roll, and yaw are related to the astronauts, who face in the +Z direction in Fig. 1. Attitude rates are ± 2 deg/sec about any axis.

Two design landing weights were selected on the basis of minimum and maximum usage of expendables during the descent from lunar orbit. In general, the maximum landing weight is critical for the energy absorption requirements of the landing gear. The minimum landing weight, which also has the highest center-of-gravity position, is critical for the stability requirements.

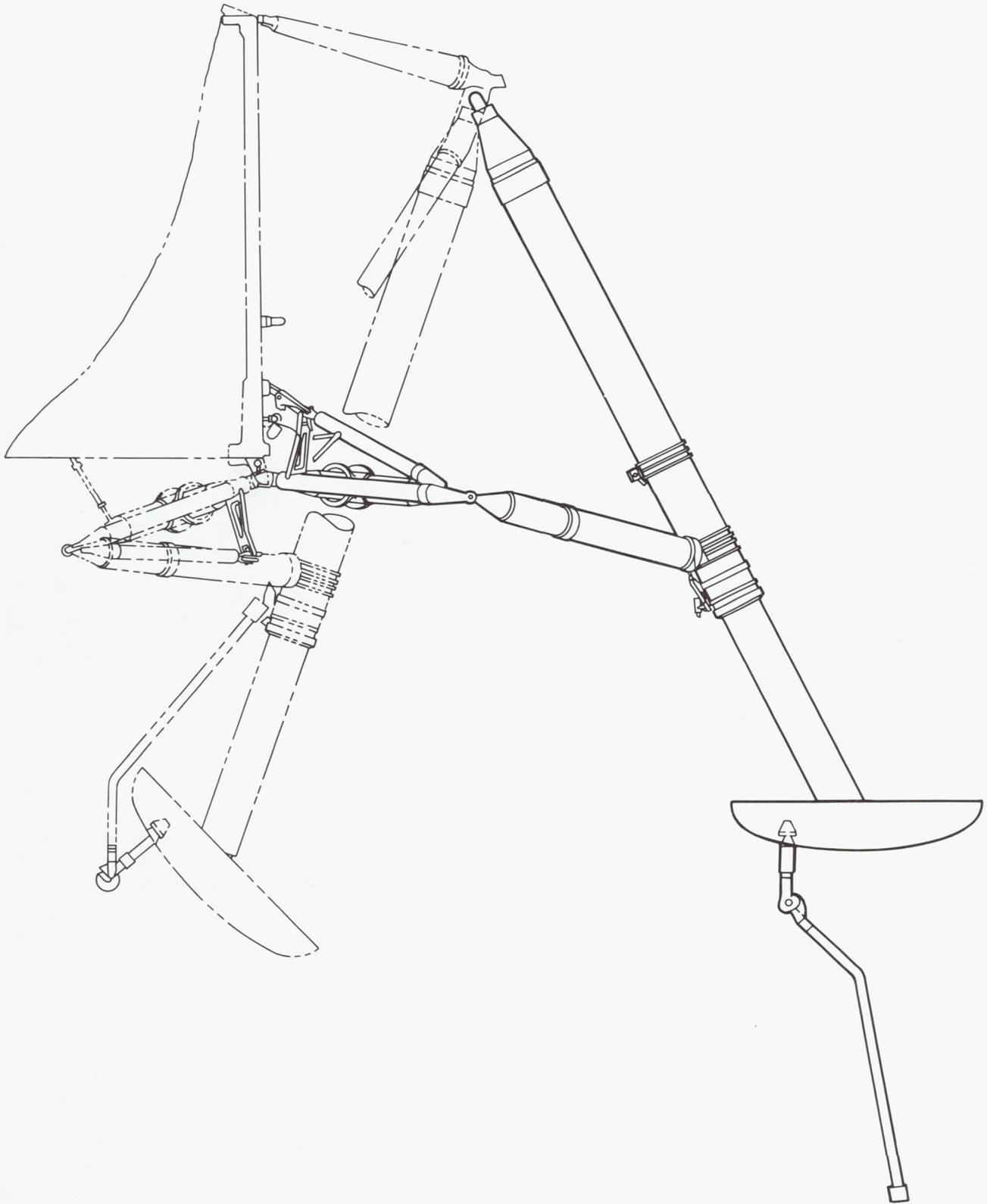


Fig. 3. Landing gear general arrangement

IV. General Description of the Landing Gear

The LM landing gear consists of four assemblies at the ends of the descent stage box beams. As shown in Fig. 3, each assembly consists of a primary strut and two secondary struts. The secondary struts are attached to the descent stage through the deployment truss. The primary strut consists of an inner cylinder with a footpad at its lower end, an outer cylinder connected through a universal joint at its upper end to the outrigger truss, and a honeycomb cartridge that acts in compression to absorb energy. Each secondary strut consists of an outer cylinder connected through a ball joint to the primary strut, an inner cylinder connected through the deployment truss to the base of the descent stage, and an arrangement of honeycomb cartridges that can absorb energy while the secondary strut is extending or compressing.

The footpad has area and strength to provide flotation and minimal impact penetration on surfaces of low bearing strength. Attached to each footpad is a lunar surface sensing probe. Each footpad is located 167.57 in. from the LM centerline.

V. Energy-Absorbing Devices

The energy-absorbing devices contained within the struts are aluminum honeycomb cylinders, constructed so that load-deformation characteristics of Fig. 4 are available. Note that load staging with stroke is possible. This feature was utilized in order to optimize a gear that must function as an initial impacting gear and as a secondary, or even tertiary, impacting gear. In general, if the landings were biased insofar as direction is concerned, such as for aircraft, each gear assembly would optimize to a different characteristic.

Various devices were evaluated in the search for an efficient energy absorber. These devices included friction mechanisms, frangible tubes, and variations of airplane-type shock absorbers, in addition to honeycomb of different materials. The aluminum honeycomb was chosen because of its high efficiency, its availability, its suitability for the lunar environment, and its relative insensitivity to stroking velocity. Further, load-stroke curves could be tailored in a simple manner with good assurance of repeatability from cartridge to cartridge. Extensive testing was required to obtain close tolerances on the cartridge crush levels.

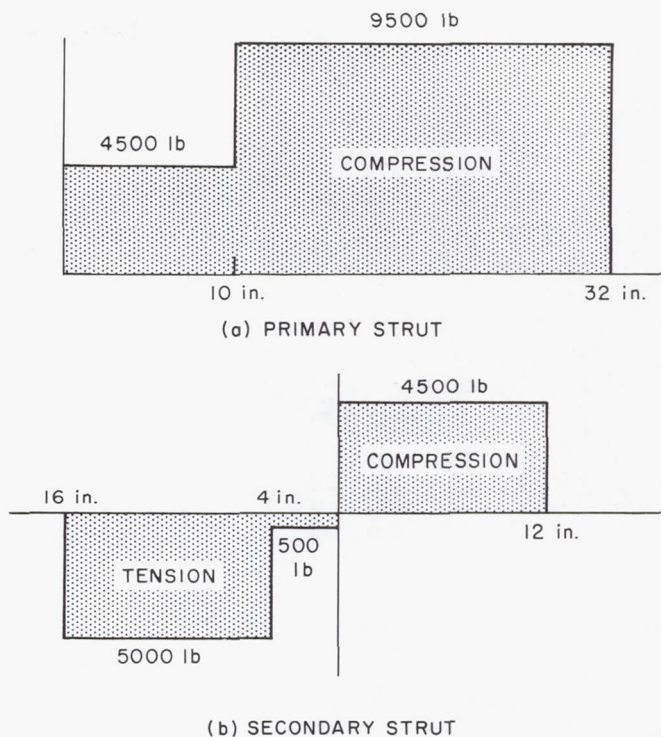


Fig. 4. Strut load-stroke curves

VI. Lock Mechanism

A pair of down-lock mechanisms lock each gear after deployment. A sketch of this mechanism is shown in Fig. 5. Solid lines indicate the deployed position; phantom lines indicate the stowed position. In the stowed position the gear is held by a pyrotechnic up-lock device between the descent stage and a point on the primary strut above where the secondary struts are attached. When the up-lock is broken the gear is rotated to the deployed position by the leaf spring shown in the sketch. As the latch roller truss approaches the latch, a roller-cam arrangement (not shown) allows the latch freedom to close. When the latch roller impacts its stop, the latch is locked downward by the compressed coil latch spring. Structural compression load on the latch roller truss member is taken by the stop; tension load is taken through the latch. An electrical switch (not shown) operated at the locked position of the latch activates a light, indicating to the astronauts that the gears are down and locked.

VII. Surface-Sensing Probe

The surface-sensing probes are used to provide the astronauts with an indication that the vehicle is about

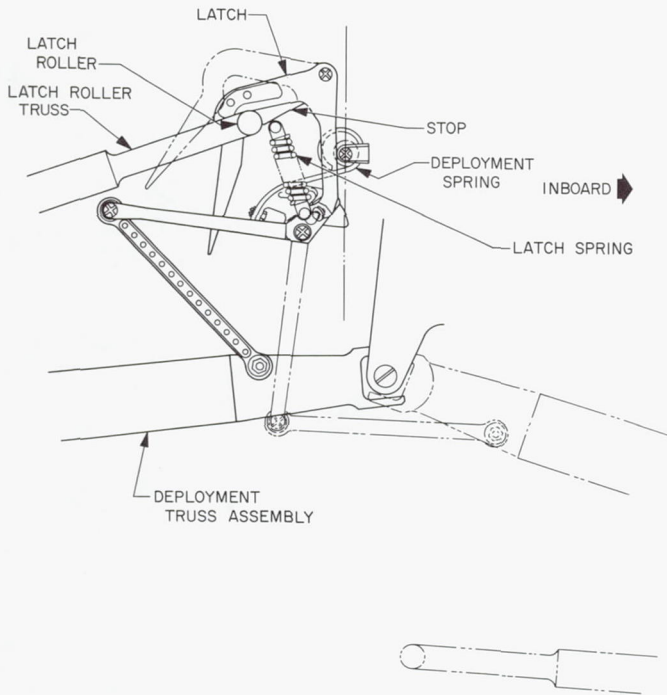


Fig. 5. Landing gear deployment and down-lock mechanism

4 ft from the surface. The probes are essentially aluminum tubes attached to the footpads. Electrical switches at the lower ends of these tubes are triggered by surface contact. Each probe is stowed against its landing gear primary strut as shown in Fig. 3. During gear deployment, when the primary strut has rotated about 30 deg, the probe's up-lock device is released by motion of the secondary strut relative to the primary strut. The probe's deployment mechanism is sketched in Fig. 6 in its down-locked position (phantom lines indicate the stowed position). The deployment leaf spring causes rotation of the lower member of the probe; the latching roller moves along its cam to the latch position. The latching spring holds the mechanism locked. Indication that the probes have locked is obtained visually from the command module. Appropriately painted indicator strips assist in this observation. Microswitches located at the foot of each probe activate a warning indicator when surface contact is made. After contact the probes are designed to break off so as to preclude interference with the remainder of the landing maneuver.

VIII. Lunar Model

Criteria for the design of the landing system are closely related to the characteristics of the landing site. Contro-

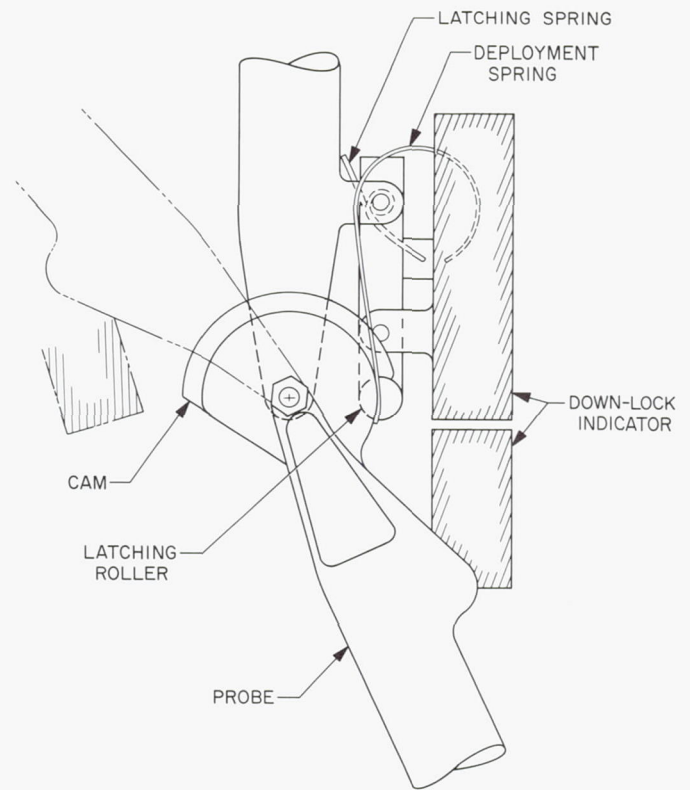


Fig. 6. Probe deployment mechanism

very concerning selected site parameters, upon which the gear design is based, will exist until hard and fast data become available. Since information about the moon's surface is limited, the problem of site selection became a matter of using reasonable engineering values for the design characteristics, in order to include a wide range of possible surfaces. These possible surfaces included hard substrata covered with dust, hard overburden, depressions (natural or by erosion caused by descent engine plume impingement), outcroppings (protuberances), and overall terrain slope at the landing site.

The selected lunar surface model has the following characteristics:

- (1) Terrain mean slope exists.
- (2) Depressions and protuberances exist in combinations not exceeding 24 in. in height.
- (3) The bearing strength of the surface material is between 12 psi and infinite rigidity.
- (4) Shearing or sliding resistance may be encountered as a friction coefficient from 0.4 to 1.0. Further, the surface material is considered to be randomly

distributed within the landing site, so that partial or complete motion restraint may occur.

A large number of reasonable landing sites may be produced by the combination of the preceding parameters. *Surveyor I* information indicates that its immediate landing site would have been suitable for a LM landing, in that the surface slope and protuberance heights were well within the LM design model. Data available at this writing do not permit firm conclusions regarding the dynamic bearing strength of the lunar surface, although the static bearing strength does appear to be adequate for the LM.

IX. Analysis and Results

Since landing dynamics are of major concern in the program to develop the LM, analysis has been used extensively as a tool in the design and the performance evaluation of the landing gear. Initial studies concentrated on landings where motion of the center of gravity was planar. Vehicle orientation with one gear leading, two gears behaving symmetrically, and one gear trailing has been designated the 1-2-1 case. Another symmetric case has two gears leading and two trailing and is called the 2-2 orientation. In most symmetric landings, the 2-2 case is critical for stability, whereas the 1-2-1 case is most often critical for energy-absorption requirements.

Results of symmetric studies of landing performance for uphill and downhill landings on a 6-deg slope are shown in Fig. 7. The indicated stability line represents the boundary between stable and unstable 2-2 landings. Combinations of initial velocities (i.e., horizontal velocity V_H and vertical velocity V_V) to the left of this line result in stable landings. Velocity combinations to the right of the line result in unstable landings. The initial attitude of the vehicle is nose-up 7 deg; two 24-in. depressions are present at the lead gears; and all footpads are fully constrained upon surface contact.

The line indicated to be energy-absorption critical is similarly defined. Combinations of velocities to the right of this line would require less than the available secondary compression stroke. Velocities to the left of the line would result in over-stroking. The results shown are for a 7-deg nose-down 1-2-1 landing. Critical stroking occurs at the lead gear; the footpad on this gear is fully constrained when in contact with the surface.

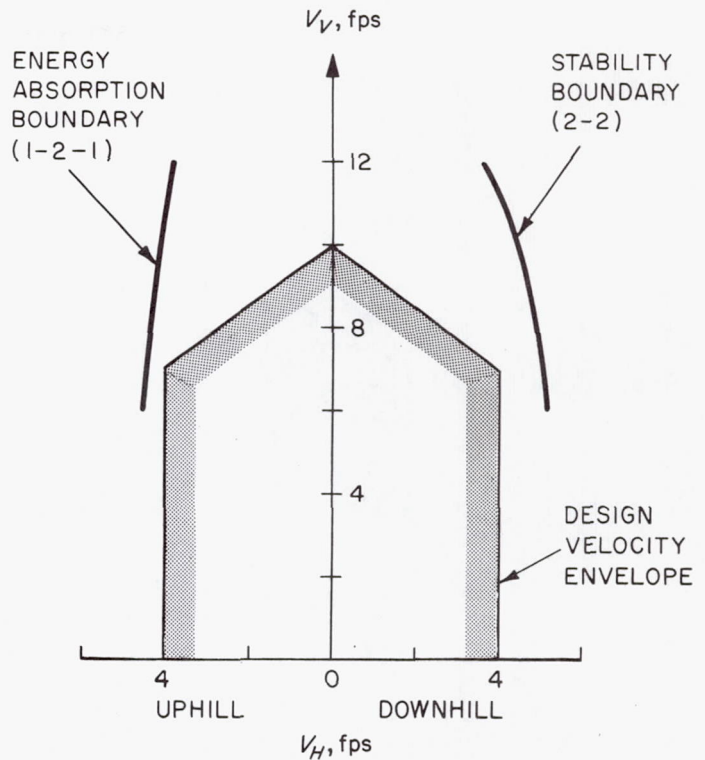


Fig. 7. Symmetric landing performance

Since purely symmetric landings appear unlikely, it is desirable to determine the effect of introducing asymmetric parameters into the initial conditions. Thus, effects of yaw angle and vehicle flight path with respect to the lunar slope have been examined. Similar characteristic curves and even three-dimensional surfaces have been calculated and drawn to depict landing performance.

The parameters discussed are only a few of the parameters that would lead to unsymmetric landing. When surface characteristics and all vehicle attitudes, attitude rates, and headings are considered, the number of parametric combinations becomes tremendous. Since the number of landings that could be investigated is infinite, only a boundary set can be examined. By actually examining the effects of certain parameters such as roll and roll-rate, etc., a critical set has been evaluated for investigative purposes. For simplicity the net combined effect, regardless of the unsymmetric parameters involved, is depicted by considering the components of the net velocity at touchdown. Figure 8 is a résumé of the compiled analytic results of alignment system performance. Note that stability and secondary strut stroke boundaries are critical for unsymmetric cases. However, the primary strut stroke is critical for the symmetric 1-2-1 landing.

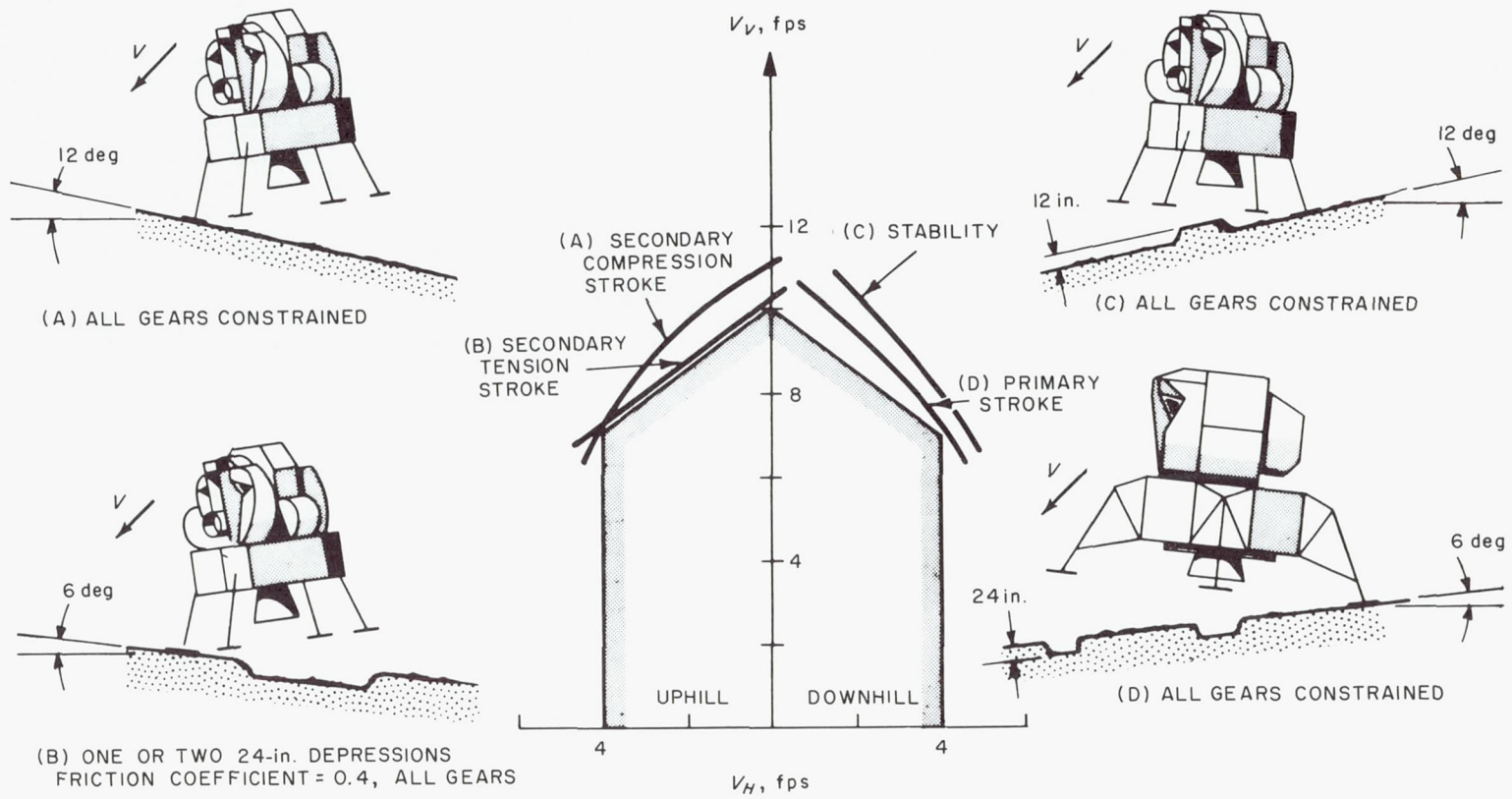


Fig. 8. Unsymmetric landing performance

X. Model Testing

In order to establish the validity of predicting the alightment system performance by analysis, a model test program was initiated. The unique feature in the LM model testing is the different gravitational environment of model and prototype. The model is 1/6 scale for all important dimensions. Scaling mass and mass moment of inertia to $(1/6)^3$ and $(1/6)^5$, respectively, results in a simple, easily handled, untethered vehicle. To avoid distorting significant rigid body phenomena, the model has been fabricated to exhibit as little elasticity as possible. The landing gear geometry is scaled and energy absorption is accomplished using aluminum honeycomb cartridges similar to those to be used in the prototype. Velocity and initial attitude of the model are obtained using a four-bar pendulum drop mechanism. Provision is available for a variety of sloped surfaces of various materials.

Since it was impossible to update the model continually as the gear prototype design progressed, an extensive program of model landing analysis was undertaken to establish that model behavior could be predicted using the technique employed on the prototype. Analytic correlation with test results concerned itself both with gross aspects of landing, such as the *go, no-go* view of stability or strut stroking, and with the detailed examination of time variance of the important parameters of vehicle acceleration and velocity.

Figure 9 compares test and analytic results of model stability. The landings are of the 2-2 type on a 5-deg plywood slope with a 4-in. depression at the lead gears. Small spikes were fitted to each primary strut to simulate complete constraint of a footpad when in surface contact. Other pertinent data are listed in the figure. Although only stability correlation is shown, other parameters were examined and correlated as well.

XI. Full-Scale Gear Tests

In order to establish the functional capabilities of the landing gear, a complete series of full-scale tests is planned. These include functional, static, and vibration tests. A full-scale single-gear assembly is currently being drop-tested. The purpose of this program is to check the various gear parameters, such as honeycomb load and bearing friction, as well as to test the assembly as a working mechanism. Since the energy-absorbing components

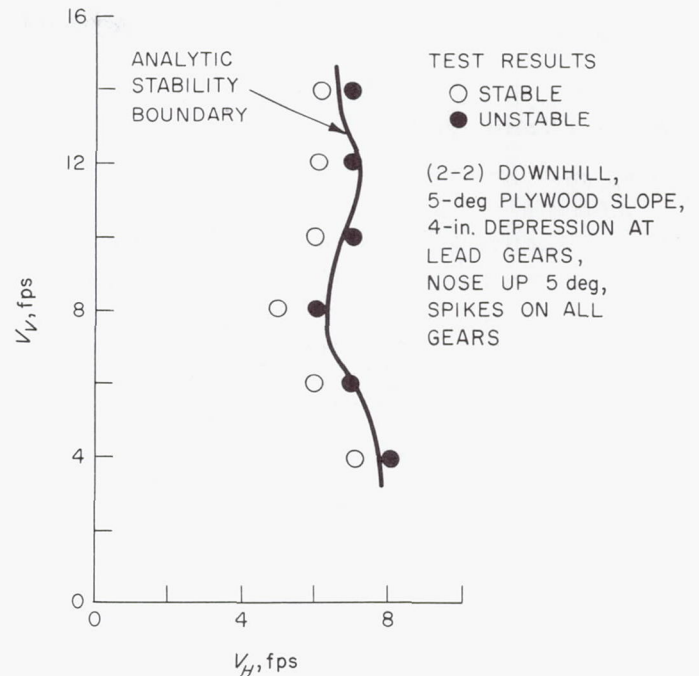


Fig. 9. Model stability results

in this test are prototype items, this test also provides structural dynamic testing of the system. The test jig consists of a variable-weight drop carriage to which the gear is attached. By orienting the gear assembly in the carriage and by adjusting the impact surface plane with respect to the horizontal, a great variety of initial conditions can be tested. The impact surface can be altered to simulate conditions on the footpad which range from low surface friction to full constraint, including some drops into a bin containing granular soil. Results of numerous drops indicate the gear is functionally and structurally sound.

Deployment tests under thermal vacuum, both at high and low temperature, as well as tests following a salt fog environment, have shown that the stored energy mechanical drive-out operates reliably. To date, no problems have arisen with regard to the mechanism transients such as accelerations, time for deployment, or latch lock loads.

XII. Conclusions

Full-scale and model tests have indicated that analysis can account for the significant dynamic effects of an LM landing. Performance evaluation of the designed system

indicates that a successful lunar landing is possible at sites far more severe than that encountered by *Surveyor I*.

XIII. Acknowledgment

Portions of the material in this paper were presented by the authors at the AIAA/ASME Seventh Structures and Materials Conference, Cocoa Beach, Florida, April 18-20, 1966, and published in the *AIAA Journal of Spacecraft*

and *Rockets*, Volume 3, No. 10, October 1966. The authors wish to extend their appreciation to the AIAA for permission to use this material.

Many Grumman Aircraft Engineering Corporation personnel contributed their efforts in connection with the work described. The authors wish to specifically acknowledge V. Sturiale, M. Romanelli, B. Dawkins, and W. Haynes (LM Mechanical and Explosive Subsystems).

Mechanical Design of Scanning Instruments

G. A. Bunson
Santa Barbara Research Center
Santa Barbara, California

The mechanical characteristics of the Surveyor Canopus sensor and the Project Scanner dual radiometer are representative of the types of optical mechanical instrument design that have been required for space applications. These instruments have recently performed successfully in space: one was a star-tracking guidance system utilizing the visible spectrum; the other was a research package for measurement in the infrared. This paper describes the mechanical configurations and design solutions generated for these instruments which are, in general, applicable to similar instruments.

I. Introduction

During the *Surveyor I* spacecraft's 66-hour voyage to the moon, a 4.9-lb sensor provided roll orientation information for midcourse guidance by identifying the star Canopus and providing electronic signals that enabled the spacecraft to "lock on" to it. The star was identified by comparing its brightness with a precisely known fraction of solar irradiance collected at the instrument by an auxiliary optical path. A proportional roll angle error signal was generated over ± 2 deg to control the roll attitude of the spacecraft with respect to the separately acquired sun spin axis to an accuracy of ± 0.1 deg.¹

Two dual radiometers,² part of a spin-stabilized space probe payload and designed to measure the earth's hori-

zon radiation gradient at high spatial resolution in the 14- to 16-micron carbon dioxide band and the 20- to 40-micron water vapor band for NASA's Project Scanner, have successfully performed their mission after launch from Wallops Island, Virginia. Image resolution is essentially diffraction-limited. Scan is linear with time to a repeatability of better than ± 0.01 deg, and scan position pulses are telemetered to ground stations for line-of-sight determination.

II. The Canopus Sensor

A. Functional Description

The optical light paths required for the Canopus sensor are shown in the diagram in Fig. 1. Starlight enters through the window in the cover. It is reflected first from the acquisition mirror, then from the scan mirror into an objective lens. The objective lens focuses the light on the chopper disk through a field-of-view aperture stop located just above the chopper disk. This starlight is

¹The Canopus sensor was developed by the Santa Barbara Research Center (SBRC) for the Jet Propulsion Laboratory, California Institute of Technology, sponsored by the National Aeronautics and Space Administration under Contract NAS 7-100.

²The dual radiometer was developed by SBRC for the Langley Research Center under Contract NAS 1-3827.

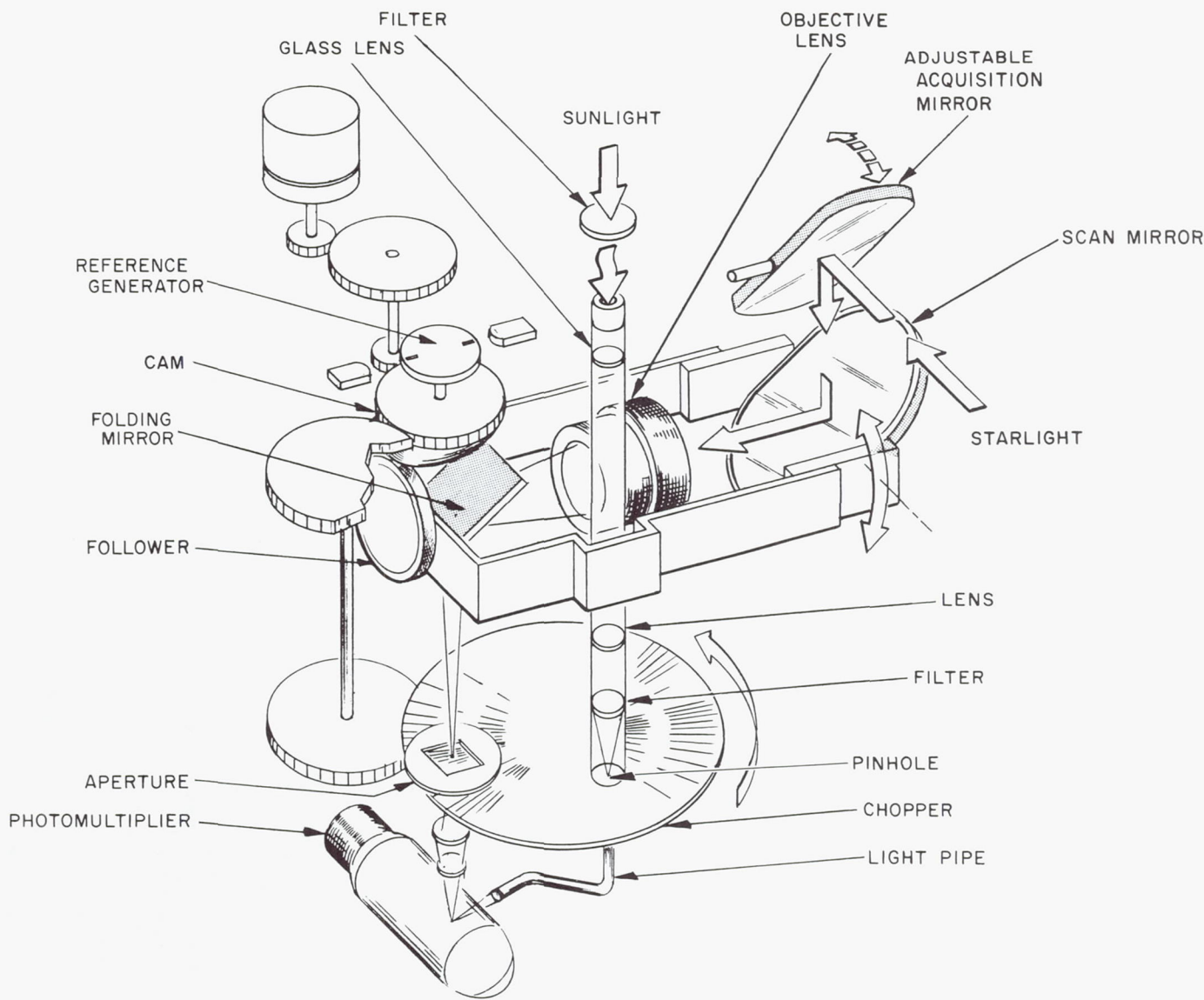


Fig. 1. Schematic drawing of Canopus sensor

chopped at a frequency of 3.9 kc and then beamed onto the photocathode of a 1P21 photomultiplier tube. Since the position of the star Canopus with respect to the earth's orbit (ecliptic plane) will vary with time of launch, the acquisition mirror must be externally adjustable ± 15 deg.

Sunlight enters the sun telescope through an attenuating filter and aperture. An opal glass diffuser at the telescope entrance allows for a variation of incidence angle of the sun's rays. Relay lenses focus the sunlight on the exit aperture (pinhole) through a color-correction filter.

The sunlight then emerges from the pinhole in the base of the sun tube, is chopped at 2.3 kc, collected in a fiber optics light pipe, and beamed onto the photocathode.

The star and sun signals from the photomultiplier are separated and processed electronically so that the star signal output is directly proportional to the ratio of illumination by the star and sun. Since the known ratio of Canopus intensity and that of the sun is set into the instrument in the form of amplitude thresholds, the instrument is capable of discrimination between Canopus and the next brighter and dimmer stars.

Modulation of the star signal is produced by the motion of a cam-driven scan mirror. This motion is linear through the field, and reversal takes place in less than 10% of the 50-msec scan period. The modulation phase detector compares the modulation envelope of the star signal with a reference signal square wave and delivers a dc output proportional to the position of the star along the roll axis.

The phasing is such that there is a positive voltage when the star is to the right of center, a negative voltage when the star is to the left of center, and no output when the star is at the center of the roll axis. During the reversals, the phase-detected signal is blanked by pulses generated from the reference signal pulses.

B. Design Description

The envelope for the Canopus sensor is a cylinder approximately 5 in. in diameter and 11 in. high. The Canopus sensor, with and without its protective cover, is shown in Fig. 2. The optical requirements allowed the use of glass windows so that the mechanism could be sealed in dry nitrogen and would not be exposed to space vacuum. All openings were sealed with O-rings fabricated from Viton rubber. A pressure switch, giving *go, no-go* remote electrical indications of internal pressure, was incorporated into the design to facilitate a check of the seal condition. The sensor base, which contained the electronics and provided the spacecraft mounting interface, was machined from AZ31B magnesium alloy; the upper cover was a dip-brazed aluminum alloy assembly.

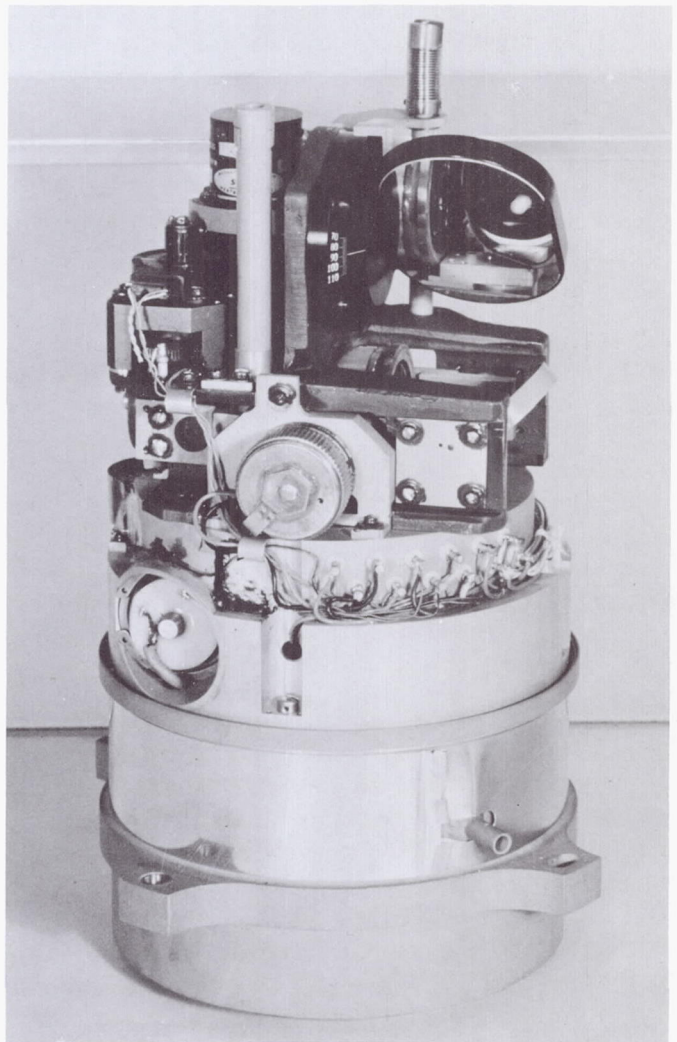
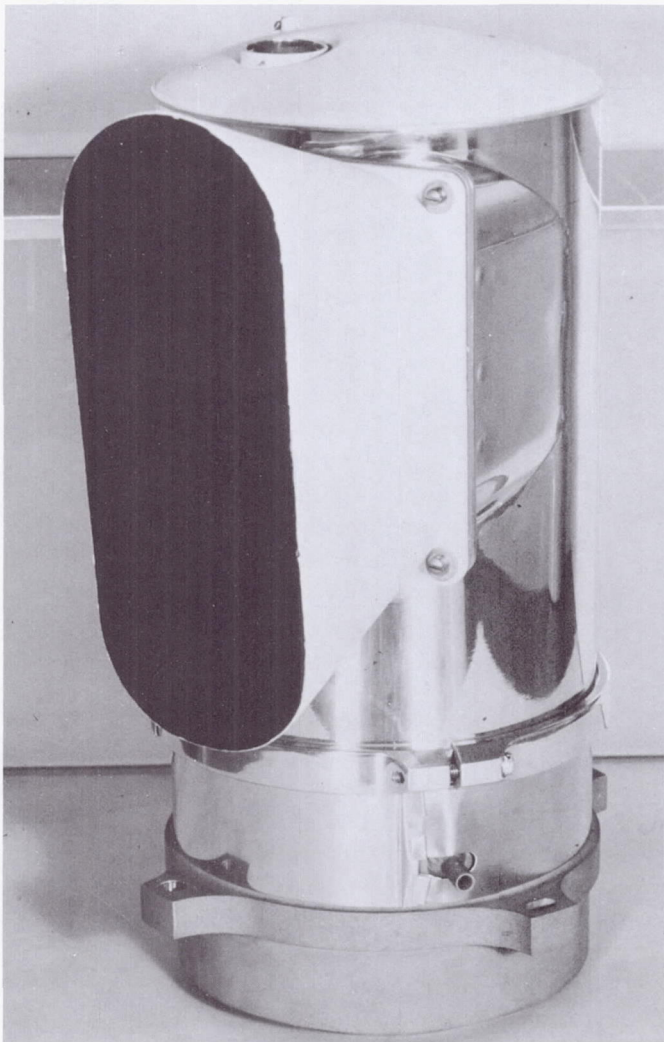


Fig. 2. Surveyor Canopus sensor (with and without cover)

The chopper wheel and star scan mirror were driven by a single 400-cps hysteresis synchronous motor. Magnetic "pip" generators activated by two magnets attached to the scan drive camshaft provided the reference pulses and activated the blanking circuits during scan reversal. All bearings were lubricated with uniform distribution of approximately 3 mg/in.² of Beacon (Standard Oil Company of New Jersey) 325 grease per MIL-G-3278.

The scan mirror was supported by torsion bars machined from hardened beryllium copper. Cylindrical snubbers were provided to protect the torsion bars in bending. The cam surface was 440 stainless steel and the follower, fabricated from Fiberglas, had a dry-lubricated rim. Wear and dimensional changes between the cam and follower would directly affect roll error output accuracy, and although several tested material combinations were acceptable for a wear consideration, the chosen material combination best withstood the impact loading that occurred between the cam and the follower during low-frequency launch vibrations.

All mirrors were glass and were bonded to aluminum frames with an elastomer. A fiber optics light pipe (image conduit) was used to carry the sunlight to the photocathode of the photomultiplier tube.

Light from the sun and the moon, as well as spurious spacecraft reflections, were blocked from the sensor by an 8- × 3-in. cross section optical baffle that extended 5 in. from the star window. The conical frame of the light shield was a dip-brazed assembly utilizing 0.008-in.-thick aluminized sheeting. Individual baffle plates were fabricated from 0.002-in. stainless steel and epoxy bonded into the conical frame. The entire light shield weighed less than 3.5 oz.

A reliability model of the scan and chopper drive mechanism was operated for over one year without failure. Two reliability demonstration models, selected at random from the 13 flight models fabricated, successfully survived 27 simulated missions. It is interesting to note that, after the testing, when the seal on one of the reliability demonstration models was purposely broken and the unit run in a vacuum, 66 hours of successful operation were logged. At the end of this time the unit was mechanically noisy and the measured bearing torque had increased by a factor of three, but no other defects in performance were noted.

III. The Dual Radiometer

A. Functional Description

An artist's drawing of the dual radiometer is shown in Fig. 3. The equipment essentially consists of two vertical telescopes associated with flat object space-scan mirrors that are synchronously scanned in elevation and that view the horizon in diametrically opposite azimuthal directions. The radiometer field of view is scanned in azimuth by the vehicle's nominal spin rate of 27 deg/sec.

The scan mirrors, driven by a common gear train through a cam and follower linkage, provide a 15-deg sawtooth scan at 10 deg/sec centered about a predetermined horizontal depression angle of 22 to 26 deg.

In one telescope the detector array is associated with an optical filter to limit the bandpass to 14 to 16 microns, and, in the second telescope, 20 to 40 microns. Each detector array assembly includes a pulsed lamp arrangement for calibration purposes. The electronics essentially consists of (1) amplifiers for the ten detector channels and (2) position pickoff circuitry to define the scan position. Temperature sensor assemblies read out the detector temperature environment.

The radiometer structure supports a passively scanned star telescope (not shown in Fig. 2), which is boresighted in the plane of the elevation scan and perpendicular to the radiometer's longitudinal axis. This star telescope views the star field as the vehicle spins and transmits a series of pulses over the telemetry, thereby allowing ground data reduction to determine a time history of the vehicle's coordinate axes relative to the local earth. Precise knowledge of the angular position of the radiometer elevation scan mirror allows the vehicle information to be transformed into instantaneous field-of-view pointing information relative to the solid earth's horizon.

The use of a solid rocket booster subjects the radiometer to high thrust accelerations, the maximum being approximately 28 g in the vertical direction near second-stage burnout. The spin rate of 280 rpm imposes a centrifugal acceleration gradient of approximately 2.2 g/in. displacement from the spin axis. The payload stage rocket motor is a rough-burning unit and causes vibrations that approach 40 g (0 to peak) along the vertical in the 525- to 625-cps frequency range and one-sixth of this in the horizontal directions. A "yo-yo" despin mechanism causes angular deceleration about the vertical axis, approaching 150 rad/sec². Because of spacecraft structural

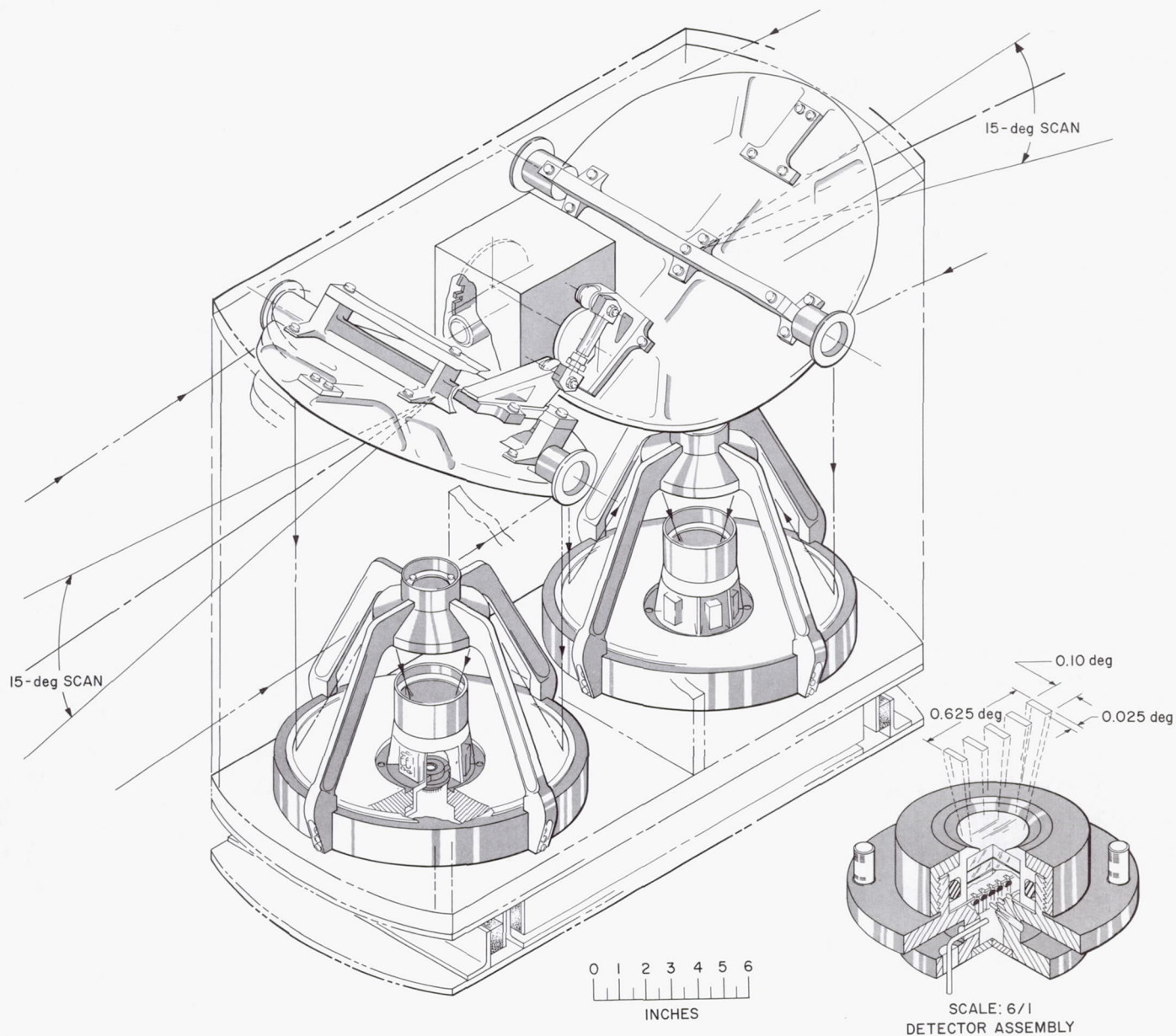


Fig. 3. Schematic drawing of dual radiometer

limitations, the 20-in.-high radiometer frame that supports the 35-lb star mapper must be base-mounted, and the fragility level of the star mapper requires that the vibration amplification through the radiometer frame to the star mapper be limited to one-to-one in the critical 525- to 625-cps frequency range. The radiometer must endure the preceding environment and then operate under zero-g conditions and at ambient pressures that exist at an altitude of 200 to 600 nautical miles.

B. Design Description

A photograph of the dual radiometer is shown in Fig. 4. The instrument, less spin-balance trim weights, weighed 93.5 lb. The frame was a structurally ribbed AZ91C magnesium alloy casting. To meet the specification requirements in regard to vibration inputs to the star mapper, an isolation mount was required. A relatively

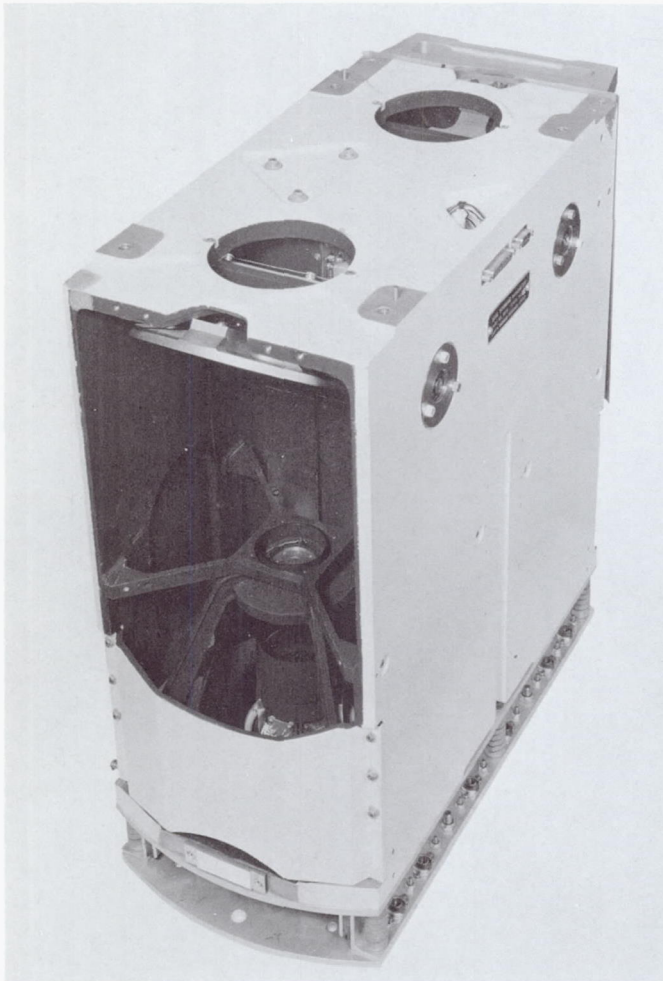


Fig. 4. Dual radiometer

stiff mount (resonant at 100 cps, transmissibility of 2.5) was designed using both elastomer in shear and six machined springs. This mount provided less than 0.5 transmissibility in the input critical frequency range and maintained optical alignment with respect to the spacecraft to within the 0.1 deg required. The base-mounted system was shown to be stable at spin rates of over 400 rpm.

To achieve minimum weight and maximum stability, nickel-plated beryllium mirrors were used where possible in the design. Variations in plating hardness and the necessity of polishing in small localized areas make the fabrication of accurate aspheric optical surfaces difficult on metal mirrors. The aspheric primary mirror was successfully fabricated from beryllium; however, to meet the accuracy requirements, the secondary mirror was fabricated from silicon. The primary and secondary mirror blanks, with surfaces contoured to within ± 0.0005 in., were supplied to the optical finishing house along with a matched 4140 steel secondary mirror support. The mirrors were then polished and inspected, together with the supplied support, and delivered as a matched set. This sequence permitted maximum final accuracy while maintaining reasonable fabrication tolerances.

The scan mirrors were driven by the cam and follower mechanism shown schematically in Fig. 5. Cam A and its shaft rotate on an axis parallel to the mutually parallel pivot axis H of the two scan mirrors. Followers G and K are rigidly attached to scan mirrors M and C, respectively, by supports L and F. Hence, as the cam rotates, its change in profile produces a rotation of the scan mirrors about their pivot axes. The tension link B connects the two followers G and K and ensures a positive rolling contact between the followers and the cam profile under all conditions. The axial travel of the spring in the tension link during one revolution is 0.003 in.

A rise in cam profile produces a clockwise rotation of both mirrors; conversely, a fall in cam profile produces a counterclockwise motion of both mirrors. The cam is profiled to have a rising contour at follower K and a falling contour at follower G during 180 deg of cam rotation, which produces a clockwise motion of mirror C (radiometer A) and a counterclockwise motion of mirror M (radiometer B). Since the mirror motions are reversed during the 180 deg of cam rotation, one complete synchronous scan cycle occurs during each 360 deg of cam rotation.

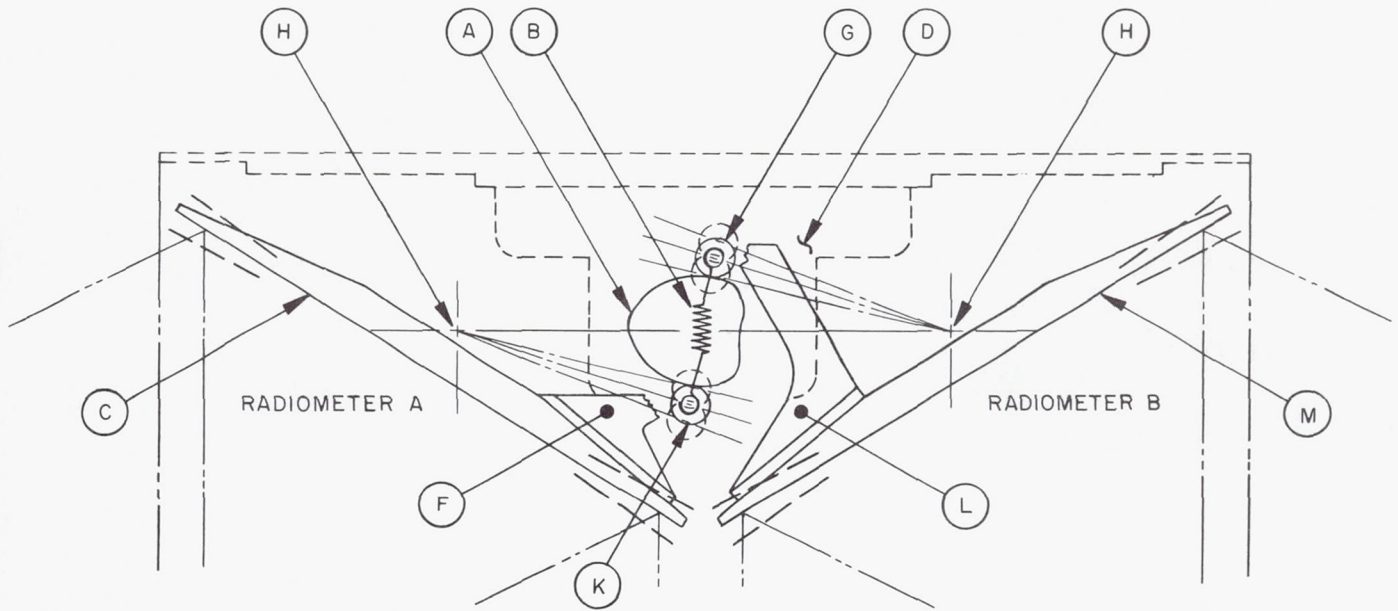


Fig. 5. Scan drive schematic

To obtain identical mirror motion, the follower radius arms G-H and K-H are made of equal length. Also, the cam's axis of rotation is on a straight line joining the two scan mirror pivot axes and centered between them. As a result of this geometry and the fact that both mirrors are driven by the same cam, it is inherent in the design that the scan cycle periods will be equal.

Centering of the scan range and adjustment of the depression angle are both determined by the angular position of the scan mirror surface relative to a line through the centers of the mirror pivot and the cam follower. Hence, both may be adjusted by inserting an appropriate spacer between the cam follower support and the scan mirror.

Since the scan mirrors complete one cycle for each revolution of the camshaft, the scan rate is directly dependent on camshaft speed. The camshaft gear train is enclosed in a dust cover which prevents contamination of the optics by lubricants or contamination of gear train bearings by outside contaminants.

The scan mirror position readout utilizes a slotted disk mounted directly on the camshaft. The slots, in combination with a fixed-position photodiode device, initiate the mirror position readout signal and also energize the automatic calibration circuit.

IV. Conclusions

The feasibility of automatically acquiring and tracking a star to provide spacecraft navigation information was demonstrated by the Canopus sensor on *Surveyor I*. All components functioned as predicted during the mission.

The radiation profiles, made to a spatial resolution of 0.02 deg, provided by the dual radiometers will be used to compensate in future spacecraft horizon sensor design for the atmospheric variations which up to now have limited stabilization accuracies to about 1 deg.

The dual radiometer design proved the compatibility of vibration isolation mounting with accurate optical systems, and both systems demonstrated the use of spacecraft rotation to provide one direction of scan.

Collet Release Mechanism*

Daniel O. Ramos
General Electric Company
Philadelphia, Pennsylvania

This paper describes a novel, simple, reliable, and flight-proven mechanism used to separate and eject a re-entry vehicle (RV) payload from a booster. Design details, comparison with other solutions, test experience, and several flight-proven applications are included.

I. Introduction

The problem of vehicle mechanical separation implies two functions:

- (1) To provide the structural means to attach the two bodies.
- (2) To provide the means to remotely sever the structural connections. Furthermore, the separation function may require that a positive separation velocity be imparted to the two bodies being separated.

The devices normally used for separation include linear explosives (flat linear shaped charge, mild detonating fuse, primer cord, and various encapsulated designs), ex-

plosive bolts and nuts, V-band clamps, ball-locks, pin pullers, and cable cutters. The devices normally used to obtain a separation velocity or perform the ejection function include springs, thrusters, retro-rockets, and hot or cold gas systems.

With all the available methods for performing the separation and ejection function, it would appear that the designer's lot is an easy one. This is not so, however, because the various requirements, constraints, and system interplays imposed on the designer demand that he engineer a design solution that fulfills all the requirements. One such solution is presented in this paper in the form of a collet release mechanism.

II. Separation Design Requirements

As implied in the introduction, it is the requirements that force the designer to abandon his catalogues and

*The work described herein was performed for the Air Force Ballistic Systems Command under contract numbers AF 04 (694)-389 and AF 04(694)-473.

search for a design solution. This section surveys many of these requirements and, in the following section, a cursory comparison will be made between the requirements and the available solutions.

Separation design requirements include load-carrying capability, uniform load distribution, minimum electrical power for separation, long life in space, minimum system weight, minimum impulse, simultaneous actuation, minimum tip-off rates, high reliability, maintainability, reusability, survival of extreme high or low temperatures, no contamination, survival of nuclear radiation, minimum volume, compatibility with structural stiffness, long storage life (5 years), no debris, and safety.

Ejection design requirements must provide a predictable $\Delta V \pm 10\%$, minimum ΔV , minimum tip-off rates, minimum jerk, long life in space, long storage life (5 years), survival of extreme high and low temperatures, survival of nuclear radiation, no contamination, minimum weight, minimum volume, compatibility with soft structure, acceptable ejection force, maintainability, reusability, high reliability, no debris, and safety.

III. Possible Solutions

The matrices in Tables 1 and 2 show the acceptability of various separation and ejection mechanisms against a partial list of requirements.

Table 1. Comparison of separation devices

Requirement	Linear explosive	Contained linear explosive	Explosive bolts/nuts	Ball lock	V-band	Pin puller	Cable cutter	Collet mechanism
Load capability	E	G	E	G	E	G	G	E
Uniform load	E	E	G	G	E	P	P	G
Minimum shock	P	P	G	E	E	P	G	E
Minimum impulse	P	P	P	E	E	E	E	E
Minimum tip-off	P	P	G	E	G	E	E	E
Minimum electrical power	E	E	P	G	E	P	P	G
Compatibility with structure	G	P	E	E	G	G	G	E
No contamination	P	E	P	E	E	E	E	E
No debris	P	E	P	E	G	E	E	E
Maintainability	P	P	G	E	E	G	G	E
Reusability	P	P	P	E	E	P	P	E
Safety	P	P	G	E	E	E	E	E
Long life in space	P	P	E	E	G	G	E	E
Long life in storage	E	G	E	E	E	E	E	E
High reliability	G	G	E	E	E	E	P	E
Minimum weight	P	P	E	G	G	E	G	G
Minimum volume	G	G	E	G	G	G	E	P
Survival of temperature extremes	P	P	P	E	G	G	G	E
Survival of radiation	P	P	G	E	E	E	E	E

NOTE: E = Excellent, G = Good, P = Poor.

Table 2. Comparison of ejection devices

Requirement	Springs	Thruster	Rockets	Hot/cold gas	Collet mechanism
Provide minimum ΔV	E	E	E	E	E
Provide predictable ΔV	P	P	G	E	E
Minimum tip-off	G	P	G	E	E
Minimum jerk	P	G	E	E	E
Acceptable force	P	P	E	E	E
Compatibility with structure	G	E	P	P	E
No debris	E	E	P	G	E
No contamination	E	G	P	P	E
Maintainability	E	P	P	P	G
Reusability	E	P	P	P	G
Safety	E	P	P	P	G
Long life in space	G	G	E	E	G
Long life in storage	G	E	E	E	E
High reliability	E	P	E	G	G
Minimum weight	P	G	E	G	G
Minimum volume	P	P	E	G	G
Survival of temperature extremes	G	G	P	P	E
Survival of radiation	E	P	G	G	E

NOTE: E = Excellent, G = Good, P = Poor.

IV. Selected Design

An actual design problem and its solution, using a collet release mechanism, is discussed herein and in the subsequent sections.

The requirements were to separate two bodies at four attachment points with a prescribed separation velocity and a maximum tip-off rate of $\frac{1}{2}$ deg/sec. The device had to be capable of resisting high tensile loads to prevent gapping of the interface during ground and flight loads. One electrical signal of 7 amp for $\frac{1}{2}$ sec was available to perform the function.

The solution consisted of a cold gas storage system, explosive valve, balanced manifold, and four collet release mechanisms. The paper concerns itself mainly with the design of the collet mechanism.

The mechanism shown in Fig. 1, in the locked and unlocked position, and in Fig. 2 in a cross section schematic, consists of a collet housing/cylinder with a piston holding the fingers spread out in the locked position.

The mechanism can carry tensile loads when in the locked position. When gas pressure is introduced into the cylinder bore, it acts on the piston, causing it to move forward, allowing the collet fingers to collapse due to their strain energy. This action permits separation of the vehicle from the booster.

Gas pressure can be supplied from independent squibs acting at each mechanism either singly or redundantly, or by a central storage system feeding a balanced manifold.

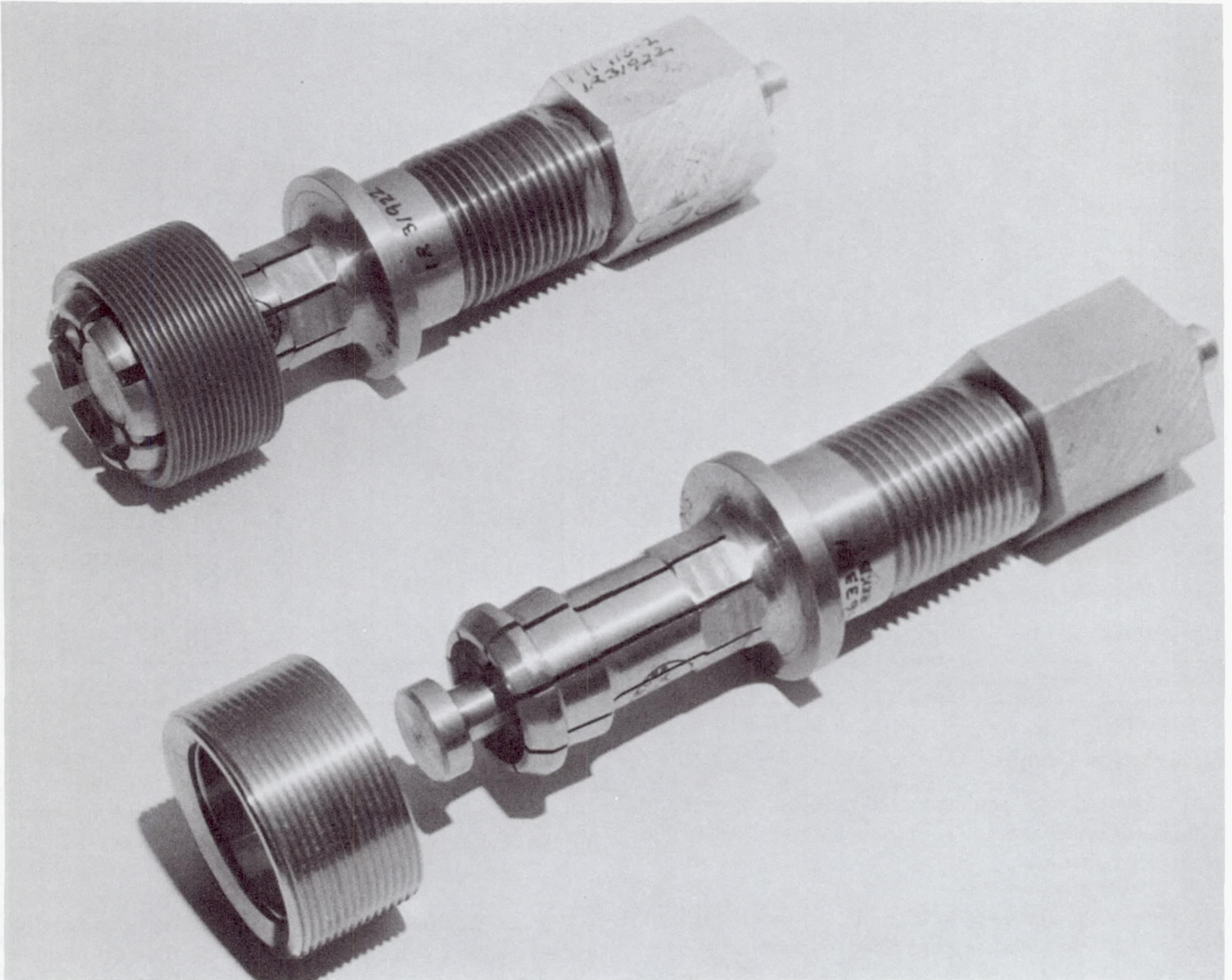


Fig. 1. Collet release mechanism

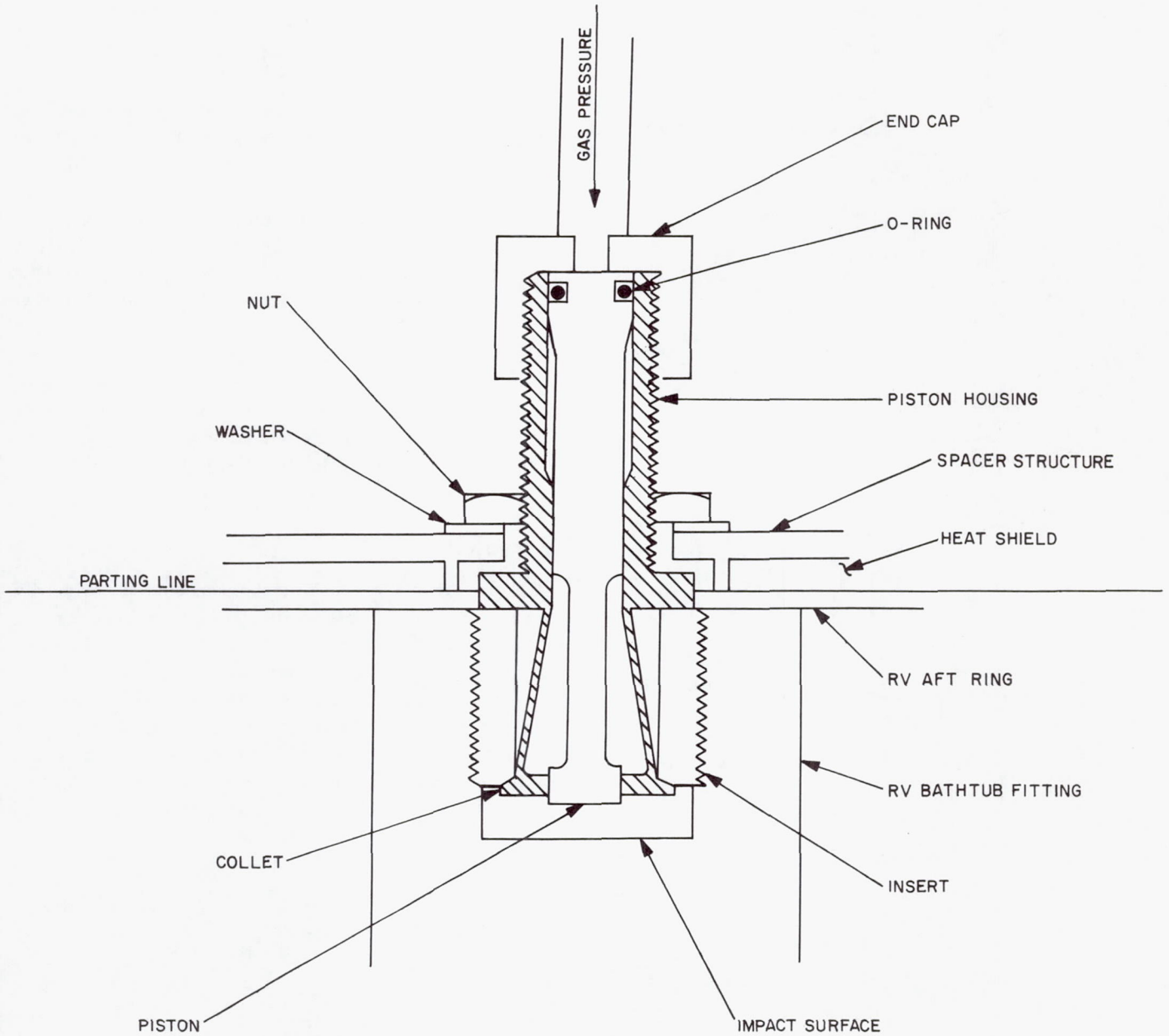


Fig. 2. Typical cross section of release mechanism

The essential dimensions of the design are as follows:

- (1) Housing: Collet diameter = 0.83 in.
Collet length = 1.5 in.
Bore diameter = 0.75 in.
Collet deflection = 0.10 in. radial
Number of fingers = 8
- (2) Piston: Stroke to unlock = 0.25 in.
Power stroke = 1.25 in.
- (3) Tank: Gas volume = 75 in.³
Gas pressure = 3750 psi, stp
- (4) Weight of each collet mechanism = 1.2 lb

The advantages of this design are that it (1) has a high-load capability, (2) has a separation velocity of 3 ft/sec at nominal gas pressure, (3) is lighter and smaller than a spring, (4) is reliable, simple, and reusable, (5) has no fragmentation, and (6) has low shock. As a matter of fact, four springs would have been prohibitively large and heavy. The system could be initiated with a single electrical signal of 7 amp.

The curves of Fig. 3 show the weight comparison as a function of separation velocity between a collet release mechanism system used to separate various payloads and an alternate system using explosive bolts and springs. For the heavy payload, four attachment points are used. The collet release system weight includes a tank, valve, and manifold. The spring weight is the optimum weight based on a parametric computer study for unguided springs ($L/D < 5$) where the spring's mean diameter was limited to 2 in. maximum. The spring volumes are considerably larger than that of the collet mechanism, especially for the high energy requirements. It can be seen in the curves that the collet mechanism is lighter than springs for separation velocities greater than 2 ft/sec.

V. Analysis

The design of the collet mechanism consists primarily of performing the stress analysis of the fingers for the anticipated load and environmental conditions. The fingers are analyzed as a cantilevered beam with an initial deflection and an axial load equivalent to either the pre-load or the worst flight load superimposed. A computer program is available which allows the engineer to select design parameters of number of fingers, finger length, finger thickness, and collet diameter based on the total allowable stress and the axial load.

The equation for total stress for a trapezoidal finger cross section is given by

$$\Sigma_{TOT} = \left[\frac{P}{\pi t(D_o - t - 0.0191n)} \right] + \frac{3E\delta}{L^2} \left[\frac{2 \sin\left(\frac{\pi}{n}\right)(R_o^3 - R_i^3)}{3\left(\frac{\pi}{n}\right) R_o^2 - R_i^2} - R_i \cos \theta \right] \quad (1)$$

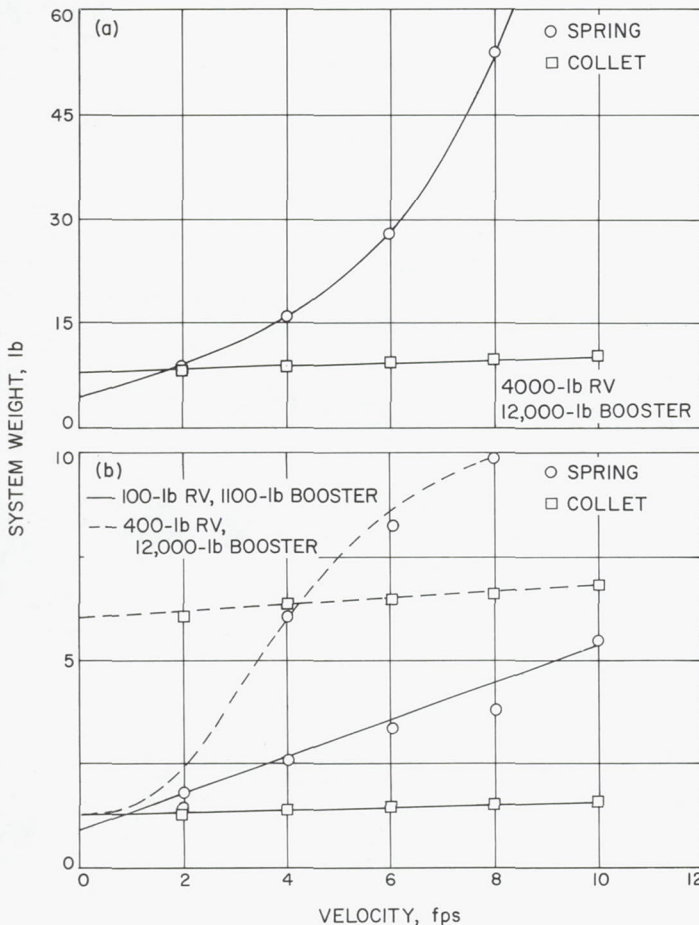


Fig. 3. Weight comparison of spring and collet mechanism vs separation velocity:
(a) for a heavier payload, and
(b) for lightweight payloads

by specifying the following inputs:

P = total preload

t = section thickness

D_o = section outside diameter

E = modulus of elasticity

n = number of fingers

L = finger length

δ = initial finger deflection

R_o = outside radius

R_i = inside radius

The computer will then evaluate Eq. (1) for all combinations of the above variables (E and δ are held constant).

The design of a separation subsystem utilizing a collet mechanism, a source of compressed gas, and suitable interconnecting manifold was analyzed to predict its performance, pressure profile, piston travel velocity, and

action times. The operation of the system is analyzed in three steps:

- (1) Isentropic expansion of the gas into the manifold after valve opening.
- (2) Unlocking the mechanism (initial 1/4-in. movement of piston).
- (3) Power stroke — continued movement of piston against the body to be ejected.

The equations used for the prediction above have been programmed for use with a time-sharing computer system so that a parametric subsystem prediction can be accomplished in a relatively short time. The program inputs are masses of the bodies to be separated, initial conditions of the gas (V , T , P , k , R), manifold length and internal diameter, piston unlocking pressure, piston diameter, maximum piston power stroke, number of release devices, and unlocking stroke of the piston. The solution given as a function of time includes piston stroke, velocity, tank pressure, and piston pressure. The governing equation is that for subcritical mass flow of a perfect gas:

$$\omega = 8.02 A \left\{ \left(\frac{P_t}{V_t} \right) \left(\frac{k}{k-1} \right) \left[\left(\frac{2}{k+1} \right)^{(2/k-1)} - \left(\frac{2}{k+1} \right)^{(k+1/k-1)} \right] \right\}^{1/2} \quad (2)$$

where

ω = gas mass flow

A = piston area

The piston velocity uses the impulse-momentum equation:

$$V_p = \frac{4P_r A \Delta t + I_0}{M_{RV}} \quad (3)$$

where

t = tank conditions

r = release mechanism conditions

M_{RV} = vehicle mass

I_0 = initial impulse of piston

The stress analysis of the collet fingers for a 10,000-lb-limit tensile load shows a stress of 168,000 psi is obtained using an eight-finger device with a finger thickness of 0.06 in. and a trapezoidal cross section. Although this

high stress yielded a small positive margin, subsequent static tests showed that the tensile rupture strength was 24,500 lb. It was reasoned that the analysis was conservative in assuming the finger to be a perfect cantilever beam, neglecting the end-fixing effect of the collar.

The pneumatic analysis showed that, operating from a 3750-psi, 75-in.³ N₂ source, the separation velocity expected was 3.2 ft/sec for a 1 1/8-in. power stroke. The total time for separation was predicted as 91 msec. Actual tests yielded separation velocities of 3.0 ft/sec, the desired goal. The 6% losses were attributed to the simplifying assumptions of no losses in the manifold, isentropic gas expansion, isothermal conditions, etc. A correction factor was added to the computer program to compensate for losses based on the results above.

VI. Test Results

The mechanical tests conducted on the mechanism were those of static tensile strength, torque vs preload, and

unlocking force. Three specimens were pulled to tensile failure, and the rupture strength averaged 24,500 lb. The point of failure was consistent in all three specimens and occurred at the predicted section (contact area between fingers and collar); failure mode was shearing of the tip. Torque preload tests gave the required torque to be 60 lb-ft to attain 6500 lb preload. The torque curve was smooth and linear over the range of 500 to 10,000 lb load. Three collet mechanisms and six preload nuts were used, and the nuts interchanged. The static unlocking pressure test showed that 900 psi will unlock against a 6500-lb preload. The data were linear, and the torque was applied by torquing, using the same three specimens described above. One mechanism was unlocked approximately 40 times under load before excessive rounding off of the load-bearing surface between the fingers and the piston was noted.

Pneumatic separation tests were conducted using independent masses hung from individual 16-ft ballistic pendulums. A set of four mechanisms were interconnected by a balanced manifold of the same configuration as the flight equipment. A solenoid valve was used in place of the explosive valve. The average separation velocity observed on three tests was 2.95 ± 0.1 ft/sec using 3750 psi. The average velocity using 3250 psi in three tests was 2.75 ± 0.15 ft/sec. Unlocking pressures were 1150 ± 200 psi as measured by high-response strain-gage pressure transducers mounted at the inlet to the release mechanisms. This dynamic measurement agrees closely with the value of 900 psi static unlocking pressure discussed above. In three full-scale separation tests, the separation velocities were 3.0 ft/sec at 3750 psi and 2.8 ft/sec at 3250 psi, using collet mechanisms with a stroke of $1\frac{1}{8}$ in. instead of 1.0 in. as tested earlier in the individual tests. The tip-off rate could not be measured in the individual tests; however, a worst-case prediction of 1 deg/sec was made, based on extreme observed values of separation velocity and unlocking times. The simultaneity of unlocking function was within 10 msec.

No tip-off was observed in the full-scale separation tests over a pendulum swing of 26 in.

Other tests have been conducted on similar devices used for separation only, without any failures to separate or any evidence of structural weakness or performance degradation. Six release mechanisms were unlocked four times each, using squibs, after completing a stringent qualification program.

VII. Flight History and Other Applications

The basic mechanism system described in this paper has flown successfully. A small unlocking collet device $\frac{1}{2}$ in. in diameter and $3\frac{1}{2}$ in. long, designed to carry a 1500-lb load and operated with redundant squibs, has flown and operated successfully eight times.

Another collet device of the same basic configuration as the first one, but used for unlocking only, has been flown successfully five times. It is operated from a 5-in.³ tank and, as the piston bottoms out, it uncovers a set of ports leading to simple ejection pistons. The merits of the collet device are many and unlimited. Another unit is currently under development and similar concepts have been proposed on numerous other programs.

VIII. Conclusions

The collet release mechanism described in this paper has an excellent history of development and flight, backed up by good, thorough, substantiated analyses. The device is best suited for application requiring ejection, since the added weight penalty incurred is usually that of the additional piston and housing length. The mechanism outperforms springs at the high energy output requirement (i.e., 200 ft-lb and higher) and imparts a gradual increasing acceleration, which is a desirable ejection characteristic.

The Surveyor Thermal Switch

T. E. Deal

Hughes Aircraft Company
Los Angeles, California

The external temperature extremes of the lunar surface dictated that a means be found to control the two electronic compartments on the Surveyor soft lunar landing vehicle within a narrower temperature band to assure satisfactory component performance. Accordingly, thermal switches were developed to conduct heat away from temperature-sensitive components while heat-generating components were operating during the lunar day, and to retain heat at night when the equipment was off.

Future equipment required to vary thermal conductivities, should this principle be employed, can benefit greatly from the results of the many problems encountered and studies made.

I. Introduction

One of the many problems that had been anticipated in placing a vehicle on the moon, and its operation after landing, was the protection of sensitive electronic components and battery power source from expected external temperature extremes.

Lunar surface operations required that a thermal control system be developed that would be compatible with operations in temperatures ranging from -300 to $+220^{\circ}\text{F}$ and would maintain temperatures of the electronic and battery compartments between 0 and 125°F (see Fig. 1).

A technique of attenuating external environment variations by some passive thermal isolation would have resulted in overheating of components during high-

temperature periods when the equipment was in operation, unless heat absorption or refrigeration systems were employed. Conversely, if high temperatures were controlled to reasonable values, then low temperatures would fall far below acceptable levels unless a heat source was provided.

Alternate systems for providing cooling during high temperatures or heating at low temperatures were studied extensively. The final conclusion was that a packaged thermal switch to vary conductivity between the outer thermal shell and the internal mounting tray was the simplest, most reliable, and most economical device.

Requirements of the packaged thermal switch were that it be capable of varying the thermal conductance by at least two orders of magnitude. A number of switches,

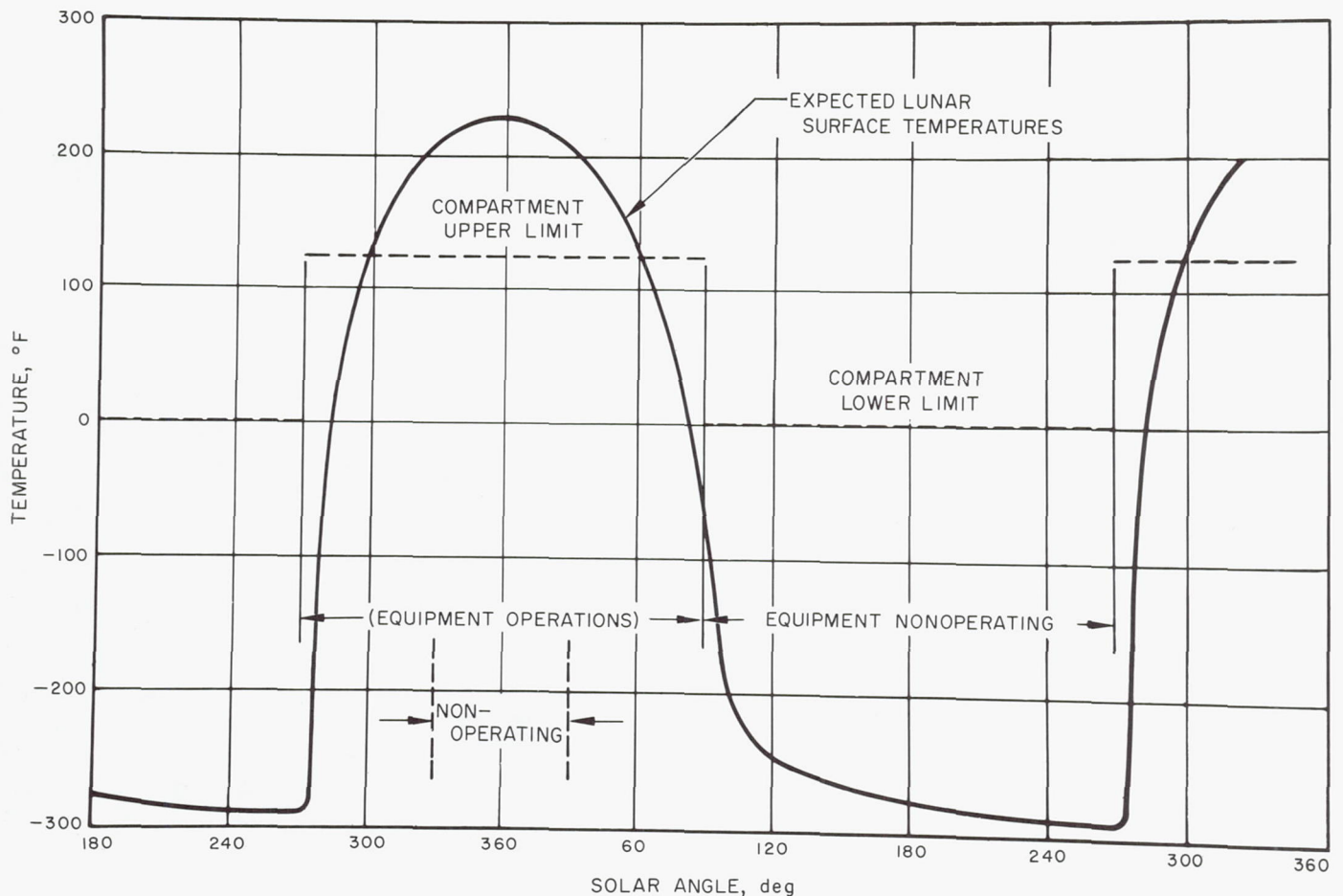


Fig. 1. Expected lunar surface temperatures and compartment temperature limits

distributed over the surface of the package, were required to allow extreme isolation design of the package, conserving internal power during low temperatures yet permitting adequate total conductance to curb overheating during high temperatures. The development of this device, in combination with rechargeable batteries, permitted lunar operation in excess of 30 days without a basic weight penalty. Heater power to overcome low-temperature thermal leakage was reduced to less than 8 w.

Several types of switch designs were considered, involving contact between solids and between liquids. Consideration of the use of solid contacts in a vacuum posed a potential problem of seizure between surfaces in contact because of the loss of surface films and absorbing acids. Liquid designs may not encounter surface seizure, but involve vacuum sealing problems and are limited in performance by vapor conductivity in the

“open” position. Liquid systems also tend to be bulky for multiple use.

A design selection was made featuring a solid contact connected directly to a radiating outer shell. Problems encountered in fabrication and test quickly resolved that each set of contacts must be directly coupled to its own radiating surface. Equating the conductance capability of the contacts (0.5 Btu/hr/°F minimum) and the emissivity characteristics of the radiative surfaces (0.85) with the total wattage dissipation required during high temperatures resulted in the use of nine switching units on the battery and electronics compartment and six on the spacecraft telemetry compartment. Where metal parts are required, the use of 1100 aluminum made it possible to hold the total weight of the switch to a minimum of approximately 0.6 lb. Radiator emissivity was controlled by the use of aluminized Vycor glass bonded directly to

an aluminum radiator substrate. The Vycor glass is transparent to the solar energy spectrum, and the aluminized surface on the back of the glass keeps the solar absorption to a low value.

Problems of thermal bending induced into the radiator because of the wide difference in thermal coefficients between Vycor and aluminum were resolved by using a silastic compound as the bonding agent.

The resultant thermal switch is shown in Fig. 2. The basic components of the switch include an outer radiating plate, exposed to the space environment, which contains an integral contact face; an inner contact plug thermally connected to the base ring by multiple layers of aluminum conduction foils; four bimetallic elements cantilevered from the base ring which engage a slotted adjustment nut on the base of the inner contact; and a low-heat-conductivity plastic case that supports the outer radiator from the base ring. The adjustment nut regulates the height of the inner contact above the bimetals, thereby permitting setting of the actuation temperature. Multiple layers of aluminized Mylar foil are placed within the case to minimize internal radiation losses in the open position. Direct coupling of the bimetals to the movable inner contact causes the inner contact to press against or pull away from the fixed radiator contact as a linear function of temperature.

A total of 135 flight-quality switches have been delivered for spacecraft vehicle units in the *Surveyor* program. Success of the operation of these units is attested by the fact that *Surveyor I* electronics were responding

as late as January 1967, having survived more than seven lunar nights. The electronics were interrogated at the end of each lunar day when the solar panel was illuminated sufficiently to operate the low-power transmitter.

II. Design Considerations

Thermal conductance across two surfaces in contact in vacuum is dependent upon the total effective area of material in contact. Microscopic ridges or waviness of the interstice can substantially reduce this effective area of contact and reduce the amount of heat transferred. To overcome this condition, specifications were imposed requiring these opposing contacts to be flat within one lightband. Later, a thin film of RTV 11 silastic was incorporated on the inner contact to compensate for the mating of microscopic ridges. A layer of molybdenum disulfide was charged into the silastic to act as a parting agent.

Alternate geometries such as spherical or conical mating surfaces were considered for the contact configuration. The advantages might have been higher contact pressure for a given force and a tendency for self-seating. The trade-off of required alignments, however, appeared to negate this approach. A flat uniform contact was the most easily utilized for the design by allowing a slight free play in the bimetal support group. Any free play for a spherical or conical design would have been prohibitive, in that a greater contact displacement would have been required to assure a true switch opening. With the flat contact, elastic compliance in the bimetal assembly and the dependence of conductance upon pressure tended to desensitize the effect of any slight misalignments. Certain parallelism standards, however, were required to prevent edge contact from conducting heat after the switch was supposedly open.

Several contact surface treatments were investigated in the design phase before RTV 11/MoS₂ was chosen. Gold plating of contacts proved to have wide variations in conductivity from unit to unit because of lack of true compliance between metallic surfaces, due to microscopic ridges and valleys. Teflon, as a compliant agent, proved unworkable because of its thermal insulation properties, together with the inherent contact surface waviness with a Teflon application process. With RTV 11, integrity of the flatness of the treated contact was maintained by curing the silastic with a weighted optical flat in contact. Grease as an interstice agent was eliminated due to the adhesive and migratory properties of those materials that

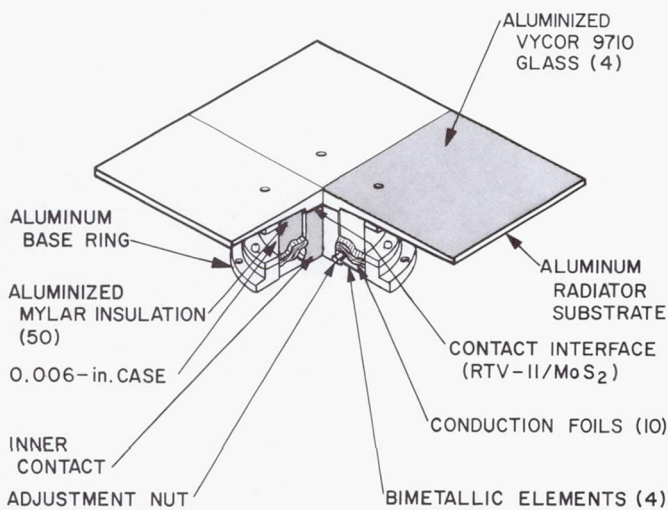


Fig. 2. *Surveyor* thermal switch

could survive the vacuum environment. Much background was obtained from work done by others regarding the conductance characteristics of a thermal joint in a vacuum (Fig. 3). The conductivity finally achieved by the *Surveyor* thermal switch is superimposed in Fig. 3 on results for other materials as investigated by E. Fried.¹

Maintaining proper heat conduction between the base ring and inner contact was achieved by welding the multilayered aluminum conduction foils to the base ring and bonding them to the inner contact by means of a silver-filled conductive epoxy. Bimetal temperatures were held in equilibrium with the base ring, or thermal tray, by virtue of a final assembly machining operation to assure an overall flatness of the base of the entire assembly.

Later, in studies of design refinements to improve switch thermal characteristics, the use of a silver-backed mirror, in place of the aluminum-backed mirror, was considered. This change would have reduced the solar ab-

¹Fried, E., General Electric Co., "Thermal Joint Conductance in Vacuum," presented at the conference of the American Society of Mechanical Engineers held at Los Angeles, Calif., March 1963.

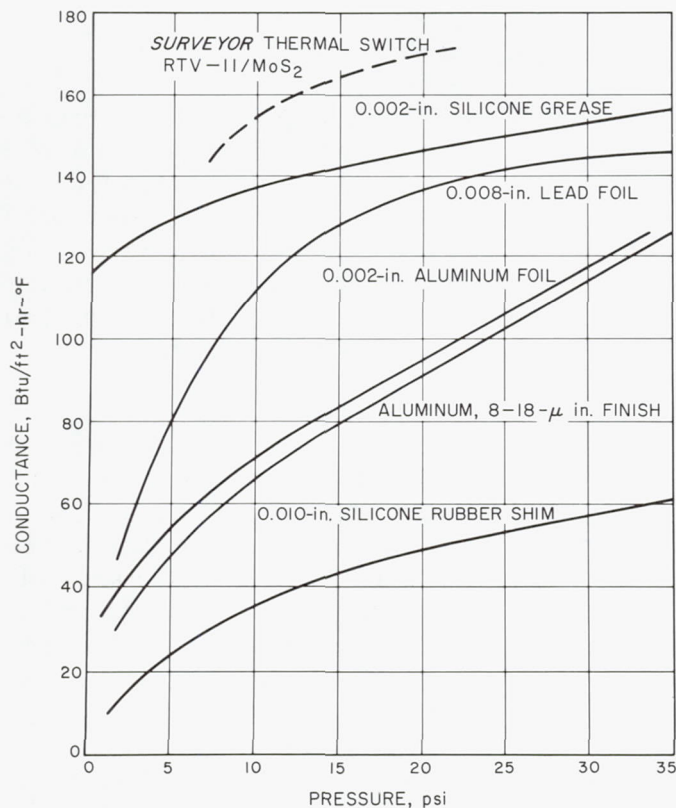


Fig. 3. Thermal joint conductance in vacuum

sorptance from 0.12 to 0.06, thereby permitting greater use of the electronics during lunar noon. The adhesion properties of silver to Vycor glass were somewhat marginal, and it was felt that the risk involved in delaminations and separations and possible breakage during severe low temperature would not make the change practical.

III. Problem Areas

Problems encountered in development, test, and fabrication can be broadly categorized into three areas: test requirements; materials and processes optimization; and thermal switch handling.

Problems in test basically stemmed from the lack of correlation between thermal conductivity in normal atmosphere versus thermal conductivity in vacuum. Elimination of the effect of convection in any conductivity measurements made in the evaluation of materials or in the final acceptance of switches for spacecraft use required a simulation of the unit operational use (Fig. 4). In addition, variations caused by air convective action would not permit the setting of the actuation temperature in room ambient conditions. As a result, units of unknown behavior were delivered to test, which added considerably to the test effort and required that many units be returned for parallelism adjustments or correction of hardware discrepancies.

Problems of materials and processes generally evolved from the contact interface area. Problems of contact seizure, which were initially investigated only in connection with contact between two base metals, appeared after units had been delivered to the first two spacecraft.

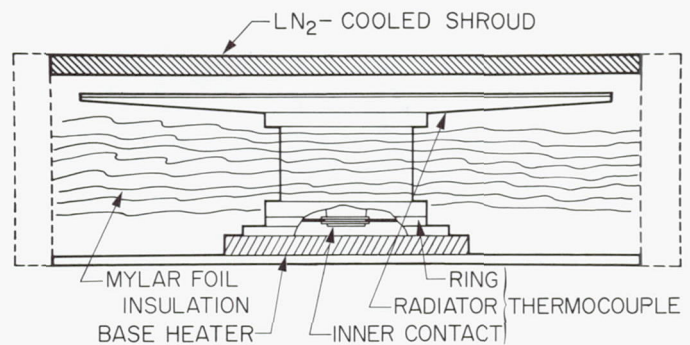


Fig. 4. General test arrangement for the *Surveyor* thermal switch

Seizure problems (or sticking contacts) were encountered on units that had completed assembly and test and had been on the shelf for a period of several months. Re-evaluation of test history showed that many of the difficulties experienced in test were directly traceable to contact sticking. In testing for thermal switch actuation points, the criterion was established that opening temperature, or temperature at which switch conductivity had reduced below a certain point during a transient cool-down, was to be used, even though switch closure data were of more import from a thermal point of view (Fig. 5). This criterion was based on the fact that normal switch opening and closing were, for all practical purposes, the same. Preconditioning the switch at a lower temperature to observe a true closing point would have required added time and equipment and would not have been economical. In the presence of sticking contacts, switch opening and closure was not the same and the nature or degree of sticking was erratic. This led to extensive test and retest and correction of discrepancies because the true nature of the problem was unknown (Fig. 6).

Sticking contacts led also to mission compromise in actual operation because excessive heat was dissipated into space during the transition from high to low temperatures, resulting in additional battery drain to overcome this effect. On the first *Surveyor* spacecraft, several of the thermal switches did not open until after compartment temperature had dropped below zero. Heater control of the spacecraft compartments was placed on manual mode, however, and temperatures were allowed to drop far enough to permit the bimetal forces to overcome the adhesive force without excessive waste of battery power. Once the contacts were broken free, they apparently did not readhere.

The cause of contact sticking was discovered to be the release of volatiles from the RTV 11 contact surface and migration of molybdenum disulfide particles into the remaining silastic elements. Free particle migration of the silastic, once the MoS_2 was absorbed, caused adhesion to the bare metal contact of the radiator.

Several approaches were attempted to correct this condition. The first approach was to return to the use of Teflon after a technique had been developed to coin a Teflon contact flat within one lightband. Results of this investigation were moderately successful, but Teflon still presented too high a thermal barrier to be used with any confidence of repeatability from unit to unit. The most

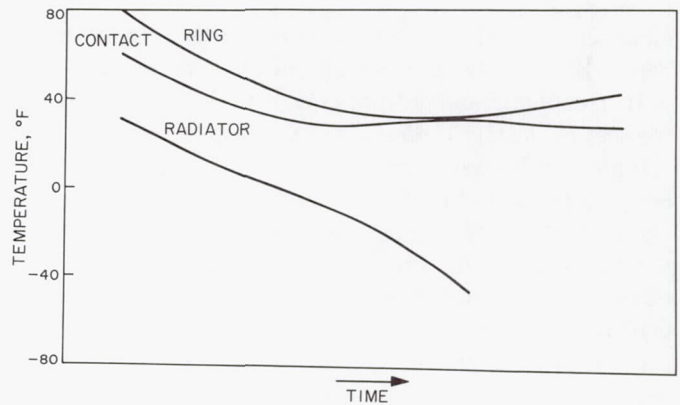


Fig. 5. Normal switch opening and closing trace

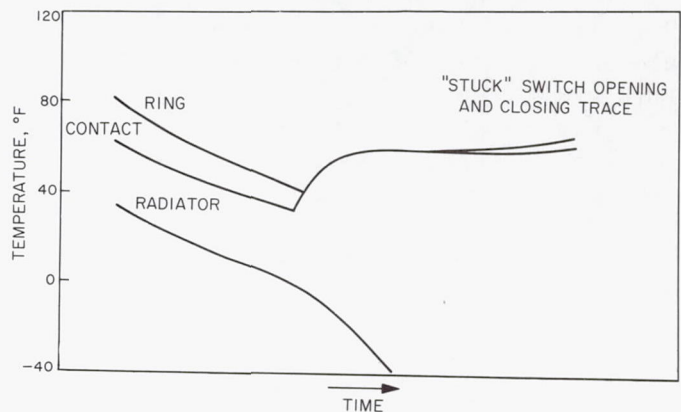


Fig. 6. "Stuck" switch opening and closing trace

promising solution was the use of a low cohesive semi-solid (a silicone oil filled with zinc oxide powder) as the interstice agent. The need to qualify this material, together with schedule restraints and the unknown effect of breakdown of the compound after repeated operation, led to the abandonment of this approach.

Using the RTV 11/ MoS_2 combination and adding a 48-hr vacuum bakeout at 300°F proved to be the final solution of the problem, with minimum impact on cost and schedules. An additional coating of MoS_2 was applied after the bakeout to provide an additional barrier against particle migration. Prior to the incorporation of this treatment, recycling switches after vibration for non-repeatability of set point was approximately 60%. After this treatment was incorporated, recycling through flight acceptance test dropped to zero.

Handling problems generally led to contamination or breakage. The unit was constructed so that during installation on the spacecraft the radiator must be removed to

gain access to the mounting studs on the compartment thermal tray. This led to the problem of exposing the switch contacts and introducing contamination between the mating surfaces. Because of the requirement for good compliance between contacts, introduction of any foreign particles reduced the capability of the switch to conduct. (On at least two occasions a small fiber from the stitching of clean room apparel was found to be the cause of poor conductivity. In another case, an eyelash was found trapped between the contacts, causing the same problem.) Cleanliness and proper handling procedures, therefore, were important to prevent compromise of switch performance. Breakage was also a major problem. The 20-mil Vycor glass was highly susceptible to damage from dropped articles at the spacecraft level. The thin-walled plastic case was also susceptible to damage and was easily and frequently punctured or separated from the support rings. Breakage of any of the parts required complete rebuilding and re-acceptance testing of the units because set temperature adjustment was dependent upon the accumulated tolerances of all of the components in the assembly compensated by the rotation of the adjustment nut. On the spacecraft level this led to complete replacement of the unit.

Variation in conductivity was always a problem but was generally related to imperfect parallelism between the opposing contacts or to an out-of-flat condition of one of them. Since unit specifications required that the unit conduct at 0.5 Btu/hr/°F minimum at 50°F above closure, misalignment would, of course, require greater force and therefore higher temperature to effect complete closure. Excessive misalignment of contacts meant poor compliance at the specified temperature, resulting in conductivity below specified limits.

The linear relationship between pressure and temperature posed another problem. As the program developed and more was known about the launch vehicle, a requirement was imposed that the switch survive parking orbit trajectory where aerodynamic heating would be present. The effect of this high temperature was to increase the internal force within the switch, together with softening the bond between the thin-walled plastic case and the Fiberglas support ring. These conditions served to change the dimensional height of contact spacing and resulted in an upward shift in opening temperature. High temperatures also, if sufficient, could increase the free particle migration tendencies of the RTV 11 material and cause slight contact sticking.

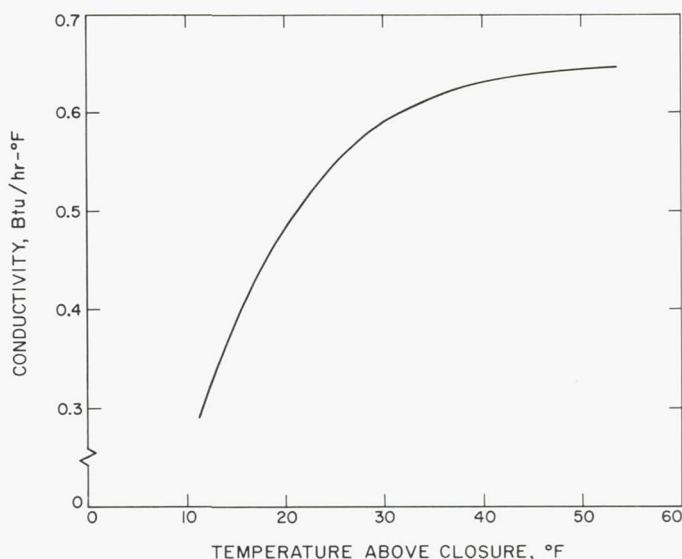


Fig. 7. Typical conductivity curve for Surveyor thermal switches

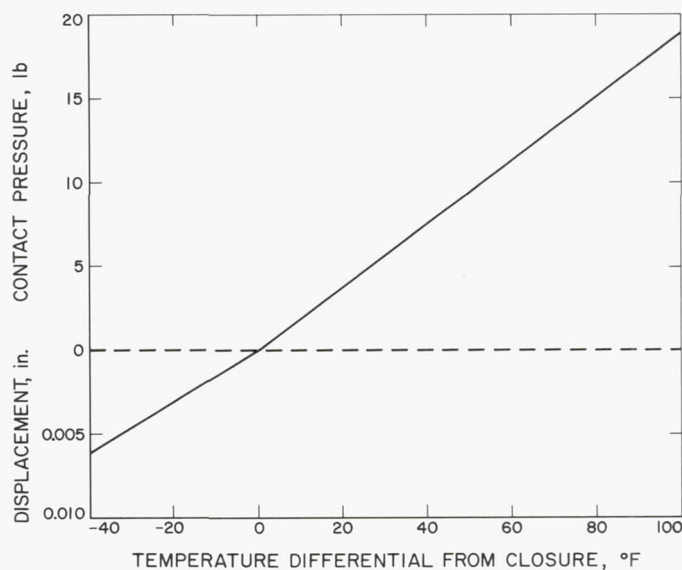


Fig. 8. Bimetal forces and motions of Surveyor thermal switches vs temperature differential

Figures 7 and 8 show a typical temperature versus conductance curve and a displacement/force versus temperature curve for the thermal switches, respectively.

IV. Future Applications

The principle of the thermal switch proved to be a workable active thermal control system in the Surveyor program. During the development of the Surveyor thermal switch, many other approaches were considered,

utilizing the same principle of operation or variations of other principles of operation. These approaches ranged from sliding contacts to fixed inner contacts and movable radiators. Several designs of snap action movement were conceived, but the inherent problem of hysteresis precluded these designs.

Single-element expansion materials could basically perform the same job as a differential expansion of the bimaterials used. A device utilizing a material phase change could provide a highly reliable unit. Details of packaging phase change or high-expansion semisolid devices would have to be resolved to assure that the action would be repeatable in the desired direction regardless of the orientation of the unit.

Future planetary vehicles will require active thermal control systems that operate on the same principle of variation in conductivity and emissivity. It is conceivable that future satellites of large size will require that certain sensitive electronic elements be protected during transit periods, or during eclipse periods, when temperature gradients can become quite high. For example, on large spinning satellites in a very high orbital path, an eclipse period of slightly over an hour can lead to surface temperatures below -150°F . Certain electronic units, without some type of thermal switching protection, could require the use of heaters during eclipse periods, or require the use of electrical power when electrical power is at a premium for other satellite operations. A variable-conductivity mounting device might be the simplest solution to this type of problem.

V. Conclusions and Recommendations

Although the principle of operation of the *Surveyor* thermal switch was simple, the problems encountered in manufacturing variations, test complexity, and subsequent handling of the spacecraft tended to reduce the advantages of unit simplicity. Future programs utilizing this type of device will benefit greatly, since many of the problems encountered and many of the minor discrepancies of the unit will have been resolved.

In future programs the design of an actuation system that will make the action nonlinear through the set point, either with a phase change device or a snap-action device (if hysteresis can be tolerated), should be investigated. The advantage to be gained from this design would be that set point adjustments could be made on the bench during manufacturing without involving phases of ther-

mal vacuum testing. This type of design would also avoid high-temperature problems where internal stresses can affect performance, and would provide greater conductivity at lower temperatures above the actuation point (since conductivity is a function of contact pressure), as well as provide a greater opening force to overcome minor contact seizure tendencies.

Another consideration that should be given to future designs is the use of a sealed unit for spacecraft installation. A sealed unit, which would have the contacts unbroken during installation, would save considerable effort in the installation process and provide a higher guarantee of unit reliability.

Consideration must be given to independent interchangeability of radiators without requiring complete replacement of a thermal switch, should damage occur. Location of the radiator on top of the thermal compartment poses potential problems from damage due to other operations on the vehicle. A built-in, slip-on, snap-on type of protective device, which could be removed prior to test or launch, should be incorporated.

All these considerations would satisfy the systems point of view for a simple, foolproof device that is invulnerable to damage, that can operate indefinitely with a minimum of attention, and that can be assembled and tested by completely untrained personnel at minimum cost. While such a dream may never be fully realized, significant approaches toward that goal can be attained.

Acknowledgments

The following Hughes Aircraft Company personnel were the major contributors to the successful development of the *Surveyor* thermal switch:

- R. J. Wensley, under whose direction the initial trade-off studies and the design and development of the thermal switch through delivery to the prototype spacecraft were accomplished.
- A. H. LaManna, who developed the test techniques employed in acceptance testing of the switch.
- P. R. Verbeke, mechanisms unit engineer, who carried the thermal switch through initial production.

Development of the *Surveyor* vehicle was done under contract to the Jet Propulsion Laboratory for the National Aeronautics and Space Administration.

The Integrated Rocket Spin-Up Launch Mechanism

John Hillan

Lockheed Missiles and Space Company
Sunnyvale, California

The integrated rocket spin-up launch mechanism is designed to ignite, spin, and launch a small rocket-propelled payload. It is unique in that several pyrotechnic and mechanical events are initiated by one electrical signal. The mechanism offers an extremely lightweight and compact system for the variety of functions performed, by taking advantage of integrating pyromechanical features provided by the rocket motor configuration. Recent test flights have proved all aspects of the mechanism operation to be completely successful.

I. Introduction

The major objective in developing the integrated rocket spin-up launch mechanism was to evolve a spin/launch system that would result in an accurate payload trajectory, with a closely controlled spin rate used to trigger payload deployment release mechanisms. Another required task was to provide a stowage capability for the payload which would not detract from the spin-up feature. This latter requirement called for a departure from clamping actions utilizing separate electrical signals to implement release of the payload. Further, the configuration was restricted by space and weight limitations, which demanded careful design packaging. In developing a small payload launcher to attain the foregoing design goal, a mode was selected that would reflect characteristics involving interchangeability, ease of handling, and economy of manufacture.

II. Design Alternatives

In order to determine the most effective concept for a spin-up launch mechanism, several methods for spin-launching rocket-propelled projectiles were investigated. The modes considered were as follows:

- (1) Rifling spin-up.
- (2) Torsion spring ejection.
- (3) Turbine spin.
- (4) Return ball and jack.
- (5) Spin motor and yoke.

A. Rifling Spin-Up

This method offers the optimum available spin-up mode, since the minimum number of external moving

Preceding Page Blank

parts is involved. Advantage cannot be taken of this mode, however, since neither the launch tube nor the payload walls lend themselves to rifle grooving. The launcher wall is too thin to accommodate the rifling attachments, and the necessary rifling grooves would require a 200% increase in wall thickness, resulting in an unacceptable weight penalty. With respect to the payload, the addition of the rifling pins and the need for grooves in the payload wall would (1) require a thicker wall and thus place a further weight burden on payload capability, and (2) prevent successful dynamic balancing of the payload.

B. Torsion Spring Ejection

The spring component in this method could not be accommodated within the allowable space envelope. It was determined that an increase of 2 to 3 in. over the allowable envelope length would be required to seat the spring in its compressed condition.

Another disadvantage of the torsion spring mode is its inability to provide a close-tolerance spin rate. Several spin tests were conducted employing this mode, and the results indicated a considerable variance from the required spin rate. Further, the manner in which the spring is loaded places the burden of safe installation on the operator rather than on the design, thus entailing a distinct hazard factor.

C. Turbine Spin

This mode (Fig. 1) consists of vanes cast into the base of the launch tube which duct the rocket-exhaust gases into canted stators on the aft skirt of the rocket payload. At ignition, the ducted gases cause the motor to spin on spring-loaded detents and a groove. The pressure then builds up, and the payload is ultimately ejected. Close appraisal of this mode revealed flaws in the design. Gas dynamic analysis showed that concentration of pressures on the tube base could cause substantial buckling of the thin tube wall. To ease this situation, tube fabrication of steel or titanium would be necessary, thus substantially increasing the weight and cost of the overall system. The results did show a certain degree of feasibility when the design was not subject to this weight penalty. All parts, such as the steel investment castings and extrusions, lend themselves to economical manufacture. However, the weight penalty was considered too great a handicap.

D. Return Ball and Jack

This method (Fig. 2) consists of cutting a groove in the rocket motor shoulder, similar to those used in automobile steering columns, and securing a ball race adapter around the groove. The adapter and motor are then clamped to the tube base. At ignition, the rocket payload spins on the ball race as it is ejected. However, this method presents two serious problems: (1) prevention of the motor from spinning off due to shock loading and (2) provision for the successful return of the balls. Neither of these questions could be satisfactorily answered, and the method was abandoned.

E. Spin Motor and Yoke

This method is based on the spin-motor concept that became the basis for the later effort. The idea of employing small motors to provide spin is not a new approach, and various previous and present examples in rocket and propulsion technology prove the effectiveness of this technique. To adapt the spin-motor technique to the proposed system, however, offered particular challenge.

The initial concept of the spin-motor design provided for securing a steel yoke with two modular spin motors mounted 180 deg apart on the shoulder of the rocket (Fig. 3). Following the firing signal, the spin motors are ignited. This action takes place 40 msec before ignition of the main propellant, allowing a spin-up period prior to ejection. Ignition of the spin motors is effected by a self-contained ignition detonation (SCID) fuse from a manifold set in the rocket motor throat. Several variations of design were studied to determine the most suitable approach. However, it was not possible to provide sufficient impulse in the spin motor to spin the payload, indicating that a greater volume of propellant was needed.

In light of the foregoing considerations, it was proposed to eliminate separate spin-motor modules in favor of an annular spin propellant chamber integrated into the rocket motor skirt, as shown in Fig. 4. The chamber was provided with three equally spaced nozzles canted at 30 deg to provide positive thrust. Following the firing signal, the spin propellant is ignited, allowing the payload to spin on ball detents and groove. Ignition of the main propellant is delayed during the spin-up phase by means of a coiled SCID fuse set into the manifold. The spring load of the retaining ball detents was designed to be overcome by the force of ejection, allowing the payload to exit the tube. The essential features of the design, it was concluded, had now been established.

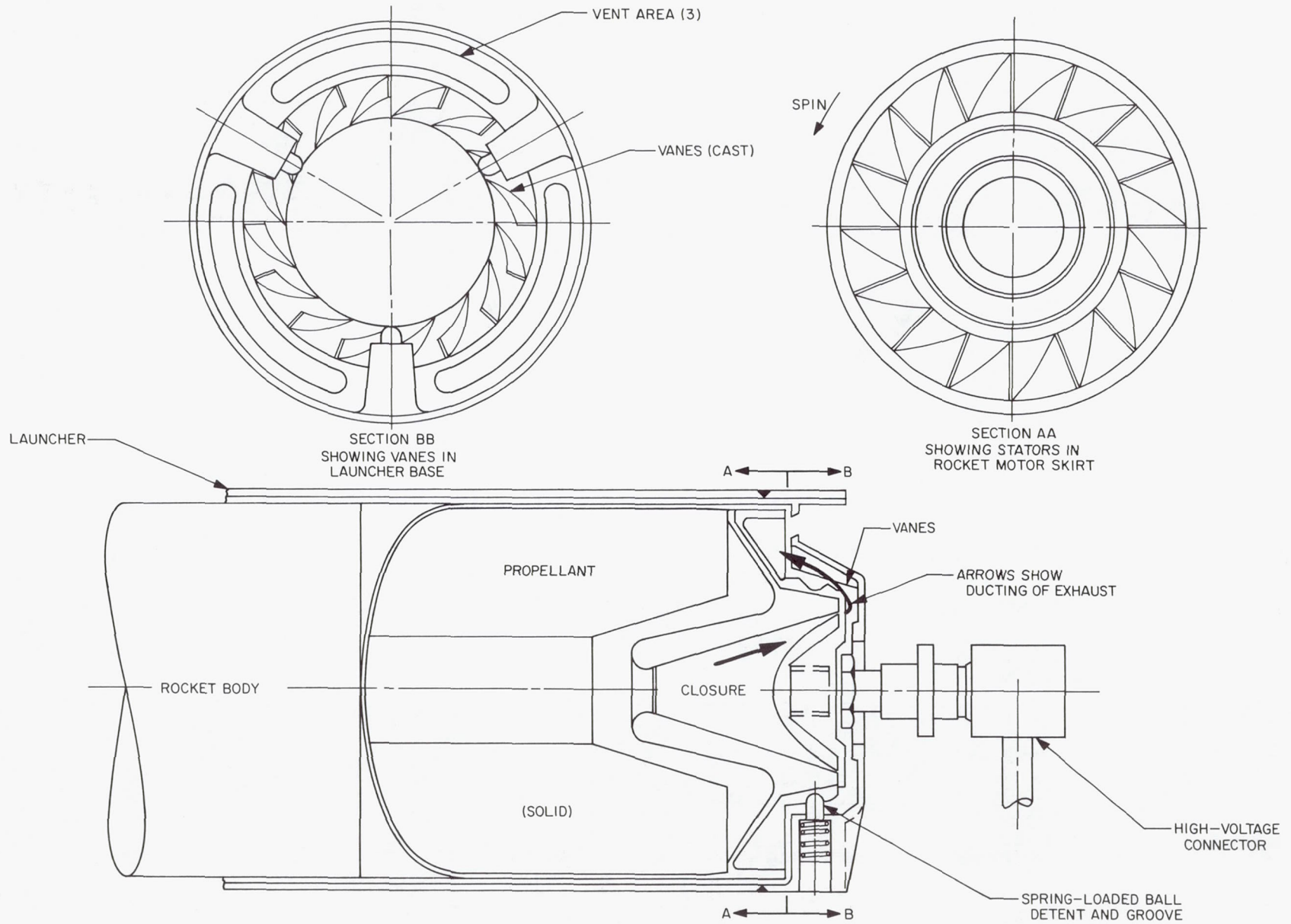


Fig. 1. Turbine spin mode

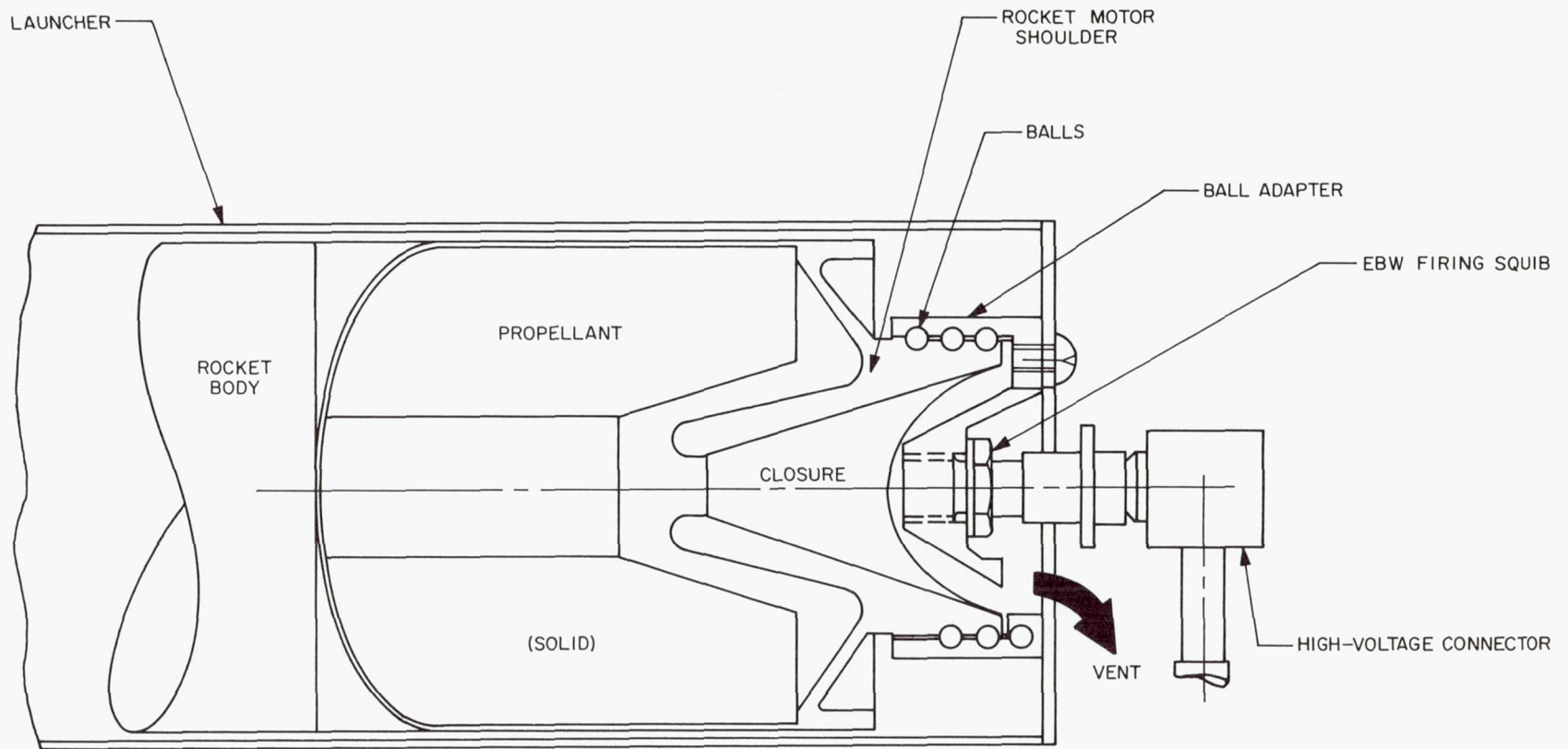


Fig. 2. Return ball spin mode

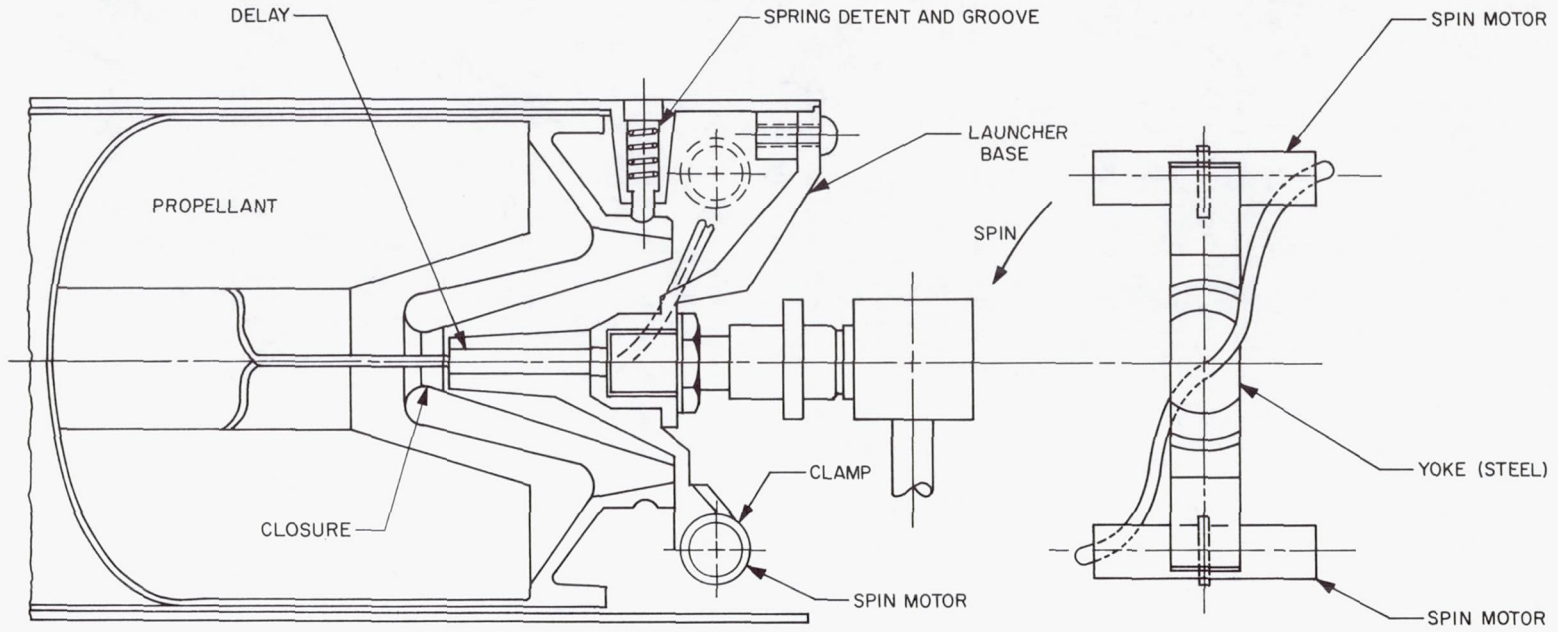


Fig. 3. Spin motor and yoke mode

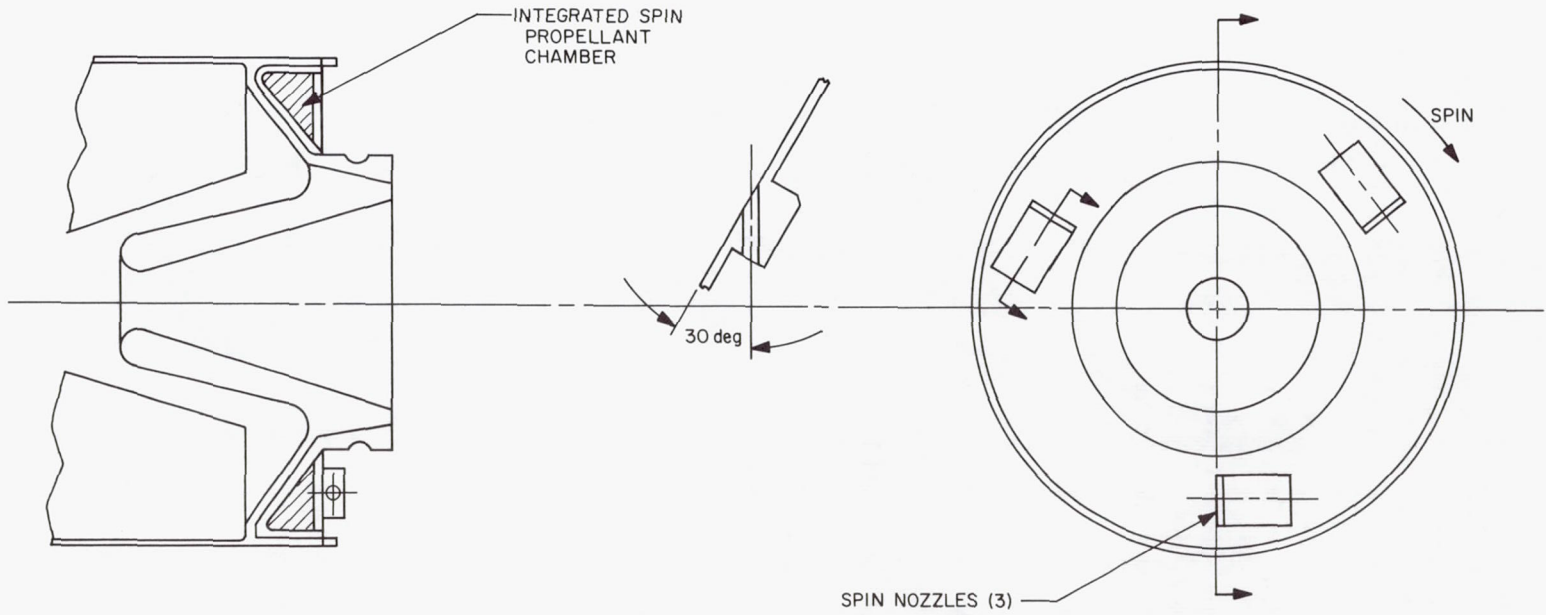


Fig. 4. Integrated spin chamber mode

III. Development of Final Design

Following establishment of the essential features of the design, steps were taken to assure adaptability in the concept. At this point, however, changes in performance requirements for the spin-up launch mechanism substantially affected the previously established design. Higher shock loads were required, which raised the maximum axial loading. More rigid stowage and human factors were introduced, compounding design problems, and analysis of the dynamics demanded more sophisticated ducting of exhaust gases. Consequently most of the conceptual design findings were of little practical use in the light of the changed requirements, which have greatly influenced the form of the final design. These requirements are as follows:

Payload spin rate	9 to 12 rps
Trajectory	± 3 deg for 1 mile
Axial loads	100 g
Electrical bonding	Class I
Allowable weight of spin-mechanism parts and launcher	3.5 lb, max
Gas ducting area	60% of launcher base area
Electrical signal	Single, 28 v

The need for a new method of stowing the payload in the launch tube became evident at the outset of the development design effort, since the effect of the increased

axial loading, acting on the ball-detent retention system, enhanced the danger of ejecting the payload prior to ignition. A separate clamping system, activated by its own electrical signal (as previously mentioned) was out of the question since the changed requirements allowed only one signal for the entire sequence of ignition, spin, and payload ejection.

A method was therefore evolved that utilized a three-legged bracket (Fig. 5) to be attached to the rocket motor by means of helical slots cut into the rocket-motor shoulder. The slots were designed to allow steel pins set into the bracket to ride onto the rocket motor at assembly and to lock in place by means of flat springs captured by the pins against the bracket leg (see Fig. 6). Small radial slots, cut into the rocket shoulder adjacent to the helical slots to accommodate the springs, were designed to prevent payload roll-off due to vibration and to prevent displacement of the payload from the retainer pins by axial shock loads. The helical slots were terminated in J slots (Fig. 7) which permitted absorption of the axial load on a plane perpendicular to the longitudinal axis and not on the canted surfaces.

The retainer pins were fabricated of steel with aluminum bushings to prevent excessive brinelling. Completion of the stowage requirements, however, required clamping the rocket motor, with the retainer bracket attached, to the base of the launcher. This attachment was accomplished by integrating the function of the ignition manifold into the retainer bracket (Fig. 5) and utilizing the exploding bridge wire (EBW) squib to attach the

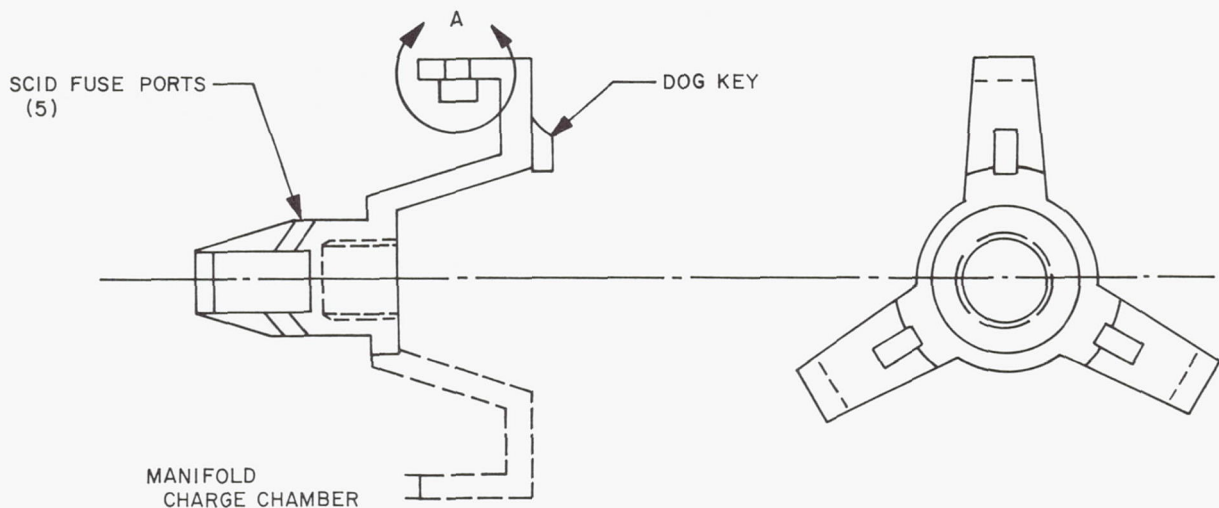


Fig. 5. Ignited retainer bracket (steel)

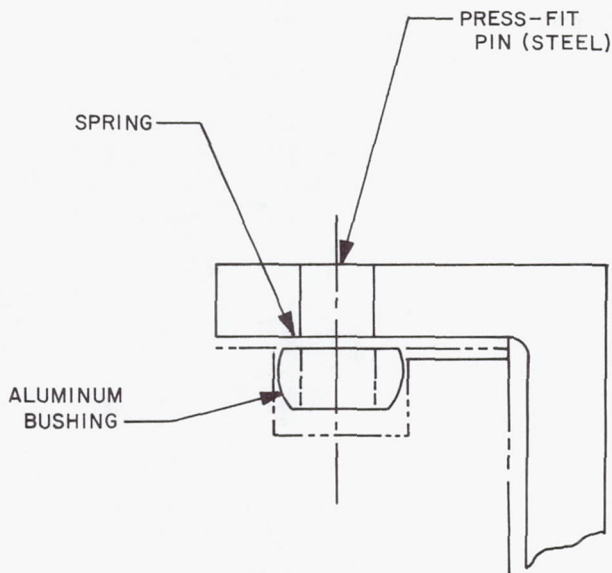


Fig. 6. Detail A of Fig. 5, showing flat spring captured by pin

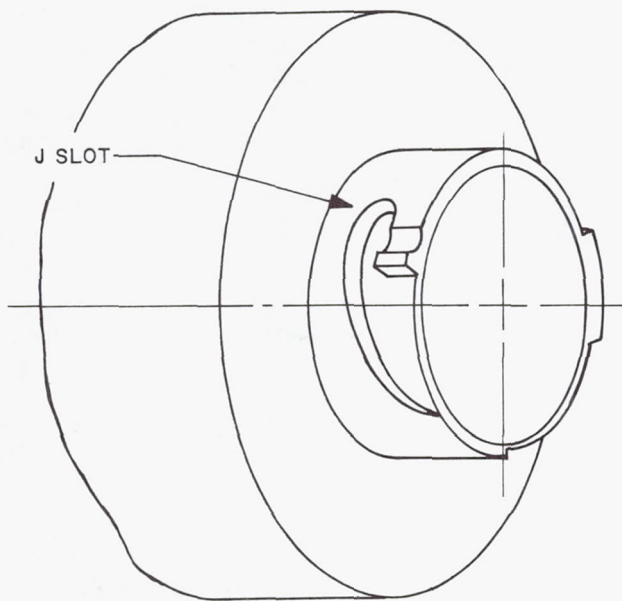


Fig. 7. Diagram showing helical slots in rocket motor shoulder

bracket through the base of the launcher. By thus keying the retainer bracket into slots in the launcher base and securing the entire payload assembly by means of the EBW squib, all stowage requirements were met. This entire arrangement was contained within a relatively compact space and was well within the allowable weight requirement.

The new requirements also influenced refinement of the exhaust venting and pyrotechnic features. It had been noted that impingement of gas pressure on the launcher base caused buckling of the tube itself. This had the effect of seizing the payload, thereby reducing the spin rate and decaying the trajectory. To eliminate this condition, improved venting of exhaust gases was indicated. An arrangement of exhaust ports was incorporated into the tube body, and the launcher base was redesigned to present a minimum of resistance to gas flow, as shown in Fig. 8. The base, which was now essentially a thin-section, three-legged spider of heat-treated 2340 steel, provided adequate strength plus venting for the system. The spider base was later converted to a steel investment casting. It was secured to the launcher by means of three No. 10-28 screws set into self-locking inserts in locally thickened sections of the tube wall.

The pyrotechnic aspects of the design were optimized by the results of a ground test program. The program was conducted to seek out problem areas affecting the systems design and to make recommendations for engineering prior to flight testing. The major trouble area uncovered was the pyrotechnic sequencing of events, which involved, essentially, the problem of timing. To spin up the motor properly required approximately 30 msec. During this period, ignition of the main (thrust) propellant had to be delayed. To accomplish this delay, an SCID fuse was routed from the ignition manifold within the retainer bracket into the spin-propellant chamber and returned to the main propellant chamber. The purpose of this arrangement was to effect spin followed by ignition of the main propellant, and the related pyrotechnic sequence was as follows (Fig. 9):

- (1) Firing signal.
- (2) Ignition of manifold propellant.
- (3) Ignition of SCID fuse (to spin chamber).
- (4) Ignition of spin propellant.
- (5) Ignition of return SCID fuse (to main propellant).
- (6) Ignition of main propellant.

It was discovered that this somewhat complicated sequence was neither mechanically effective nor reliably repeatable. Furthermore, there were many mechanical malfunctions because of damage to or premature ignition of the return SCID fuse. A relatively simple solution to these problems was achieved by routing the SCID fuse directly from the ignition manifold to the main propellant chamber instead of back from the spin propellant

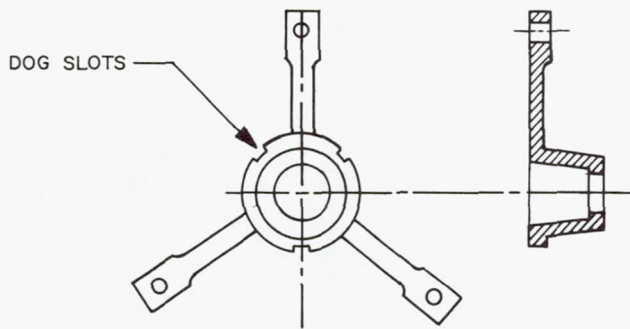


Fig. 8. Spider base

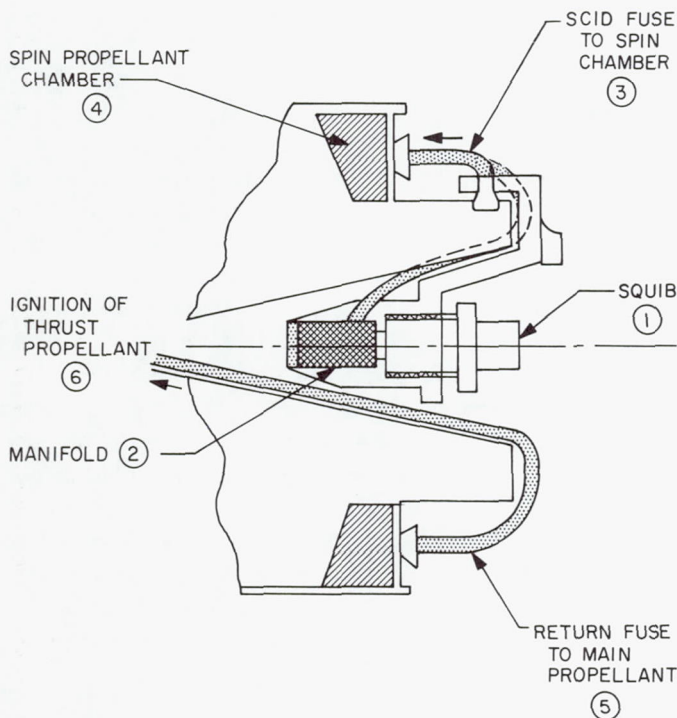


Fig. 9. Diagram showing SCID fuse routing and ignition sequence. Numbers in circles indicate the sequence of events

chamber, and by employing a pyrogen fuse as an intermediary to effect actual ignition of the main propellant. The result was the occurrence, following the firing charge, of simultaneous ignition of (1) the ignition manifold propellant, (2) the SCID fuse to the spin and main propellant chambers, and (3) the spin and main propellants (Fig. 10).

The actual gain of delay time for spin-up was provided by the time required within the main propellant chamber for the buildup of pressure required for ejection impulse.

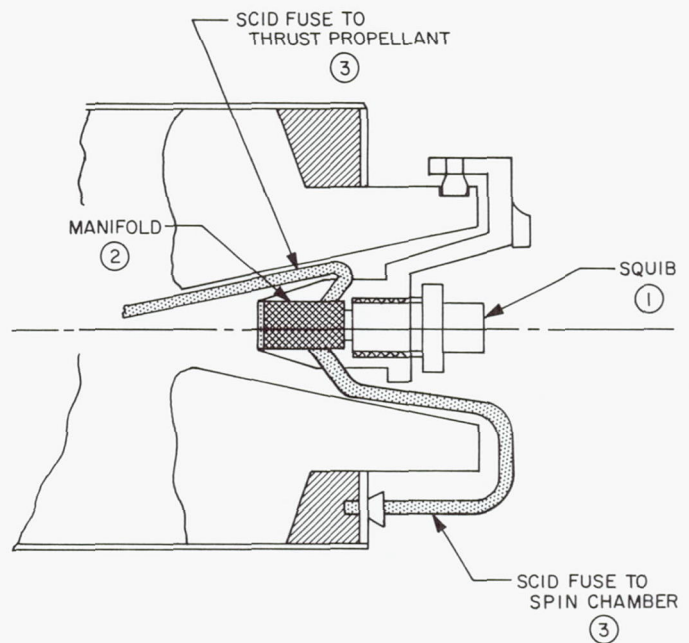


Fig. 10. Diagram showing improved method of SCID routing and resulting ignition sequence. Numbers in circles indicate the sequence of events, which occur essentially simultaneously

This period (40 msec) was sufficient to allow the motor to perform the following:

- (1) Free itself from the retainer.
- (2) Spin up to required spin rate.
- (3) Achieve required velocity impulse prior to broaching the launcher.

The pyrotechnic sequence and mode were thus established satisfactorily and have continued to provide a high degree of dependability.

A significant requirement is the need for stabilizing the rocket in the aluminum launch tube during the launch, since the total separation distance between the inner wall of the launch tube wall and the outer surface of the rocket is only 0.030 in. Such stability is achieved by means of nylon buttons pressed into the walls of the launch tube. These buttons present a smooth surface to the rocket perimeter and are designed to deflect up to a maximum of 0.002 in. as the ejection action takes place. The possibility of direct mating between the rocket and tube wall was considered, but expansion of the rocket motor as ignition proceeds would cause catastrophic jamming in the tube without intervening space between

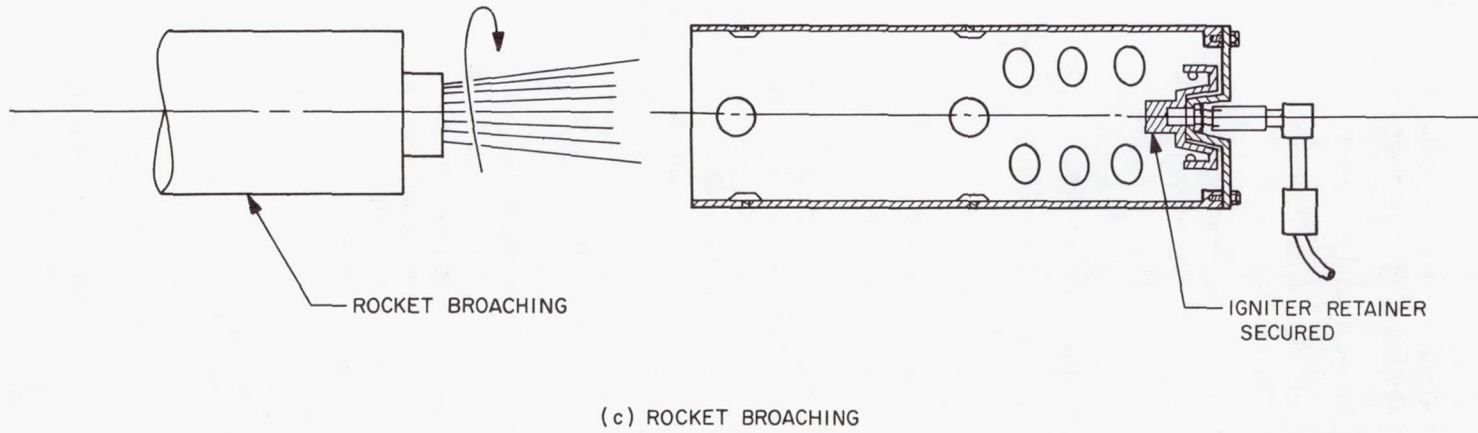
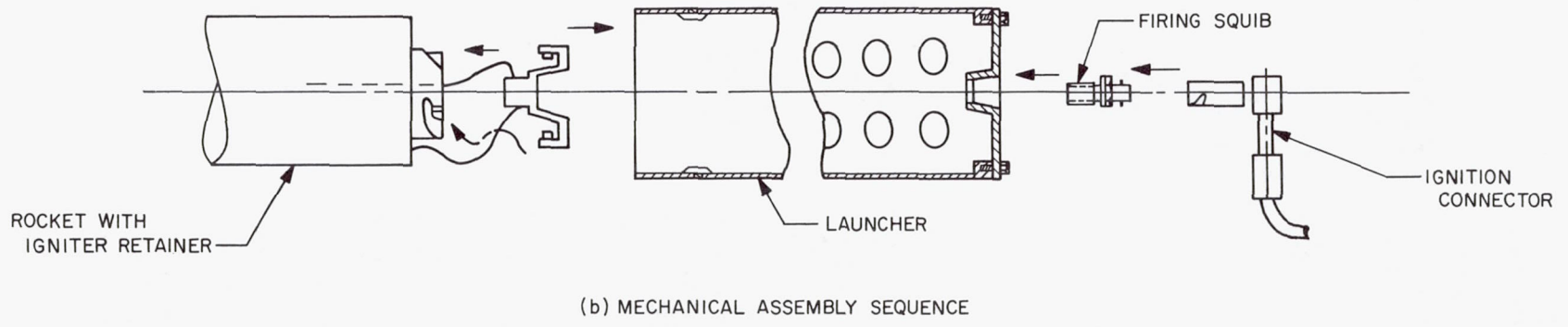
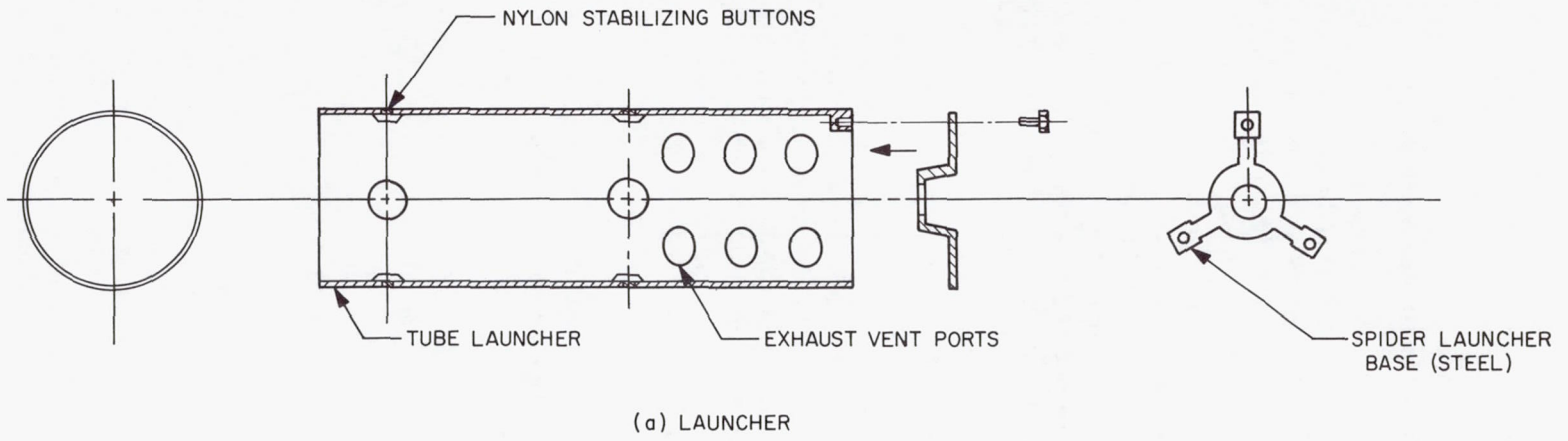


Fig. 11. Exploded view of the system: (a) launcher, (b) mechanical assembly sequence, and (c) rocket broaching

rocket and tube wall. Further, the manufacturing tolerances required for a direct mating method would be extremely difficult and costly to achieve.

Figure 11 shows an exploded view of the system, outlining the following main components:

- (1) Launcher and spider (a).
- (2) Rocket retainer/igniter bracket and squib with ignition connector (b).
- (3) Rocket broaching the tube and leaving the retainer/igniter bracket secured to the launcher base (c).

IV. Assembly Procedure

As evolved, the three main assemblies are as follows:

- (1) Launcher and base.
- (2) Rocket motor and payload.
- (3) Retainer/igniter bracket with SCID fuses attached.

The assembly procedure begins with routing and securing the SCID fuses to the spin and main propellant chambers. The igniter/retainer bracket is then secured to the rocket motor. The motor throat is then sealed by a pressure seal, and the igniter/retainer bracket is mated to the rocket motor by means of the previously described helical slot method. The rocket motor is now dynamically balanced to ensure maximum flight stability.

After balancing, the rocket, with the attached igniter/retainer, is assembled to the launch tube. This step is accomplished by lowering the rocket into the tube, where the igniter/retainer registers and keys itself to the spider base. To secure the entire payload to the launcher, the EBW squib is inserted through a clear hole in the spider base and torqued into the igniter/retainer, thus effectively clamping the payload against the spider and functioning as a fastener as well as a pyrotechnic device. The squib is provided with an O-ring, seated between the underside of the squib hex head and the spider, which ensures adequate sealing capability against ignition pressures. Following installation of the squib, the ignition connector is mated to the squib, and the system is ready for operation. (The foregoing procedure presupposes that the launcher with payload is secured by some mechanical

means to a structure that imparts the necessary inertia and support for firing.)

V. Operation of Spin-Up Launch Mechanism

At the signal to fire, the squib initiates the manifold charge located in the igniter/retainer bracket. Simultaneously, ignition takes place in the spin and main propellant chambers by means of the SCID fuse. Since the fuse burns at a rate of 22,000 fps, there is essentially no time delay from the manifold to the propellant chambers. The SCID fuse to the spin chamber is routed through the exit nozzles and ignites the solid propellant. Since the SCID fuse carbonizes completely during burning, there is no physical barrier to the exhaust gases passing through the spin nozzles. As spin-up begins, the initial impulse of the spin motors overcomes the retainer springs, and the rocket motor begins a clockwise rotary movement. The helical slots in the motor ride off the retainer pins, allowing the motor to reach a full spin rate. As the spin nozzles are canted at 30 deg to the longitudinal axis of the motor, forward as well as rotary motion takes place. By the time the main motor provides actual thrust, therefore, the payload has already traversed approximately 5 in. along the launcher. At this point—approximately halfway along the tube—the rocket motor achieves full thrust and continues onward until the tube is broached.

It is pertinent to mention that there is a minimum of free-floating debris in the tube and surrounding area following ejection of the rocket. Further, all mechanical parts are secured to the launcher and all pyrotechnic components are consumed in the launch; therefore, little if any damage will be sustained by the surrounding structures.

VI. Conclusions

The foregoing method for stowing, igniting, spinning, and launching a small rocket has resulted in successful performance under full flight conditions. The integrated rocket spin-up launch mechanism is extremely compact, lightweight, and unsophisticated in loading and handling demands. Reliability requirements of the design have been met in all aspects, and it is considered a very significant aid to rocketry research.

The Behavior of Lubrication System Components in a Vacuum Environment*

Donald H. Buckley
NASA Lewis Research Center
Cleveland, Ohio

Studies have been conducted in a vacuum environment with various lubricants and the material to be lubricated. Evaporation experiments have been conducted with various fluids, greases, inorganic compounds and soft metals. Friction, adhesion, and wear experiments have been conducted with the various materials used in lubrication systems. The results of these studies have indicated that, while relatively high rates of evaporation may be obtained for conventional oil and grease lubricants, these materials may be effectively utilized if concepts such as molecular flow seals are used to reduce evaporative losses. Further, for prolonged exposure to vacuum environment, many inorganic compounds and soft metal films have potential usefulness. In addition to evaporation losses, concern must be given to the type of lubricant that is used. With conventional lubricants, degassing of the fluids can present a problem. The results of sliding friction experiments in a vacuum environment indicate that there are basic metallic structures that have markedly superior friction wear and less tendency to adhere than bearing materials now conventionally used. Selective alloying of these metallic structures could be effectively used to prepare alloys specifically designed for use in lubrication mechanisms.

*Presented as part of the panel discussion, "Friction, Lubrication, and Bearings in Space."

I. Introduction

In any lubrication system there are essentially two major components. These are the material surface to be lubricated and the lubricant. This applies to such complex systems as instrument bearing and gear assemblies as well as to such commonplace devices as latches and hinges. While the two basic components will generally remain relatively unchanged (namely, some type of lubricant and a material to be lubricated) the environment in which the system must operate may change. The environment may be normal air at atmospheric pressure and room temperature, cryogenic fluids, a corrosive medium, operation at extremely high temperatures, or a vacuum environment simulating space conditions. The task, then, of understanding the behavior of lubricating systems and their operation in various environments becomes one of understanding the influence of that environment on the lubrication system components.

The vacuum environment of space differs from the normal atmospheric environment in two major respects. First, the ambient pressures are appreciably reduced, and second, there is a lack of oxygen. There are other factors in a space environment, such as radiation, solid particulate matter, and ionized and atomic species of gases. These latter characteristics are, because of their levels and concentrations, of only second-order importance to lubrication systems.

The reduced ambient pressure of a space environment has two major effects on the lubricants in lubrication systems. It will degas the lubricant and will enhance evaporation. Degassing will remove such gases as oxygen and water vapor. These dissolved species have been shown to have a beneficial influence under severe boundary lubricating conditions (Ref. 1). Evaporation may be a problem, particularly with organic oils and greases, since complete evaporation would result in the loss of one component of the system.

The absence of oxygen in a space environment could result in cold-welding of mechanical components where lubricants are not present or have evaporated. Present-day lubrication concepts include the presence of normal surface oxides and adsorbates on mechanical parts as a component of the integrated system.

The objective of this presentation is to examine the effects of a vacuum environment on the two major components of a lubrication system, the lubricant and the material to be lubricated. Some effects of vacuum on

lubricants to be examined will include evaporation, degassing, and adherence of solid lubricant films. With respect to the material to be lubricated, some of the properties to be examined will include the effects of reduced pressures, clean surfaces, metal structure, and selective alloying.

II. Test Apparatus

A typical vacuum apparatus used in the measurement of friction and wear is shown in Fig. 1. The basic elements of the apparatus were the test specimens (2½-in.-diameter flat disk and 3/16-in.-radius rider) mounted in a vacuum chamber. The disk specimen was driven through a magnetic drive coupling. The coupling consisted of two 20-pole magnets spaced axially 0.150 in. apart with a 0.30-in. diaphragm between magnet faces. The drive magnet outside the vacuum system was coupled to a low-speed electric motor. The driver magnet was completely enclosed with a nickel-alloy housing (cutaway in Fig. 1) and was mounted at the upper end of the shaft within the chamber. The disk specimen was at the lower end of the shaft.

The rider specimen was supported in the specimen chamber by an arm mounted by gimbals and sealed by a bellows to the chamber. A linkage at the end of the

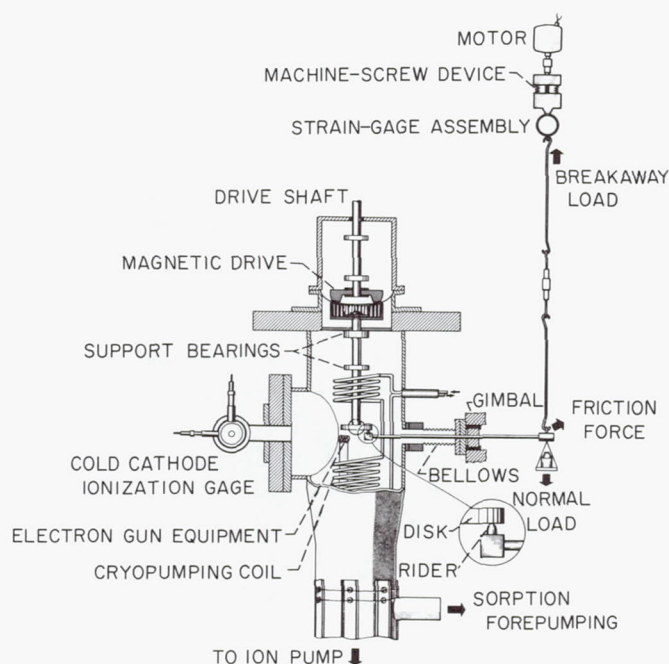


Fig. 1. Vacuum friction apparatus

retaining arm away from the rider specimen was connected to a strain-gage assembly. The assembly was used to measure frictional force. Friction coefficients reported could be determined to within ± 0.005 . Load was applied through a dead-weight loading system. Directly opposite the load (at 180 deg) was a strain-gage assembly for measuring adhesion forces.

Attached to the lower end of the specimen chamber was a 500-liter/sec ionization pump and a vacuum forepump. The pressure in the chamber adjacent to the specimen was measured with a cold-cathode ionization gage. Also in the apparatus was a diatron-type mass spectrometer (not shown in Fig. 1) for determination of gases present in the vacuum system. A 20-ft, 5/16-in.-diameter stainless steel coil was used for liquid-nitrogen and liquid-helium cryopumping of the vacuum system. The vacuum chamber and specimens were baked out at 200°C for 16 hr prior to each experiment.

III. Results and Discussion

A. Lubricants

The most severe effect that a vacuum environment simulating space conditions can generally have on lubricants, particularly organic oils and greases, is to markedly accelerate their evaporation rates. Detailed studies have been conducted in a vacuum environment simulating space conditions to determine the evaporation rates of various potential lubricating materials. These studies have been conducted under conditions such that the most severe type of evaporation is simulated; that is, there is no restriction to the evaporation process and, for the molecules leaving the surface, there is no return to the parent evaporating material. In the course of these studies, many experiments have been conducted with various organic, inorganic, and metallic lubricating materials (Refs. 1-3). Figure 2 presents some summary data obtained for various potential lubricating materials. This figure indicates the relative evaporation rates for various potential lubricants.

The organic materials of oils and greases have the highest rates of evaporation. The inorganic compounds, such as molybdenum disulphide, have some of the lowest rates of dissociation or evaporation. Some metallic films, such as gallium, indium, and tin, have extremely low evaporation rates at moderate temperatures. The evaporation experiments of Fig. 2 were all conducted at ambient temperatures of 200 to 400°F. At significantly higher temperatures or temperatures above 400°F, the

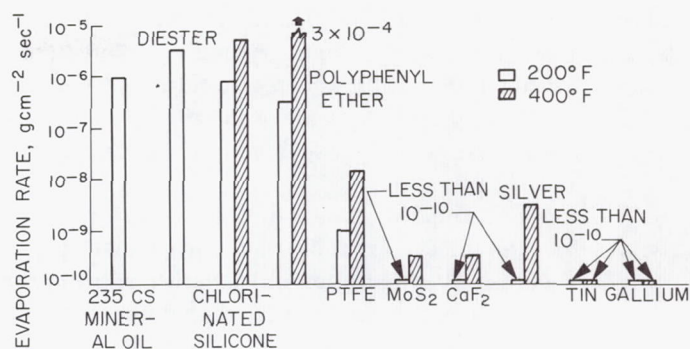


Fig. 2. Evaporation rates for various materials in vacuum. Ambient pressure, $10^{-6} - 10^{-7}$ torr

evaporation rates for the various lubricating materials can be expected to increase. Further, for some inorganic compounds, dissociation may occur much more readily.

From the data presented in Fig. 2, we can readily see that, for long-time space applications, it would certainly be desirable to utilize inorganic or metallic film materials as lubricants. While these materials have much lower evaporation rates than conventional oil and grease lubricants, they also have some notable limitations. Normally these materials are applied as thin films to the surfaces to be lubricated (Refs. 4, 5, and 6). These films then have finite endurance lives, which frequently cannot be accurately predicted. In space mechanisms we must have the maximum in reliability. Therefore, a means for considerable improvement in the reliability of such coatings would be extremely helpful.

One of the most severe limitations of the presently used solid films is their poor adherence to the component to be lubricated. In a vacuum environment, where outgassing of both substrate and coating can take place, the problem is even more critical. Techniques are being currently developed for the application of metallic and inorganic compounds without the use of binders and with markedly superior adherence to presently used coatings (Refs. 5 and 6).

In using conventional organic oil and grease lubricants, a number of techniques have been devised to reduce the loss of lubricants due to the evaporation from a space mechanism. One such device has been the utilization of molecular flow seals. The use of molecular flow seals can markedly reduce the evaporative loss of oil and greases from components to be lubricated. This means of reducing evaporation can be quite effective and provide for effective lubrication of mechanical components for long

periods. For example, in the *Tiros II* satellite, bearings operated successfully for over one year with a conventional ester lubricant utilizing the molecular flow seal concept (Ref. 7). This approach appears very attractive for use with conventional lubricants such as oils and greases.

With organic fluids it would be of interest to know what effect the molecular weight for a particular species of a fluid has on its evaporation characteristics. From the Langmuir equation one might predict that the evaporation rate for an oil or grease might be a function of its molecular weight. A series of evaporation experiments was conducted in vacuum with a polyalkylene glycol group of fluids in which each constituent fluid had a different molecular weight. The results of some evaporation experiments conducted in vacuum with this series of fluids are presented in Fig. 3. Examination of Fig. 3 indicates that the higher the molecular weight of the fluid, the lower is the evaporation rate. Further, Fig. 3 is a plot of evaporation rate as a function of temperature, and the higher the molecular weight of the fluid, the higher the temperature to which the fluid can be effectively utilized in a vacuum environment.

A vacuum environment simulating space conditions not only markedly influences the evaporation properties of the lubricating materials but also has a marked effect upon the removal of gaseous constituents dissolved in the lubricating materials (Ref. 8). In order to determine what

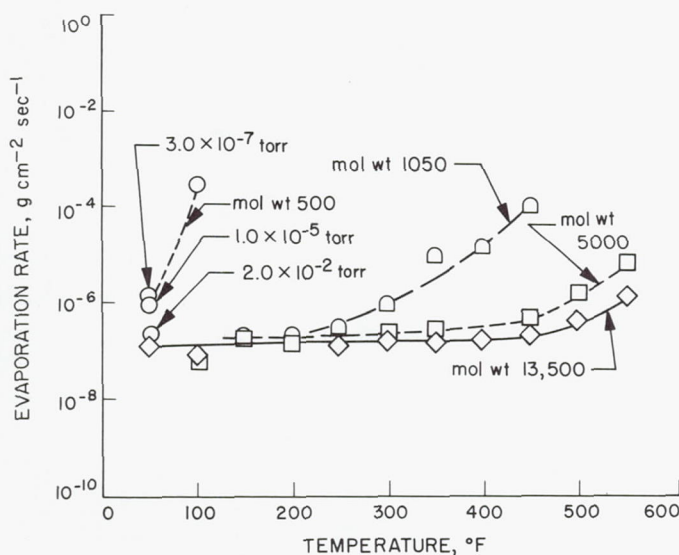


Fig. 3. Evaporation rates for various molecular weights of polyalkylene glycol. Ambient pressure, 10^{-7} torr

effect degassing or the removal of these gaseous species would have on the lubricating properties of the fluids, some experiments were conducted with fluids that were used as received, along with the same fluid after a thorough degassing to remove such gaseous species as oxygen and water vapor. Results obtained in friction and wear experiments with two typical fluids, a polyphenyl ether and a chloromethyl silicone, are presented in Fig. 4.

The data of Fig. 4 indicate that, for the polyphenyl ether, degassing markedly influences the friction and wear properties of the fluid. An increase in friction and wear was observed with the degassed polyphenyl ether fluid. With the chloromethyl silicone, however, degassing did not markedly alter the friction behavior of the fluid in lubricating nickel. With this fluid, a decrease in wear was observed with degassing.

The reason that polyphenyl ether may be markedly influenced by degassing, while the chloromethyl is not, may rest with the presence of the chlorine in the chloromethyl silicone. The chlorine in the molecule acts as an extreme pressure lubricant at the sliding interface, providing for effective boundary lubrication due to the formation of inorganic metallic chloride films. The presence of oxygen and water vapor does not improve the lubricating properties of this fluid. With the polyphenyl

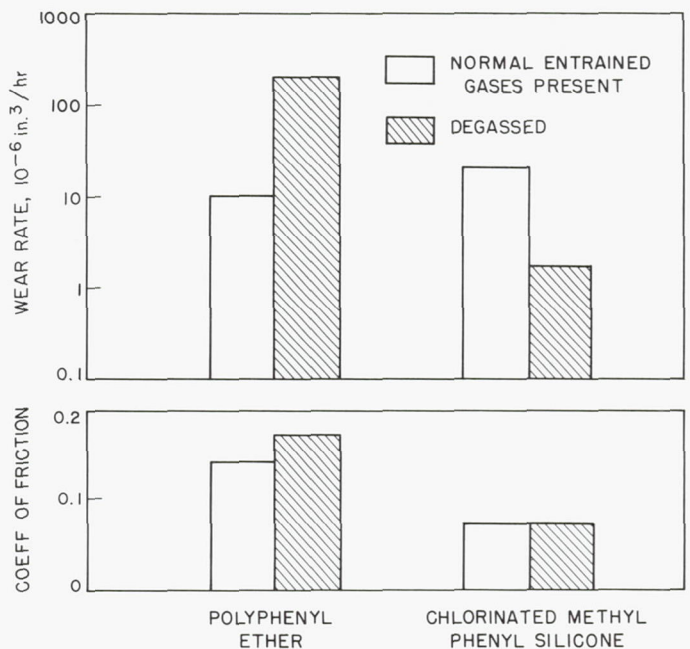


Fig. 4. Effect of gases entrained in oils on friction and wear of nickel

ether, however, no reactive atoms such as chlorine are present in the molecular configuration, and the fluid itself is inherently a poor lubricating material. Its ability to lubricate is reduced appreciably by removal of dissolved gases containing constituents that might normally react with the surface to form extreme pressure boundary lubricants.

From the results presented thus far, it becomes somewhat evident that a vacuum environment simulating space conditions certainly influences the evaporation properties of lubricants and, secondly, that the vacuum environment of space appreciably reduces the presence of dissolved gases from normal lubricants.

B. Materials for Mechanical Components of Lubrication Systems

The materials providing lubrication for mechanical components of space mechanisms are important, but of equal importance are the materials to be lubricated. These materials can take the form of bearings, gears, seals, latches, or some other mechanical device. In general, some type of lubrication is provided to adequately handle the lubrication of the mechanical component during its operation. There is, however, always the possibility that the lubricant will be lost from the system because of evaporation or some other process that could result in metal-to-metal contact. Even if a complete loss of a lubricant does not occur, and boundary lubricating conditions exist, a certain amount of metal-to-metal contact through the lubricating film will occur. Therefore, it is important to understand the friction, adhesion, and wear behavior of the mechanical component materials in the absence of lubricants.

In order to determine the influence of reduced ambient pressures on the friction properties of a material, a series of friction experiments was conducted in a vacuum environment with the very commonly used bearing steel 52100. In the initial experiments, sliding friction experiments were conducted to determine the influence of reducing the ambient pressure on friction coefficients. The results obtained in one such series of experiments are shown in Fig. 5.

The data of Fig. 5 indicate that relatively high friction coefficients, approximately 0.5, are obtained for 52100 bearing steel in sliding contact with itself. As the ambient pressure is reduced, however, the friction coefficient decreases to a minimal value in a pressure region of 10^{-4} to 10^{-6} torr. The friction coefficient then begins to increase.

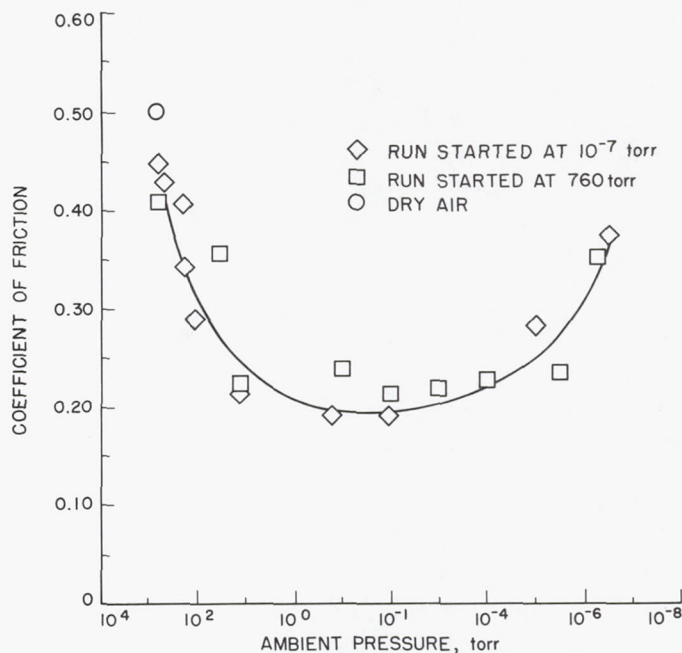


Fig. 5. Coefficient of friction for 52100 sliding on 52100 at various ambient pressures; 390 ft/min; 1000 g; 75°F

The high friction coefficient at ambient pressure of 760 torr may be associated with the presence of the higher oxides of iron on the metal surface, namely, Fe_2O_3 . As the pressure is reduced, however, less oxygen and water vapor are available for reaction with the metallic surface. As a consequence, the lower oxides of iron, namely, Fe_3O_4 and FeO , are formed. These oxides have much better lubricating properties than the higher oxide of iron (Fe_2O_3) and as a consequence a reduction in friction coefficient is observed. If, however, the pressure is further reduced, insufficient oxygen becomes available to form a continuous surface film and, as a consequence, an increase in metal-to-metal contact occurs with an increase in friction coefficient.

If a similar sliding friction experiment with 52100 steel in sliding contact with itself is conducted with liquid-helium cryopumping of the vacuum chamber to reduce the oxygen concentration, friction results similar to those shown in Fig. 6 are obtained. In Fig. 6, the initial friction coefficients, for 52100 in sliding contact with itself, were relatively low, approximately 0.5. With increasing time, however, the residual surface oxide was worn away and oxygen was not available to reform the surface film. As a consequence, the friction coefficient increased very rapidly and ultimately reached a value in excess of 5.0, at which point complete welding of the two specimens

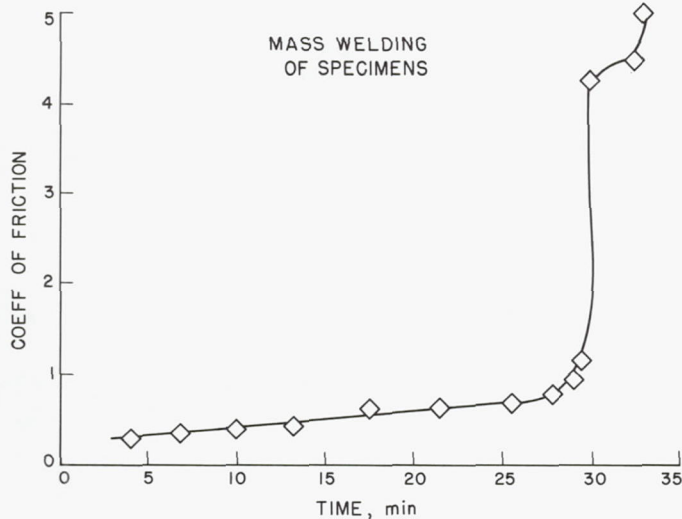


Fig. 6. Friction of 52100 sliding on 52100 in vacuum; 390 ft/min; 1000 g

occurred. The results presented in Figs. 5 and 6 with a commonly used bearing steel 52100 indicate the importance of residual surface oxides and contaminating films on the friction behavior of mechanical components of lubrication systems.

It would be desirable to have materials in mechanical components of lubrication systems with inherently low friction and wear characteristics. These materials would certainly be desirable for use in such systems to prevent the possible catastrophic welding that is observed with conventional materials such as 52100 bearing steel in the absence of lubricating films. In the course of some of our studies with simple unalloyed metals, it was found that while conventional cubic metals (body-centered cubic and face-centered cubic metals) will exhibit very high friction coefficients, adhesion, and complete welding in a vacuum environment, hexagonal metals and alloys do not exhibit the same tendency. The results obtained in some typical friction experiments with various cubic and hexagonal metals are presented in Fig. 7.

The data of Fig. 7 indicate that, for the conventional face-centered cubic metals copper and nickel in sliding friction experiments in a vacuum environment, very high coefficients of friction and complete welding of the metals will occur. With the hexagonal metals, such as beryllium, however, complete welding was not readily observed. Note particularly the relatively low friction characteristics for the beryllium.

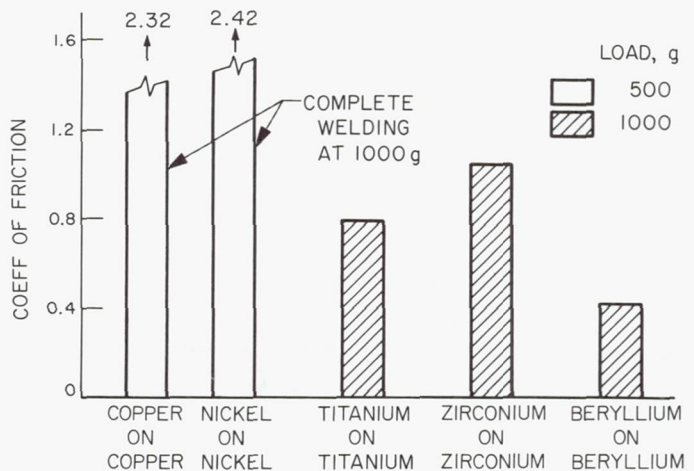


Fig. 7. Coefficient of friction for various metals in vacuum; 10^{-9} torr; 0.025 cm/sec; 25°C

It appears that crystal structure has an influence on the friction properties of metals in contact. Any metal that exhibits allomorphic characteristics (that is, transforms from one crystal form to another) should exhibit marked changes in friction properties with changes in crystal structure. A metal of considerable interest for lubrication systems applications is cobalt, which has an allomorphic transformation. Cobalt transforms from a close-packed hexagonal to a face-centered cubic structure at a temperature of approximately 800°F. In order to determine whether the transformation in cobalt from the hexagonal form to the cubic form would, in fact, exhibit an influence on friction properties for cobalt, friction experiments were conducted in vacuum with cobalt in sliding contact with itself. Results of one such series of experiments are presented in Fig. 8.

The data of Fig. 8 indicate that with cobalt in its hexagonal form the friction coefficients are relatively low, approximately 0.3. It is interesting to note that these friction coefficients are lower than those obtained with the 52100 steel in sliding contact with itself in air at 760 torr. If, however, the temperatures are increased to near that of the crystal transformation from the close-packed hexagonal to face-centered cubic form, a marked increase in friction is observed. Ultimately, complete welding of cobalt to cobalt occurs. If, however, after welding, the specimens are separated and allowed to cool to room temperature, the initial friction coefficients obtained for cobalt are once again observed. These results indicate the reversibility of the cobalt crystal transformation.

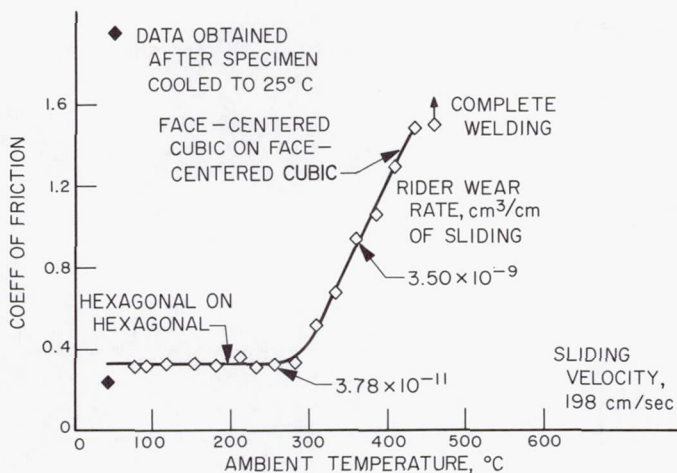


Fig. 8. Coefficient of friction for cobalt sliding on cobalt in vacuum at various temperatures; 10^{-9} torr; 1000 g

In addition to the friction coefficients being markedly influenced by the crystal transformation from a close-packed hexagonal to a face-centered cubic form, wear for cobalt is also markedly influenced. Wear measurements made at two temperatures, one for cobalt and its hexagonal form, and the second during the transformation, indicate a hundred-fold difference in the adhesive wear rates for cobalt in the two crystalline forms. The data of Fig. 8 then, with those of Fig. 7, indicate that crystal structure certainly does influence the friction and wear behavior for metals in the absence of surface films.

The desirable friction and wear characteristics for the hexagonal metals were deemed worthy of further investigation. Detailed studies were, therefore, conducted with various hexagonal metals in sliding contact with themselves and conventional bearing steels in a vacuum environment to determine whether any differences would exist in the friction properties for various hexagonal metals. In the course of these studies, a relationship was found to exist between the friction properties of various hexagonal metals and their crystallographic slip behavior. Detailed studies with single crystals of hexagonal metals with various crystallographic planes oriented parallel to the interface indicated that, in hexagonal metals, the preferred slip planes (the slip planes of highest atomic density) exhibited the lowest friction characteristics. Since crystallographic slip behavior in hexagonal metals is dependent upon lattice parameters, it was felt that some relationship must exist between friction coefficients and the lattice parameters for hexagonal metals. Detailed

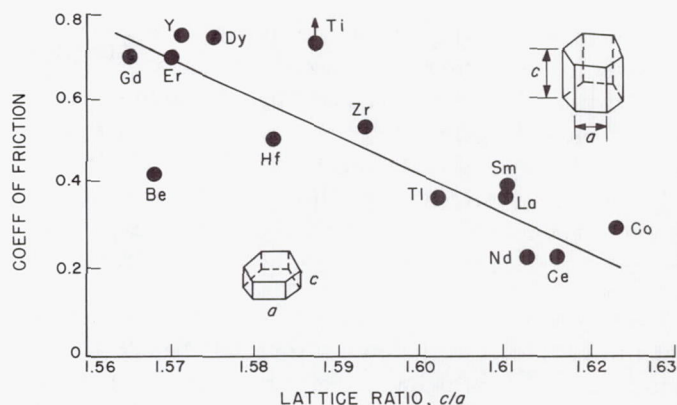


Fig. 9. Friction of various hexagonal metals; 10^{-9} torr; load, 1000 g; 390 ft/min, on 440C steel

friction experiments with a number of hexagonal metals having various lattice parameter ratios were conducted in a vacuum environment. The results of some of these experiments are presented in Fig. 9.

In Fig. 9 the friction coefficients for various hexagonal metals in sliding contact with 440-C stainless steel are plotted as a function of the interbasal planar spacing over lattice parameter a for various hexagonal metals. The term "interbasal planar spacing" is used rather than the c/a lattice ratio because, for a number of hexagonal metals in the rare earth series, more than a single set of basal planes are present in the cell. The results of Fig. 9 indicate that a direct relationship exists between the lattice parameters of hexagonal metals and their friction properties. Slip behavior, during mechanical deformation, can be correlated for various hexagonal metals with the c/a lattice ratio. Those metals exhibiting c/a lattice ratios near the ideal stacking sequence for atoms in hexagonal metals, namely 1.633, exhibit predominantly basal slip mechanisms, while those which deviate considerably, such as titanium, zirconium, and hafnium, exhibit predominantly prismatic and, secondarily, pyramidal slip mechanisms.

Although beryllium has a lattice ratio that deviates considerably from the ideal stacking ratio, it slips predominantly on basal planes. This fact accounts for its relatively low friction coefficients despite its position on the curve of Fig. 9.

The data of Fig. 9 are certainly interesting. However, the question that arises is how these data can be effectively utilized to reduce the friction properties and adhesion tendencies of bearing materials. A practical

application of the curve presented in Fig. 9 might be to selectively alloy various hexagonal metals to improve their friction characteristics. For example, titanium is a metal frequently considered for use in space systems. However, because of mechanical strength considerations, it is most frequently used in the form of cubic alloys. Titanium has notoriously poor friction and wear properties and is extremely prone to cold-weld.

There are, however, a number of alloying elements that can be added to titanium to expand the c/a lattice ratio in titanium, bringing it closer to the ideal stacking sequence for basal slip hexagonal metals such as cobalt (Ref. 9). Some of these alloying elements are oxygen, tin, and aluminum. Experiments were conducted, therefore, with titanium to which varying percentages of two elements were added. In one series of experiments, a simple binary series of titanium-tin alloys was prepared, and, in the second series of experiments, a series of titanium-aluminum alloys was prepared. The alloying material was added to titanium to maximum solubility. Care was taken to avoid the formation of second phases. X-ray determinations were made for the lattice parameters of the hexagonal binary titanium alloys formed. Friction experiments were also conducted with these alloys. Lattice parameters and friction coefficients for these alloys in sliding contact with themselves are presented in Fig. 10. The results of Fig. 10 indicate that as the c/a lattice ratio for titanium-tin and titanium-aluminum alloys increases, the friction coefficient decreases. These results would indicate, then, that selective alloying can be utilized to reduce the friction properties of metals.

In addition to altering the lattice parameters for hexagonal metals by selective alloying, the crystal transformation temperatures for hexagonal metals can also be altered in some instances. For example, the addition of 25 wt % molybdenum to the hexagonal metal cobalt can increase the transformation temperature appreciably. If a hexagonal metal is considered for use at somewhat elevated temperatures and it is desirable to retain the hexagonal crystalline form to these higher temperatures, selective alloying with elements such as molybdenum may be effectively utilized to achieve desirable friction properties over a broader temperature range. Some simple binary cobalt-molybdenum alloys were prepared. A 25 wt % molybdenum in cobalt alloy was used in sliding friction experiments to determine whether, in fact, elevating the crystal transformation temperature would have an effect on friction properties. The results obtained in some sliding friction experiments, together with data for unalloyed cobalt, are presented in Fig. 11.

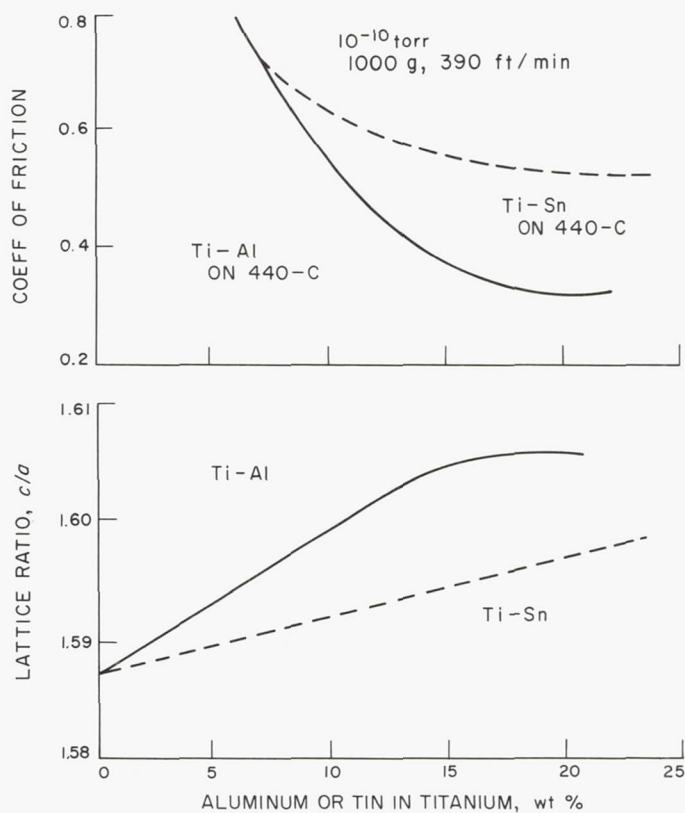


Fig. 10. Friction and lattice ratio (c/a) for titanium alloys

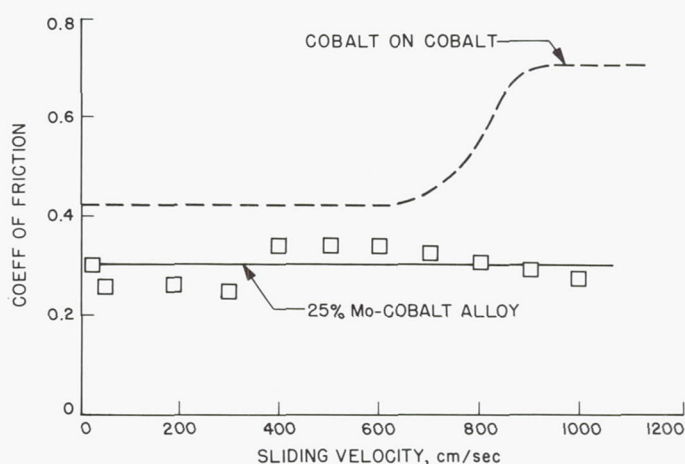


Fig. 11. Coefficient of friction for molybdenum-cobalt alloys sliding on disks of the same material in vacuum; 10^{-9} torr; 1000 g; 25°C

The data of Fig. 11 present the coefficients of friction for the cobalt-molybdenum alloy as a function of sliding velocity. With increased sliding velocity, increases in interface temperature occur. In a range where a marked

change in friction properties for cobalt was observed in sliding contact with cobalt, a change in the friction properties for the cobalt molybdenum alloy did not occur. These results, then, indicate that such selective alloying techniques can be effectively utilized to retain a desirable hexagonal form for metals over a broader temperature range.

The results presented in Figs. 10 and 11 indicate that by selective alloying we can improve the friction behavior characteristics for elemental metals. While these studies were conducted with simple binary alloys, which by no means represent bearing compositions or materials for gear applications, they do, however, point to a direction in which the formulation of alloys may be made with the intent of the alloy being specifically designed for lubrication systems. That is, the alloy has inherently good friction, wear, and low-adhesion properties, which are designed into the alloy in its formulation. This would seem to be a much more desirable approach to the use of materials in lubrication systems than the most frequently and conventionally used technique of simply obtaining alloy compositions from other scientific fields of endeavor, such as the tool steel industries. In a vacuum application or extreme vacuum environment in space conditions, it certainly would be desirable to have the low friction, wear, and adhesion properties of the hexagonal metals and alloys in the event of lubrication failure.

In addition to the alloying concepts provided in Figs. 10 and 11, other mechanisms have been effectively utilized to reduce the friction, wear, and adhesion properties of alloys. Such concepts as alloying with inclusion compounds in materials to reduce the friction properties have been effectively utilized. For example, sulphur has been effectively added to conventional bearing steels to replace, in the process of sliding contact, the normally formed metal surface oxides (Ref. 10). In these alloys, an inclusion compound is built into the alloy structure to replace surface films when they are worn away. Another alloy concept that can be effectively used to reduce friction properties of materials in a vacuum environment is the old lead copper bearing concept. This concept, however, has been updated to include some high-temperature alloy systems and solid lubricants (Ref. 11). Again, this type of selective alloying approach can be effectively

used to reduce the friction, wear, and adhesion behavior of materials in contact. This not only applies to materials in contact in the absence of lubrication but also under boundary lubricating conditions where some metal-to-metal contact will occur.

IV. Concluding Remarks

The discussion in this presentation has dealt with the two major components involved in lubrication systems intended for use in a space environment: the lubricant and the material to be lubricated.

With respect to the lubricant, concern must be given to the accelerated evaporation of lubricant materials in a vacuum environment simulating space conditions. Further, the influence of the vacuum environment on degassing conventional lubricating materials, such as oils and greases, can also markedly alter their performance characteristics. In addition, with the application of solid film lubricating materials such as inorganic compounds and soft metallic films, extreme care must be taken to provide for adequate adherence of these films to the substrate materials. Adherence of these coatings to the substrate material will determine to a large extent the effectiveness of these coatings in providing lubrication for long periods.

In reference to the materials to be lubricated, a considerable improvement in friction and wear and a reduction in the adhesion tendencies may be obtained from materials of lubrication systems, if selective alloying or duplex alloying concepts are utilized. Conventional bearing materials will weld readily in a vacuum environment simulating space conditions. There are, however, alloy structures with basic hexagonal crystal forms which have much less tendency to cold-weld in a vacuum environment. These systems certainly offer considerable promise for use in advanced spacecraft devices. Data have been presented for the two components of a lubrication system. It must be indicated, however, that an interrelationship between the lubricant and the material to be lubricated exists, and this must also be considered in any study of lubrication systems.

References

1. Buckley, D. H., Swikert, M. A., and Johnson, R. L., "Friction, Wear and Evaporation Rates of Various Materials in Vacuum to 10^{-7} mm Hg," *ASLE Trans.*, Vol. 5, pp. 8-23, 1962.
2. Buckley, D. H., and Johnson, R. L., "Degradation of Polymeric Compositions in Vacuum to 10^{-9} mm Hg in Evaporation and Sliding Friction Experiments," *SPE Trans.*, pp. 306-314, October 1964.
3. Buckley, D. H., and Johnson, R. L., *Evaporation Rates for Various Organic Liquid and Solid Lubricants in Vacuum to 10^{-8} Millimeter of Mercury at Temperatures from 55 to 1100°F*, NASA TN D-2081, National Aeronautics and Space Administration, Washington, D. C., 1963.
4. Atlee, Z. J., Wilson, J. T., and Filmer, J. C., "Lubrication Vacuum by Vaporized Thin Metallic Films," *J. Appl. Phys.*, Vol. 11, pp. 611-615, 1940.
5. Spalvins, T., and Buckley, D. H., "Vapor Deposited Gold Thin Films as Lubricants in Vacuum (10^{-11} mm Hg)," *J. Vac. Sci. Technol.*, Vol. 3, No. 3, 1966.
6. Spalvins, T., Przybyszewski, J. S., and Buckley, D. H., *Deposition of Thin Films by Ion Plating on Surfaces Having Various Configurations*, NASA TN D-3707, National Aeronautics and Space Administration, Washington, D. C., November 1966.
7. Weinreb, M. B., *Results of Tiros II Ball Bearing Operation in Space*, Meteorology Branch, NASA Goddard Space Flight Center, National Aeronautics and Space Administration, Washington, D. C., 1961.
8. Buckley, D. H., Johnson, R. L., and Brainard, W. A., *Influence of Entrained Gases and a Halogen Additive on Boundary Lubrication of Four Oils at Temperatures to 1000°F*, NASA TN D-2686, National Aeronautics and Space Administration, Washington, D. C., 1965.
9. Buckley, D. H., "The Influence of Various Physical Properties of Metals on Their Friction and Wear Behavior in Vacuum," Paper presented at the National Metal Exposition and Congress of the American Society for Metals, Oct. 31-Nov. 3, 1966, Chicago, Ill. (To be published in the May 1967 issue of *Metals Eng. Quart.*)
10. Buckley, D. H., and Johnson, R. L., *Friction and Wear Characteristics of Some Sulfur-Modified Steels and Nickel-Aluminum Alloys in Vacuum to 10^{-9} Millimeter of Mercury*, NASA TN D-2307, National Aeronautics and Space Administration, Washington, D. C., 1964.
11. Boes, D. J., and Bowen, P. H., "Friction-Wear Characteristics of Self-Lubricating Composites Developed for Vacuum Service," *ASLE Trans.*, Vol. 6, pp. 192-200, 1963.

Lubrication As Part of Total Design*

Francis J. Clauss
Lockheed Missiles and Space Company
Sunnyvale, California

Oils and greases, if properly selected, may solve many lubrication problems in space. Ball bearings must also be properly selected and must be protected from contamination. Operating temperatures should be accurately specified. For heavily loaded gears, MoS₂ films have been used successfully.

Since the middle of 1959, when I first became involved in lubrication at Lockheed, I've had the opportunity both to conduct research in this area and to advise many programs on the lubrication of spacecraft mechanisms. This morning I'd like to summarize some of my thoughts and observations, discuss some problems and their cures, and perhaps increase your appreciation for the importance of lubrication as part of *total* design.

I find it unsatisfactory and not very helpful if one avoids discussing actual hardware, yet security restricts me from identifying specific systems. Such being the case, let me talk about common components, beginning with miniature ball bearings. These are generally operated under light loads and at speeds ranging up to 24,000 rpm, which is the top speed you can get with a

2-pole ac motor operating off a 400-cps power supply. The bearings must usually operate at ambient temperatures between -40 and $+200^{\circ}\text{F}$, although sometimes they have to start up at temperatures as low as -100°F . Sometimes they're in hermetically sealed enclosures, but more often they're in packages that are sealed against dust.

Here's a quick summary on how to lubricate them for the usual conditions: Use a properly selected oil or grease. How long will an oil or grease last in space? Despite some stories you've heard about oils and greases being sucked up by the space vacuum almost as soon as the parts get into orbit, we've operated ball bearings with certain oils and greases for over 4 years in vacuum without stopping to relubricate them even once. Let me caution you that many other oils and greases failed in less than 6 months under the same conditions. So get help in making your selection.

*Presented as part of the panel discussion, "Friction, Lubrication, and Bearings in Space."

Don't go to bonded molybdenum disulfide (MoS_2) films or sapphire balls *on ball bearings* unless you really have some special requirements and can take the necessary precautions. A number of years ago we tried MoS_2 films and sapphire balls in ball bearings in a prototype unit for a data link switch. The sapphire balls shattered under dynamic operating loads, and the MoS_2 film flaked off and jammed the bearings. Oil lubrication has worked much better.

Next, don't specify requirements that aren't really needed. If bearings must start up at low temperatures, there are oils that don't freeze even at -100°F , but their lifetimes and load-carrying capacities are less than other oils that would otherwise be preferable. Or, if the least amount of oil contamination can't be tolerated on nearby optical surfaces, reinforced Teflon retainers or even MoS_2 films can be used if the other conditions allow it, but oils and greases would give better lubrication.

A short time ago I consulted on a sine-function generator that was unable to pass the 14-day qualification test. This unit has a small, 26-v synchronous motor operating at 8000 rpm through a very large gear reduction. I suggested changing from crown-type retainers in the ball bearings to Synthane retainers and lubricating with F-50 oil. The unit then not only passed the 14-day "qualification test," but the motors and gearheads from 2 qualification units subsequently ran an additional 30 days at altitude with no signs of failure. In three flights to date, there have been no failures.

Note that my recommendations were not just for a certain oil, but also for a certain type of bearing retainer. This is important. You not only must use the right lubricant, but you must also use it properly. If you're going to use oil in a bearing, you have to keep it there. One of the most serious problems in precision rotating equipment today — one that the Navy recognized several years ago with a failure in the Polaris fire-control system — is oil migration *away* from the points where it's needed, particularly when the units must be stored for some time before use. One possible solution is to use barrier films. These are complex organic fluorocarbons that have low enough surface energies to prevent oils from crawling over them. Although effective, they're difficult to use and the quality control measures are horrendous. If you'll direct your attention to the ball bearing retainer, you can avoid these problems.

Most ball bearings have crown-type retainers of pressed steel. The principal reason is that they're cheap, and for

many applications they're adequate. They also cause minimum drag within the bearing. But neither they, nor the ribbon-type retainer, are very good for keeping oil in a bearing. Machined retainers of Synthane, which is a porous phenolic laminate, or of microporous sintered nylon, are much better. Oils can be vacuum-impregnated into these retainers for later release as lubrication is needed. Oil-impregnated retainers of Synthane and microporous nylon are standard on the spin-axis bearings for most gyroscopes. The disadvantages of these retainers are that they cost a few cents more and they're difficult to make for bearings smaller than an R3 size (3/16-in. shaft diameter). Note that I said difficult, not impossible. Synthane retainers are a standard item with the bearing manufacturers, so you're not asking for something new when you specify them.

This leads me to the next problem — and that's *getting* ball bearings. Things were different a few years ago, but right now the bearing industry is operating night and day to fill orders. Procurement takes over a year on some bearings, and delivery in six months is more the rule than the exception. So review your requirements early, and place your orders as soon as possible. If you have two alternate designs and don't plan to finalize your choice for another few months, order bearings for both designs now. Ball bearings aren't terribly expensive, but delays are.

The next point is to avoid contamination. It's an understatement to say that ball bearings don't run well with dirt in them. Some years ago we had a short-time failure on a flight unit, and since no one knew at the time how long the oil would really last, it seemed all too easy to call it a lubrication failure. I had run only a few tests at the time, but I was convinced that the oil was good enough for a much longer life — and subsequent testing has indeed borne this out. I therefore insisted it must be something else, and together with the engineers we started looking for other causes. We found that the unit was so mounted on the bird that fine debris during separation could get through an opening and into the bearings. When this was corrected, the unit operated satisfactorily with the original type of oil.

Another point is temperature. Your designs call out operation at specified *ambient* temperatures. Your specifications don't identify the actual *operating* temperatures. Everyone knows that motors heat up during operation, sometimes getting so hot you can't put your hand on them. Without air to cool them, motors heat up even more in vacuum. If you just run short-time qualification tests at the specified ambient temperatures, you're likely

to miss some problems here unless you've also put thermocouples at critical points on your unit. If your upper ambient temperature is specified as 200°F, and if your motor heats up another 150°F in vacuum, and if your oil or grease starts to break down at 300°F, you'd better know it and do something about it. One of the jobs I had a few years ago was to consult with another aerospace company with this same problem. The solution was a relatively minor redesign to carry away the heat from the motor more effectively, and the *same* grease that had previously failed now worked perfectly.

Gears are another common type of component, and some of the same comments I made regarding the lubrication of bearings are applicable here. But with gears, one has the possibility of making them with a number of plastic, self-lubricating materials, such as MoS₂-filled nylon, reinforced Teflon, phenolic laminates, and others. Such materials have worked satisfactorily in several units developed at Lockheed. Metal gears are more common, though, and they're stronger and can withstand heavier loading.

In lubricating metal gears, one should recognize that many oils and greases that work well under light loads and hydrodynamic lubrication fail under heavy loads, where we operate under boundary lubrication. Hydrodynamic lubrication occurs when mating surfaces are kept apart by a thin film of fluid, such as an oil film or, in the case of gas bearing, a gas film. But if the load is heavy, a fluid film may not be able to support it, and the two surfaces are then pushed into contact with one another, and we have boundary lubrication. In this case we must rely on surface films of solids to keep the metals apart. There are many ways to provide solid film lubricants, and I haven't time to discuss them all, but only to illustrate their use.

Some time ago we were failing heavily loaded gears on a drive system, and the problem was solved by burnishing MoS₂ onto the gear teeth and adding a dispersion of MoS₂ to the grease. We've also used a MoS₂-filled grease for engine gimbal bearings, which are heavily loaded journal bearings and must operate during engine restart in space. In another instance, bonded MoS₂ films were successfully used on exposed gears on a solid array drive mechanism.

Again, other design and fabrication details are important. Some years ago I worked with a group to solve a bearing problem. We weren't really happy about the

gears either, but as the gears had never failed and the bearings had, and because a quick-fix was necessary to make the flight schedule, we were asked not to change the gears. Well, as you might have guessed, the very next qualification unit suffered a gear failure. On checking further into cause of the failure, we found that one of the gears had been replaced before qual testing, because of wear, but that nothing had been done about the improper alignment that had caused it. No wonder the replacement gear also wore rapidly! If we buy a new set of tires, don't we check the wheel alignment and balance, especially if we got poor mileage out of our last set of tires? A year or two later on another prototype drive system, gears again were failing. The responsible engineer recognized that the failures were caused by poor alignment and workmanship, and he insisted that the vendor correct them, and the unit has since flown successfully. Be aware of this type of problem. It's one you can't cure by changing the lubricant.

Problems with contacts for transferring data signals across sliding interfaces were well demonstrated by some tests we ran years ago with the slip ring for the old 461 Program. This was a fairly conventional slip ring, with rings of electrodeposited silver and wire brushes of a precious metal alloy. It worked fine in air, but over a period of 100 hours in vacuum, the noise level increased by a factor of 30 and obscured the data signals. About that time the liquid nitrogen trap in our vacuum system warmed up, thereby releasing a small amount of diffusion pump oil into the vacuum chamber. Although the vacuum was still good, about 5×10^{-6} torr, there was still enough oil vapor to reduce the noise level to its former low value. In a later experiment we soaked up a few grams of the oil into six small discs of sintered nylon, and we mounted these with small screws to the undersides of three of the cover plates of the slip ring assembly. With this arrangement we operated over 4000 hours in vacuum with no detectable signal degradation and with no visible wear on the brushes or rings. This is a very cheap and effective way to make metal-to-metal slip rings for data transmission work satisfactorily in vacuum.

With larger brushes, typical of those used to transmit electrical power, wear problems are generally solved by using self-lubricating brush materials. This is done under normal atmospheric conditions by using silver-graphite brushes, which are familiar to many of you. The silver provides good electrical conductivity, while the graphite provides lubrication. For use in vacuum, where graphite is no longer effective, one substitutes molybdenum disulfide.

We had an opportunity several years ago to improve slip-ring brushes as part of an Air Force contract I directed on a system for transmitting about 1 megawatt of power to a large solar simulator. This was for the Mark II Space Chamber — the 200-ft-diameter chamber that the Air Force proposes to build at Tullahoma, Tennessee. Under typical service conditions involving 700 hours of operation in a vacuum of 10^{-9} torr, conventional Ag-graphite brushes wore about 0.25 in.; they badly scored and undercut the ring against which they operated, and the noise level increased by a factor of about 100. The brushes of the new alloy wore only about 0.01 in., their rings were only lightly scratched, and the noise level remained low. Since these tests, the Air Force has operated brushes of our new material in vacuum without trouble at current densities as high as 425 amp/in². The material is now being considered for several solar array, antenna, and space linkage devices.

I wish I had more information about dc motor brushes. We've used dc motors often, and the wear problems have usually been solved with brushes of graphite having MoS₂ cores or brushes with a fluoride, MoS₂, or some other doping agent dispersed in the graphite. Brushes of Ag-MoS₂ were also used in one application that I recall, and in another application we're currently evaluating our new slip-ring alloy. DC motor brushes undergo a rapid succession of make-and-break contacts at significant current levels as the motor commutator rotates, and this subjects them to a great deal of electrical erosion so that dc motor brushes are a more complex problem than brushes on continuous slip rings.

To put the matter of lubrication into its proper perspective, let me remind you of some of the alternative solutions you might also consider. Flexure joints can be

used in place of joints that pivot on bearings, provided that rotation is limited to oscillation about a central point, and such joints are being used in one model of horizon sensor I have consulted for. Harmonic drives are a good substitute for gear trains, since they minimize the wear action of gear teeth, although they do not eliminate it entirely. As an alternative to slip rings, rotary transformers are available that can transmit electrical signals with very little distortion. And as alternatives to brush-type dc motors, there are both optically commutated motors and motors with special stator windings and electronic switching that can operate off a dc supply, or one can go to an ac motor with an inverter, or even to spring-driven motors.

One last example: A few years ago a certain device was having trouble with brush wear on a dc motor, and the project engineers thought they might go to a solid-state device. As it turned out, the solid-state device to do the same job was about 3 times as big and 3 times as heavy and 10 times as expensive as the electromechanical device, even without qualification costs, and no one could really say that it would work better. The brush problem was then solved by finding a motor manufacturer who could provide a better quality product, and the program stayed with the electromechanical device.

Trade-offs must be made with both types of systems, and they are not always in favor of solid-state devices over electromechanical devices, or vice versa, nor is the proper choice clear without a thorough analysis. I hope that my comments, and those of the other speakers at this symposium, will redirect your attention and help you make more thorough analyses, and that lubrication will receive a greater appreciation as an important part of *total* design.

Surface Interaction Between Aluminum Single Crystals at 10^{-10} Torr*

Joseph Frisch
The University of California
Berkeley, California

Friction and adhesion between metallic surfaces in ultrahigh vacuum have been studied by subjecting aluminum crystals to forces of 0.1 to 10 lb at 10^{-10} torr. Surface galling, distortion, and adhesion resulted. The adhesion was apparently caused by localized interaction of asperities that "welded" together and prevented separation of the crystals.

The problem of friction and adhesion between metallic surfaces in ultrahigh vacuum is indeed an acute one, considering the difficult engineering efforts relative to space vehicles where success or failure depends entirely on reliable designs and material selection. The absence of a large body of basic knowledge on the interaction of metallic surfaces in the severe environment of space cannot be rapidly circumvented by extrapolations from known behavior under "normal" atmospheric condition. Similar problems have frequently been encountered on the frontiers of engineering; however, the simulation of the actual environment has never been as costly and difficult as the current one of providing a mock-up of space in an earthbound laboratory. It is therefore a difficult

task to evaluate the relative merit of performing experiments under actual flight conditions in space as a means of providing engineering design information. A categorical yes or no answer cannot be given, since the information on surface behavior from past vehicle flights and laboratory tests in each instance will serve as the input for the decision on where the next round of friction and adhesion tests will yield the most reliable and economical set of data.

At the University of California in Berkeley we have built a 10-in.-diameter by 10-in.-high vacuum chamber system for pumpdown to 10^{-11} torr. We have provided the capability for ion bombardment of metallic specimen surfaces, a hydraulic system with bellows feed-through for moving specimens relative to each other in the chamber, and a two-force electric strain gage dynamometer

*Presented as part of the panel discussion, "Friction, Lubrication, and Bearings in Space."

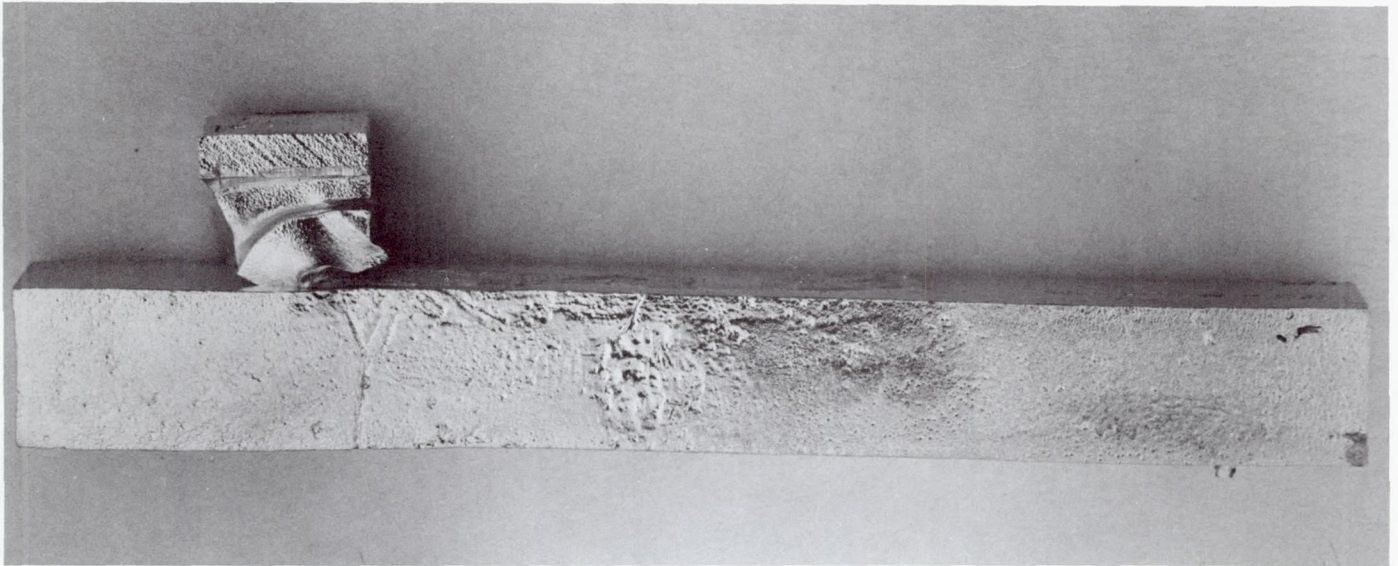


Fig. 1. Adhesion of $\frac{1}{2}$ - \times $\frac{1}{2}$ -in. aluminum single crystal surfaces after friction test at 10^{-10} torr (normal force = 10 lb)

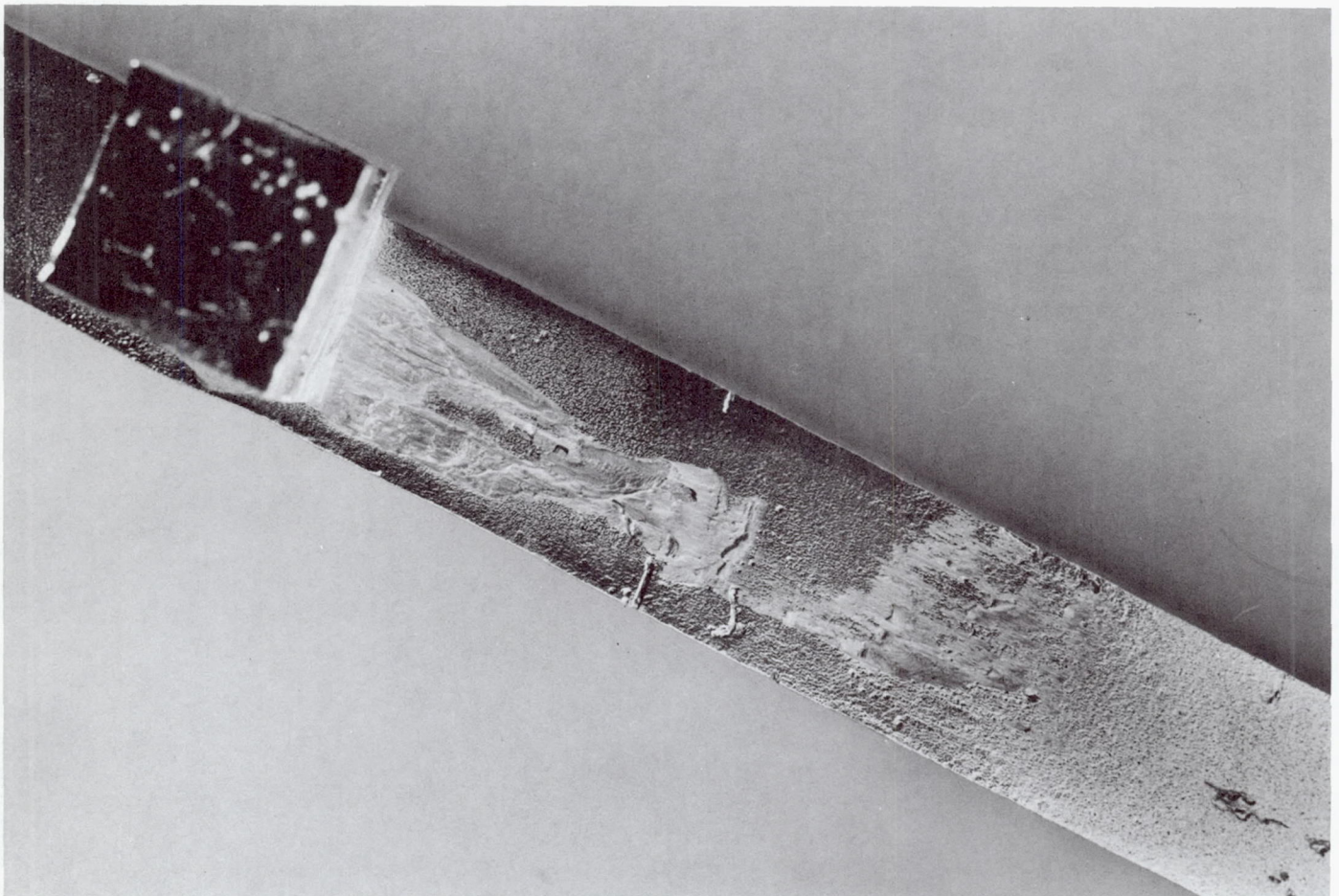


Fig. 2. Surface distortions due to "sliding friction" between two aluminum single crystals at 10^{-10} torr

which functions inside the chamber and yields data on the normal and tangential forces seen by the specimen pair during a friction test.

The initial purpose of this experimental build-up was for a study of the effect of crystallographic orientation on the magnitude of the friction coefficient using flat $\frac{1}{2}$ - \times - $\frac{1}{2}$ -in. surfaces of single crystals of pure aluminum. Flat surfaces, rather than cylinders or hemispheres, which provide line or point contact respectively, were considered a better simulation of actually encountered conditions; however, the difficulty of obtaining numerical data is considerably increased because of this geometry. Nevertheless, the qualitative results are enlightening since they show that the concept of adhesion and all its ramifications is the predominant feature of ductile surface behavior in ultrahigh vacuum.

In Fig. 1 can be seen a $\frac{1}{2}$ -in. aluminum crystal cube adhering to a $\frac{1}{2}$ - \times - $\frac{1}{2}$ -in. prismatic single crystal of 99.999% pure aluminum after it was pulled under a normal force of 10 lb. The contacting surfaces were ion-bombarded before being brought together, and the sliding action occurred within the 20-min time lapse before surface contamination could again be expected. The severe distortion of the lower portion of the cube is due to the heavy galling and large tangential forces encountered in the final stages of the test. Figure 2 shows the severe surface distortion preceding the final location of the adhering specimens; however, galling marks can also be seen at the area where the test was initiated. Indeed, it was found in subsequent tests that normal loads as low as 0.1 lb will immediately produce surface galling. Figure 3 is a closeup view of the severely distorted surface which, in fact, contributes to adhesion under

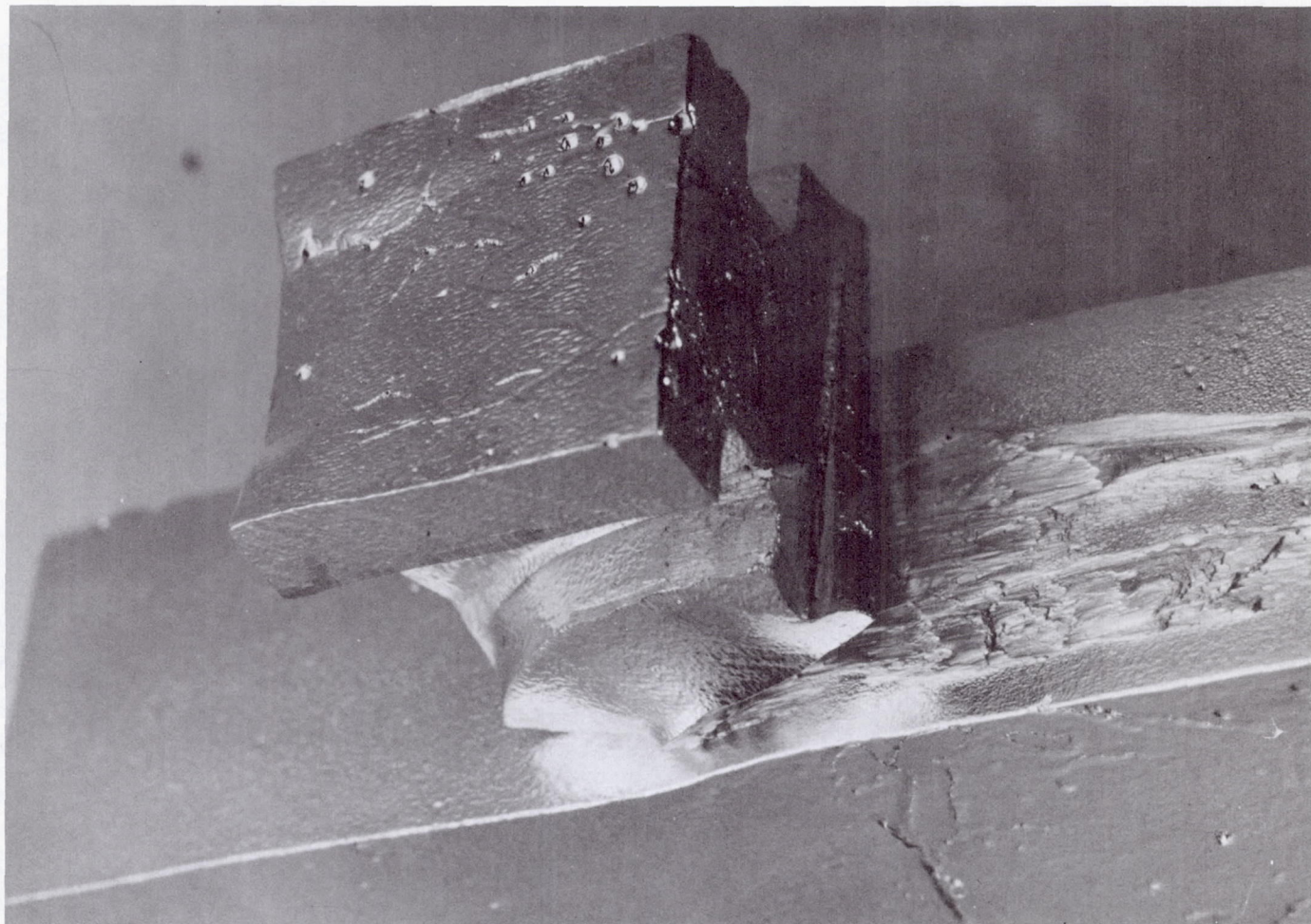


Fig. 3. Surface distortion before complete adhesion of aluminum single crystals at 10^{-10} torr

vacuum conditions. If the pulling action had stopped in this area, it is reasonable to assume that adhesion would have existed.

Figure 4 shows a side view of the leading edge at 200 magnification, and the effect of plastic deformation is well illustrated. However, the dark area of the cross section in Fig. 5 shows very clearly the severe deformation of the subsurface material, particularly at the leading edge. The contracting pair of surfaces are shown in 200 magnification in Fig. 6. The picture illustrates the fact that adhesion is not provided by a continuous bond but by localized interaction of a sufficiently large number of asperities that are "welded" together and prevent separation of the two bodies. Since the bond was not broken under a measured tensile force, the bond strength is not

known. Further magnifications up to 36,000 were obtained on a Steroscan-Electron microscope. The resulting views show the existence of discontinuities within an asperity, and the application of existing theories on the elastoplastic behavior between contacting asperities may have to be modified to account for this geometry.

In summary, the expectation for our particular research effort is a widening understanding of the mechanisms of surface behavior during friction-adhesion conditions in the ultrahigh vacuum of the space environment. The resultant knowledge, we trust, will lead to modifications of existing theoretical models and give further substance to the selection of design parameters for reliably engineered space vehicles and mechanisms.

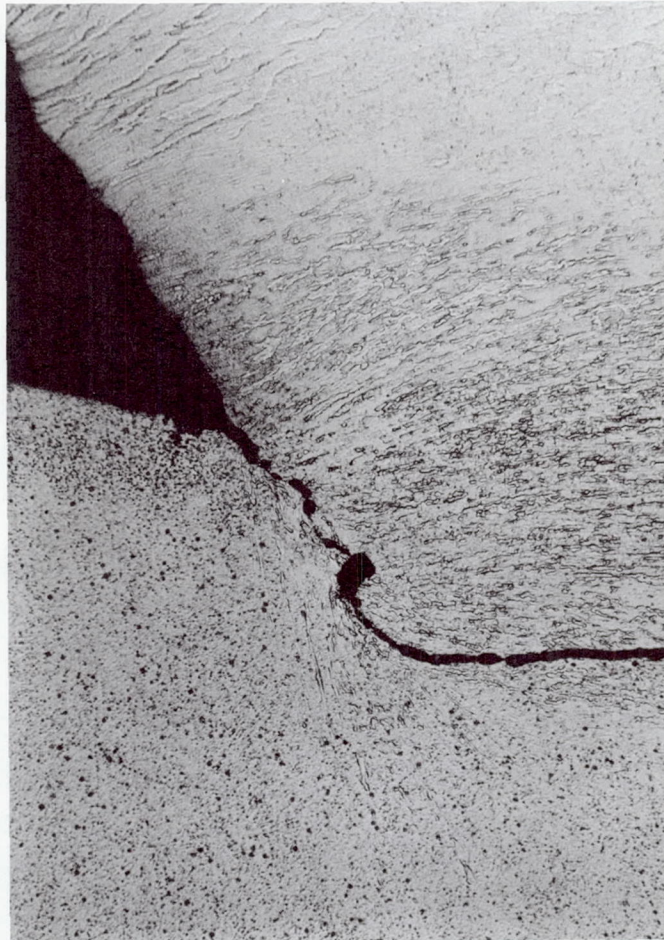


Fig. 4. Edge view of friction surfaces interface after test at 10^{-10} torr (200 \times)

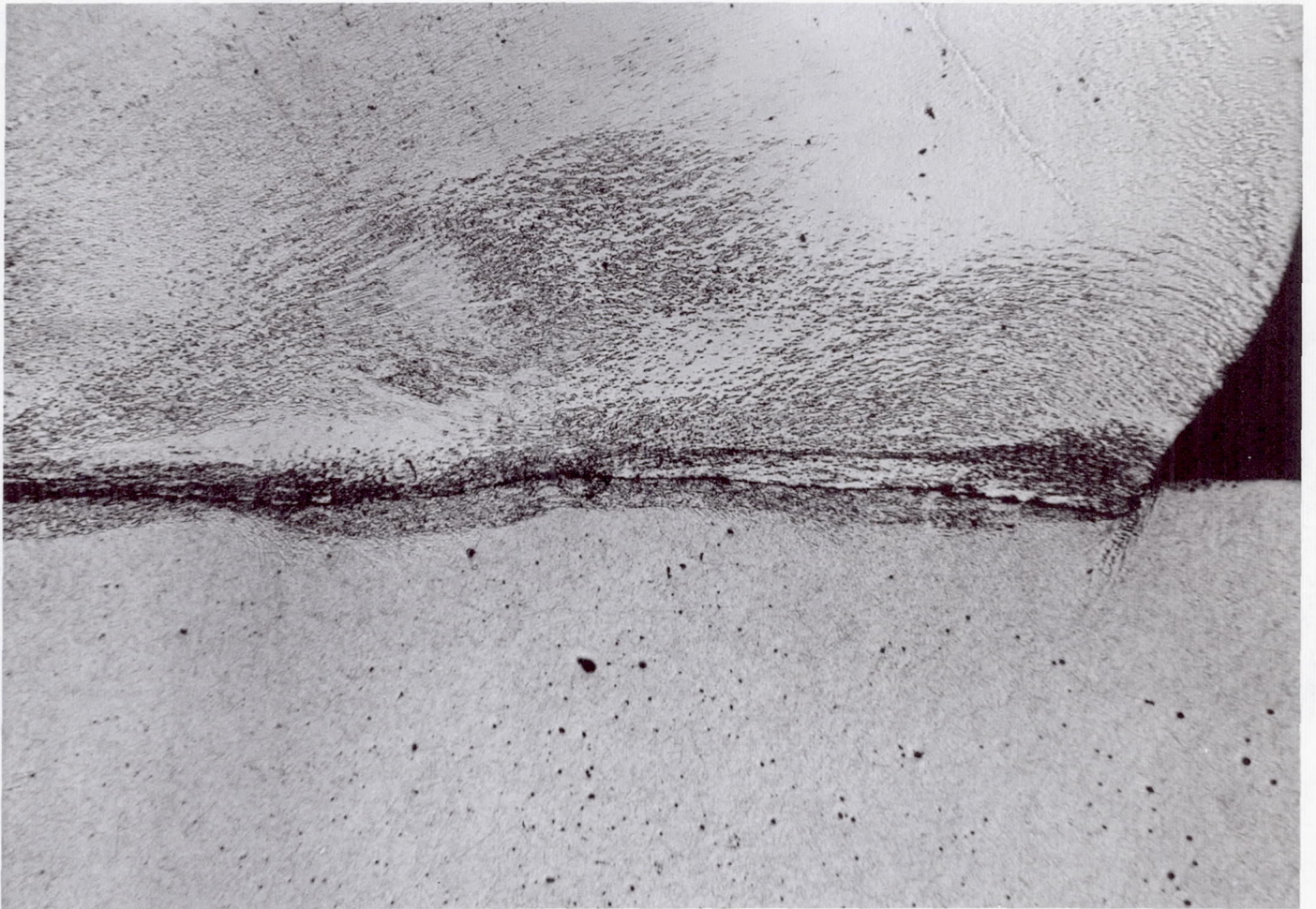


Fig. 5. Section showing distortion of aluminum single crystal adhering at 10^{-10} torr (25 \times)

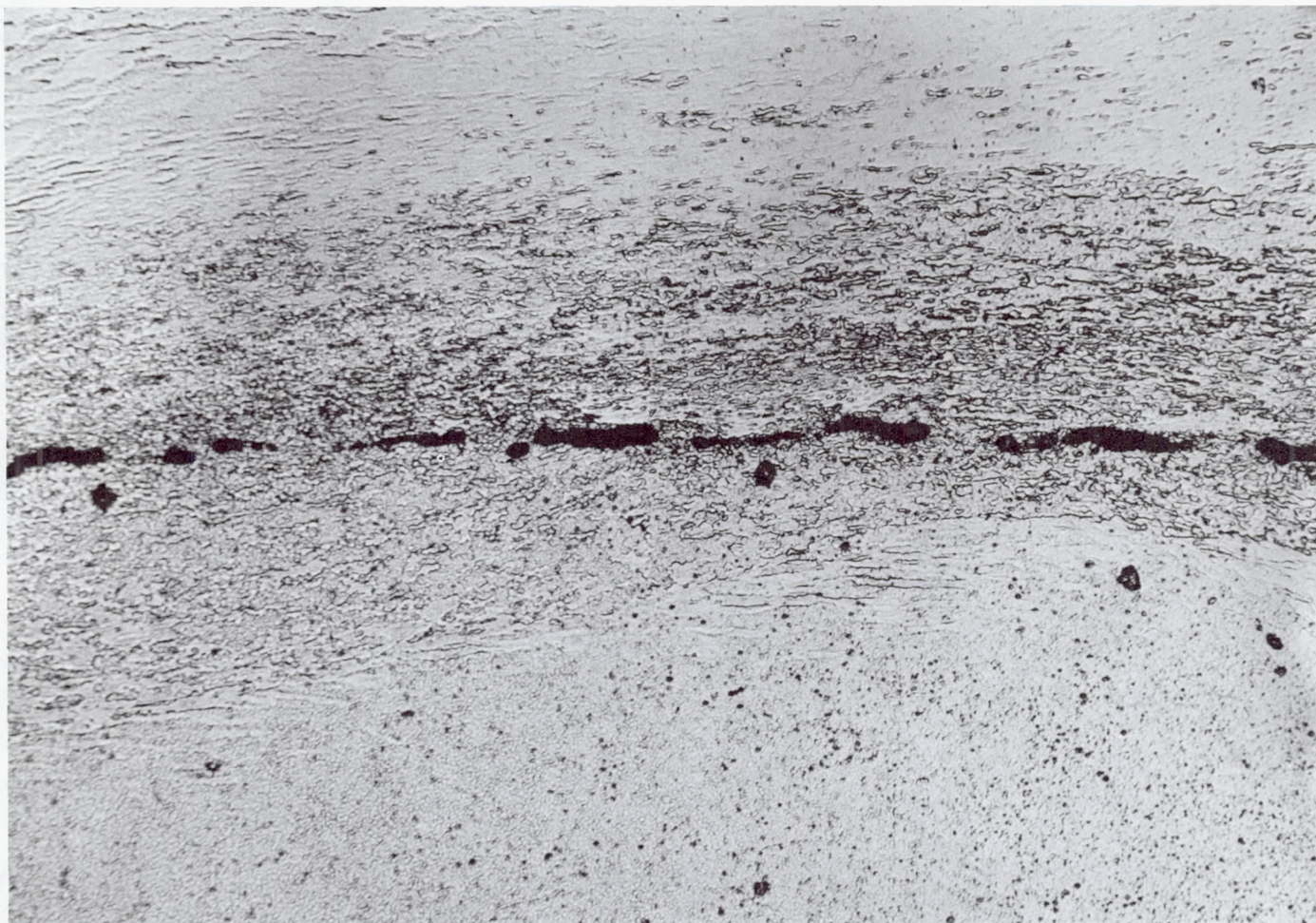


Fig. 6. Adhesion at surface irregularities (200×), aluminum single crystal friction test at 10^{-10} torr

Double-Acting, Rotary-Solenoid-Actuated Shutter*

Allen G. Ford
Jet Propulsion Laboratory
Pasadena, California

The development of a focal-plane shutter for use in the Surveyor spacecraft cameras is described. The shutter action is performed by two blades that are suspended on parallelogram linkages and driven by rotary solenoids. The solenoids utilize a permanent magnet rotor to provide magnetic latching and reversal of motion by reversal of current.

I. Introduction

A shutter may be defined as a mechanism that allows light to pass through an optical system for a specific length of time to expose a light-sensitive image surface from which a picture may be obtained.

The shutter described in this paper utilizes two blades, one to open and the other to close the aperture. Since the blade speeds are essentially identical, a uniform exposure is assured. Each blade is guided by two arms in a parallelogram linkage, the driving arm pivoting on the shaft

of a rotary solenoid and the following arm merely guiding the blade. The solenoid developed for this application utilizes a permanent magnet rotor that drives the blade in either direction in response to the direction of current in a driver coil and holds it in the desired position when the coil is de-energized.

By making the moving parts very light, a high speed of operation was obtained, permitting uniform exposure times as low as 20 msec.

The engineering test model, shown in Fig. 1, was designed and built at the Jet Propulsion Laboratory. On the basis of this design, the flight model was developed and built by the Hughes Aircraft Company for use on the *Surveyor* spacecraft.

*This paper presents the results of one phase of research carried out at the Jet Propulsion Laboratory, California Institute of Technology, under Contract No. NAS 7-100, sponsored by the National Aeronautics and Space Administration.

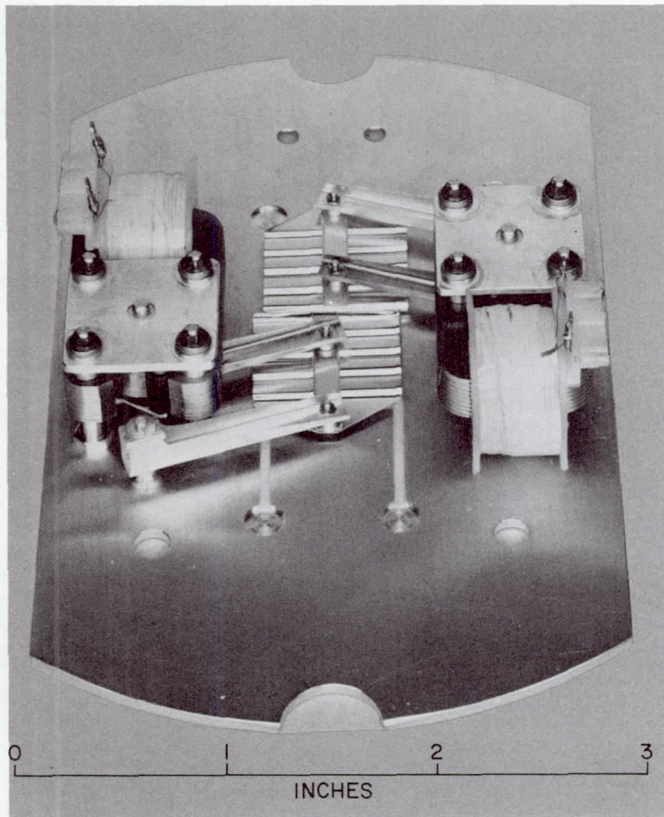


Fig. 1. Photograph of prototype shutter

II. Requirements

Requirements for the shutter were as follows:

- (1) Exposure time: 20.0 ± 1.0 msec for the approach camera and 150.0 ± 2.0 msec for the survey camera.
- (2) Aperture: 0.560×0.560 in.
- (3) Uniformity: A variation of not more than 1 msec exposure between any two points in the field of view.
- (4) Actuating pulse: 15.0- to 26.3-v dc pulses of 20-msec duration.
- (5) Environment:
 - (a) Shock: 25 g at 5- to 7-msec half-sine wave.
 - (b) Vibration: 54 g axial, 48 g lateral at 20-150 cps, 13.5 g at 100-1500 cps.
 - (c) Temperatures: storage -300 to $+250^\circ\text{F}$, operation -65 to $+165^\circ\text{F}$.
 - (d) Operation at 10^{-11} torr.

- (6) Life: 60,000 exposures with 0.999 reliability.
- (7) Space: 1.040 in. high, 3.000 in. wide, and 5.000 in. long.
- (8) Weight: 5.7 oz maximum.
- (9) The closed shutter must be capable of absorbing the heat of direct sunlight for a period of 300 sec without damage, in the event the sun comes into view during the spacecraft search maneuver.

III. Evolution of the Design

The following is a discussion of the critical design considerations and of the solutions that were employed.

A. Uniformity of Exposure

Since the exposure time had to be held within 1 msec, the uniformity of exposure appeared to be the most critical condition to be met. On the premise that an opaque curtain would be used to control the passage of light and that straight edges of the curtain or curtains crossing the aperture would regulate the exposure, four basic systems were considered:

- (1) Parallel edges traversing the aperture at uniform speed. The commercial focal-plane shutter, with a slit in an opaque curtain crossing the aperture, is an example. To keep the speed of the curtain to a reasonable level, the slit would have to be narrow. The resulting time lag between exposure of various parts of the picture would cause distortion.
- (2) Radial edges on a disk rotating at a constant speed. This is a variation of the first system, with a similar constraint.
- (3) Radial edges uniformly accelerated by independent actuators. This would require concentric shafts, with linkages to adjacent actuators. Rotating disks, while traversing an angle sufficient to cross the aperture at the edge nearest their axis, must traverse an arc whose length is much greater than the width of the aperture at the tip unless the radius is much greater than the aperture.
- (4) Parallel edges uniformly accelerated by independent actuators. This system was chosen for the *Surveyor* shutter because of its compatibility with the two-pulse actuation and its inherent economy of motion.

B. Linkage

To maintain the desired orientation of the blades, a parallelogram linkage was used, in which the blade was supported by two parallel arms of equal length, as shown in Fig. 1. Two identical linkages were used in the shutter, providing two blades individually actuated by drivers applying a torque to the innermost arm, called the drive arm. The first pulse moves the blade initially covering the aperture, to open the shutter. Then the second pulse, spaced to obtain the desired exposure, moves the other blade to close the aperture. To minimize the electronic circuit redesign, it was decided to reset the shutter by using a third pulse to return both actuators simultaneously to their original positions. To assure accuracy of exposure and eliminate undue time lag during exposure, a rapid motion was considered essential. This approach called for minimum inertia and friction.

- (1) To provide a blade with sufficient rigidity and minimum weight, a 3003-H14 aluminum sheet 3 mils thick was used. Corrugations 0.030 in. deep were formed laterally, and a longitudinal stiffening member, supporting the pivot pins, was riveted to the formed sheet.
- (2) The parallel arms were formed channel sections, the drive arm being formed from 2024-T3 clad aluminum 0.010 in. thick, and the follower arm from the material used in the blade.
- (3) Teflon bushings were used for all pivots. The use of ball bearings was avoided because the loss of lubrication in vacuum would jeopardize the reliability of the bearings and could contaminate the optical surfaces. The edges of the blades were guided by Teflon strips, dovetailed into the base, to stabilize the blades during their travel and while under vibration. A clearance of 0.001 to 0.003 in. was maintained by shimming the arms to the proper heights.
- (4) The arms are 1 in. long and rotate 40 deg, giving the blades a travel of 0.684 in.

C. Stopping Blades

The energy supplied to the linkage in driving it through its travel must be absorbed at the end of the stroke without excessive overrun or rebound. Since the stop is provided within the driver, the drive arm transmits the load as a cantilever beam, and the center stiffening bar distributes the load to the blade and the follower arm.

There is sufficient resilience in the system to absorb the energy of the opening blade, but when the closing blade reaches the end of its stroke, it impacts the other blade. The small gap provided between blades is greatly exceeded by the overrun due to flexure, thus causing an impact between blades. In the original configuration, shown in Fig. 1, the leading edges of the blades became bent and finally tore loose after several thousand cycles. A bumper block was then inserted in the center channel, and the leading edge of the blade was cut back so that contact between blades would be made only by the bumpers. This prolonged the life, but failures began to occur at the back end of the bumper block due to compression in the center channel. Finally, the bumper and channel were replaced by a bar 0.028 by 0.154 in. extending the entire length of the blade, and no more failures were experienced.

D. Solenoid Drive

A driver was required to rotate the drive arm 40 deg in either direction and to latch at the end of each stroke. This was to be done in response to a single dc pulse for each stroke. To accomplish this, a rotary solenoid was developed which utilized a permanent magnet as a rotor, to provide magnetic latching and to permit reversal of force in response to reversal of flux generated by the coil.

Figure 2 shows the configuration used. The magnet is a disk 0.50 in. in diameter and 0.25 in. thick, secured to the drive arm and to a shaft that pivots in Teflon bushings at each end. The magnet is provided with notches at both magnetic poles, in which soft iron detent bars are retained by means of spring clips. The flux of the magnet passes through the detents and the pole piece, thus providing a closed path holding the rotor in place. When enough current is passed through the coil windings to produce a flux equal and opposite to the permanent magnet field, equal and like poles are generated at the detents, which are repelled. The magnetic gradient in the air gap at the periphery of the rotor produces a constant torque, and as the detents approach the end of the stroke they are attracted to poles of opposite polarity. Reversing the current flow in the coil reverses the rotor travel in an identical manner.

Figure 3 shows the torque curves of this unit. It will be noted that when the coil is de-energized, a latching force of 0.25 in.-lb is maintained by the magnet. The threshold input is 254 amp-turns, and a normal input of 534 amp-turns produces a torque of approximately 0.06 in.-lb. A bifilar winding was used in the coil to

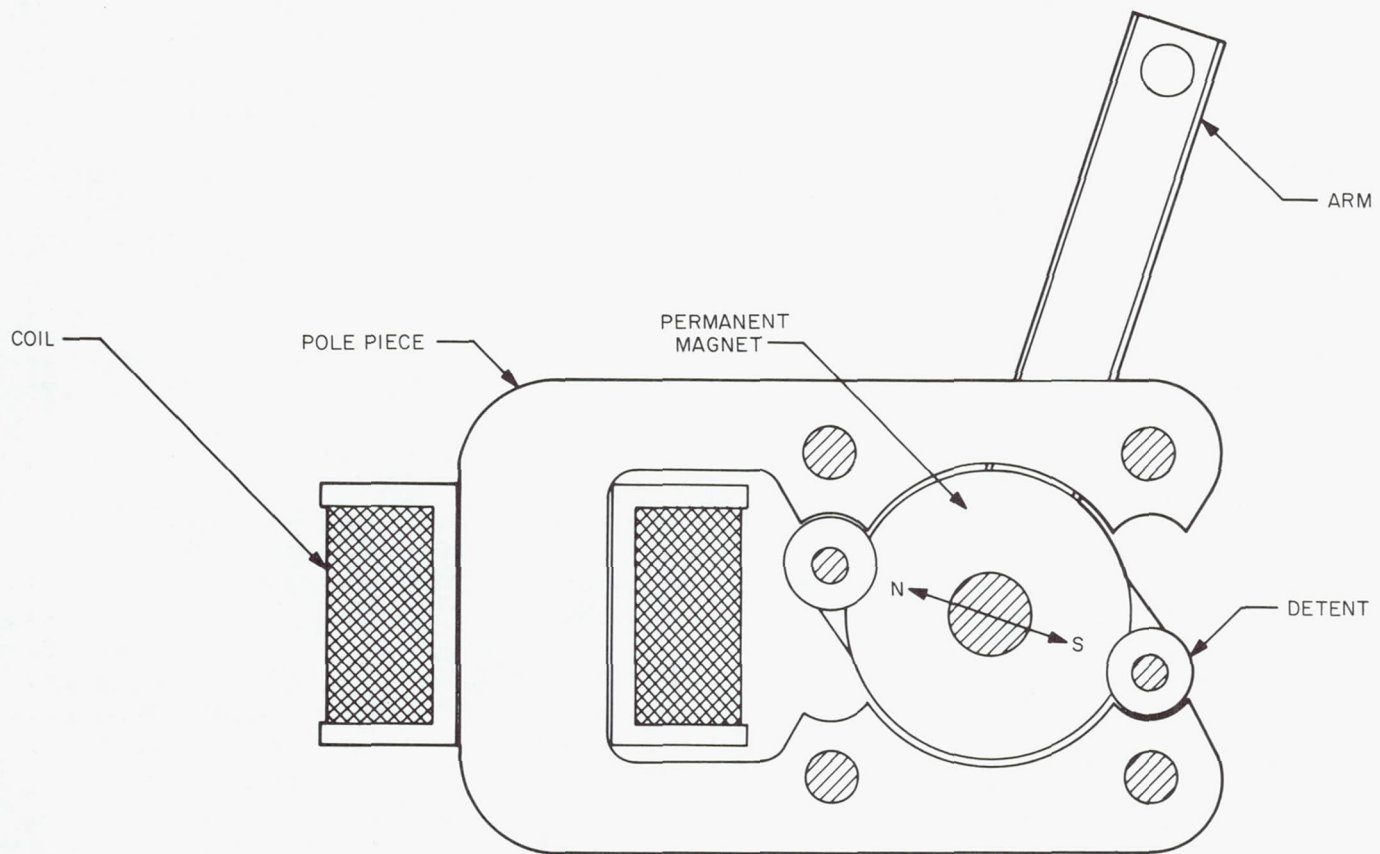


Fig. 2. Solenoid diagram

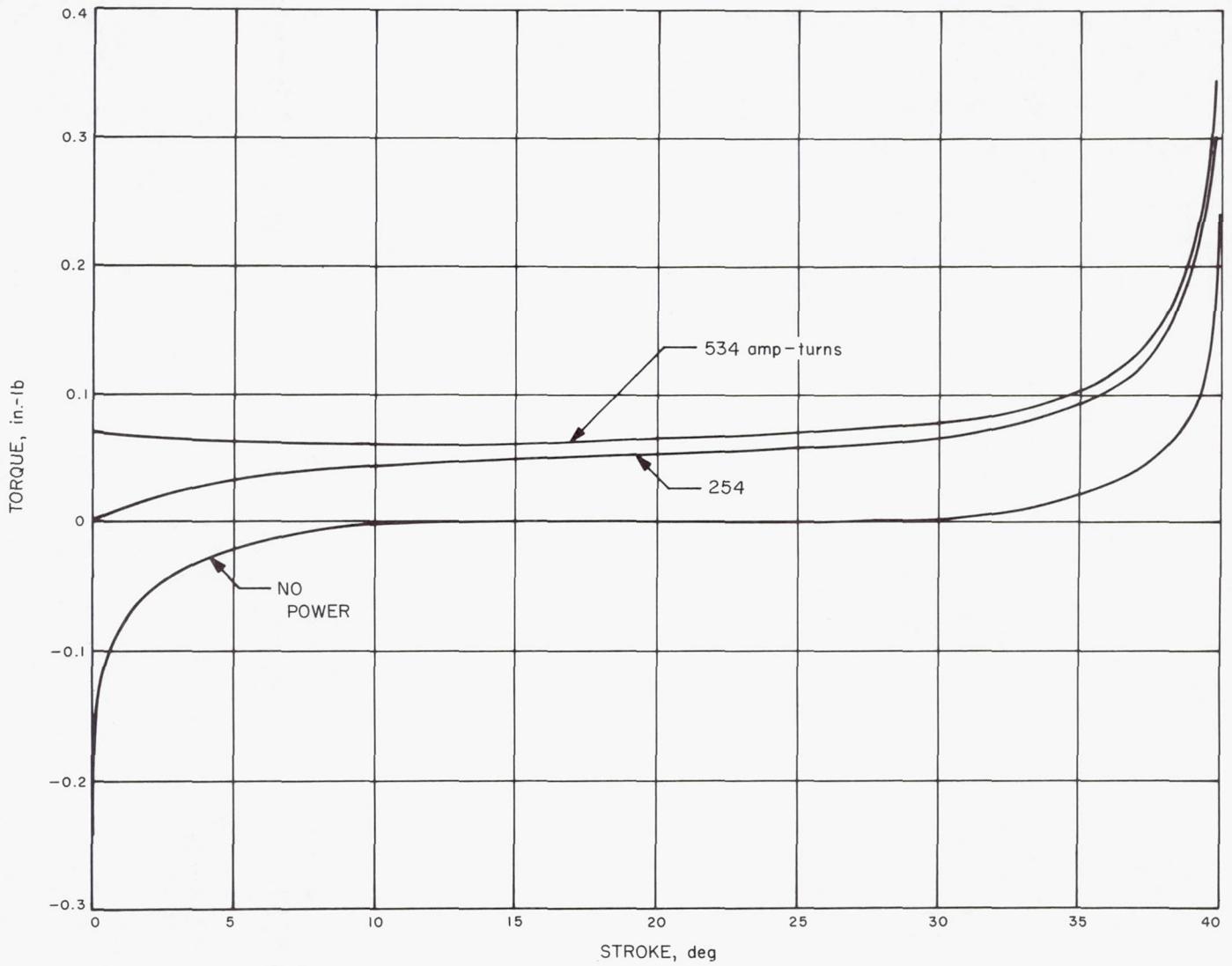


Fig. 3. Solenoid torque curves

simplify the switching circuitry by pulsing different terminals to reverse the stroke, rather than reversing the current. Each winding contains 850 turns of 34-gage wire, with a resistance of 32 ohms. With the specified voltages, the coil will produce 390 to 700 amp-turns using 7.0 to 21.6 w.

Soft iron transformer laminations were used to make the pole pieces in the prototype, but higher efficiency was obtained by using Permendure 2V in the flight configuration. Figures 4 and 5 show the manner in which the solenoid and drive arm are assembled and installed.

The total travel time of each blade is 9 msec, in which the aperture is traversed in 6 msec.

E. Surface Finish

All aluminum surfaces except the forward surfaces of the blades are black-anodized to reduce reflection of stray light. The surfaces are prepared for anodizing by dry

honing with 100/240 grit to obtain a dull finish. The front surfaces of the blades are left bright to reduce the heat absorbed in the event the sun comes into view of the camera during spacecraft maneuvers.

IV. The *Mariner 69* Camera Shutter

A modification of the *Surveyor* shutter is currently being developed for use in a telescopic camera to be flown on the *Mariner 69* spacecraft.

A. Pertinent Requirements

The pertinent requirements are as follows:

- (1) Exposure time: 5 to 20 msec.
- (2) Aperture: 0.72×0.84 in. in the plane of the blades.
- (3) Space: 3.50-in. diameter, concentric with the aperture, $\times 2$ in. high.

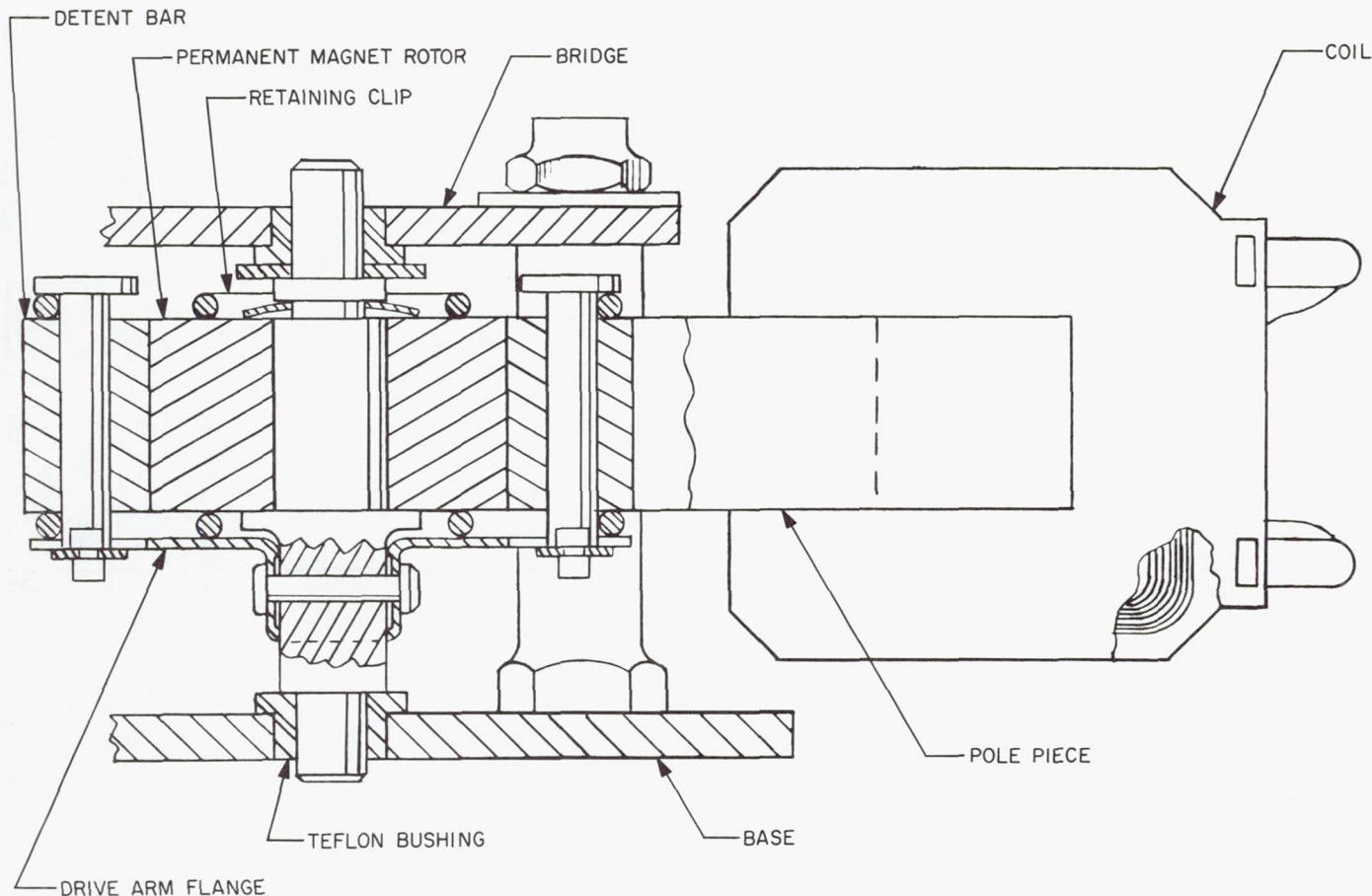


Fig. 4. Solenoid assembly

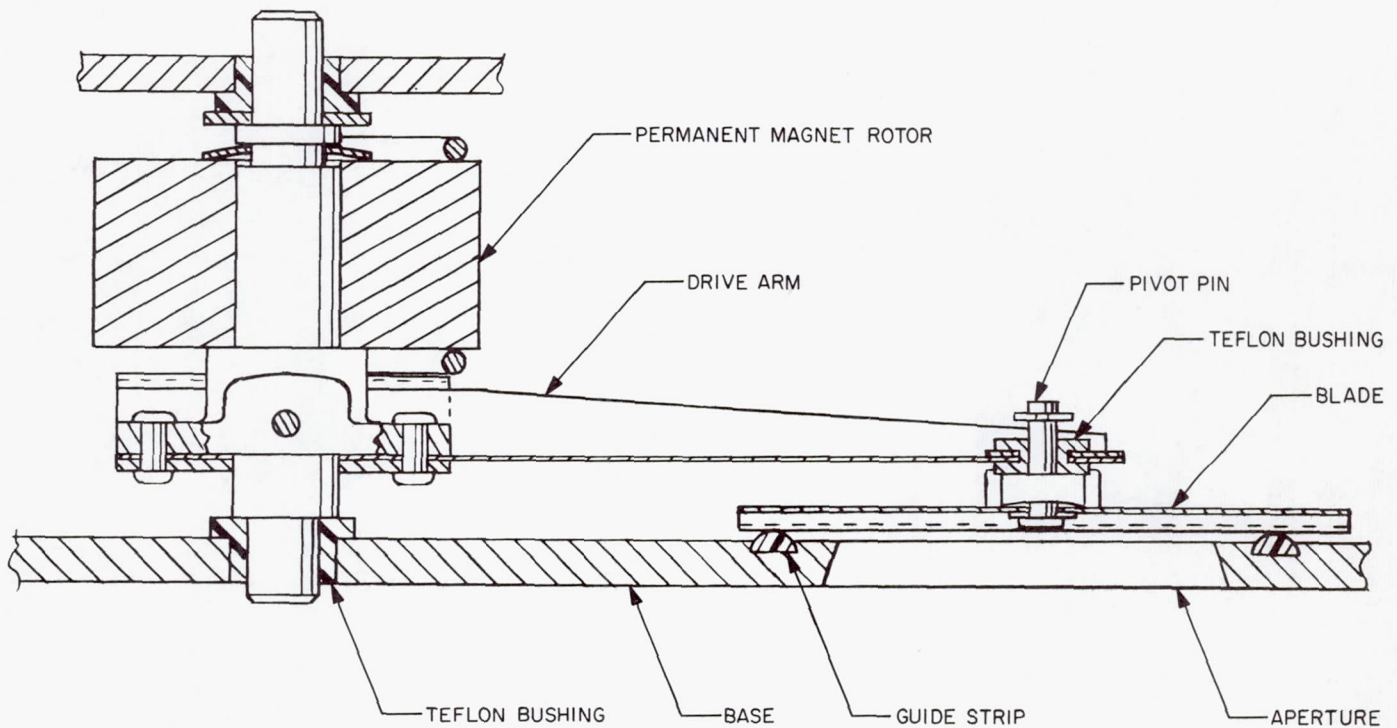


Fig. 5. Drive arm installation

B. Significant Design Changes

The significant design changes are as follows:

- (1) To accommodate the larger aperture, the length of the arms was increased from 1.00 to 1.25 in. and the blade area was increased from 0.623 to 0.847 in.².
- (2) The leading edges of the blades were offset to eliminate the impact between blades at the end of the closing stroke. This permits a reduction in the cross section of the longitudinal bar, effecting a reduction in weight.
- (3) The drive arm was redesigned for greater lateral flexibility by using a rectangular cross section in the shank. An extended hub at the outer end to house dual bushings provided sufficient stability to suspend the blade on the arm, eliminating the guide rails and thereby reducing the friction.

C. Anticipated Performance

Because of the inherent increase in inertia due to the larger blades and longer arms, the opening time will be

increased to a calculated 8.8 msec, but by reducing the friction to that of the pivots it is anticipated that the speed characteristics will be sufficiently repetitive to assure the maintaining of the required exposure tolerances.

V. Conclusion

The shutter, as developed in the final flight configuration, was capable of fulfilling all of the requirements set forth in the specifications.

By keeping the inertia of the system to a minimum, the speed of operation was sufficient to maintain the required uniformity of exposure of within 1 msec. The simplicity of the mechanism made possible by the double-acting rotary solenoid and Teflon pivots resulted in a reliable, rugged device.

The shutter's reliability was demonstrated in the *Surveyor I* mission, in which it made over 11,000 exposures without malfunction.

The BI-STEM — A New Technique in Unfurlable Structures

J. D. MacNaughton

H. N. Weyman

E. Groskopfs

Special Products and Applied Research Division
The de Havilland Aircraft of Canada, Limited
Malton, Ontario

The BI-STEM is a new development of the Storable Tubular Extendible Member (STEM), which is used for erecting unfurlable structures in space. The BI-STEM is described, and data are presented on the analytical and structural characteristics of this mechanism.

I. Introduction

The STEM (Storable Tubular Extendible Member) (Ref. 1) element is a thin strip of metal, heat-treated into a circular overlapped cross section as depicted in Fig. 1. The bending strength of a STEM element is almost equivalent to that of a seamless tube of the same diameter and wall thickness. The element is stored on a drum by a flattening and rolling process, and very long lengths of tubular structure may be extended and retracted from a small mechanism by rotating the drum in the appropriate direction.

A further development of this principle is a mechanism that employs two diametrically opposed "underlapped" elements in a "front to front" configuration as shown in Fig. 2. These BI-STEM elements may be stored on single or multiple drums in much the same fashion as STEM elements.

This paper describes the BI-STEM and highlights some of its significant advantages over the more conventional STEM for certain applications.

II. The BI-STEM Principle

The BI-STEM principle is shown in Fig. 2. The elements are made from thin strips of metal, heat-treated into a circular cross section such that the angle ψ is approximately 60 deg.

One element is placed inside the other so that the concave sides of each element face one another. This two-element configuration forms the basic BI-STEM tubular structure. Additional elements may be nested within this basic structure to increase its strength, in the same fashion as that used for the STEM.

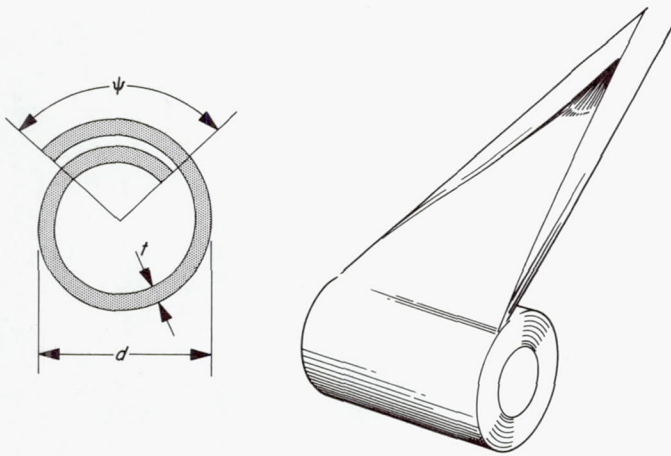


Fig. 1. The STEM principle

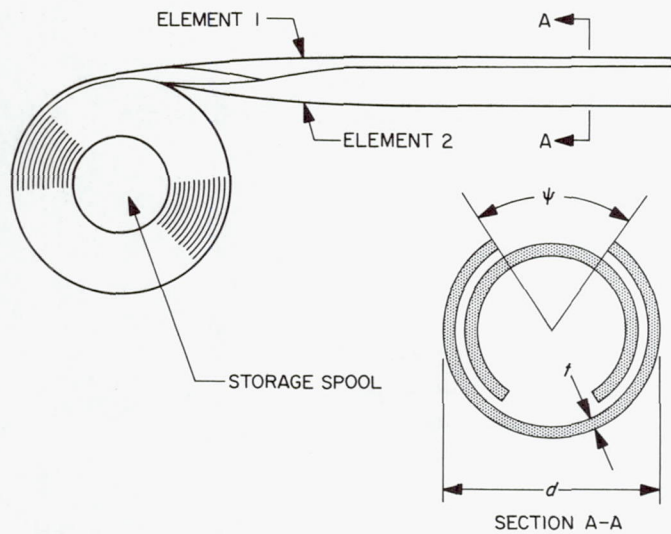


Fig. 2. The BI-STEM principle

The elements are flattened by a guidance system composed of rollers and specially shaped formers to allow smooth extension and retraction from a conventional storage drum.

III. Comparative Performance of the BI-STEM

Some important characteristics of the BI-STEM are described below and compared with those of the conventional STEM.

A. Package Size

By referring to Figs. 1 and 2, it may be seen that the size of a basic STEM mechanism is governed by the fol-

lowing geometrical characteristics of the tubular structure to be deployed:

- (1) Diameter
- (2) Strip width
- (3) Strip thickness
- (4) Element length

The following discussion develops order-of-magnitude comparative figures for STEM and BI-STEM mechanisms. Governing equations are

$$b = \gamma \pi d \quad (1)$$

$$\gamma = \left(1 + \frac{\psi}{2\pi} \right) \quad (2)$$

$$D = 1.5 d \quad (3)$$

$$D_1 = \left[\frac{4(l - l_1)t}{\pi} + 2.25 d^2 \right]^{1/2} \quad (4)$$

$$t = k_1 d \quad (5)$$

$$l_1 = k_2 b \quad (6)$$

1. Deployment unit width. Figure 3 shows that the mechanism width is a strong function of element width. The conventional STEM has an overlap factor $\gamma = 1.5$, which corresponds to an overlap angle ψ of 180 deg. The BI-STEM, on the other hand, is designed such that ψ is approximately 60 deg open, which results in an overlap factor $\gamma = 0.833$.

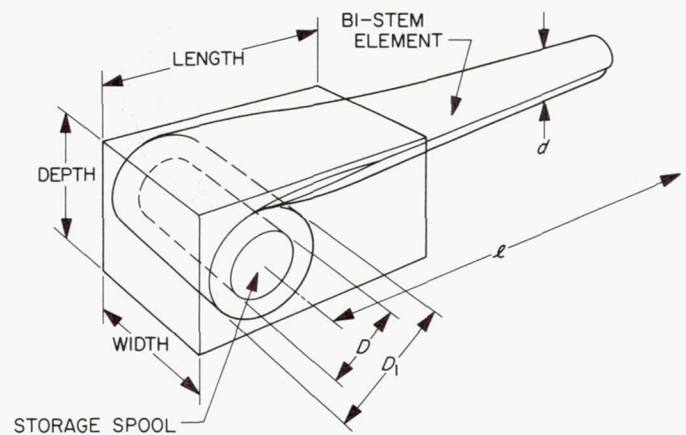


Fig. 3. BI-STEM dimensions

Thus, from an examination of Eqs. (1) and (2), the BI-STEM element width will be approximately 55% that of a comparable STEM. Hence, the BI-STEM mechanism width will be smaller than the equivalent STEM in approximately the same proportion.

2. Deployment unit length. In Fig. 3, it can be seen that the length of the mechanism will be a function of ploy length l_1 and overall drum diameter D_1 .

From Eq. (6), it follows that the ploy length is proportional to element width; hence the ploy length of a BI-STEM will be 55% that of an equivalent STEM. However, the overall drum diameter will be somewhat greater for the BI-STEM, since twice the element thickness must be stored on the drum.

For example, from Eqs. (3), (4), and (5), a 0.5-in.-diameter STEM element, 0.002 in. thick and 50 ft long, will have an overall drum diameter of

$$D_1 = 1.45 \text{ in.}$$

while, for the equivalent BI-STEM,

$$D_1 = 1.9 \text{ in.}$$

This diameter increase is significant, as, in the above example, l_1 is reduced from approximately 15 to 8 in. by using the BI-STEM approach.

Thus, for the example used, the BI-STEM length will be approximately 60% of that of a conventional STEM.

3. Deployment unit depth. Again referring to Fig. 3, it can be seen that the mechanism depth is essentially a function of overall drum diameter D_1 . The example of the previous section serves to show that the depth of a BI-STEM mechanism will be somewhat greater than that of the equivalent STEM.

4. General. The net effect of the BI-STEM approach is to change the shape of the deployment mechanism by reducing its length and width and increasing its depth. The reduced length is of extreme importance in spacecraft applications, as the unit structure is usually mounted with its long axis at right angles to the thrust axis of the launch vehicle, and this dimension is generally severely limited.

This feature is dramatically depicted in Fig. 4, which shows a photograph of typical STEM and BI-STEM

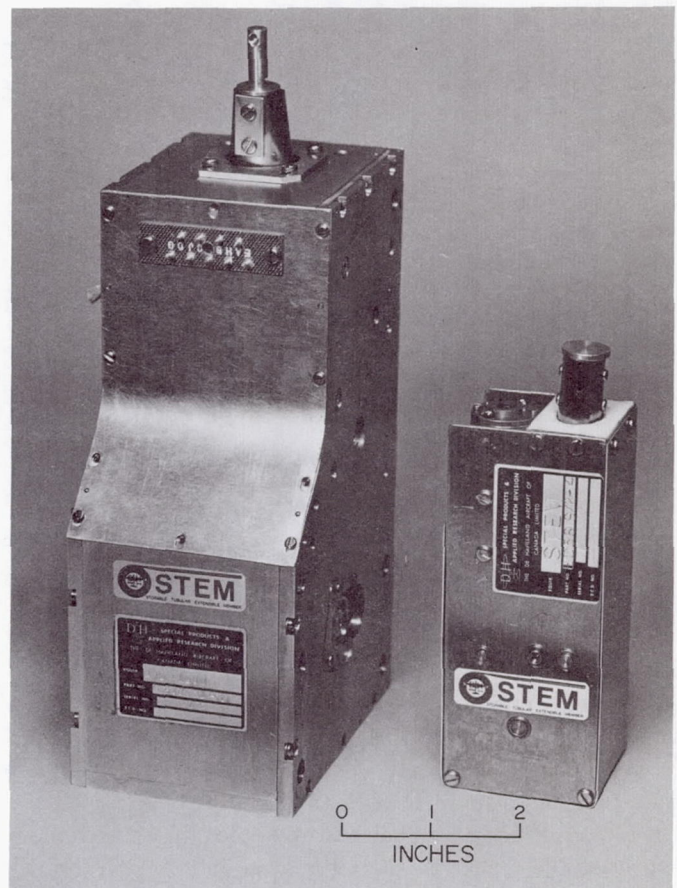


Fig. 4. STEM/BI-STEM size comparison

units, both of which deploy 0.5-in.-diameter tubular elements.

B. Element Weight

The BI-STEM employs two elements, each of which is 55% the width of a conventional STEM. The weight per unit length of a BI-STEM element will therefore be 10% greater than that of an equivalent STEM element. This increase is more than offset by the reduction in deployment mechanism weight resulting from the reduced unit length.

C. Bending Strength

The moment of inertia of a BI-STEM element cross section can be shown to be greater than that of the equivalent STEM element cross section. As a result, the BI-STEM can withstand a critical bending moment some 20% higher than that of the conventional STEM.

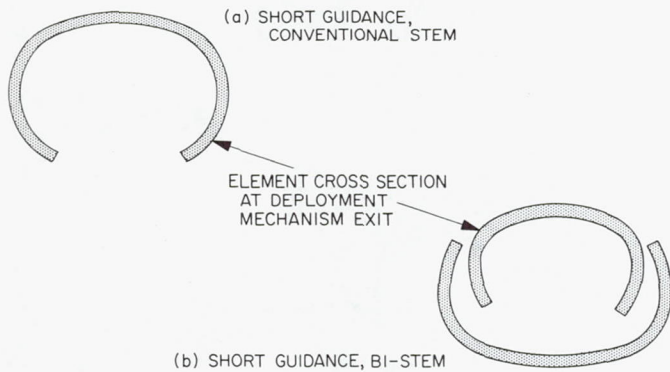


Fig. 5. Element cross section at guidance exit

To reduce the deployment mechanism length of a conventional STEM unit, it is common practice to terminate the element guidance system before the element has formed into a full round section, as shown in Fig. 5. Thus, only a partial utilization of the full bending strength of the element is realized, because of the resulting open section. As can be seen from Fig. 5, the BI-STEM does not suffer from this factor, and hence it can develop full bending strengths with a guidance much shorter than usual. This feature, coupled with its naturally short length, results in a deployment mechanism at least 65% shorter than the conventional STEM for element lengths up to 50 ft.

D. Element Straightness

The conventional STEM has a distinctive "ploy shape" due to stress distribution in the element as it changes from the flat to the round condition (see Fig. 6). These stresses are composed of those induced naturally by flattening the element and those imposed by the guidance system. The BI-STEM, however, has an inherently straight ploy, since the two elements are "front to front" and the stresses oppose one another.

This effect also improves the natural straightness of the complete boom, as the manufacturing process tends to introduce element bow in a known and essentially repeatable direction. Thus, the inherent curvatures of the individual BI-STEM elements tend to cancel one another out.

E. Torsional Behaviour

Although not yet reduced to mathematical form, tests have indicated that the BI-STEM element is torsionally

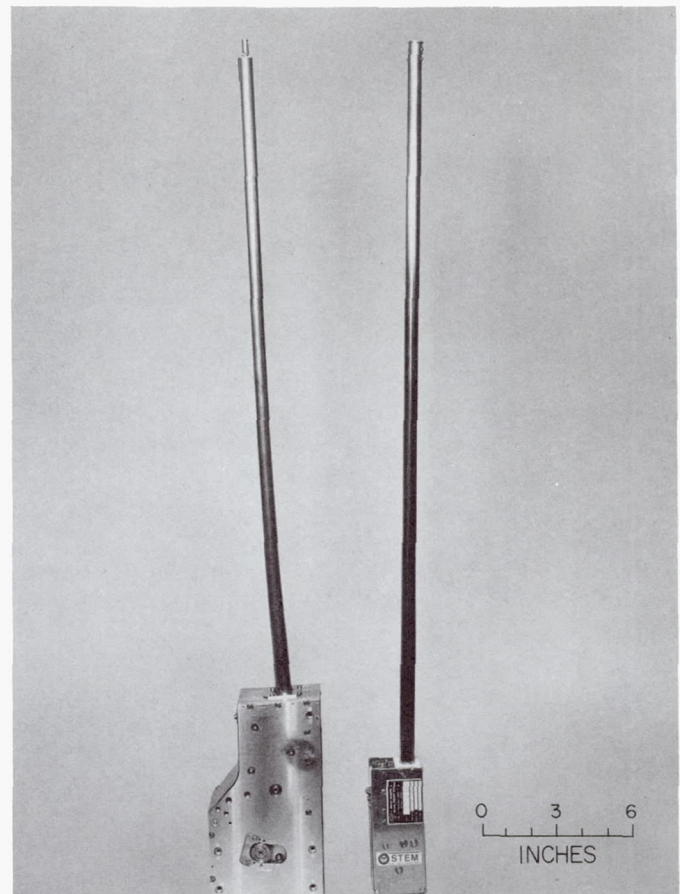


Fig. 6. STEM/BI-STEM element deployment comparison

stiffer than the conventional STEM and is also more repeatable in terms of angular position. This results from the more positive element fixations at the tip and root with the BI-STEM.

F. Power Requirements

The BI-STEM requires some 10% more metal in the structural element than the STEM, with the result that self-extension forces will be somewhat higher than usual. Conversely, retraction forces will also be slightly higher, thus increasing the power required for retraction.

G. Thermal Behaviour

A satisfactory mathematical model describing thermal deflection characteristics has not yet been derived. Preliminary inspection of the element configuration (Fig. 2) has revealed that thermal deflections due to solar radiation will be marginally smaller than those associated with a conventional STEM unit.

H. Damping (Ref. 2)

No sophisticated testing or analysis has yet been performed on the BI-STEM configuration. Initial tests indicate that structural damping in bending will be much improved over the conventional STEM, as interleaf motion is greatly accentuated. Damping in torsion is expected to be similar to that of the conventional STEM.

IV. BI-STEM Applications

The BI-STEM is suited to the three normal types of STEM operation, as follows:

- (1) *Motorized* – to allow extension and retraction of the boom.
- (2) *Self-extendible* – where there is no requirement for retraction.
- (3) *"Push-Pull"* – where it is desirable for the element to be manually extended and retracted; for instance, by an astronaut in extra-vehicular activity (EVA).

BI-STEM devices have been developed for the element diameters shown in Table 1. Approximate bending strength figures are also given for reference.

Table 1. Characteristics of BI-STEM devices developed to date

Diameter, in.	Thickness, in.	Material	Bending strength per element, ft-lb
0.25	0.0014	BeCu 25	0.40
0.50	0.002	BeCu 25	1.45
0.50	0.003	Stainless steel	5.6
1.00	0.005	Stainless steel	27
1.34	0.007	Stainless steel	82

Extrapolation of the results shown in Table 1 allows calculation of BI-STEM element strengths for other element sizes. Typical examples are presented in Table 2.

BI-STEMS, utilizing single storage drums, have been developed by de Havilland for boom lengths up to 50 ft. It is felt that two storage drums will be required for greater lengths.

Typical BI-STEM applications could include:

- (1) Solar panel actuators.

- (2) EVA astronaut attachment structures.
- (3) Spacecraft docking booms.
- (4) Booms for deploying instruments.

An artist's impression of these applications is shown in Fig. 7. In addition, the BI-STEM principle is well suited for use in an antenna on rocket payloads.

The BI-STEM is ideally suited to these applications since each requires the ability to support large loads, as described below:

- (1) Solar panel actuator loads result from solar pressure, manoeuvring, and docking; in addition, compressive loads are involved in extending the panels.
- (2) Rocket antenna loads usually result from Coriolis bending moments due to despinning the payload as the antennas are deployed. Reducing antenna extension speed lowers these moments; however, because of the short experiment time available from a rocket shot, it is more desirable to extend the antenna quickly and have it capable of withstanding the associated moments.
- (3) In spacecraft docking, loads are imparted during the docking manoeuvre itself, owing to the residual relative velocities of the docking vehicles.
- (4) For instrument-carrying booms, the BI-STEM, with its inherent positional accuracy and small package size, is far more attractive than the conventional STEM, which in turn has been marginally competitive with articulated or telescopic devices in the past.

Table 2. Calculated BI-STEM element strengths for various sizes

Diameter, in.	Thickness, in.	Material	Bending strength per element, ft-lb
0.25	0.0014	Stainless steel	0.68
0.75	0.004	BeCu	8.81
	0.004	Stainless steel	15
1.00	0.005	BeCu	15.7
1.34	0.007	BeCu	48
	0.010	Stainless steel	250
2.0	0.010	BeCu	146
	0.010	Stainless steel	250
3.12	0.014	BeCu	450
	0.014	Stainless steel	770

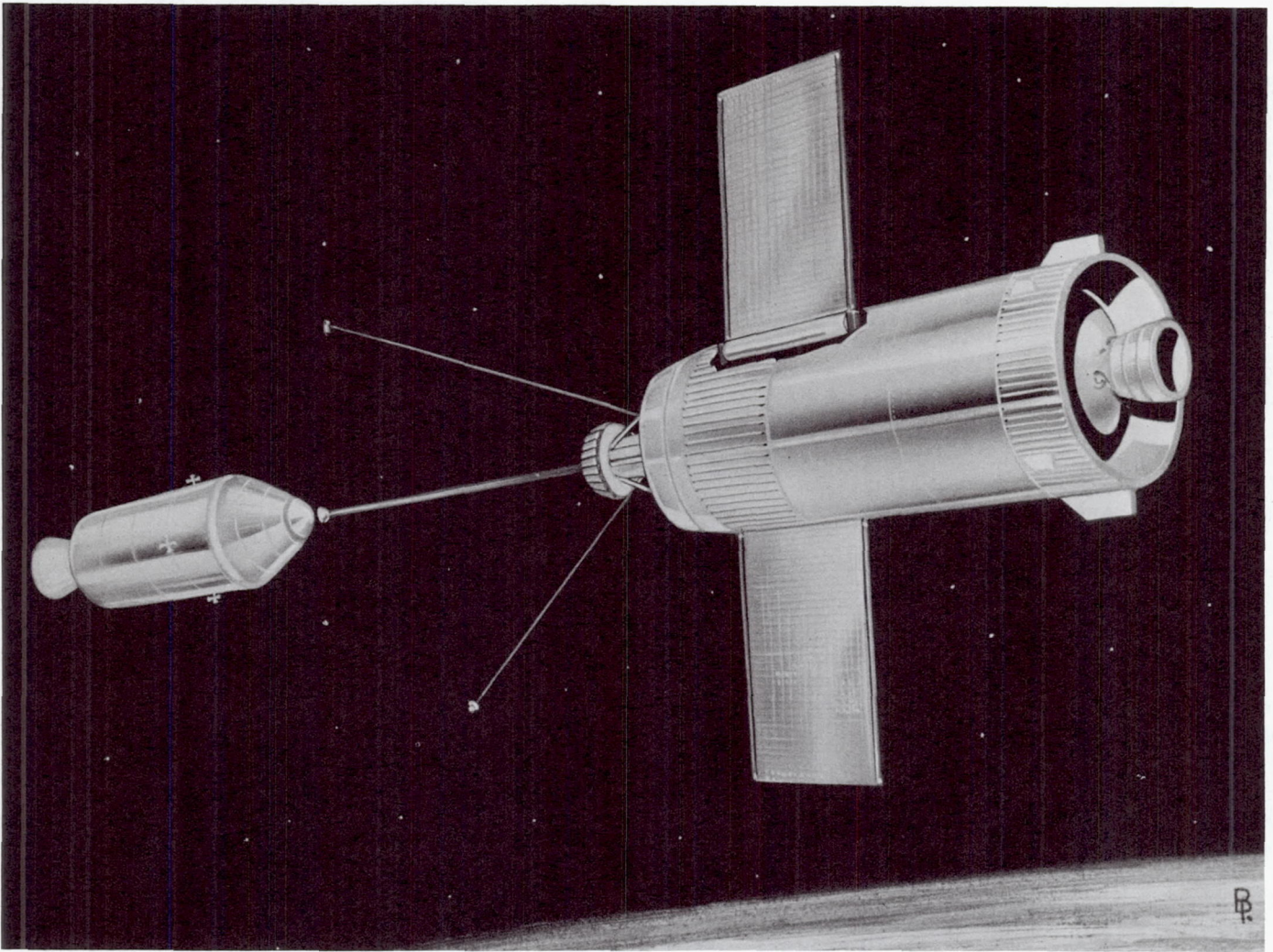


Fig. 7. BI-STEM applications

V. Conclusions

The BI-STEM is a new unfurlable structure with significant advantages over the conventional STEM for tubular structures up to 50 ft in length. These advantages are:

- (1) Reduced mechanism length.
- (2) Reduced mechanism width.
- (3) The capability of carrying higher bending loads.
- (4) Greater torsional stiffness.
- (5) Straighter deployment.

The BI-STEM should be seriously considered for the remote positioning of a variety of experimental devices, such as magnetometers, antenna arrays, sensors, and engagement devices. It also provides an especially attractive technique for deploying very large solar panel arrays, with minimum volume and weight penalties.

Acknowledgment

The authors wish to thank The de Havilland Aircraft of Canada, Limited, for permission to publish this paper, and to acknowledge the contributions of the technical staff of the Special Products and Applied Research Division.

Nomenclature

b	strip width, in.	k_1	a constant
d	element diameter, in.	k_2	a constant
D	drum diameter, in.	t	element thickness, in.
D_1	diameter of drum plus stored element, in.	γ	overlap factor
l	element length, in.	ψ	overlap angle, rad
l_1	element ploy length (the length necessary for the element to form from the flat to the tubular condition), in.		

References

1. MacNaughton, J. D., "Unfurlable Metal Structures for Spacecraft," *Can. Aeronaut. and Space J.*, Vol. 9, No. 4, pp. 103-116, 1963.
2. Rimrott, F. P. J., "Storable Tubular Extendible Member - A Unique Machine Element," *Machine Des.*, Dec. 9, 1965.

Despinning the ATS Satellite

J. P. Dallas
Hughes Aircraft Company
Los Angeles, California

The ATS synchronous gravity-stabilized spacecraft is designed to be despun by a two-stage yo-yo in combination with a nutation damper. The unique advantage of the ATS despin mechanism arises from the use of a two-stage yo-yo system in which the off-axis rate errors of the first stage, starting from 100 rpm, are damped out by a nutation damper prior to releasing the second-stage yo-yo, starting from 10 rpm.

I. Introduction

The synchronous gravity-stabilized advanced technology satellite (ATS) will have a two-stage "yo-yo despin mechanism" designed to reduce a 100-rpm rate to $+0.145 \pm 0.2$ rpm. The despinning of a spacecraft with a yo-yo mechanism is a passive technique wherein the initial angular momentum of the spacecraft is transferred to a number of masses attached to cables initially wrapped around the circumference of the spacecraft. The momentum transfer occurs during the unwrapping of the cables and is complete when the masses and cables are released, leaving the spacecraft with little or no angular velocity.

Extensive studies were made of various methods by which despin of this vehicle could be achieved. The despin methods considered were:

- (1) A single-stage yo-yo
- (2) A free-wheeling single-stage yo-yo
- (3) An all-gas-jet despin system
- (4) Combination single-stage yo-yo and gas jet systems
- (5) Combination single-stage yo-yo and inertia wheel system
- (6) A two-stage yo-yo system with a nutation damper

Because of its simplicity, high accuracy control of spin rates, and lowest mission risk, the two-stage yo-yo despin system was chosen for the ATS application. Subsequent design and test experience discussed in this paper supports the wisdom of this choice.

In this two-stage yo-yo despin system, the first stage despins the spacecraft from 100 rpm to 10_{-2}^{+1} rpm. Before the second-stage yo-yo is released, time is allowed for a nutation damper to reduce the error, or off-axis rates, to a negligible value. During this period reasonable gyroscopic stability, desirable to prevent tumbling, is provided by the 10-rpm spin rate. Despin off-axis rate errors are proportional to the initial spin rate. Accordingly, smaller residual errors can be achieved by a final stage when rates have first been reduced as much as practical by a preliminary stage. Such a system is the simplest system providing the required performance. No spin rate control instrumentation or electronics is required. The principal disadvantage is the impracticality of testing the low-rpm second-stage yo-yo in a 1-g environment as a prototype assembly. Upon release, the bobs would fall to the ground before completely unwinding. However, a simulated weightless release has been studied.

The complete system consists of four bob weights, four cable assemblies, a rim for mounting the bobs and cables, and a release mechanism for each bob. The release mechanism includes a latch assembly and squib pin pullers which provide electrical and mechanical redundancy. The system is located in a plane at approximately 8 in. aft of the spacecraft's center of gravity. The weight of the despin system is 15.696 lb (Fig. 1).

II. Operation of a Two-Stage Yo-Yo Despin System

When the spacecraft is in the proper orbit and it is desired to despin, a command signal via the ground-to-spacecraft radio command system will ignite the pin pullers of the first stage. The latch assemblies that retain the first-stage bobs to the track are released, allowing the bobs to unwind about the spacecraft's spin axis. The system is designed so that when either of the two pin pullers restraining each bob is actuated, the bob is released. Two independent squib drivers will be employed. Each squib driver will detonate a pair of squibs (one corresponding to each bob). When the two first-stage bobs have extended to the full length of their cables (354 in., or two complete wraps), each cable eyelet slides off a hook, and the bobs and cable assemblies leave the spacecraft. As a result of this operation the portion of the spacecraft's angular momentum transferred to the yo-yo bobs and cable assembly reduces the spin speed to approximately 10 rpm. Before the second-stage yo-yo despin bobs are released, time is allowed for a nutation damper to reduce

nutation caused by first-stage off-axis rates to a negligible value.

The second-stage bobs have cables attached that are 174.66 in. long (one wrap) and function identically as the first stage. After the second-stage despin is complete, the spacecraft is spinning at a rate of $+0.14 \pm 0.2$ rpm, and the despin system has performed its complete function.

III. Mechanics of a Yo-Yo Despin System

The basic factors governing the transfer of angular momentum of a rotating spacecraft to masses attached to cables wrapped about the circumference of the vehicle are most simply described by J. V. Fedor (Ref. 1). The Fedor equation is

$$\frac{1+r}{1-r} = \frac{I}{\left(m + \frac{KL}{3}\right)(L+R)^2}$$

where

r = final rate/initial rate

I = vehicle inertia

m = combined mass of bobs

K = combined linear density of cables

L = length of cable

R = radius about which cable is wrapped

Inspection of the Fedor equation yields an interesting and valuable fact. If the final spin rate is to be zero, r will equal zero, and if r is equal to zero, the final rate will be independent of the variations in the initial rate. If the final rate is to be small compared with the initial rate, the effect of variations in the initial rate on the final rate will be small and diminish to zero as the final rate approaches zero. This is a very important fact in considering a two-stage yo-yo despin system. Errors in the first stage resulting in deviations from the expected final rpm of the first stage will have little effect on the final stage rpm if it is designed to closely approach zero rpm.

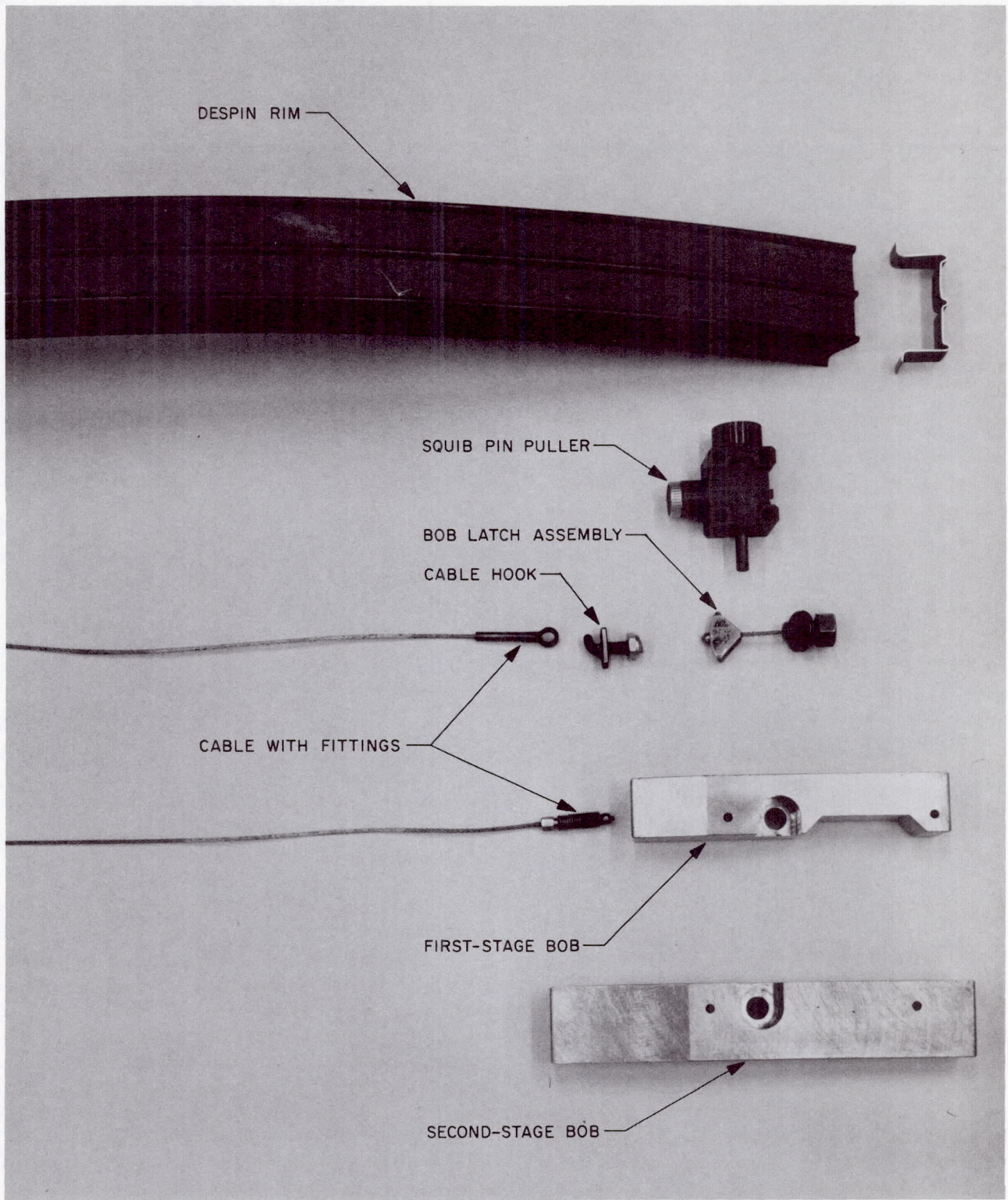


Fig. 1. ATS despin system components

IV. Thermal Design

A. General Considerations

Thermal design was the major problem with the despin rim. During the 90-min period between shroud separation and spin-up, and after despin, the temperature differential around the rim could range from -100°F to $+320^{\circ}\text{F}$. The spacecraft is thermally controlled in critical areas to a range of $+40$ to $+100^{\circ}\text{F}$. The despin rim must be thermally insulated from the internal structure of the spacecraft because the large rim area of 750 in.^2 would impose an impossible thermal load on the spacecraft's thermal control system. While the spacecraft is spinning, the rim temperature is estimated to be $+120^{\circ}\text{F}$. The maximum circumferential expansion of the rim will be approximately 0.580 in. from room temperature assembly conditions.

A radially disposed, pivoted support link was used to provide for thermal expansion movement at all except one spacecraft attachment point for each section of a four-section despin rim. This construction results in a rim with substantially constant diameter for temperatures ranging from -100°F , in an eclipse of the sun, to $+320^{\circ}\text{F}$. In this way, the aluminum rim is at a relatively constant temperature, thus avoiding all thermal problems. The despin rim support links and fixed mountings are made of thermal insulating materials to reduce heat conduction from the despin rim to the spacecraft at rim mounting points. A thermal blanket is provided between the back of the despin rim and the spacecraft to stop direct thermal radiation from the despin rim to the spacecraft. The despin rim doubler channels and rim fittings provide ten cable separation guides distributed around the rim. The ten guide sections have a guide groove 0.150 in. deep for each 0.062-in. -diameter cable.

B. The Effects of Differential Expansion Between the Steel Cable and the Aluminum Rim

The seven-strand, 0.062-in. -diameter, MIL-C-18375, stainless steel, nonmagnetic cable will have a $9.2\ \mu\text{in./in.}/^{\circ}\text{F}$ coefficient of linear thermal expansion. One side of the rim and cable coil will receive solar radiation and will approach 320°F , while the shadowed side will approach -100°F . The cable is Teflon-coated. The coefficient of friction with the rim will not exceed 0.1 . We may expect the cable tension from the varying thermal conditions around the rim to equalize because of the low coefficient of friction with the rim. Each turn of the cable about the 57.750-in. -diameter rim will change circumferentially 0.443 in. for a temperature range of 270°F . Since

the rim will not change significantly in circumference, two sets of diametrically disposed cable tensioners will be used to prevent excessive cable slack.

V. Sliding Surface Lubrication

Surfaces of parts that will have any sliding or moving contact with each other will be coated with a molybdenum disulfide solid-film lubricant. This material will be used primarily to prevent high friction coefficients and adhesion due to frictional movement in space vacuum. The particular lubricant, Dri-Lube No. 6, was used extensively on critical mechanisms in the successful *Surveyor I*, including the heavily loaded, fully exposed worm gear drive for the antenna solar panel. The high-vacuum adhesion and bearing problem on the ATS despin system is not considered as critical as on the *Surveyor*, since no prolonged operation with moving contact of parts is required. The only serious problem could come from vibratory movement of parts that subsequently must release with very low force, such as the second-stage bobs. In this case, the close-fitting ball end dowels locating the bobs on the fitting and the 100-lb tension of the latch should prevent vibratory fretting of the dry-film-coated contact surfaces between the fitting and the bob.

VI. Assembly Considerations

Assembly fixtures will be employed to achieve a track plane perpendicular to the true spin axis within 0.25 deg , and a total runout relative to the true spin axis of 0.09 in. or less, to minimize off-axis rates after the despin operation. The accuracy of despin assembly and location on the spacecraft will not depend on manufacturing tolerances. Two 0.062-in. adjustable shims are provided at each of the ten spacecraft attachment positions, allowing for adjustment of despin rim concentricity and axis angle to the spacecraft. At assembly the spacecraft will be mounted in an assembly jig with provision for precisely rotating the vehicle about its spin axis. Each of the ten despin system mounting stations of the vehicle will be gaged for conformity to the drawing tolerances, and precise measurements will be taken from which the actual shim thicknesses for that position will be determined. These shims will be mounted permanently between the spacecraft structure and the thermal insulator despin rim mounting support. Disassembly and reassembly can be accomplished without disturbing the initial installed accuracy of the shim adjustment. To remove a despin section or the whole unit, only the outer pivot pins and four

bolts in the fixed end mounting are removed, without disturbing the position adjustment shims under the brackets, which remain attached to the spacecraft.

VII. Test Programs

A. Testing of Prototype Despin System

A prototype despin system was tested insofar as the limitations of the sea-level air-pressure and gravity environment permitted. A set of experimental hardware was fabricated in which all dimensions and materials considered significant to the test were identical with the flight article. The despin assembly was mounted on a cylinder with a diameter similar to that of the spacecraft and an inertia equal to the roll axis inertia of the spacecraft at the time the tests were run (63 slug/ft^2). The simulated vehicle was attached to a low-friction bearing mount on a stand secured to the ground at the center of a 70-ft circle. The area was enclosed by a fence and sealed off with sand bags sufficient to stop a released first-stage bob.

Three 400-frame/sec, high-speed cameras were used. Two cameras overlooked the simulated vehicle atop an overhead-boom-supported camera platform. This coverage included a wide-angle and a telephoto lens on the overhead cameras. The despin system and simulated spacecraft were driven at speeds of 100 to 98 rpm during the release cycle. Ten first-stage despin operations were simulated. Two second-stage runs were made: one at an initial 10 rpm, and another at an initial 100 rpm.

The following was concluded from a detailed analysis of the photographic record:

- (1) The first-stage despin system performed within predicted values, when the effects of air drag in slowing down the bob and cable velocity are accounted for.
- (2) The angular displacement between first-stage bobs at final cable separation from the spacecraft varied from 0 to 3 deg. The hook release angle of the cable was 90 to 93 deg. The off-axis rate error for 3 deg of difference in release angle is 0.0323 rpm.
- (3) All twelve releases of the despin bobs occurred without fault.
- (4) The second-stage despin tests at the specified initial speed of 10 rpm could not result in deployment of the bobs or in despin action. The test was run to check the bob release mechanism at the low

centrifugal force of 0.27 lb generated at 10 rpm. The bob release action was entirely satisfactory.

- (5) The motion pictures showed considerable rotation of the bob and twisting of the cable during the release cycle. Aerodynamic effects may be responsible for a major part of the bob rotation. In any event, the bob and/or cable rotation did not prevent a satisfactory result.

B. Second-Stage Bob Release Test

Because the centrifugal force acting on the second-stage bob at 10 rpm is only 0.273 lb, and the latch mechanism design to provide the mechanical redundancy of the two pin-puller release systems is somewhat complex, additional tests were made of the second-stage bob release mechanism. The despin rim, one cable assembly, and one low-speed bob were assembled on the test fixture with $5_{-0.5}^{+0}$ lb cable tension. The low-speed bob was supported by two very flexible, 6-ft radio dial cables in order to simulate a weightless condition. A horizontally disposed cable with a pulley and weight was attached to the bob in a line passing through the center of gravity and was arranged to provide 0.27 lb of force on the bob in a direction to simulate 10 rpm centrifugal force on the bob (Fig. 2). Motion pictures at 600 frames/sec provided the means of analyzing the bob motion in detail for the critical first 6 in. of release travel. A photographic record of each single pin-puller release action, each normal or dual pin-puller release action, and a run of manual pin-puller operations was made and analyzed. Before making the photographic record, 20 manual releases were made. All release action was entirely satisfactory and without irregularities of any kind.

VIII. Error Analysis

The results of an analog study indicated that the maximum expected spin-axis offset (from the geometric axis), approximately 0.014 ft, produces imperceptible off-axis rates at the end of the second stage. In fact, with the wrap plane 1 ft from the vehicle's center of gravity, and a spin-axis offset of 0.5 ft (35 times the expected value), the maximum off-axis spin rate is only 0.25 rpm. The time difference between bob releases under these conditions is only 0.64 sec. The most significant off-axis rate error contributor appears to be the wrap plane inclination. Considering all the other errors negligible, the wrap plane must be within $\frac{3}{4}$ deg of the normal to the spin axis in order to maintain the off-axis rates within the

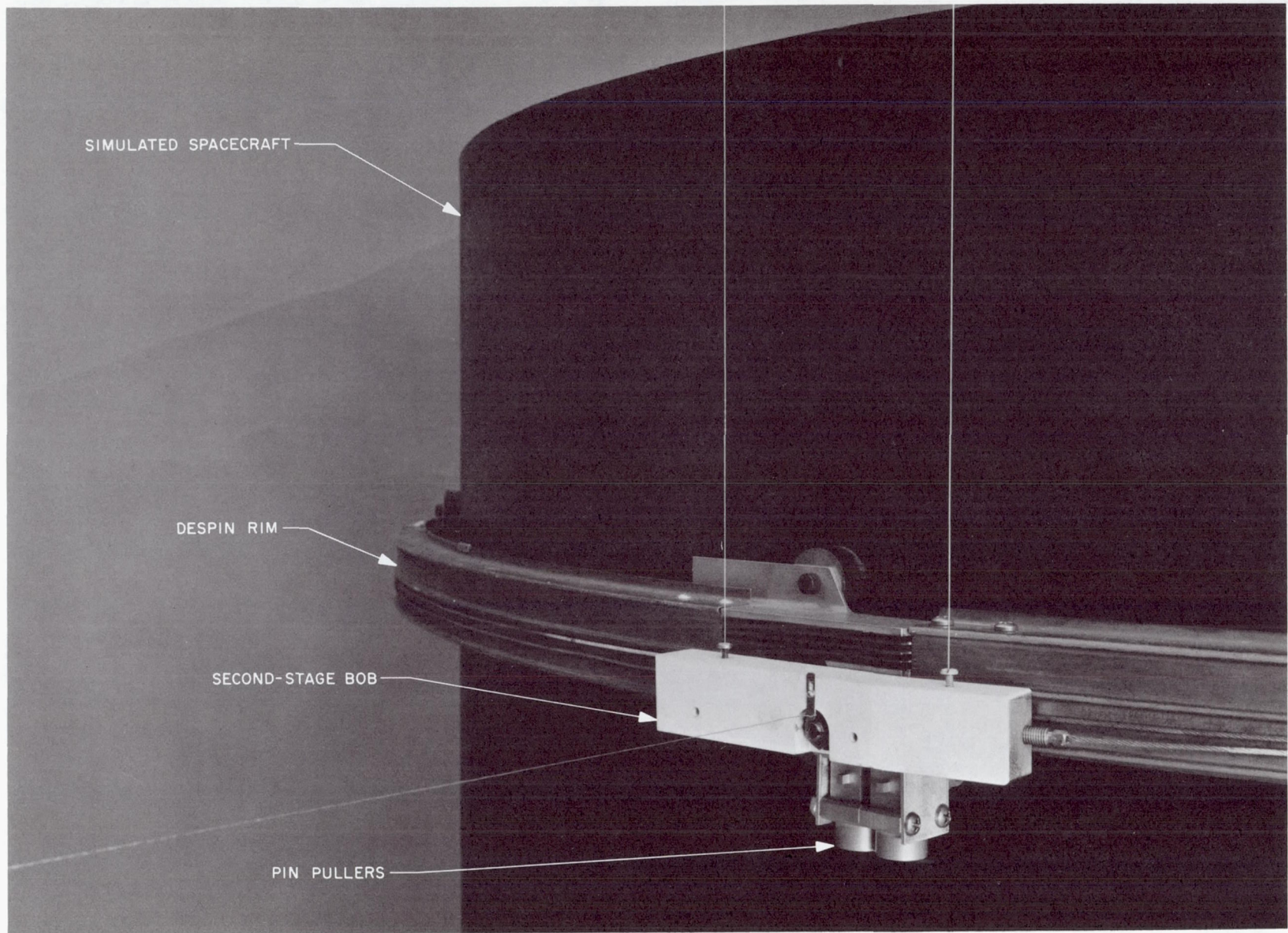


Fig. 2. Second-stage yo-yo bob release test

specified tolerance of 0.2 rpm. Expected error is $\frac{1}{4}$ deg, giving an off-axis rate of approximately 0.015 rpm.

An analysis of the uncertainties associated with the vehicle and yo-yo physical properties established the total worst cases due to these uncertainties. The assumed tolerance uncertainties are:

- (1) The combined bob mass is controlled to within ± 1 oz.
- (2) The inertia can be predicted to within 1%.
- (3) The vehicle radius uncertainty due to tolerances and temperature effects is $\pm 1/16$ in.
- (4) The cable length is cut and fastened to ± 0.02 in.
- (5) The error in initial spin rate is 2.5%.
- (6) The error in bob release angle is ± 4 deg.

IX. Conclusions

Conclusions are as follows:

- (1) A two-stage yo-yo despin system, operated with a nutation damper to reduce first-stage off-axis rates prior to release of a low-initial-rpm second-stage yo-yo, provides the despin accuracy necessary for a gravity-gradient-stabilized synchronous satellite.
- (2) The dimensional elements of this two-stage yo-yo despin system are noncritical compared with other systems considered. This should favorably influence reliability and cost. Reliability is favorably affected because the margin of predicted performance over required limits can be made comfortably large.
- (3) Critical thermal problems and high-vacuum bearing problems have been solved with large margins of safety.

References

1. Fedor, J. V., *Theory and Design Curves for a Yo-Yo Despin Mechanism for Satellites*, NASA TN D-708. National Aeronautics and Space Administration, Washington, Aug. 1961.
2. Eide, D. G., and Vaughan, C. A., *Equations of Motion and Design Criteria for the Despin of Vehicles by the Radial Release of Weights and Cables of Finite Mass*, NASA TN D-1012. National Aeronautics and Space Administration, Washington, Jan. 1962.

Weld-Alloy

John C. McDonald and J. C. Olsen
Lockheed Missiles and Space Company
Sunnyvale, California

Weld-alloy research described in this paper has verified the hypothesis that an overlaid weld of specific metal would produce a predictable alloy with a given base metal, and that the resultant weld-alloyed seam would have predictable mechanical properties. The intended use of this technique was development of peripherally weld-alloyed removable areas of stressed-skin vehicle structure. Laboratory tests to indicate weldability, alloying tendencies, tensile strengths, and susceptibility to bending and shock were performed. As a result of these investigations, it is concluded that predictable alloying and mechanical properties were indicated. It is felt that considerable research will have to be done to develop production techniques.

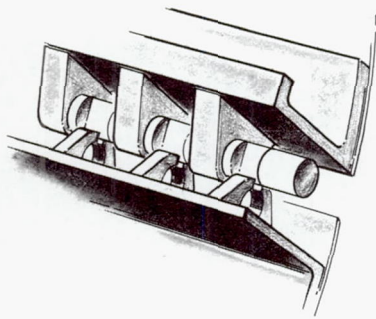
I. Introduction

Aerospace vehicles usually require load-carrying systems that are removable by mechanical means or by stressed-skin separation; such systems include booster adapters, nose shrouds, and deployment or emergency hatches (see Fig. 1). The mechanical systems range from hinged or pinned doors to explosive bolts, while stressed-skin systems are usually separate stressed-skin structures, bridged to the primary structure by notch-sensitized doubler strips.

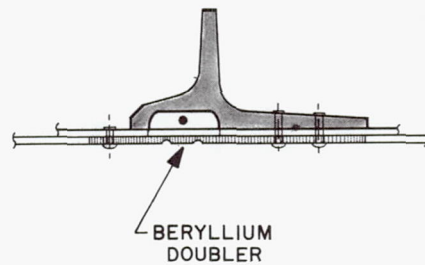
Mechanical systems have proved to be quite effective; however, reliability can be a problem in certain situations. Since mechanical systems function in series,

total system reliability is a function of the number of components; furthermore, mechanical systems in general impose weight penalties. Because of their positive sealing and high-reliability features, stressed-skin panels held in place by notch-sensitized doublers are usually chosen. Both expendable nose cones and deployment hatches currently in aerospace use are predominantly of the notch-sensitized doubler type; however, they have the major disadvantages of higher cost, greater weight, and fabrication difficulty. Although lighter than mechanical systems, they still weigh at least 1.5 times the weight of basic structure. From the cost standpoint, even the present stressed-skin systems are (per unit area) probably the most expensive structure in a vehicle. At the present time, however, this technique is considered satisfactory

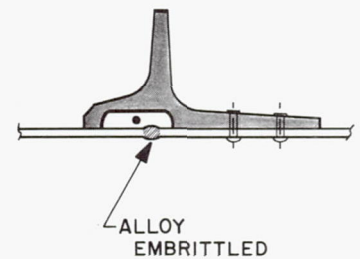
(a) MECHANICAL RELEASE



(b) FRANGIBLE DOUBLER



(c) FRANGIBLE STRUCTURE (WELD-ALLOY)



(d) APPLICATION OF WELD-ALLOY SYSTEM

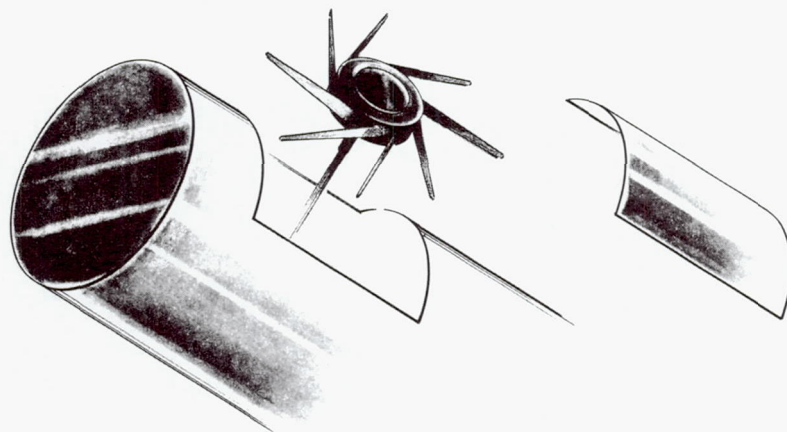


Fig. 1. Mechanisms to meet the requirement for an aerospace separation system

for unmanned spacecraft, although it is not applicable for projected commercial jet aircraft emergency hatches or similar uses.

If it would be possible to remove stressed-skin structure, without incurring the weight of a mechanical system, or the cost and fabrication difficulty of the notch-sensitized doubler systems, it would have to be by means of a unique removal system. This paper describes a process that would predictably change the physical properties of specified regions of stressed-skin structure to allow removal by shock loading or local bending. Or, in other words, the engineering principles of the "pop-top can" have been brought to the aerospace industry.

This paper also describes a proposed process that can selectively embrittle the periphery of the section of stressed-skin structure to be removed, and then, by applying a local shock load, remove the embrittled region,

thus creating an opening in the basic structure, with no fabricated door and no separate break plates. The embrittlement would be accomplished by alloying the selected region of the stressed-skin structure by "in-place welding." To accomplish the preselected degree of embrittlement and load-carrying ability, the alloying would need to be predetermined by careful selection of weld alloying elements.

The art of alloying has been exploited for many years to obtain certain characteristics in metals. The art has been refined and codified, and in most instances preselection of compatible elements is possible. More recently, metallurgical theory has provided techniques of predetermining stress/strain relationships of proposed alloys. The importance of this knowledge is that it creates the possibility of providing a region on the basic load-carrying stressed-skin structure whose periphery is capable of carrying flight-bending or hoop-tensile loads, but which

is also sensitive to local bending. This peripherally embrittled area may be removed by several proven techniques. One satisfactory method uses "Zip Cord".¹

II. Weld-Alloy

A. Anticipated Loading

The proposed technique of developing breakaway areas in basic stressed-skin structure must begin with appreciation of anticipated loading efficiency and accepted aerospace industry practices. Loading efficiency is based on recognition of material failure mode. Cylindrical shell structures are designed to function with their maximum expectation limited by buckling failures. On the other hand, rings are limited by material compressive failure.

Therefore, both geometry and the physical properties of material will limit specific design efforts. Accepted aerospace industry practices establish the following definitions:

Limit load	= maximum anticipated load
Yield load*	= 1.00 × limit load (unmanned) 1.15 × limit load (manned)
Ultimate load**	= 1.25 × limit load (unmanned) 1.50 × limit load (manned)

* Structure will not yield below this load.

** Structure will not fail below this load.

With regard to these requirements, there is the option of designing a ring or narrow axial region that can provide failure mode strength equal to the required ultimate strength of the basic stressed-skin structure, but has a different failure mode.

Normal axial and flight bending loads are transmitted through the stressed-skin structure as shown in the load diagrams of Fig. 2. These are reduced to line loads, i.e., those due to flight bending (N_{x_m}) and those due to axial thrust or reacting pressure (N_{x_A}). In pressurized vehicles, the hoop tensile loads (N_{x_h}) are incorporated and provide further modification to the axial compressive (N_{x_C}) or tensile (N_{x_T}) load the vehicle will have to

¹Leaman, Audley B., "Noncontaminating Separation Systems for Spacecraft (Project ZIP)" in *Proceedings of the First Aerospace Mechanisms Symposium*, pp. 61-71. University of Santa Clara, Calif., May 1966.

endure. Mathematical technique for calculating the required material strength or section is provided with the load diagram.

B. Material Considerations

Commonly used aerospace structural materials develop maximum area under the stress-strain curve. They are capable of carrying the required loads as well as absorbing the anticipated energy of vibrational and shock loading. As tests at the Lockheed Missiles and Space Company (LMSC) have shown, it is almost impossible to fracture these materials without generating prohibitively large shock loads. Under these circumstances, the question arises of how to break out sections of such tough, high-strength materials.

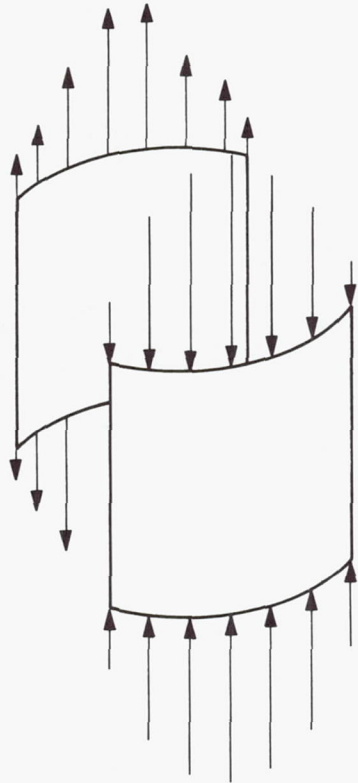
The answer was found in changing the mechanical properties of the material on the periphery of the desired removal section. Of the several methods investigated, the most practical approach appeared to be alloying the peripheral material to reduce its toughness. By selective alloying, LMSC was able to reduce the energy absorption characteristics while maintaining strength at tolerable levels. Careful selection of alloying agents allowed reduction of the area under the stress-strain curve, while maintaining a relatively high yield point.

Of the several processes investigated, alloying the peripheral material offered an additional advantage: alloying can be accomplished by in-place welding. This welding may be scheduled at any convenient phase of the fabrication sequence. Any desired area of basic stressed-skin structure may be removed after fabrication, like a pop-top can, if the periphery of this area has been selectively embrittled by weld-alloying.

C. Discussion of Research

An initial feasibility study was made to determine whether a brittle seam could be made in a base of strong, tough metal. The metal-using industry is well aware of the problems in designing welded structures. In all too many cases, it is impossible to join by welding or develop a joint that is as strong as the parent metal. The emphasis in welding research and development has always been to strive for welds of higher and higher strength. The proposed welding application is distinctive in that its objective is the direct opposite; namely, a weld that is sensitive to local bending. The problem is to create, in a sheet-metal structure, a line of arbitrary contour that is considerably less tough than the parent metal. As mentioned

(a) UNPRESSURIZED VEHICLE LOADS



$$\text{BENDING MOMENT} = \frac{\text{MOMENT}}{\text{SECTION MODULUS}} = \frac{Mc}{I}$$

$$\text{AXIAL LOAD} = \frac{\text{AXIAL REACTION}}{\text{AREA}} = \frac{P}{A}$$

$$N_{xm} = \frac{\text{MOMENT}}{\pi (\text{RADIUS})^2} = \frac{M}{\pi r^2}, \text{ lb/in.}$$

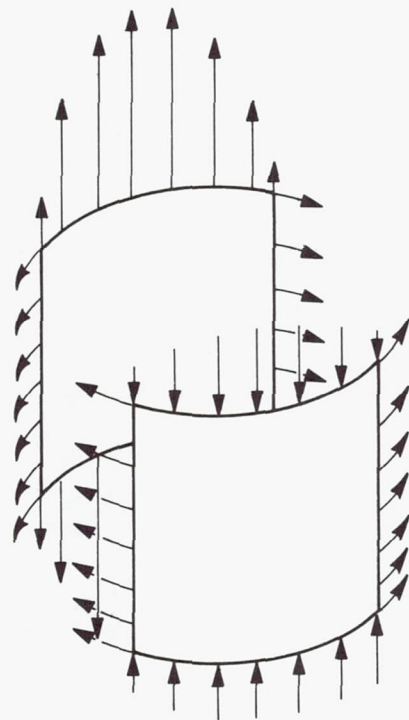
$$N_{xA} = \frac{\text{AXIAL LOAD}}{\pi (\text{DIAMETER})} = \frac{A}{\pi d}, \text{ lb/in.}$$

$$N_{xC} \text{ OR } N_{xT} = \pm N_{xm} \pm N_{xA}$$

STRUCTURE THICKNESS = t

$$\frac{N_x}{t} = \text{STRESS (lb/in.}^2\text{)}$$

(b) PRESSURIZED VEHICLE LOADS



IN PRESSURIZED VEHICLES, LOADS
REDUCE TO:

$$N_{xh} = f_h t = Pr \text{ (HOOP TENSILE LOAD)}$$

$$\frac{1}{2} N_{xh} = \frac{Pr}{2} \text{ (LONGITUDINAL LOAD)}$$

$$N_{xC} - \frac{1}{2} N_{xh} \text{ (AXIAL LOAD, COMPRESSION)}$$

$$N_{xT} + \frac{1}{2} N_{xh} \text{ (AXIAL LOAD, TENSION)}$$

Fig. 2. Typical flight loads

previously, such a concept would have no place except in a structure that is critical under compression loading, but in which there is no critical tensile requirement.

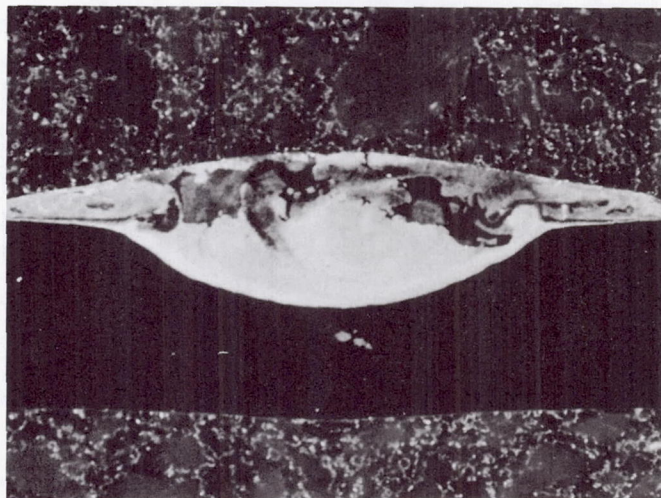
The specific material of concern here is the Al-6.3% Cu alloy known under the Aluminum Association's designation as Al 2219. In the commonly used temper of highest strength, -T87, previous experiment had shown that the explosive charge required to cut a reduced section at minimum tolerable gage would produce a shock loading considerably greater than desirable. The published literature on the welding of this alloy indicates that a weld bead of the same composition will have a typical ultimate strength of 40 ksi. The yield strength of this metal is relatively low, about 20 ksi, with a typical elongation of around 20%. The metal is tough and ductile, and would probably require as much explosive to break as that required for a thinned-out section of parent metal.

The solution to the problem appeared to lie in the brittleness and low-strength characteristics of intermetallic compounds. The published phase diagram for magnesium and aluminum indicates that a 50-50 alloy of the two metals would consist of a mixture of such compounds. In the tests performed, a pure compound MgAl exists over a narrow range of resultant samples.

Producing a mixed composition poses some special problems not ordinarily encountered in welding. In principle, magnesium wire can be fed into the arc of a welding torch that is melting underlying aluminum, thus permitting a mixture of the metals to form in the weld pool. However, unless good mixing is obtained, the much lighter magnesium will simply float on the aluminum. Alloying would occur at the interface, of course, producing at least a layer or zone of brittle intermetallic compounds; this was the case in the experiments reported in this paper. Further work is required to determine whether complete mixing is needed and what process conditions will be required to achieve that objective.

Tungsten-inert gas (TIG) welding with ac current was tried on 0.063-in.-gage Al 2219-T87. The weld wire was the commonly used alloy AZ92A (9% aluminum plus 2% zinc); shielding gas was 75% He plus 25% Ar; voltage and current were 14 v and 80 amp, respectively. A carriage speed of 30 in./min was used with a wire feed of 25 in./min. The macro and micro structures of the resulting bead are shown in Fig. 3. The photomacrograph of the sectioned weld shows that mixing was only partially obtained; furthermore, that mixing was not com-

(a) PHOTOMACROGRAPH, 20X MAGNIFICATION



(b) PHOTOMICROGRAPH, 200X MAGNIFICATION

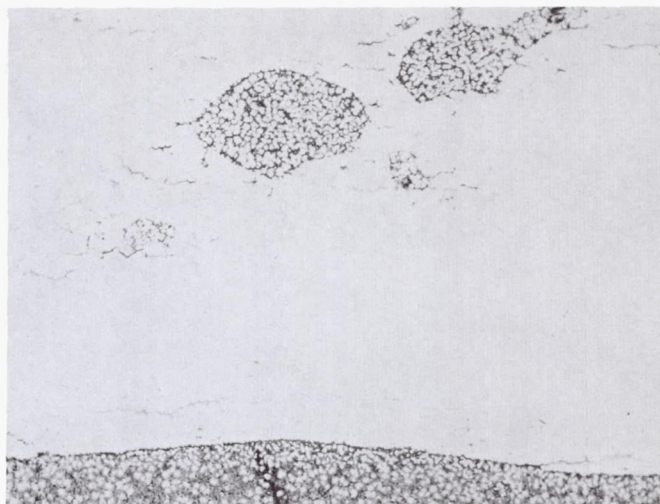
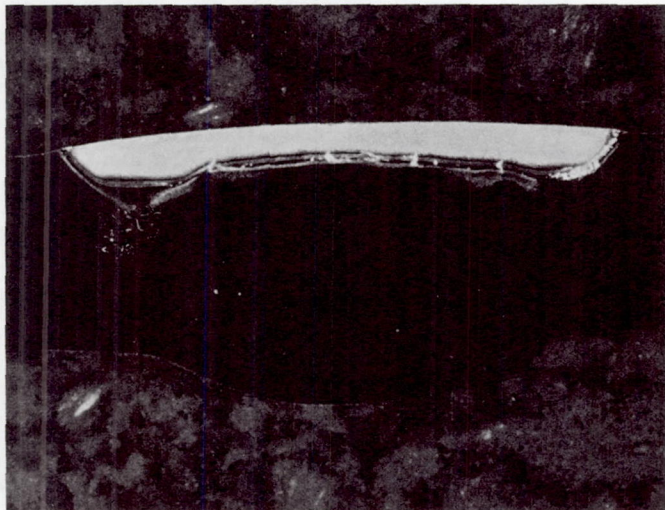


Fig. 3. Structures of AZ92A wire/Al 2219-T87 plate, ac weld

pletely homogeneous. The photomicrograph shows that some of the material is substantially single-phase (possibly pure compound), whereas other regions are two-phase. The weld was aged to the -T87 temper (24 hr at 325°F). A standard tensile bar was obtained transverse to this weld and showed an ultimate strength of 12.5 ksi when pulled to failure.

A similar test was run with dc current, straight polarity, using high frequency at the start at 15 v and 125 amp with pure helium shielding (other conditions were the same). The micro and macro sections of this weld are

(a) PHOTOMACROGRAPH, 20X MAGNIFICATION



(b) PHOTOMICROGRAPH, 100X MAGNIFICATION

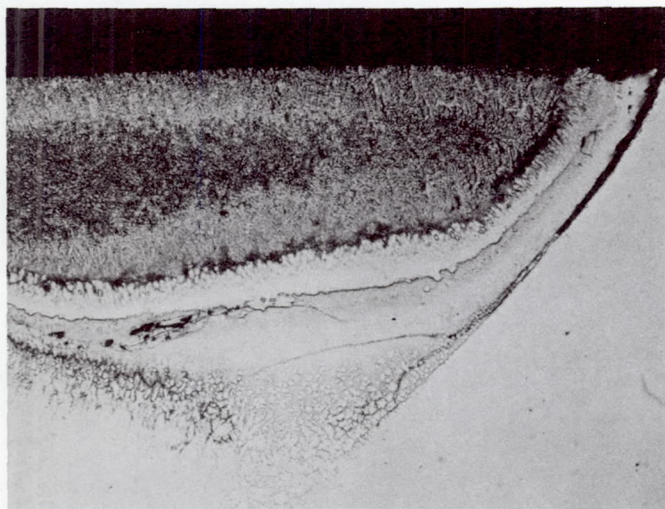


Fig. 4. Structures of AZ92A wire/A1 2219-T87 plate, dc weld

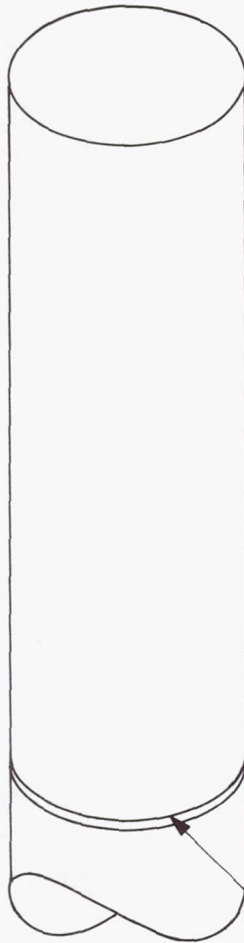
shown in Fig. 4. While melting of the aluminum was achieved, little mixing was noted. The structure at the top is substantially cast magnesium alloy; however, there is a thin zone of the brittle intermetallic compounds between the magnesium and the cast aluminum underneath. A number of tensile bars from this specimen varied in strength from about 14 to 23 ksi. This is considerably less than would have been predicted from the strength of a weld-bead of 2219 aluminum and the ratio of areas of that part of the bead to the remaining magnesium-rich portion.

It was decided to prepare a specimen for field trial, using the second of the two techniques just described. Tensile specimens obtained from the panel that was actually used in the field tests had strengths of 24–25 ksi (3 bars). A “Zip Cord” charge of 2 grains per foot fractured this specimen cleanly.

Obviously, considerable development work will be required to establish process variables and process control techniques for the optimization of this type of weldment. It is perhaps surprising that anticipated results were achieved without getting full mixing through the thickness of the metal. If enough time is allowed for good mixing, it should be possible to achieve the original goal completely; however, there would be extra metal in the drop-through. (This drop-through may be machined off.) In theory it should be possible to produce an alloy in the cast bead of almost any desired composition between that of the base aluminum alloy and the base magnesium alloy in the weld rod. It may or may not be necessary or desirable to achieve a more or less fixed intermediate composition. The magnesium filler rod itself, when cast pure, has minimal ductility, and a strength only in the 30-ksi range.

Validity of the results should be viewed in light of the preliminary research reported in this paper. Specifically, an attempt was made to experimentally verify or refute the hypothesis that we could not only alloy by welding, but that the extent of embrittlement could be predicted. It is LMSC’s opinion that the research did verify the hypothesis and that further extensive research should be done to establish a matrix that will specify base metal, alloy metal, percent embrittlement, and resultant tensile strength.

In all cases, the base metal had its mechanical properties significantly changed in the region of the weld. As the base metal was a continuous sheet prior to welding, any changes in the area of the weld were due to the welding action. Bend tests of specimen coupons showed the bending tolerance to be significantly reduced. Although tests of compressive ultimate strength were not run, it follows that in a structure critical in buckling, tensile ultimate strengths are conservative estimates of ultimate strength. In the calculations for a “Stress Weld” full-ring interface, a ¼-in.-thick weld-alloyed seam, subjected to line loading, would conservatively satisfy the design limit requirements (see Fig. 5).



ASSUME: CYLINDRICAL SHELL $d = 5$ ft

$$\therefore \text{AREA} = \pi r^2 \cong 2830 \text{ in}^2$$

$$\text{CIRCUMFERENCE} = 2\pi r \cong 188 \text{ in.}$$

ASSUME: TYPICAL IMPOSED LOAD

$$\text{AXIAL} = 60 \times 10^3 \text{ lb COMPRESSION}$$

$$\text{BENDING} = 12 \times 10^6 \text{ in.-lb}$$

$$\text{THEN: } N_x = \pm \frac{\text{BENDING MOMENT}}{\text{AREA}} + \frac{\text{AXIAL LOAD}}{\text{CIRCUMFERENCE}}$$

$$N_{x_c} = \frac{(12)(10^6)}{(28)(10^2)} + \frac{(60)(10^3)}{188} \cong 4.6 \times 10^3$$

$$\cong 4.6 \times 10^3 \text{ lb/in.}$$

$$N_{x_T} = -\frac{(12)(10^6)}{(28)(10^2)} + \frac{(60)(10^3)}{188} \cong 4 \times 10^3$$

$$\cong 4 \times 10^3 \text{ lb/in.}$$

DESIGN LIMIT:

BUCKLING OF SHELL AND COMPRESSION
OF FRANGIBLE SEAM

$$\therefore (N_{x_c})(1.25) \cong 5.8 \times 10^3 \text{ lb/in.}$$

Fig. 5. Calculations for "Stress Weld" full-ring interface

Although it would require an excessive shock to rupture a tough metal² with capacity for the loading under consideration, a brittle material capable of withstanding this loading could be fractured with a 2-grain/ft "Zip Cord," as noted previously. A frangible, 1/4-in.-thick weld-alloyed seam, capable of tolerating 5.8×10^3 lb/in. compressive loading, would satisfy the design limit requirement (based on ultimate load, nonmanned structure).

²Typical of the tough, high-strength, aerospace materials investigated in this work was Al 2219-T87. Tensile strength = 65 ksi, elongation 18%, bend prior to crack = 150 deg.

The notation of Fig. 2, explained in the preceding text, applies to these calculations.

III. Conclusions

The key conclusion from the research to date is that predictable alloys of base metal and weld metal can be produced repeatedly by the welding techniques investigated. Further, it was verified that these alloys would develop predictable mechanical properties. Practical and economical fabrication techniques, however, require further exploration.

New Closed Tubular Extendible Boom

Bruce B. Rennie
The Boeing Company
Kent, Washington

A new concept has been added to the family of extendible booms. The Boeing-developed MAST (Multiple Applications Storable Tube) is a closed, collapsible tube that may be used to transport fluid and transmit torque in addition to the other functions performed by currently used extendible booms. Data are presented to serve as a design guide, and the development work is described.

I. Introduction

Extendible booms, which can be rolled up compactly on a cylindrical drum for stowage and can be deployed to serve as rigid structural members, are well suited for space applications. Their growing popularity for use in space is due to the increasing need for long antennas and large structures and the requirement that these devices must be compactly stowed and firmly supported during the launch of the spacecraft. Furthermore, these rather light and thin-walled tubes can be used in space applications where they are exposed to the relatively low acceleration forces imposed by orbital maneuvers. As an attachment or tethering device, the collapsible tube (good in compression and torsion as well as tension) may be used for space applications where a flexible line (good in tension only) would be unsatisfactory.

II. Background

The need for extendible booms has stimulated the development of the collapsible tube constructed of flat-sheet, spring-temper material, formed into a tubular shape and capable of being flattened and wound on a mandrel. The extendible boom concept that has received the most attention and widest application to date in the United States' space program is the de Havilland STEM (Storable Tubular Extendible Member). This device is based on an extension of the "carpenter's rule" principle; i.e., it derives its stiffness from a cross section that is the arc of a circle. The STEM tube cross section is a 540-deg arc ($1\frac{1}{2}$ turns) instead of the 15 or 20 deg typical of the carpenter's steel tape. Design data (Ref. 1) for this type of extendible boom were presented in a report prepared for the United States Air Force by the American Machine

and Foundry Company. The STEM is an open tube, incapable of transmitting torque or transporting fluid.

III. The Multiple Applications Storable Tube (MAST)

To overcome the torque and fluid transport limitations of the open tube, the Boeing Company is investigating a new type of closed tubular extendible boom called the MAST. Figure 1 is a photograph of a 20-ft-long tube of 0.008-in. PH 15-7 MO stainless steel installed on a reeling mechanism with a 10³/₄-in. drum diameter.

The MAST boom is a closed tube that flattens and rolls up on the drum as a double sheet, in contrast to the STEM, which rolls up as a single sheet. The radius of the tube, thickness of material, and diameter of the reel are chosen so that maximum stress does not exceed the elastic limit of the material.

A. Applications

The name "Multiple Applications Storable Tube" is appropriate for this concept in view of the many possi-

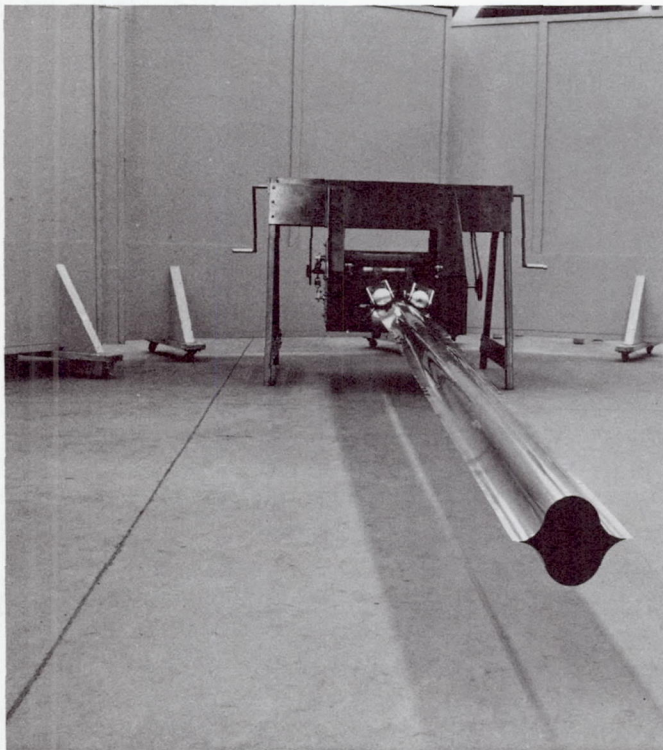


Fig. 1. Demonstration MAST boom

bilities for space- and earth-based applications. A few space applications are shown in Fig. 2. Other potential space applications are as docking booms, pressurized antennas, gravity gradient booms, extendible grappling booms, rigging masts, and flexible panel deployment and support. An extendible boom of this type has been proposed (Ref. 2) for deployment and support of a flexible solar array. A tube of similar cross section was proposed (Ref. 3) for a fluid transport application by NASA researchers.

B. Design Considerations

Factors that must be considered in designing a MAST for a particular application include the types of stress discussed below.

1. *Stress induced by flattening.* Tensile (or compressive) stress induced by flattening the collapsible tube is a function of the radius-to-thickness ratio and is defined by

$$S_x = \frac{E}{2(R/t)(1 - \nu^2)} \quad (1)$$

where

S_x = tensile (or compressive) stress at the tube surfaces, psi

E = Young's modulus, psi

R = radius of curvature, in., as defined in Fig. 3

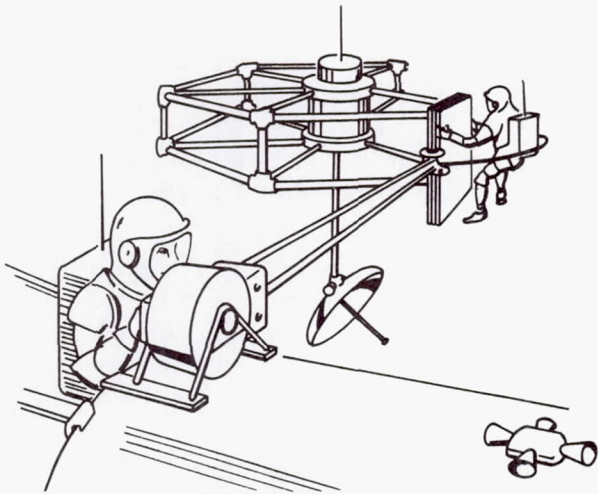
t = thickness of material, in.

ν = Poisson's ratio

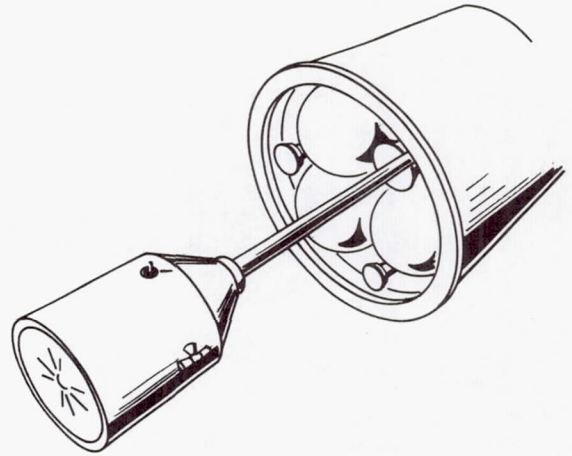
2. *Stress induced by winding on drum.* When the flattened tube is wound on a drum, longitudinal and transverse stresses are induced at the tube surfaces. The tensile (or compressive) stress S_y , induced by drum curvature, is directed parallel to the tube centerline and normal to the stress S_x induced by flattening the tube. The stress S_y is a function of drum diameter and is defined by

$$S_y = \frac{2tE}{D(1 - \nu^2)} \quad (2)$$

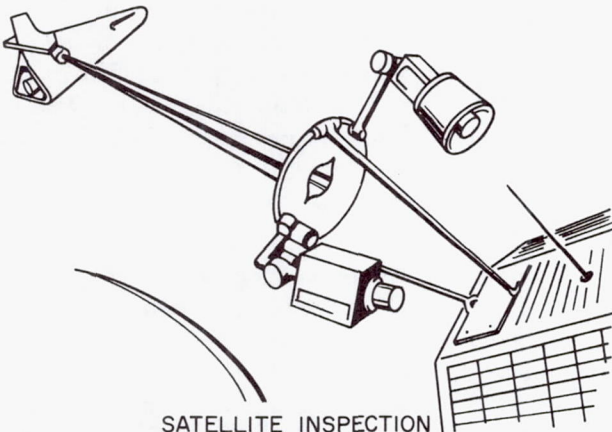
where D is the drum diameter in inches.



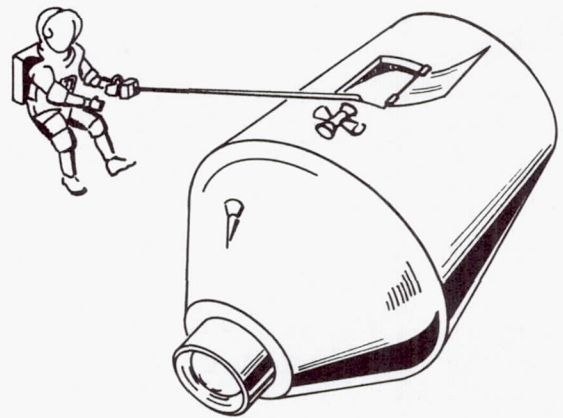
ASSEMBLY IN SPACE



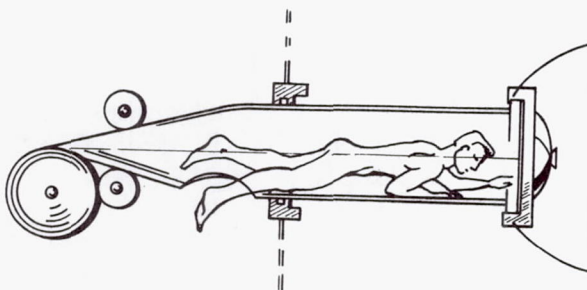
FUEL TRANSFER



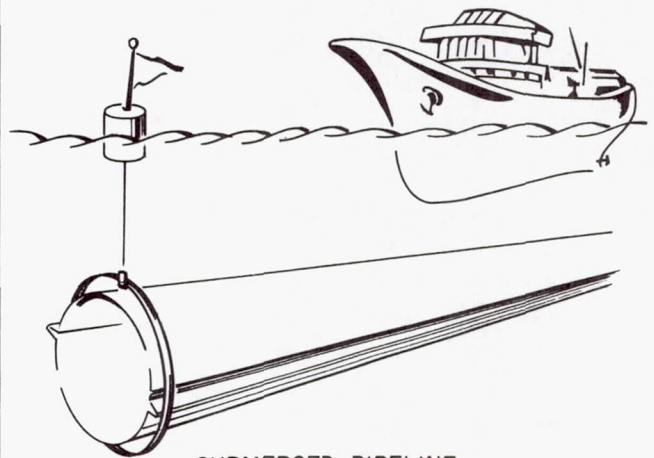
SATELLITE INSPECTION



ASTRONAUT'S "CANE"



CREW TRANSFER



SUBMERGED PIPELINE

Fig. 2. MAST boom applications

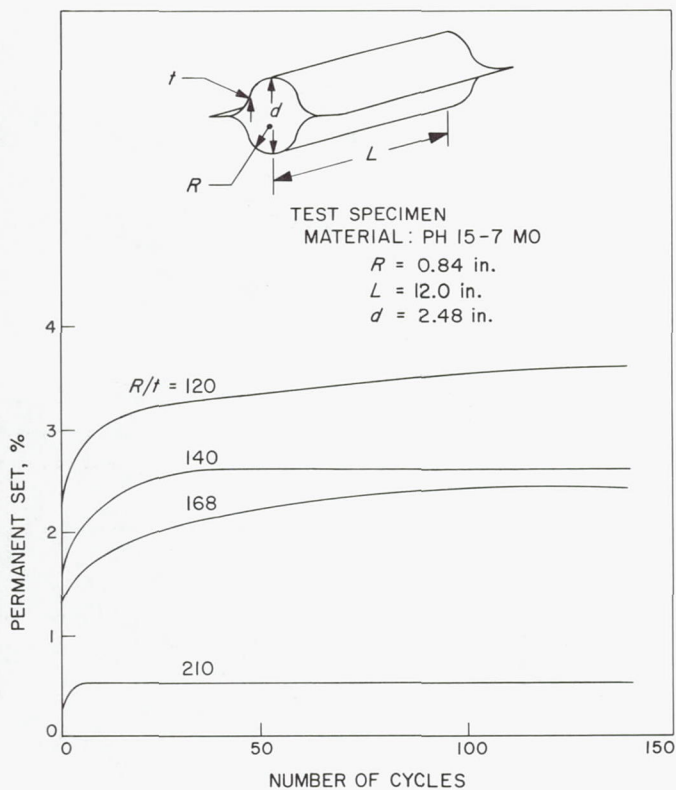


Fig. 3. Permanent set vs flattening cycles

3. *Maximum shear stress.* Shear stresses that arise from the perpendicular tensile (or compressive) stresses S_x and S_y are maximum over a cross section whose normal is inclined at 45 deg to the direction of S_x . Maximum shear stress is defined by

$$(S_s)_{max} = \frac{S_x - S_y}{2} \quad (3)$$

In this calculation, tensile stress is considered as positive and compressive stress as negative.

Radius-to-thickness ratio and drum diameter must be large enough so that the normal stresses S_x and S_y do not exceed the tensile or compressive yield strength, and so that $(S_s)_{max}$ does not exceed the shear strength of the material.

C. Manufacture

To investigate the feasibility of the MAST concept, Boeing has constructed a number of sample tubes for demonstration and test purposes. Two different methods of manufacture have been used.

1. *Two forming methods.* In the first method, the forming process starts with the sheet material in the annealed condition. The two sheets are joined along the edges by spot welding or seam welding. The tube is formed into the correct shape by mounting it in the forming jig and then subjecting it to the heat-treat cycle.

In the second method, the forming process starts with the sheet material in the heat-treated condition. Each tube half is brake-formed into the required shape. The two tube halves are then flattened by clamping between flat plates while the flanges are joined by spot welding.

2. *Fabrication of long tubes.* The length of tube that can be fabricated by the first method is limited by the length of the heat-treat furnace. The length of tube sections formed by the second method is limited by the length of the forming brake. However, longer tubes have been satisfactorily formed with the second method, by joining tube halves end-to-end through welding with a tungsten-inert gas (TIG) welding process. The two built-up tube halves are then flattened and the flanges are joined by spot welding. At present, a 50-ft tube is being fabricated by this method for installation on the winch assembly shown in Fig. 1.

For relatively high production rates, a facility can be designed for fabricating very long collapsible tubes, using a modified version of the first method. The process is continuous, with the material moving at constant speed over a forming mandrel, through the welder, and through the heat-treat chambers. Thus, each increment of the tube is exposed to the same heat-treat cycle. The process starts with a storage drum of annealed material wound as two sheets and ends with a storage drum on which the completed tube is coiled.

3. *Materials.* A list of candidate materials and the properties that are of interest is presented in Table 1. Boeing has constructed tubes from beryllium copper, 1095 steel, AM 350 CRT, PH 15-7 MO, and 18N250 maraging steel. Most of the fabrication and test work has been done with PH 15-7 MO stainless steel.

D. Testing

A limited amount of testing has been done by Boeing, to verify concept feasibility and to investigate the suitability of PH 15-7 MO stainless steel as a boom material; compression testing has also been performed to obtain data on local buckling.

Table 1. Properties of candidate materials

Material	$(R/t)_{min}$	Yield strength/density at 70°F, in. × 10 ³	Yield strength/density at 400°F, in. × 10 ³	Thermal conductivity, (Btu-in.)/(ft ² -hr °F)	Coefficient of thermal expansion, (in./in. °F) × 10 ⁻⁶	Electrical resistance, μohm-cm	Magnetic
Beryllium copper: 25	52	605	537	750	9.3	8	No
Spring steel: 1095 sheet	122	482	434	327	6.2	18	Yes
Precipitation hardening steels:							
17-7 PH (TH1050)	86	656	585	146	9.5	31	Yes
PH15-7 MO (TH1050)	80	710	656	146	8.5	31	Yes
AM 350 (DA)	97	594	490	106	6.3	32	Yes
AM 355 (SCT850)	87	664	525	106	—	—	Yes
Maraging steel:							
200	77	657	623	138	5.6	30	Yes
250	58	899	830	138	5.6	30	Yes
300	52	1003	865	138	5.6	30	Yes
Maraging stainless: Almar 362	93	612	523	—	6.0	—	Slightly
Titanium: Ti-6AL-4V (aged)	60	938	812	50	4.9	178	No
Invar 36	282	137	—	73	0.655	32	—
Inconel X (aged)	136	419	386	83	7.0	48	No
Aluminum: 7075-T6	83	660	300	1580	13.1	5.7	No

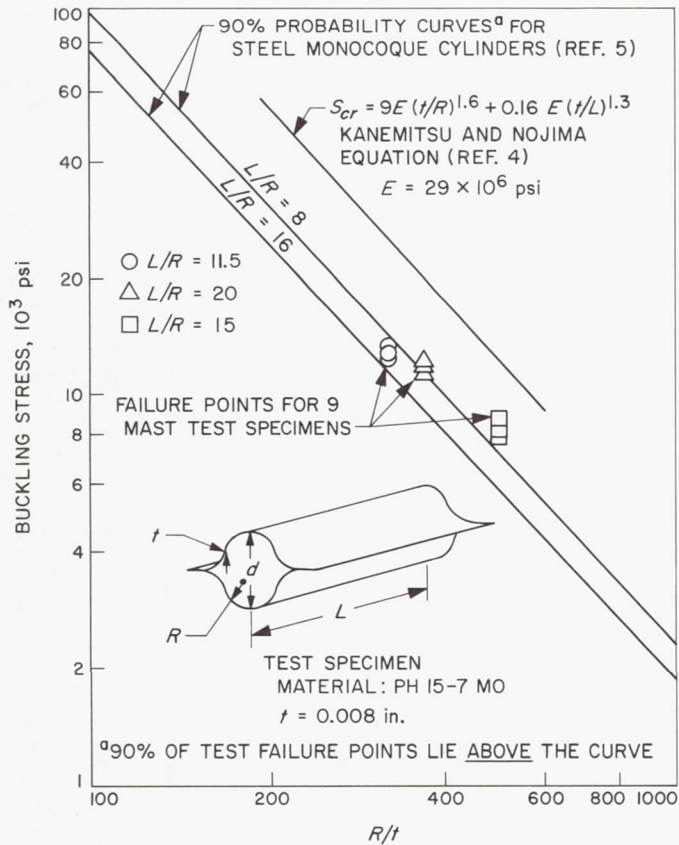


Fig. 4. Results of compression tests (short-column buckling)

1. *Permanent set vs flattening cycles.* Four tubes, each 1 ft long, were constructed of PH 15-7 MO material using sheet thicknesses of 0.004, 0.005, 0.006, and 0.007 in. The radius of curvature was 0.84 in. for all four tubes, so that the R/t ratio was 210, 168, 140, and 120 respectively. The diameter of each tube was measured initially and the tube was then completely flattened by compressing between two flat rigid plates. This was repeated for 140 cycles and measurements were taken between cycles to obtain data for permanent set as a function of flattening cycles. Results are plotted in Fig. 3.

2. *Compression tests (short-column buckling).* Nine test specimens of PH 15-7 MO material 0.008 in. thick were subjected to short-column buckling tests. Three specimens were 30 in. long and the other six specimens were 60 in. long. The ends were ground parallel and the specimens were loaded in axial compression past the point of local buckling to the point where increasing deflection resulted in decreasing load. Results are shown in Fig. 4, which compares these data with failure prediction curves applicable to steel monocoque cylinders. The top curve is a plot on the log-log scale of the Kanemitsu and Nojima equation (Ref. 4):

$$S_{cr} = 9E \left(\frac{t}{R}\right)^{1.6} + 0.16E \left(\frac{t}{L}\right)^{1.3} \quad (4)$$

where

S_{cr} = buckling stress, psi

L = length of tube, in.

The two lower curves in Fig. 4 are 90% probability curves (Ref. 5) for steel monocoque cylinders. These data show that buckling stresses for these specimens of the MAST configuration are compatible with those of monocoque cylinders of equivalent R/t and L/R ratios.

IV. Conclusion

The MAST concept provides a new type of extendible boom. When retracted, the boom is collapsed and wound up on a reel as a double sheet. When extended, the MAST boom becomes a closed tube with torsional strength and fluid-carrying capability. The feasibility of this concept has been demonstrated by fabrication of sample tubes, preliminary tests, and installation on a hand-operated demonstration reel. The MAST concept is suitable for numerous space- and earth-based applications. Considerable development and test work remains to be done, but the potential for its useful applications appears to be sufficient to warrant the required additional effort.

References

1. Robins, H., DeMartino, P., and Moshavi, D., *Design of Tubular Extendible Booms for Structural Applications*, AFFDL-TR-65-62. American Machine and Foundry Company, York Division, York, Pa., for the Air Force Flight Dynamics Laboratory, Wright-Patterson Air Force Base, Ohio, June 1965.
2. *Preliminary Development Report for Deployable Large Area Solar Array Structure*, Report 20869-1. Ryan Aeronautical Company, San Diego, Calif., July 1965.
3. Gertsma, L. W., Dunn, J. H., and Kempke, E. E., Jr., *Evaluation of One Type of Foldable Tube*, NASA TMX-1187. Lewis Research Center, National Aeronautics and Space Administration, Cleveland, Ohio, Dec. 1965.
4. Peery, D. J., *Aircraft Structures*, p. 389. McGraw-Hill Book Company, Inc., New York, 1950.
5. Bruhn, E. F., *Analysis and Design of Flight Vehicle Structures*, pp. C8.3 and C8.6. Tri-State Offset Company, Cincinnati, Ohio, Jan. 1965.

Self-Destruct Charge Ordnance Component of the Agena D Vehicle Self-Destruct System

Allan Howard Smith
Lockheed Missiles and Space Company
Sunnyvale, California

The self-destruct charge ordnance component of the destruct system launched with the Agena D satellite vehicle is briefly described. Emphasis is placed on design philosophy, flight performance criteria, and testing techniques. Results of simulated vehicle destruction tests are compared with data from an actual flight destruction of an Agena D vehicle. The self-destruct charge is also compared with two similar ordnance components used for liquid-propellant destruct systems.

I. Introduction

When a satellite vehicle is launched from a national test range, range safety policies require that the satellite vehicle have flight-termination capability. For a liquid-propellant vehicle such as the Agena D satellite vehicle, the capability both for zero thrust and for propellant dispersion must be provided in accordance with safety procedures and directives. The flight-termination system for the Agena D satellite vehicle meets the requirements of the Range Safety Manual (Ref. 1) and is commonly referred to as the vehicle self-destruct system.

The self-destruct system consists of several electrical components, such as radio antennas and signal receivers,

electrical circuitry, and two power sources, as well as the two ordnance devices: one, the safe-and-arm initiator, and the other, the actual vehicle-destruct charge. This system is located in the booster adapter section — the vehicle section that joins the Agena satellite vehicle to its launch vehicle. It is a fully qualified system that meets the Agena D program requirements, and it has performed within the design criteria when vehicle destruction was required during launch.

For the purpose of this paper, the vehicle-destruct charge (called the self-destruct charge) was selected because of its unique application and adaptation to a space or satellite vehicle-destruct system.

II. Design and Performance Criteria

A. Design Philosophy

The range safety policies for liquid-propellant vehicles require that the vehicle provide both a zero-thrust condition and a propellant dispersal condition during a flight termination. It was the design philosophy of the *Agna D* program to meet these two conditions by (1) cutting off the liquid propellant's flow to the thrust engine of the space launch vehicle to achieve the zero-thrust condition and (2) dispersing the two liquid propellants by allowing them to mix together and burn spontaneously as a result of their hypergolic characteristic. The engine cutoff was to be achieved through the space launch vehicle's propulsion system, while a separate destruct system was required for the dispersion of the *Agna D* vehicle's liquid propellant.

As shown in Fig. 1a, the two liquid propellants are carried in two aluminum tanks in a longitudinal arrangement with the top or forward tank containing the fuel—unsymmetrical dimethylhydrazine (UDMH) and the bottom or aft tank containing the oxidizer, inhibited red fuming nitric acid (IRFNA). These tanks are approximately 60 in. in diameter, with hemispherical bulkheads having a wall thickness of 1/16 in. The fuel feed pipe from the fuel tank runs through the oxidizer tank to the thrust engine, which is located below the oxidizer tank bulkhead.

In order to mix the two propellants, either the internal tank bulkhead had to be ruptured or the fuel feed pipe had to be ruptured inside the oxidizer tank. In addition to the requirement for rupturing the propellant tank bulkhead or the fuel feed pipe, the destruct system was weight-constrained to the condition in which none of the destruct system components could remain with the *Agna D* vehicle in space flight. Other design criteria required that the destruct system be impervious to environmental conditions of ground storage, ground transportation, normal launch pad operation, and launch conditions.

The self-destruct system was designed to remain with the booster adapter section and the booster vehicle and was therefore located on the booster adapter skin. This location of the self-destruct charge required the penetration of the oxidizer propellant tank through 52 in. of propellant and two tank bulkheads of 1/16-in. thickness. In addition, the self-destruct charge was located at a 25-deg angle with the longitudinal axis of the vehicle to sever the fuel feed pipe at its junction with the fuel tank inside the oxidizer tank. These penetration requirements dic-

tated an explosive component composed of a shaped charge with a metal cone.

This application of a shaped charge was unique, since this type of charge was originally developed for military applications where penetration of steel, ground, concrete, and other solid media was required. The penetration capability of the shaped charge in metals was dependent on the velocity of the metal jet formed when the explosive component exploded and collapsed the metal cone. It was not usually applied to designs that required travel of the jet through liquids, since the liquids drastically affected the jet velocity. The normal practice was to rate the shaped-charge design in terms of mild steel penetration or of armor steel penetration. This method of rating had no direct correlation with the behavior of the jet nor with the capability of the jet to penetrate a liquid. Therefore, the available data on shaped-charge design as applied to penetration in liquids was very limited in its usefulness.

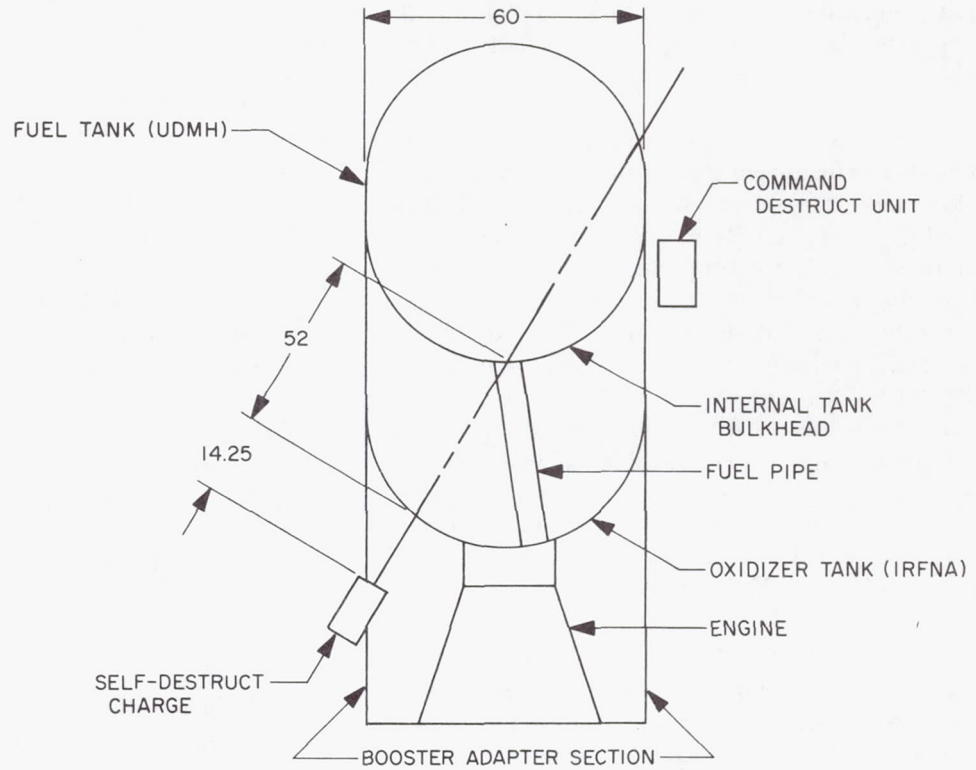
B. Performance Criteria

Through an extensive development program in which the parameters controlling the jet penetration in both mild steel targets and simulated vehicle propellant tanks were investigated, a final shaped-charge design was selected for the self-destruct charge (Fig. 1b), consisting of a charge of plastic-bonded RDX explosive pressed over a nickel-chrome-plated, 60-deg angle, truncated copper cone for the shaped-charge effect, and encased in an aluminum housing. A lip was provided at the bottom of the housing to retain the charge and cone assembly. The opposite end of the housing was threaded to receive a closure plate. The closure plate had six helicoils embedded in the top for mounting the initiator and contained a machined recess to hold a booster pellet. With sealant applied at the closure plate and at the cone-to-casing joint, the shaped-charge unit was sealed against moisture and tampering. The self-destruct charge had a 3.6-in. outer diameter and was 5.37 in. long; maximum weight was 4.0 lb.

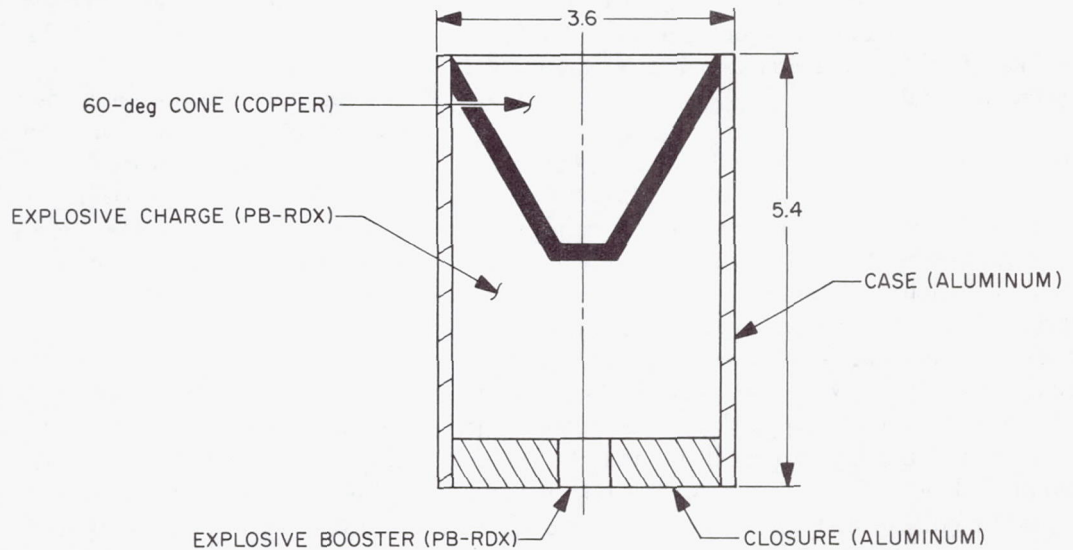
The self-destruct explosive charge contained 800 g of PB-RDX. The PB-RDX composition was 90% RDX, 8.5% polystyrene, and 1.5% dioctylphthalate. This composition was pressed to a uniform density of 1.6 to 1.7 g/cm³.

This final shaped-charge design penetrated a distance of 14.0 to 17.5 in. into a mild steel target at a standoff distance of 9.2 in. The optimum standoff was calculated at 21.3 in., with a corresponding penetration distance of 18.9 in. in mild steel. The jet velocity had been calculated

(a) AGENA D VEHICLE PROPELLANT TANK



(b) SELF-DESTRUCT CHARGE



DIMENSIONS IN INCHES

Fig. 1. Propellant tank and self-destruct design features

to range from 2,000 m/sec to 7,000 m/sec for penetration of the steel target. These values compare favorably with the jet velocities for mild steel penetration presented in Ref. 2. At a 14.25-in. standoff, this final shaped-charge design also penetrated two 1/8-in.-thick aluminum bulkheads, separated by 60 in. of oxidizer propellant IRFNA with a density of 1.6 g/cm³.

The formation of the jet, the initial jet velocities, and the initial slug velocities are the same for both types of penetration, since these characteristics are dependent on the shaped-charge design. The mechanism of penetration for the mild steel target is primarily dependent upon the velocity of the jet. The velocity of the slug is too slow for any effective penetration and can be disregarded. The mechanism of penetration for the oxidizer propellant is primarily dependent upon the velocity of the slug and secondarily upon the jet. The velocity of the jet drops rapidly from the initial levels of 2,000–7,000 m/sec in the sonic region to the subsonic region in the first 11 to 13 in. of travel in the oxidizer propellant and then proceeds through the balance of the tank (47 to 49 in.) in the subsonic region at 300 to 600 m/sec.

The velocity of sound in the oxidizer propellant at ambient temperature is 910 m/sec. The initial slug velocity was calculated at 500 to 650 m/sec (subsonic) and was slightly reduced by the oxidizer propellant to 400 to 450 m/sec. Another factor that affected the propellant penetration was the mass of the slug (120 g) versus the mass of the few jet particles (5 to 10 g) that fully penetrated the propellant and the second aluminum bulkhead. These shaped-charge characteristics are consistent with data presented in Ref. 3.

Performance testing, to date, includes 40 tests for mild steel penetration and 36 tests for oxidizer/propellant penetration. The mild steel penetration test data present an average depth of penetration of 15.84 in. and a standard deviation of 0.89 in. The oxidizer propellant penetration test data indicate 35 successful penetrations in 36 tests. The one failure occurred on a unit considered marginal because of excessive open cracks in the explosive. Analysis of 36 simulated tank tests indicates the jet fully penetrated the liquid propellant and the second aluminum bulkhead 92% of the time, while the slug fully penetrated, except for the one case noted above, 100% of the time. Also, analysis of the penetration of a 1-in.-thick aluminum witness plate, located 4 in. behind the second aluminum bulkhead in the same test setup, indicates the jet penetrated the plate 55% of the time while the slug penetrated 83% of the time.

III. Manufacturing and Testing Techniques

The manufacture and the acceptance testing of each flight lot of self-destruct charges are programmed at the Santa Cruz Test Base facilities of the Lockheed Missiles and Space Company. Programming is normally set to produce a flight lot of 50 to 60 self-destruct charges with a minimum flight lot of 25 charges. Each flight lot is acceptance-tested before it is released for flight. Ten self-destruct charges are randomly selected from each flight lot and are subjected to simulated ground and flight environmental conditions before being tested for penetration performance. Minimum penetration performance levels of 12.75 in. in mild steel, and a tank bulkhead penetration hole area of 0.8 in.², have to be met before the lot is accepted for flight use.

The manufacture of the self-destruct charge is not a complicated technique, but it does require good process control to maintain uniformity, quality, and reliability of penetration performance. Essentially, the assembly consists of the following operations:

- (1) Machining and plating of the metal parts, the aluminum case and closure, and the copper cone.
- (2) Mechanically pressing the PB-RDX explosive charge onto the copper cone.
- (3) Pressing the PB-RDX explosive booster pellet.
- (4) Assembling the explosive charge and explosive booster pellet into the aluminum case and closure.

Good process control must be observed during the machining of the copper cone, pressing of the explosive charge onto the copper cone, and pressing of the explosive pellet. This is necessary since the wall thickness and concentricity of the copper cone and the overall pressed density of the explosive charge significantly affect the penetration performance.

Each self-destruct charge that is selected for acceptance testing is submitted to a dimensional and X-ray inspection for conformance with drawing and specification requirements. Three X-ray films are taken of each self-destruct charge and read for any anomalies such as excessive and open cracks in the explosive component, deformation of the copper cone, air gaps at the explosive component/copper cone interface and the explosive component/explosive booster interface. If a self-destruct charge does not meet the drawing and specification requirements, it is rejected and a new sample is selected

in its place and is submitted to the same inspection criteria.

After each self-destruct charge is accepted, the charges are divided into two groups: one group to be subjected to a mild steel penetration test, and the other group to be subjected to a simulated vehicle tank penetration test. However, prior to the performance tests, one charge is removed from each group as a control sample and the remaining four charges in each group are submitted to a 7-day, MIL STD 331 temperature and humidity test, per method 105, to simulate ground storage and launch pad environmental conditions. Next, the same four charges from each group are submitted to launch-simulated mechanical environments, such as a shock test, acceleration test, and a vibration test (including both sinusoidal and random levels).

After completion of the launch mechanical environmental tests, the four charges of each group are divided into two subgroups of two charges each. Then each of the two subgroups and the control group from the two performance test groups are submitted to the pertinent performance test at various flight environmental conditions of temperature and altitude. The control groups are performance-tested at ambient temperature and altitude; two of the subgroups are tested at 260°F and ambient altitude; the last two subgroups are tested at 200°F and a simulated minimum altitude of 200,000 ft.

IV. Flight Performance

Since full-scale vehicle-destruct testing is very costly and is not practical, only two simulated full-scale destruct tests have been performed with the self-destruct charge. The first test was performed in September 1960 at the beginning of the *Agena* program, and the second test was performed in August 1965 at a vehicle design improvement milestone. There was a minor tank design change between the two tests that affected the vehicle destruct system. In the first test, the tank configuration was the same as that shown in Fig. 1a (*Agena B* or *Agena D*, S-01A configuration). In the second test, the fuel pipe connection to the inner fuel tank bulkhead had been redesigned to include a spherical sump (*Agena D*, S-01B configuration). The sump wall reduced the travel distance of the jet and slug in liquid propellant from 52 in. to 50 in.

Analysis of the damaged simulated tank resulting from the first test (S-01A configuration) indicated that the self-

destruct charge had successfully penetrated the fuel tank inner bulkhead and severed the fuel pipe at the junction with the inner bulkhead. The tank damage occurred on the aligned "line of sight" of the self-destruct charge.

Analysis of the damaged simulated tank resulting from the second test (S-01B configuration) again indicated successful penetration of the fuel sump and the fuel tank inner bulkhead. Figure 2 shows the damage to the initial oxidizer tank bulkhead and to the fuel tank sump. To be noted is the configuration of the slug and of the impact area of the slug on the 1-in.-thick aluminum witness plate. The damage to the fuel tank inner bulkhead was recorded on another photograph and was not available for the paper.

Figure 3 summarizes the damage caused by the self-destruct charge to an *Agena* vehicle propellant tank (S-01A configuration) during an actual flight destruction. An analysis and inspection of the recovered propellant tank showed that the self-destruct charge severed the fuel pipe at the line of sight, 57 to 58 in. from the oxidizer bulkhead. Penetration of the fuel tank bulkhead was achieved, since the fuel tank wall showed evidence of propellant burning. The self-destruct charge penetrated the oxidizer tank bulkhead on the line of sight and made a hole approximately 6 in. in diameter.

A visual comparison between the actual flight destruct damage and the destruct damage of both full-scale simulated tank tests indicated that the flight self-destruct charge functioned as required. It penetrated the oxidizer tank and fuel tank at the line of sight, with sufficient force to initiate mixing, dispersion, and burning of the two liquid propellants. In addition, the condition of zero thrust was achieved by the space launch vehicle as the *Agena D* satellite vehicle was placed in a tumbling trajectory that broke the vehicle apart.

V. Comparison of Similar Ordnance Components

A brief description of two other similar ordnance components is presented to illustrate other design principles used for liquid-propellant vehicle-destruct systems. One component is the optional destruct unit (command destruct) for the *Agena* satellite vehicle; the other is the explosive destruct charge for a space launch vehicle that uses a liquid-propellant system. The command destruct unit is flown on the *Agena* satellite vehicle if the capability for vehicle destruction is required after launch vehicle separation, and in early orbital trajectory.

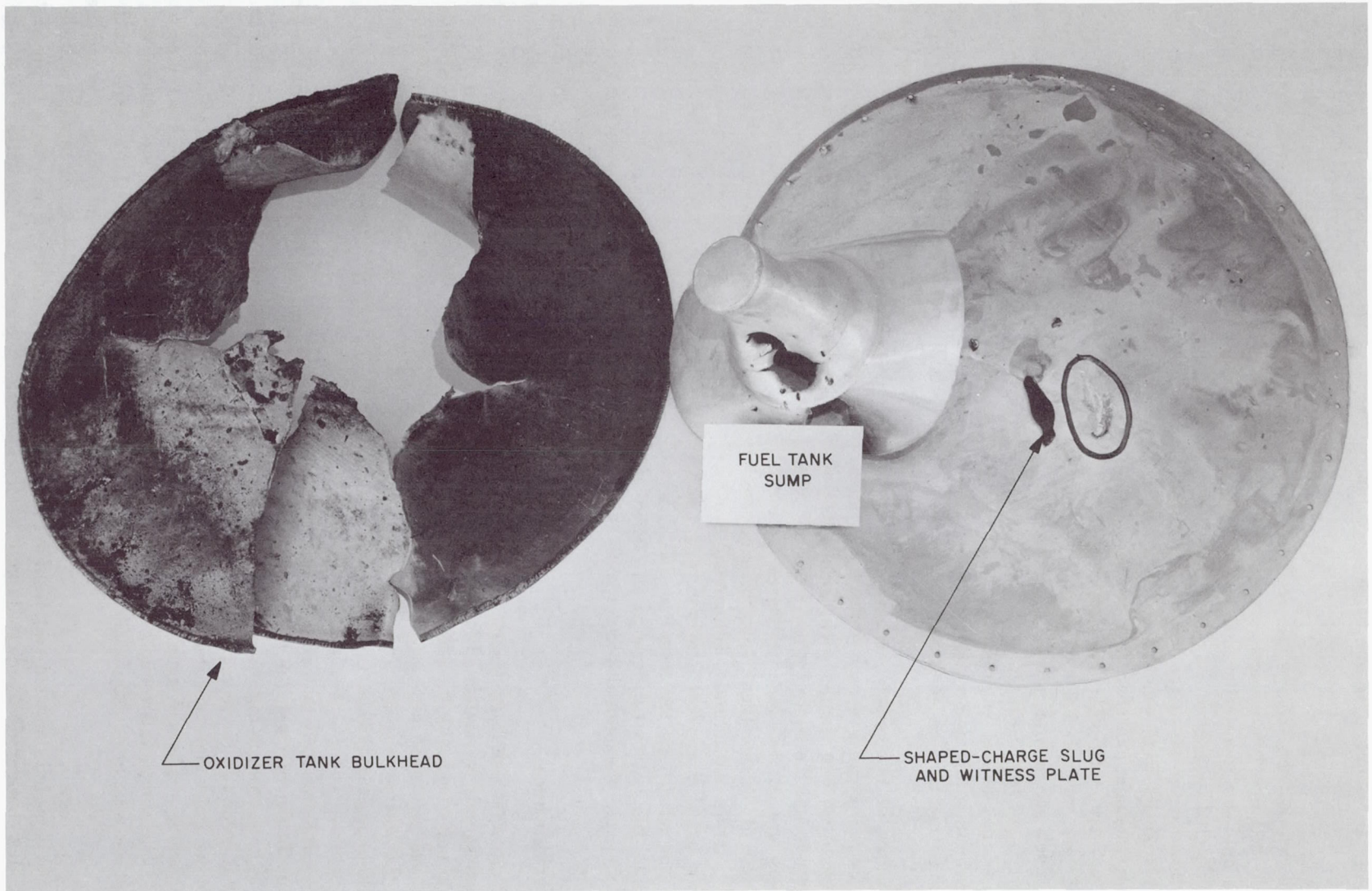


Fig. 2. Tank damage, S-01B configuration, for simulated full-scale destruct test

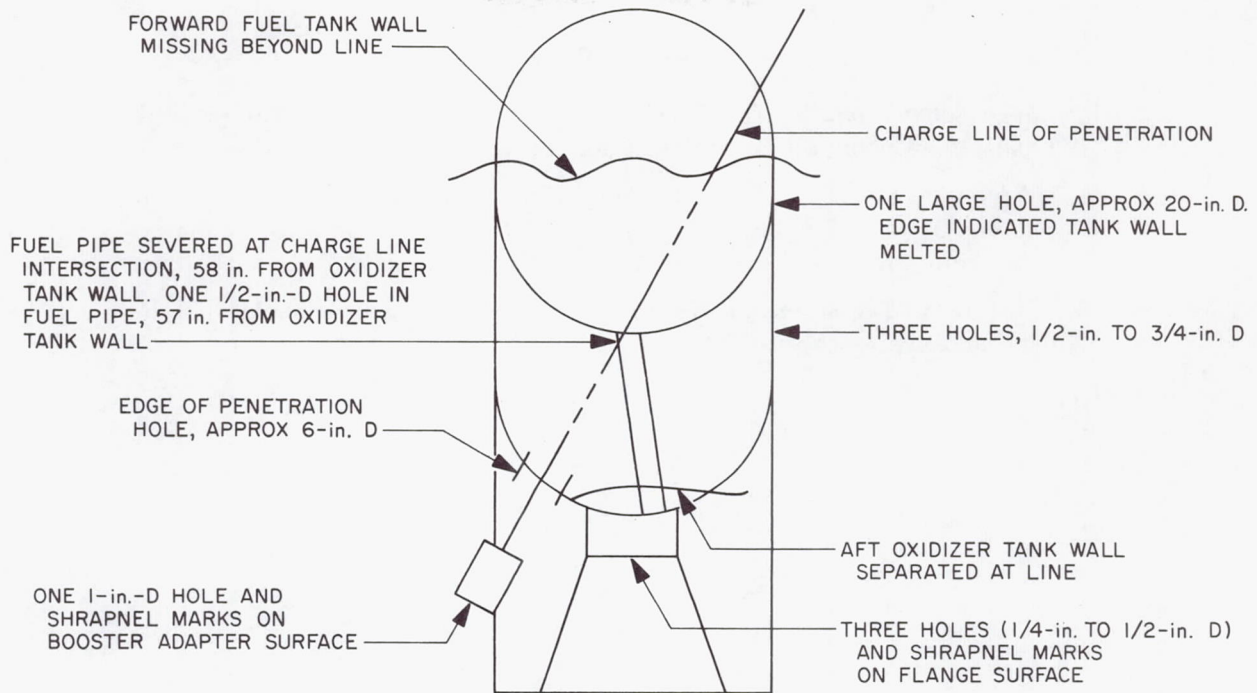


Fig. 3. Propellant tank damage pattern for a flight destruction

Since the command destruct system is designed to remain with the satellite vehicle during flight, the command destruct unit (Fig. 1a) is located on the vehicle skin at the junction of the fuel tank with the oxidizer tank (Y-ring). This location requires penetration of the vehicle skin and the diaphragm between the two propellants to achieve vehicle destruction. A small explosive pellet (the main charge assembly), which weighs 13 g, provides the explosive blast energy required for tank penetration. The command destruct unit is required to penetrate the inner diaphragm of the fuel tank with a minimum projected area of 2 in.², and to be capable of causing a minimum dent of 0.050 in. in mild steel block.

A full-scale destruct test was successfully conducted by destroying an *Agena D* (S-01A configuration) fuel tank loaded with propellants with one command destruct unit. Complete destruction of the fuel tank was achieved in less than 1 sec, and the propellants were dispersed in less than 100 msec. This is a qualified design, which accomplishes the same purpose with 13 g of explosive as does the self-destruct charge with 807 g of explosive. However, the use of the command destruct unit and the associated electrical equipment adds approximately 15 lb of on-orbit weight to the vehicle.

The destruct system for the space launch vehicle uses two explosive, bidirectional destruct charges located between the opposing oxidizer tank and the fuel tank. They achieve propellant mixing and dispersion by blasting a large hole (approximately 5 ft in diameter) in the bottom of the oxidizer tank above, and in the top of the fuel tank below. One destruct charge is sufficient to produce the required bidirectional explosive energy, but two destruct charges are used for redundancy. Each destruct charge consists of a flat, explosive charge contained between thin metal plates and completely encased in a thin-walled metal container. The overall weight of each charge is 5 lb maximum, and the explosive weight is approximately 500 g.

VI. Conclusion

The self-destruct charge has successfully accomplished the range safety requirements for liquid-propellant flight vehicle destruction, as demonstrated by the destruction of the *Agena D* satellite vehicle. In this demonstration, the design philosophy was proved, and good agreement was observed with the simulated tank test data.

References

1. *Range Safety Manual*, AFWTRM 127-1, pp. D-1. Air Force Western Test Range, Vandenberg Air Force Base, Calif., February 25, 1966.
2. DiPersio, R., Simon, J., and Merendino, A. B., *Penetration of Shaped-Charge Jets into Metallic Targets*, BRL Report 129. Ballistic Research Laboratories, U. S. Army Materiel Command, Aberdeen Proving Ground, Md., Sept. 1965.
3. Cook, M. A., *The Science of High Explosives*, pp. 226-264. Reinhold Publishing Company, New York, 1958.

List of Attendees

- ABBOTT, HELEN M.
 Lockheed Missiles and Space Company
- ABBOTT, WILTON R.
 Lockheed Missiles and Space Company
- ADAMS, JAMES L.
 Stanford University
- ALLEN, DONALD C.
 General Electric Company
- ALLEN, JOHN H.
 Martin Marietta Corporation
- ANDERSON, ALTON L.
 Philco-Ford Corporation
- ANDERSON, ROY F.
 Lockheed Missiles and Space Company
- ANGERS, THOMAS C.
 Purdue University
- BAKER, DONALD R.
 TRW Systems Group
- BANDAK, MICHAEL N.
 Hexcel Products Inc.
- BELZ, DONALD J.
 Bellcomm, Inc.
- BERRY, THOMAS G.
 Fairchild Hiller Corporation
- BERRY, WILLIAM E.
 NASA Ames Research Center
- BINGEMANN, KARL G., JR.
 Hughes Aircraft Company
- BLOCKINGER, ROY A.
 Lockheed Missiles and Space Company
- BOHLMANN, OTTO
 Lockheed Missiles and Space Company
- BOSSERT, WALTER J.
 Lockheed Missiles and Space Company
- BRACCINI, AL A.
 Dalmo Victor Company
- BRADLEY, GEORGE
 The Boeing Company
- BRANSTETTER, BARTON F.
 University of California, Berkeley
- BREWER, DARRELL D.
 Lockheed Missiles and Space Company
- BROADBENT, KENNETH
 Lockheed Missiles and Space Company
- BROWN, JERRY C.
 Lockheed Missiles and Space Company
- BUCKLEY, DONALD H.
 NASA Lewis Research Center
- BUEHLER, MARY FRAN
 Jet Propulsion Laboratory
- BUSH, KENNETH S.
 NASA Langley Research Center
- BUZZARD, WALLACE C.
 Wright-Patterson Air Force Base
- CAMPI, RICHARD B.
 Lockheed Missiles and Space Company
- CERBONE, VINCENT F.
 Lockheed Missiles and Space Company
- CHAMNESS, O. VAUGHAN
 General Precision Link Group, Ordnance
 Division
- CHASE, DAVID R.
 Lockheed Missiles and Space Company
- CHRISTIAN, WILLIAM D.
 Philco-Ford Corporation
- CLAUSS, FRANCIS J.
 Lockheed Missiles and Space Company
- CLEVETT, MERTON L.
 Martin Marietta Corporation
- COLE, CHARLES W.
 Jet Propulsion Laboratory
- COLLINS, WALTER S.
 Lockheed Missiles and Space Company
- DALLAS, JAMES P.
 Hughes Aircraft Company
- DAVIDSON, ROBERT H.
 NASA Ames Research Center
- DEACON, RICHARD W.
 Microseal Corporation
- DEAL, T. E.
 Hughes Aircraft Company
- DE JONG, PETER N.
 Applied Technology, Inc.
- DEMPSTER, WAYNE E.
 TRW Systems Group
- DRACE, CHARLES A.
 Lockheed Missiles and Space Company
- DUBOWSKY, STEVEN
 Perkin-Elmer Corporation
- DUNKERLY, WILLIAM C.
 Applied Technology, Inc.
- EBERWINE, DONALD A.
 Lockheed Missiles and Space Company
- EDBERG, JAMES R.
 Jet Propulsion Laboratory
- EDWARDS, ROBERT W.
 Lockheed Missiles and Space Company
- ENGELBERT, DAVID F.
 NASA Ames Research Center
- ENGELDER, PAUL O.
 Consultant
- ENYEDY, GABRIEL J.
 Sylvania Electric Products, Inc.
- ERICKSON, EARL W.
 Lockheed Missiles and Space Company
- FALKENTHAL, GEORGE E.
 NASA Ames Research Center
- FERRERA, JOHN D.
 Jet Propulsion Laboratory
- FINKIN, EUGENE F.
 Douglas Aircraft Company
- FINOCHIO, DAN F., JR.
 Quantic Industries, Inc.
- FISHER, EUGENE J.
 University of Santa Clara
- FLEMING, ALAN W.
 Stanford University
- FORD, ALLEN G.
 Jet Propulsion Laboratory
- FRESHOUR, JAMES W.
 Lockheed Missiles and Space Company
- FRISCH, JOSEPH
 University of California, Berkeley
- FUCHS, HENRY O.
 Stanford University
- FURLONG, DALE A.
 United Technology Center
- GATCOMBE, E. K.
 United States Naval Postgraduate School
- GAUTSCHI, GUSTAV H.
 Lockheed Missiles and Space Company
- GEORGES, RANDALL W.
 Sylvania Electric Products, Inc.
- GERBASI, MARTIN J.
 Lockheed Missiles and Space Company
- GIATTINO, PAUL
 International Business Machines
 Corporation
- GIBBONS, GLEN D.
 Lockheed Missiles and Space Company
- GLASSOW, FRANK A.
 Hughes Aircraft Company
- GLOVER, PERRY
 Lockheed Missiles and Space Company
- GOLDBACH, GERHARDT O.
 United Technology Center
- GRADISAR, ALBIN H.
 Philco-Ford Corporation
- GRAM, MARSHALL B.
 Jet Propulsion Laboratory
- GROSCHOPFS, ERNEST
 DeHavilland Aircraft of Canada, Ltd.
- GUDIKUNST, JAMES B.
 Hughes Aircraft Company
- GUSTAFSON, GARY B.
 Eastman Kodak Company
- HACKER, RUSSELL
 Lockheed Missiles and Space Company
- HADLAND, WAYNE O.
 NASA Ames Research Center
- HALLETT, RALPH K.
 NASA Ames Research Center
- HAYES, DUDLEY W.
 Lockheed Missiles and Space Company

List of Attendees (contd)

- HEIM, JOSEPH R.
Lockheed Missiles and Space Company
- HERZL, GEORGE G.
Lockheed Missiles and Space Company
- HEYDON, DOUGLAS A.
TRW Systems Group
- HILLAN, JOHN
Lockheed Missiles and Space Company
- HIMMELRIGHT, RUSSELL M.
NASA Ames Research Center
- HINRICHS, ERIC G.
Lockheed Missiles and Space Company
- HOEPTNER, HERBERT W.
United Technology Center
- HOLM, WESTON
Vitro Laboratories
- HOTZ, HARRY E.
Northrop Corporation
- HOWARD, EARL A.
Jet Propulsion Laboratory
- IMUS, ROBERT E.
Jet Propulsion Laboratory
- INGWERTSON, D. R.
Lockheed Missiles and Space Company
- JEWETT, SAMUEL O.
Jewett Company
- JOFUKU, TOMIO
Sylvania Electric Products, Inc.
- JOHNSON, MANLY E.
Philco-Ford Corporation
- JONES, KENNETH L.
Lockheed Missiles and Space Company
- KAEHLER, ALFRED E.
Lockheed Missiles and Space Company
- KAEHLER, HANS J.
Quantic Industries, Inc.
- KARAM, JAMES T., JR.
United States Air Force
- KEYES, JAMES A.
Lockheed Missiles and Space Company
- KILERT, ALBERT H.
Stanford Linear Accelerator Center
- KINDRED, BOB A.
Dalmo Victor Company
- KIRKPATRICK, DONALD L.
General Electric Company
- KJONTVEDT, ARTHUR J.
Fairchild Hiller Corporation
- KOCSIS, ROBERT W.
Jet Propulsion Laboratory
- KOONTZ, OWEN L.
NASA Ames Research Center
- KRUG, KENNETH L.
Lockheed Missiles and Space Company
- KUSKIE, GERALD E.
United Technology Center
- LAMVERMEYER, DONALD J.
Aerojet-General Corporation
- LAYMAN, WILLIAM E.
Jet Propulsion Laboratory
- LEDBETTER, DANIEL R.
General Motors Corporation Defense
Research Laboratories
- LEMKE, E. R.
Lockheed Missiles and Space Company
- LEMKE, JOHN L.
Lockheed Missiles and Space Company
- LINDBERG, DALE E.
Lockheed Missiles and Space Company
- LOCATELL, FRANK C., JR.
University of California, Berkeley
- LOTT, DAN R.
Lockheed Missiles and Space Company
- LUND, ADOLPH W.
Philco-Ford Corporation
- LYMAN, PETER T.
Jet Propulsion Laboratory
- MACLEAN, CHARLES F.
Lockheed Missiles and Space Company
- MACNAUGHTON, JOHN D.
DeHavilland Aircraft of Canada, Ltd.
- MACOMBER, THOMAS W.
Lockheed Missiles and Space Company
- MAHONEY, JOHN J.
Lockheed Missiles and Space Company
- MANTUS, MORTON
Grumman Aircraft Engineering Corporation
- MATHEWS, RICHARD G.
Ball Brothers Research Corporation
- MCCREARY, RAYMOND A.
Jet Propulsion Laboratory
- MCLERNAN, CHARLES W.
Ohio State University
- MIATECH, GERALD J.
NASA Ames Research Center
- MICHAEL, GRANT
Abrams Instrument Corporation
- MORRIS, WILLIAM L.
Hughes Aircraft Company
- MUELLER, WILLIAM H.
Grumman Aircraft Engineering Corporation
- NEITZEL, FREDERICK J.
Santa Barbara Research Center
- NEW, WILLIAM
Lockheed Missiles and Space Company
- NG, LAWRENCE SO PING
NASA Ames Research Center
- NORMAN, DAVID A.
Lockheed Missiles and Space Company
- NORRIS, ROBERT J.
Stanford Linear Accelerator Center
- NORTON, GEORGE H.
Sperry Rand Corporation
- NOTHWANG, GEORGE J.
NASA Ames Research Center
- O'BOYLE, RICHARD C.
Lockheed Missiles and Space Company
- OETH, PHILLIP J.
Eastman Kodak Company
- OLSEN, JOSEPH C.
Lockheed Missiles and Space Company
- PACKER, ROBERT
Radio Corporation of America,
Astro-Electronics Division
- PARCEL, R. WAYNE
Lockheed Missiles and Space Company
- PAUL, ROBERT
Lockheed Missiles and Space Company
- PEFLEY, RICHARD K.
University of Santa Clara
- PERPI, ROBERT E.
Lockheed Missiles and Space Company
- PILACINSKI, JERZY
Lockheed Missiles and Space Company
- POWNALL, WALLACE H.
United Technology Center
- QUICK, JAMES D.
Edgerton, Germeshausen & Grier, Inc.
- RADOVCICH, NICK
Lockheed Missiles and Space Company
- RAMOS, DANIEL O.
General Electric Company
- RENNIE, BRUCE B.
The Boeing Company
- RINALDO, ALFRED L.
Lockheed Missiles and Space Company
- ROMVARY, ERNEST
Jet Propulsion Laboratory
- ROTH, BERNARD
Stanford University
- SAAD, MICHEL A.
University of Santa Clara
- SAMUELS, RONALD L.
TRW Systems Group
- SCHIMANDLE, WILLIAM J.
Jet Propulsion Laboratory
- SCHWARTZ, WILLIAM
Philco-Ford Corporation
- SEELIG, FREDERICK A.
Bendix Corporation
- SELENE, LLOYD J.
Stanford Linear Accelerator Center
- SHAPERO, CHESTER B.
NASA Ames Research Center
- SHIGEMOTO, JOHN M.
Lockheed Missiles and Space Company

List of Attendees (contd)

SINGLETARY, JOHN B.
Lockheed Missiles and Space Company

SMITH, ALLAN H.
Lockheed Missiles and Space Company

SMOLA, JAMES F.
Johns Hopkins University

STEIDEL, ROBERT F.
University of California, Berkeley

STICKLEY, ROSS A.
Martin Marietta Corporation

STRAIN, JEROME D.
Sylvania Electric Products, Inc.

STRIBLING, MAURICE D.
Hughes Aircraft Company

SUMSION, H. T.
NASA Ames Research Center

SUPPLE, RODNEY W.
NASA Ames Research Center

THIELKE, JOHN F.
Varian Associates

THOMPSON, ALBERT L.
General Precision Link Group, Ordnance
Division

THOMSON, CHARLES M.
Lockheed Missiles and Space Company

THUET, RONALD K.
Sperry Rand Corporation

TORRES, DAVID
Lockheed Missiles and Space Company

TOTAH, N. I.
Philco-Ford Corporation

UBER, EDWARD F.
Lockheed Missiles and Space Company

UPTON, DEAN T.
Santa Barbara Research Center

VENTURA, ANGEL H.
Lockheed Missiles and Space Company

VOGEL, RONALD W.
Microseal Corporation

WATTENBARGER, ROBERT L.
TRW Systems Group

WEISSENBARGER, STEIN
University of Santa Clara

WEYMAN, HUGH N.
DeHavilland Aircraft of Canada, Ltd.

WHEELER, BRYCE A.
Hughes Aircraft Company

WICKHAM, DALE D.
Lockheed Missiles and Space Company

WIEDEMAN, ROBERT A.
Philco-Ford Corporation

WILHELM, JOHN B.
Martin Marietta Corporation

WILLIAMS, DAVID R.
Ryan Aeronautical Company

WILLIAMS, F. L.
Lockheed Missiles and Space Company

WILLIAMS, JOHN A.
Lockheed Missiles and Space Company

WORTZ, JAMES H.
Sylvania Electric Products, Inc.

WUTHERICH, HERMANN A.
Hughes Aircraft Company

YANG, AN T.
University of California, Davis